

Electronic Thesis and Dissertation Repository

3-21-2019 2:15 PM

Corrosion Studies on Lightweight Automotive Alloys: The Effect of Microstructure and Fundamental Mechanisms

Wilfred J. Binns
The University of Western Ontario

Supervisor
Shoesmith, David W.
The University of Western Ontario

Graduate Program in Chemistry
A thesis submitted in partial fulfillment of the requirements for the degree in Doctor of Philosophy
© Wilfred J. Binns 2019

Follow this and additional works at: <https://ir.lib.uwo.ca/etd>

 Part of the [Analytical Chemistry Commons](#), and the [Physical Chemistry Commons](#)

Recommended Citation

Binns, Wilfred J., "Corrosion Studies on Lightweight Automotive Alloys: The Effect of Microstructure and Fundamental Mechanisms" (2019). *Electronic Thesis and Dissertation Repository*. 6054.
<https://ir.lib.uwo.ca/etd/6054>

This Dissertation/Thesis is brought to you for free and open access by Scholarship@Western. It has been accepted for inclusion in Electronic Thesis and Dissertation Repository by an authorized administrator of Scholarship@Western. For more information, please contact wlsadmin@uwo.ca.

Abstract

Owing to their excellent strength-to-weight ratio and low density, magnesium alloys have the potential to significantly reduce the weight of automobiles leading to decreased emissions and greater range for electrical vehicles. However, the practicality of magnesium alloys for automotive and aerospace applications is severely hindered by their poor corrosion resistance in aqueous environments. Despite intensive research effort, the underlying mechanism(s) responsible for this poor corrosion resistance remains elusive. Further complicating the situation is the presence of secondary microstructures which are necessary for desirable physical properties but lead to microgalvanic coupling which exacerbates the poor corrosion resistance of magnesium alloys. This work utilizes a combination of electrochemical and surface analytical techniques to investigate the role of microstructure in magnesium alloy corrosion.

The role of magnesium as an alloying addition to another lightweight material, aluminum, has been investigated. A combination of bulk electrochemistry (E_{CORR} and PDP), localized electrochemistry (SECM) and surface analysis (SEM) are utilized. Bulk electrochemistry reveals that greater amounts of magnesium, which is insoluble in aluminum, leads to activation of the matrix towards oxidation. Time dependent SECM tracking local cathodes over several days reveals very little difference on the cathodic kinetics as a function magnesium content.

The effect of microstructure size and distribution of secondary microstructures present in an Mg AM50 alloy are investigated as a function of Cl^- concentration, electrolyte solvent, time and microstructure size and distribution using EIS. By fitting data with a physically justified equivalent electrical circuit values of R_p are extracted. This shows that as conductivity of solution decreases the effect of microstructure size and distribution diminishes, trending toward unity in highly resistive electrolytes.

Cathodic galvanostatic polarization of a Mg ZEK100 alloy is shown to exhibit cathodic current densities at anodic applied potentials. Surface analysis (XRD and SIMS) reveals that the pretreated sample is enriched with magnesium hydrides. Furthermore, the hydrides are

shown to exist within and leading the common “filiform-like” corrosion morphology that is typical of magnesium alloys.

Wedge casting is utilized to examine the effect of cooling rate on the corrosion performance of Mg ZEK100 alloy. A combination of bulk electrochemistry and surface analysis are utilized to show that a faster cooling rate leads to the initiation and propagation of filiform-like corrosion more quickly than slower cooling rates.

Keywords

Magnesium alloys, magnesium, aluminum alloys, corrosion, lightweight alloys, electrochemistry, negative difference effect, anomalous hydrogen evolution, anodic hydrogen evolution, surface analysis, microstructure.

Co-Authorship Statement

This thesis contains published data. For the work I was the lead investigator and writer and performed the experimental portions with assistance from:

Chapter 3: J. Henderson assisted with SECM experiments and D. Shoesmith assisted with editing.

Chapter 4: M. Asmussen assisted with experimental design, A. Kirkey assisted with electrochemical experiments and D. Shoesmith assisted with editing.

Chapter 5: J. Chen assisted with experimental design, F. Zargarzadah assisted with electrochemical experiments, G. Good assisted with SIMS experiments, V. Dehnavi assisted with XRD experiments and D. Shoesmith and J. Noël assisted with editing.

Chapter 6: M. Asmussen assisted with alloy design, A. Kirkey assisted with electrochemical experiments and D. Shoesmith assisted with editing.

Acknowledgments

First and foremost, thank you to Professor Dave Shoesmith. Without your knowledge and guidance none of this would have been possible. I, like so many others, will be forever in your debt for the positive influence you have exerted on my personal and professional development. Your scientific achievements and contributions are world-class and are exceeded only by the quality of your character. It makes you wonder how a man with such sound judgement can root for Newcastle United, but then again, whom among us is perfect?

To the four-horsemen of the group: Dr. Jamie Noel (now professor, congratulations), Dr. Zack Qin, Dr. Dmitrij Zagidulin and Dr. Jian Chen, thank you for the many discussions, questions and teachings. Much of my development both experimentally and theoretically is because of you. I am grateful that we will be able to work together in the future and look forward to the many scientific discussions, arguments and fights that follow. In addition to Jamie's electrochemical mastery, Zack's impedance wizardry, Dmitrij's laboratory prowess and Jian's passion, your friendship is greatly appreciated.

For all fellow Shoesmith graduate and undergraduate students, past and present, your comradery and companionship were always welcome distractions from tough lab days, weeks and months. To Dr. Matthew Asmussen and Dr. Pellumb Jakupi, much like Dave your exceptional guidance and teaching has led me to this point. Also like Dave, your judgement in sports teams leaves much to be desired but at least we can agree on the Blue Jays. Working with you guys during my fourth-year undergraduate thesis (and beyond) was the single most influential and inspiring experience of my scientific career. I can't thank you enough for your willingness to include me in scientific, tutoring and culinary endeavors throughout the years, even though I always had to share a bed with "Bad Dad".

To the L.A. Batts, the greatest beer-league hockey team in South Western Ontario, thanks for all the memories. The few yearly gatherings and GM meetings have helped to keep me grounded during graduate school. Here's to many more games and one day hoisting the revered Stonetown Easter Tournament Cup!

To my family, your unwavering support throughout this chapter of my life is something that I will never forget and can only hope to repay in the future. Mom and Dad, your grounding

gave me the confidence and perseverance needed to see this project through to the end. Nathan and Melissa, the fishing trips and BBQs have helped me clear my head and forget about the lab for a day or two, which, beyond being great fun have contributed to my creativity as a scientist. Andrew, Natalie and Blake, you have been my rock. The countless (free) dinners and craft beer nights are what made London feel like home. To Jordan (yes, it is Jordan) and Cassie, you have truly made my transition to Toronto a breeze. Thanks for all the love, support and discussion (arguments) at Kilgour's.

Table of Contents

Abstract	i
Co-Authorship Statement.....	iv
Acknowledgments.....	v
Table of Contents	vii
List of Tables	xii
List of Figures	xiii
List of Symbols and Acronyms.....	xxv
1 Introduction	1
1.1 Background.....	1
1.2 Light-weighting of Vehicles: Magnesium Alloys.....	6
1.3 Fundamentals of Aqueous Corrosion.....	7
1.3.1 Thermodynamics of Corrosion	7
1.3.2 Electrochemical Kinetics and Corrosion Kinetics	14
1.4 Aqueous Corrosion of Magnesium and its Alloys	20
1.4.1 Corrosion of Mg: The Basics	20
1.4.2 Effect of Secondary Phases: Microgalvanic Coupling	21
1.4.3 Corrosion Morphology.....	24
1.4.4 The Anomaly of Anodic Polarization	26
1.4.5 Role of Alloying Elements in the Corrosion of Mg Alloys.....	28
1.4.6 Effects of Microstructure on Magnesium Corrosion	31
1.5 Scope of Thesis	33
1.6 References	35
2 Experimental	42
2.1 Materials and Material Preparation.....	42

2.1.1	Al Alloys	42
2.1.2	Mg Alloys	43
2.2	Chromic Acid Treatment	46
2.3	Microscopy	47
2.3.1	Optical Microscopy.....	47
2.3.2	Scanning Electron Microscopy	50
2.3.3	Energy Dispersive X-ray Spectroscopy	55
2.3.4	Focused Ion Beam (FIB) Cross Sectioning	58
2.3.5	Electron Backscatter Diffraction.....	59
2.3.6	Confocal Laser Scanning Microscopy	61
2.4	Electrochemical Methods.....	63
2.4.1	Corrosion Potential	65
2.4.2	Potentiodynamic Polarization	66
2.4.3	Electrochemical Impedance Spectroscopy	66
2.4.4	Scanning Electrochemical Microscopy.....	69
2.5	X-ray Diffractometry	72
2.5.1	Diffraction Principles.....	72
2.5.2	Instrumentation	74
2.6	Dynamic Secondary Ion Mass Spectrometry.....	75
2.6.1	Dynamic SIMS Principles.....	75
2.7	References.....	79
3	The Effect of Mg Content on the Corrosion Behaviour of Al-Mn-Cu-Mg Alloys for Automotive Heat Exchanger Brazing Sheets.....	80
3.1	Introduction.....	80
3.2	Experimental.....	81
3.2.1	Material Preparation.....	81

3.2.2	Bulk Electrochemical Experiments.....	82
3.2.3	SECM Arrangement.....	82
3.3	Results.....	84
3.3.1	Microstructure.....	84
3.3.2	Electrochemistry and Corrosion Experiments	88
3.3.3	SECM.....	93
3.4	Discussion.....	100
3.5	Conclusions and Future Work	102
3.6	References.....	104
4	Impedance Study on the Effect of Casting Procedure on the Corrosion Behaviour of Mg AM50 Alloy.....	105
4.1	Introduction.....	105
4.2	Experimental.....	107
4.2.1	Materials and Preparation	107
4.2.2	Electrochemical Experiments	108
4.2.3	Microscopy	109
4.3	Results.....	109
4.3.1	Material Characterization.....	109
4.3.2	Electrochemical Experiments	111
4.4	Discussion.....	126
4.5	Conclusions.....	128
4.6	References.....	130
5	Physical and Electrochemical Evidence for the Role of a Mg Hydride Species in Mg Alloy Corrosion.....	133
5.1	Introduction.....	133
5.2	Experimental Procedure.....	135
5.2.1	Materials and Material Preparation.....	135

5.2.2	Electrochemical Experiments	136
5.2.3	X-ray Diffraction Analysis	137
5.2.4	Scanning Electron (SEM) and Optical Microscopy.....	137
5.2.5	Dynamic Secondary Ion Mass Spectrometry.....	138
5.2.6	In situ Corrosion Monitoring	139
5.3	Results.....	139
5.3.1	Electrochemical Characterization of As-polished and Cathodically Pretreated Mg ZEK100 F.....	139
5.3.2	Physical Characterization of Cathodically Pretreated Alloys.....	141
5.3.3	In situ Monitoring of Corrosion.....	143
5.3.4	Physical Characterization of Mg ZEK100 Corroded at E_{CORR}	147
5.4	Discussion.....	153
5.5	Conclusions.....	159
5.6	References.....	161
6	The Effect of Cooling Rate on the Corrosion Properties of Mg ZEK100	164
6.1	Introduction.....	164
6.2	Experimental.....	166
6.2.1	Materials	166
6.2.2	Electrochemical Measurements	168
6.2.3	Microscopy	168
6.2.4	Corrosion Product Removal.....	169
6.3	Results.....	169
6.3.1	Wedge Cast Microstructure	169
6.3.2	Electrochemical Behaviour.....	174
6.3.3	Analysis of Corroded Surfaces	178
6.4	Discussion.....	185

6.5 Conclusions.....	189
6.6 References.....	190
7 Summary and Future Work.....	192
Curriculum Vitae	195

List of Tables

Table 1.1: List of alloying elements common to magnesium alloys and their influence on alloy properties.....	31
Table 2.1: Compositions of the three Al alloys investigated.....	43
Table 3.1: Chemical compositions of each Al alloy in wt%. Compositions were supplied by CANMET Materials, Hamilton, Ontario, Canada.....	84
Table 4.1: Equivalent electrical circuit element values for SC, GC and DC Mg AM50 alloys immersed in 0.3, 0.03 and 0.003 M NaCl solution for 10, 20 and 30 h.....	121
Table 6.1: Inductively coupled plasma mass spectrometry (ICP-MS) elemental analysis for sections A, D, G and M of a wedge cast Mg ZEK100 alloy in weight %.....	169

List of Figures

Figure 1.1: Concentration of CO ₂ (in ppm) versus time since 1950. Data was gathered by measuring the [CO ₂] as a function of depth in ice cores recovered from Greenland and the Arctic. Figure from https://climate.nasa.gov/vital-signs/carbon-dioxide/ . ⁶	2
Figure 1.2: Global surface temperature as a function of year recorded by four independent agencies. Temperatures are given as their deviation from a standard reference point. Figure from https://climate.nasa.gov/vital-signs/global-temperature/ . ¹²	2
Figure 1.3: Total mass of carbon in megatonnes emitted by different Canadian economic sectors as a function of year. Figure from https://www.ec.gc.ca/indicateurs-indicators/default.asp?lang=en&n=F60DB708- . ¹⁵	4
Figure 1.4: The effect of vehicle mass on fuel consumption for an automobile. Note the exponential increase in fuel savings with decreasing vehicle mass. Figure from reference 21.5	
Figure 1.5: Examples of current applications of magnesium alloys in vehicles. Notably, each application occurs on the interior of the vehicle to prevent exposure of the magnesium alloy to the environment. Figure from reference 22.	5
Figure 1.6: Pourbaix diagram for magnesium immersed in water at 25°C and a [Mg ²⁺] = 10 ⁻⁵ mol/L. ⁻¹ . ²⁴	9
Figure 1.7: Pourbaix diagram for magnesium immersed in water at 25°C. The red arrow indicates the effect of decreasing [Mg ²⁺] and the blue arrow indicates the effect of increasing pH. The numbers associated with the lines are [Mg ²⁺] expressed logarithmically. Figure from reference 25.....	12
Figure 1.8: Current-potential relationship (solid line) for a generic, reversible electrochemical reaction with anodic and cathodic transfer coefficients equal to 0.5. This process is described by the Butler-Volmer relationship. E is the applied potential, E ^e is the equilibrium potential, η is the overpotential and I ^o is the exchange current density. The dashed lines show the currents associated with the forward and reverse reactions.....	15

Figure 1.9: (black) Current-potential relationship for a generic metal oxidation coupled to an oxidant reduction where E_{CORR} is the potential at which the current for the cathodic half-reaction equals the current for the anodic half-reaction which equals I_{CORR} . (blue) & (red) Current potential relationship for the oxidant reduction and metal oxidation reactions, respectively. 20

Figure 1.10: Schematic representation of the microgalvanic coupling process occurring on a Mg AM50 alloy. Here, the more noble secondary phase ($Mg_{17}Al_{12}$) supports the cathodic reaction while the magnesium matrix is oxidized..... 22

Figure 1.11: Evans diagram illustrating the effect of a galvanic couple on the corrosion kinetics of a noble, uncoupled metal (blue) and an active, uncoupled metal (red). The result of the galvanic couple is illustrated in black..... 23

Figure 1.12: (a and b) SEM micrographs of a corroded Mg ZEK100 alloy surface showing the morphology of the general corrosion product and corrosion product domes. (c) SEM micrograph showing the enhanced dissolution of the magnesium matrix compared to regions occupied by secondary microstructures on a Mg AM50 alloy. (d) Optical micrograph showing the morphology of the filiform-like corrosion morphology on a Mg ZEK100 alloy. 24

Figure 2.1: (a) Mg ZEK100 wedge cast ingot, with a 30 cm ruler as a reference scale, and series of six thermocouples attached to one end. (b) End view of the Mg ZEK100 wedge cast with 5 cm of the end removed to cut out the thermocouples. A 1 cm thick portion was sectioned down the center line to create samples with gradients in cooling rate. (c) Final samples are labelled alphabetically with sample A being taken from the narrow tip of the wedge cast. 45

Figure 2.2: Scanning electron micrographs of a corroded Mg ZEK100 wedge cast alloy (a) before and (b) after a chromic acid treatment to remove the $Mg(OH)_2$ corrosion product. ... 46

Figure 2.3: Schematic illustration of the basic optical principles of image formation and magnification in an optical microscope. The theoretical focal lengths for the objective and ocular lens are indicated by f_o and f_e , respectively. 47

Figure 2.4: Schematic of a scanning electron microscope (SEM).....	51
Figure 2.5: Diagram showing the interaction volume of a primary electron beam with a sample and the possible outputs resulting from electron-specimen interactions.....	53
Figure 2.6: SEM micrographs recorded on the same microstructural feature of a Mg ZEK100 alloy. (a) is recorded utilizing the BSE mode which is sensitive to compositional differences. Here, the white regions correspond to a Zn-rich secondary phase and the dark areas the Mg matrix. (b) is recorded utilizing the SE mode which is sensitive to topographical features. The fine needle-like corrosion product layer is clearly visible.	54
Figure 2.7: Diagram demonstrating the production of characteristic X-rays. An incident electron expels an electron from its orbit causing an electron from a higher orbital to relax to fill the void with the excess energy emitted as an X-ray.	56
Figure 2.8: (a) EDX spectrum recorded on an Al A005 sample showing the measured counts versus the x-ray energy. (b) EDX maps recorded on the same sample showing the correlation between the SEM micrograph and the elemental composition of Mn, Fe and Al.	58
Figure 2.9: FIB cross-section of a Mg ZEK100 wedge cast alloy corroded for 24 h in 0.16 wt% NaCl solution. Fine vertical lines are a result of the FIB bombardment process.	58
Figure 2.10: (a) Schematic illustration of the EBSD experimental setup. (b) Image showing the Kikuchi bands produced as a result of the electron diffraction process which is recorded on a phosphor screen. Software analyses the Kikuchi bands to extract a myriad of information about the sample including crystallographic structure and grain boundary properties. (c) A map of the crystallographic orientation of grains in a Mg ZEK100 wedge cast alloy. The inverse pole figure at the bottom of the map shows the relationship between grain colour and orientation with respect to the surface normal.....	60
Figure 2.11: (a) Schematic of a CLSM microscope. (b) Sample topographic micrograph produced by CLSM on a Mg AM50 alloy corroded for 96 h in a 1.6 wt% NaCl solution.....	62
Figure 2.12: Typical three-electrode, three-compartment electrochemical cell used for all electrochemical experiments except for scanning electrochemical microscopy studies. The	

cell houses a WE, RE and CE (when necessary) in three distinct compartments. Each electrode is connected to a potentiostat via external circuitry.	63
Figure 2.13: Diagram illustrating the concept of a corrosion potential. The two green curves represent the current-potential relationship for the two half-reactions, water reduction and Mg oxidation. The red curve represents the current-potential relationship of the coupled half-reactions, i.e. the corrosion reaction. The E_{CORR} occurs when the rate of the anodic reaction equals the rate of the cathodic reaction.	65
Figure 2.14: Diagram showing the relationship between the input potential (dashed line) and the output current (solid line) response for an EIS experiment. The phase shift between the potential and current waves is shown by θ	67
Figure 2.15: (a) Nyquist plot showing the imaginary impedance (Z'') versus the real impedance (Z') for a Mg AM50 sample immersed in ethylene glycol before and after the addition of H_2O . The corresponding Bode plots for the magnitude of impedance ($ Z $) versus frequency and the phase angle (theta) versus frequency are shown in (b) and (c), respectively.	68
Figure 2.16: Diagrams showing electrochemical responses for an UME that is (a) far away from a substrate (b) close to a conducting substrate and (c) close to an insulating substrate.	70
Figure 2.17: Schematic of a simple SECM instrument. Note, in this thesis a pseudo RE electrode was used to perform the CE and RE roles simultaneously rather than the separate CE and RE shown in the figure.	71
Figure 2.18: Diagram illustrating the XRD diffraction phenomenon and the mathematical relationship between wave length and lattice spacing (Bragg's Law).	72
Figure 2.19: (a) Schematic showing the instrumental setup for a typical XRD experiment. In this case the detector rotates around the Measuring circle and the intensity of the diffracted x-rays is measured as a function of the angle of the detector, 2θ . (b) Sample output from an XRD experiment with the corresponding Miller indices of the crystal which cause each peak.	74

Figure 2.20: Schematic illustrating the basic principles of dynamic SIMS.....	75
Figure 2.21: Schematic of a quadrupole mass analyzer employed in dynamic SIMS experiments. Secondary ions from the source enter and pass through the quadrupole where they are separated based on their m/z ratio before striking the detector.....	77
Figure 3.1: SEM micrographs of a polished Al A004 surface. A. Low magnification micrograph showing the general microstructure of the alloy which is representative of the A002 and A005 alloys as well. B. High magnification image of alloy A004 detailing the coarse microstructure ($d > 1\mu\text{m}$), likely $\text{Al}_6(\text{Fe},\text{Mn})$ particles. C. High magnification image of the highlighted area in B showing the fine dispersoid particles ($d < 1\mu\text{m}$).....	85
Figure 3.2: SEM micrographs and corresponding EDX analyses of the coarse microstructures present in A. A004 – 2.06 wt% Mg, B. A002 – 1.00 wt% Mg and C. A005 – 0.11 wt% Mg alloys. Red boxes indicate the regions chosen for EDX analysis. In all three alloys, coarse particles are enriched in Fe (blue maps) and Mn (purple maps) indicating that they are likely $\text{Al}_6(\text{Fe},\text{Mn})$. Mg (orange maps) and Cu (red maps) show no enrichment of either alloying element indicating that they are dissolved in solid solution.....	86
Figure 3.3: A SEM micrograph recorded in BSE mode and the corresponding elemental maps for B. Fe; C. Mn and D; Cu for the A005 alloy. These maps indicate that the fine dispersoid particles have various compositions in addition to Al, Fe and Mn.....	87
Figure 3.4: A. SEM micrograph recorded in BSE mode and the corresponding elemental analysis, B and C, generated from EDX spot analysis on alloy A004. Spectrum B shows slight Cu enrichment in the indicated particle while spectrum C shows slight Si enrichment in the indicated particle.....	88
Figure 3.5: SEM BSE micrographs of A. A004; B. A002; and C. A005 following immersion in a 0.6 M NaCl + 0.1 M acetic acid solution (pH ~ 3.2) for 96 h. Each specimen exhibits extensive corrosion damage indicated by the high number density of pitting sites. Columns of corrosion products protrude from large pitting sites as indicated with a white arrow.....	89
Figure 3.6: A. E_{CORR} measurements recorded for 96 h in a 0.06 M NaCl + 0.1 M acetic acid solution for the A004, A002 and A005 Al alloys. B, Magnification of A showing similar	

E_{CORR} behaviour for each alloy during the first 6 h of immersion. C. Magnification of the 10 to 20 h period in A, E_{CORR} correlates with Mg content with greater Mg concentration leading to lower E_{CORR} values. D, Magnification of the 80 to 90 h period in A. Fluctuations in E_{CORR} increase with time with A005 exhibiting the greatest change in potential during potential transients.....90

Figure 3.7: PDP scans for alloys A004, A002 and A005 recorded in a 0.06 M NaCl + 0.1 M acetic acid solution following A. 0.5 h, B. 24 h and C. 48 h immersion at open circuit.....92

Figure 3.8: A. Schematic of the feedback loop utilized in the SECM instrument. The mediator, HQ is oxidized to Q at the 10 μm Pt tip and diffuses to the alloy surface to be reduced at a cathodic site. Q then diffuses back to the Pt tip and is reoxidized. B. CV recorded at the Pt microelectrode in bulk solution. The CV shows a steady-state current plateau where the current is transport limited. The red arrow indicates the imaging potential of 0.800 V vs Ag/AgCl chosen for SECM experiments. C. Chronoamperometric curve recorded at the 10 μm Pt tip in bulk solution for 600 s; the length of an SECM mapping experiment.....93

Figure 3.9: PACs recorded in a 0.06 M NaCl + 0.1 M acetic acid solution containing 1 mM hydroquinone after 1, 2, 3, 4, 8, 12 and 24 h of open circuit exposure for alloys A. A004, B. A002 and C. A005. Initially, each alloy exhibits negative feedback indicating insulating behaviour before evolving to increasingly positive feedback with time indicating greater reactivity towards the reduction of hydroquinone. Each PAC was initiated 200 μm from the alloy surface.....95

Figure 3.10: A, B, C, E, F and E are SECM maps of the same region recorded after 12, 24, 36, 48, 60 and 72 h of immersion in a 0.06 M NaCl + 0.1 M acetic acid containing 1 mM HQ solution using alloy A004 as the substrate. D and H are the EDX analysis for Fe and the corresponding SEM BSE micrograph of the same region analyzed with SECM. Purple, green and white arrows indicate the locations of $\text{Al}_6(\text{Fe},\text{Mn})$ coarse particles.....96

Figure 3.11: A, B, C, D and E are SECM maps of the same region recorded after 4, 8, 12, 24 and 36 h of immersion in a 0.06 M NaCl + 0.1 M acetic acid solution containing 1 mM HQ using alloy A002 as the substrate, respectively. White arrows indicate the location of $\text{Al}_6(\text{Fe},\text{Mn})$ coarse particles.....97

Figure 3.12: A, B, C, D and E are SECM maps of the same region recorded after 4, 8, 12, 24 and 36 h of immersion in a 0.06 M NaCl + 0.1 M acetic acid solution containing 1 mM HQ using alloy A005 as the substrate, respectively. White arrows indicate the location of Al₆(Fe,Mn) coarse particles.....97

Figure 3.13: SEM BSE image of alloy A002 following the SECM experiments shown in Figure 11. Large topographical variations are present across the entire alloy surface.....99

Figure 4.1: (a, e and i) SEM BSE micrographs of as-polished sand, graphite and die cast Mg AM50 alloy. The corresponding EDX elemental maps for Mg, Al and Mn are shown for the sand cast (b, c and d) graphite cast (f, g and h) and die cast (j, k and l), respectively. The white regions in the SEM micrographs correspond to Al-Mn intermetallics, the gray areas correspond to Mg₁₇Al₁₂ β-phase and the dark gray corresponds to the α-Mg matrix.....110

Figure 4.2: E_{CORR} measurements recorded on a sand cast (SC), graphite cast (GC) and die cast (DC) Mg AM50 alloys in (a) 0.3 M NaCl solution, (b) 0.03 M NaCl solution and (c) 0.003 M NaCl solution for 24 h. Note, at 0.03 M NaCl the SC alloy exhibits two types of behaviour; one is characterized by a smooth increase and plateau (black) while the other experiences a sudden breakdown and onset of fluctuations (green).....112

Figure 4.3: (a, d and g) Nyquist plots recorded for a SC, GC and DC Mg AM50 alloy, respectively, with the corresponding impedance modulus (b, e and h) and phase angle plots (c, f and i) following 10, 20 and 30 h of immersion in a 0.3 M NaCl solution. Recorded data points are indicated with symbols while the equivalent electrical circuit fit is indicated with a solid line.....114

Figure 4.4: (a, d and g) Nyquist plots recorded for a SC, GC and DC Mg AM50 alloy, respectively, with the corresponding impedance modulus (b, e and h) and phase angle plots (c, f and i) following 10, 20 and 30 h of immersion in a 0.03 M NaCl solution. Recorded data points are indicated with symbols while the equivalent electrical circuit fit is indicated with a solid line.....116

Figure 4.5: (a and c) E_{CORR} measurements recorded on the SC alloy in 0.03 M NaCl solution and the corresponding Nyquist plots (b and d) recorded following 10, 20 and 30 h of immersion.....117

Figure 4.6: (a, d and g) Nyquist plots recorded for a SC, GC and DC Mg AM50 alloy, respectively, with the corresponding impedance modulus (b, e and h) and phase angle plots (c, f and i) following 10, 20 and 30 h of immersion in a 0.3 M NaCl solution. Recorded data points are indicated with symbols while the equivalent electrical circuit fit is indicated with a solid line.....118

Figure 4.7: Equivalent electrical circuits used to fit impedance data which exhibited (a) a single time constant response and (b) a two time constant response. In some cases, a constant phase element was used instead of a capacitor to more faithfully fit the data. In these cases the exponent is ≥ 0.9120

Figure 4.8: Impedance derived polarization resistance (R_p) as a function of $[Cl^-]$ (0.003 – 0.3 M) and time for a (a) SC, (b) GC and (c) DC Mg AM50 alloy. Each plot is constructed on the same axes scale for comparison. R_p values are colour coded according to the scale at the right.....123

Figure 4.9: E_{CORR} measurements recorded for sand, graphite and die cast Mg AM50 alloys in an aqueous and ethylene glycol solvent, both containing 0.003 M NaCl.....124

Figure 4.10: Nyquist plots for sand, graphite and die cast Mg AM50 alloys recorded in ethylene glycol containing 0.003 M NaCl following 30 h of immersion.....125

Figure 5.1: (a) Anodic polarization scans performed on rolled Mg ZEK100 sheet alloy in 0.1 M NaOH for an as-polished and galvanostatically treated specimens. Galvanostatic treatment consisted of -5 mA/cm^2 in 0.1 M NaOH for various intervals. (b) shows the area indicated in (a) in greater detail.....140

Figure 5.2: (a) XRD spectra recorded on an as-polished Mg ZEK100 sheet specimen (black) and the same alloy pre-treated at -5 mA/cm^2 for 2 h. (b) Higher magnification image of the black box shown in (a).....141

Figure 5.3: (a) Dynamic SIMS isotopic maps for Mg^{26} , D^2 and O^{16} $\sim 2 \mu\text{m}$ below the surface of an as-polished, wedge cast Mg ZEK100 specimen with the corresponding post-SIMS SEM micrograph, (d). Similar elemental maps are shown for a sample charged for 1 h in 0.1 M NaOH made with D_2O in the (b) near surface region and (c) $\sim 2 \mu\text{m}$ below the surface with

the corresponding post-SIMS SEM micrograph in (e). Dashed white lines indicate the corresponding grain boundary in each image.....142

Figure 5.4: *In-situ* images recorded for a sample subjected to 1 h cathodic pre-treatment and immersed in 0.03 M NaCl for (a) 0.5, (b) 1, (c) 3, (d) 5 and (e) 20 min. The inset in (a) shows the area indicated with a dashed white line in greater detail and the arrows show black initiation sites for filiform-like corrosion. (f-j) show the corresponding images for an as-polished Mg ZEK100 sheet alloy in the same immersion environment at identical intervals.....144

Figure 5.5: (a) Optical and (b) SEM micrographs of the filiform-like corrosion which occurred on a sample subjected to 1 h cathodic pre-treatment and immersed in 0.03 M NaCl for 30 min. (c) and (d) are a similar set of micrographs showing a similar filiform-like corrosion occurring on an as-polished Mg ZEK100 F sample in 0.03 M NaCl for 30 min.146

Figure 5.6: Dynamic SIMS elemental maps for Mg²⁶, D², O¹⁶ and Zn⁶⁴ at approximately 2, 7, 11 and 20 μm depth of an aged corrosion filament formed on a wedge cast Mg ZEK100 alloy during free corrosion in a 0.03 M NaCl solution made with D₂O. The area contained by the dashed white lines indicates the location of the corrosion filament.....148

Figure 5.7: SEM micrograph and corresponding EDX elemental maps recorded on a polished Mg ZEK100 wedge cast alloy. The image shows that a Zn and Nd-rich phase segregates to grain boundaries.....149

Figure 5.8: (a) SEM micrograph of the crater left after dynamic SIMS analysis of an aged corrosion filament shown in Figure 6. (b) and (c) are the corresponding EDX elemental maps for Mg and O, respectively.....150

Figure 5.9: Dynamic SIMS isotopic maps for Mg²⁶, D², O¹⁶ and Zn⁶⁴ at approximately 6, 12, 18 and 23 μm depth of the leading edge of a corrosion filament formed on a wedge cast Mg ZEK100 alloy during free corrosion in a 0.03 M NaCl solution made with D₂O. The position of the original filament tip is clearly indicated by the O¹⁶ signal.....151

Figure 5.10: Dynamic SIMS depth profiles for Mg²⁶, D² and O¹⁶ recorded on a wedge cast Mg ZEK100 alloy specimen corroded in 0.03 M NaCl solution made with D₂O for 36 h.....153

Figure 5.11: Physical model of a corrosion filament occurring on a Mg ZEK100 alloy based on SIMS isotopic mapping and depth profiles.....159

Figure 6.1: (a) Photo of the Mg ZEK100 wedge cast ingot with 30 cm ruler for scale. Thermocouples can be seen sticking out of the left side of the ingot. (b) Image showing the centerline section of the ingot which was used to prepare samples. (c) Final samples cut from the center line of the wedge cast ingot. Samples are labelled alphabetically from the narrow portion of the wedge (Section A) to the thick portion (Section M). 167

Figure 6.2: (a-d) SEM micrographs recorded in BSE mode for section A, D, G and M of the Mg ZEK100 wedge cast, respectively. A Zn-rich Mg_7Zn_3RE T-phase which segregates in the grain boundaries is indicated with red arrows and Zr-rich intermetallic particles are indicated with green arrows. (e-h) EDX elemental maps for Zn for section A, D, G and M of the alloy. (i-l) the corresponding EDX elemental maps for Zr. 172

Figure 6.3: (a-d) EBSD crystallographic orientation maps recorded on Mg ZEK100 wedge cast alloy for section A, D, G and M, respectively. The inverse pole figure is in the bottom right and displays the colour code for each hcp Miller indices. 173

Figure 6.4: E_{CORR} measurements recorded in 0.03 M NaCl solution for section A, D, G and M of a wedge cast Mg ZEK100 alloy for 30 h. 174

Figure 6.5: (a-d) E_{CORR} measurements recorded for section A, D, G and M of a wedge cast Mg ZEK100 alloy in 0.03 M NaCl for 0.5 (black), 10 (red), 20 (blue) and 30 (pink) h, respectively. (e-h) PDP curves recorded directly following the E_{CORR} measurements in a-d in the same solution. Sections of the wedge have corresponding colours in the E_{CORR} and PDP measurements. PDP scans were initiated -0.25 V vs. SCE and scanned in the positive direction. 176

Figure 6.6: (a) Cathodic current densities as a function of immersion time extracted from PDP curves in Figure 5. i_c values were extracted by Tafel analysis of the cathodic branch of the polarization curve extrapolated to the E_{CORR} . Optical micrographs of section A following

the PDP analysis conducted in figure 5 following (b) 0.5 and (c) 30 h. The black areas in (c) are the result of filiform-like corrosion..... 177

Figure 6.7: Optical micrographs of section A (a & e), section D (b & f), section G (c & g) and section M (d & h) of a Mg ZEK100 wedge cast alloy following 24 h immersion in 0.03 M NaCl solution. Red arrows indicate the locations of the filiform-like corrosion morphology. 178

Figure 6.8: SEM micrographs recorded in BSE mode for wedge cast ZEK100 (a) section A, (b) section D, (c) section G and (d) section M following immersion in a 0.03 M NaCl solution for 24 h. Note the differences in the scale bar from image to image. Images show the corrosion morphology of the general alloy surface which is characterized by microgalvanic coupling..... 179

Figure 6.9: (a) SEM micrograph recorded in SE mode of section A of a Mg ZEK100 wedge Alloy following a 24 h immersion in 0.03 M NaCl environment showing the buildup of Mg(OH)₂ corrosion product on Mg₇Zn₃RE T-phase. (b) EDX elemental map for Zn and (c) the corresponding SEM micrograph of the as-polished sample to show that the Mg(OH)₂ buildup in (a) does occur on the T-phase..... 180

Figure 6.10: SEM micrographs recorded in BSE mode for wedge cast ZEK100 (a) section A, (b) section D, (c) section G and (d) section M following immersion in a 0.03 M NaCl solution for 24 h. Note the differences in the scale bar from image to image. Images show the filiform-like corrosion morphology which exists on each specimen..... 181

Figure 6.11: SEM micrograph of a corrosion filament formed on section A of a Mg ZEK100 alloy following 24 h immersion in 0.03 M NaCl. Arrows indicate regions where a pre-existing surface layer has been undermined by the propagation of a filament. 182

Figure 6.12: SEM micrographs recorded in BSE mode for wedge cast ZEK100 (a) section A, (b) section D, (c) section G and SE mode for (d) section M following removal of the corrosion product film with a chromic acid etch. Prior to the etch samples were immersed in a 0.03 M NaCl solution for 30 h. Note the differences in the scale bar from image to image. Images show both the general surface and the filiform-like corrosion morphology which exists on each specimen. 183

Figure 6.13: Depth profiles recorded on section A, D, G and M of a wedge cast Mg ZEK100 alloy following 30 h immersion in a 0.03 M NaCl solution and removal of the accumulated corrosion product with a chromic acid solution. Three line scans per sample were performed with CLSM in regions that contained corrosion filaments. 184

List of Symbols and Acronyms

Symbols

a	Activity
α	Transfer coefficient
atm	Atmospheres
β_a	Anodic Tafel slope
β_c	Cathodic Tafel slope
c	concentration
$^{\circ}\text{C}$	Degrees Celsius
cm	Centimeter
e^-	Electron
E	Applied potential
ΔE	Change in potential
E^e	Equilibrium potential
E°	Standard state potential
E_{CORR}	Corrosion potential
F	Faraday's constant (96,485 C/mol)
ΔG°	Gibbs free energy change under standard state conditions
ΔG	Gibbs free energy change
g	Gram

H⁺	Proton
i	Current
I_{anode}	Anodic current
I_{cathode}	Cathodic current
I_{CORR}	Corrosion current
k	Rate constant
kg	Kilogram
km	Kilometer
K_{sp}	Solubility product
L	Litre
m	Mass
M	Molar mass
mol	Moles
η	Overpotential
n	Number of electrons
pH	Power of hydrogen
R	Gas constant (8.314 J/mol·K)
T	Temperature
t	Time
μm	Micrometers

V Volts

wt% Weight percent

Acronyms

ACC Anthropogenic climate change

DFT Density functional theory

EIS Electrochemical impedance spectroscopy

EDX Energy dispersive x-ray spectroscopy

GM General Motors

HE Hydrogen evolution

HER Hydrogen evolution reaction

IMP Intermetallic particle

NASA National Aeronautics and Space Administration

NDE Negative difference effect

ppm Parts per million

PDP Potentiodynamic polarization

SEM Scanning electron microscope

SECM Scanning electrochemical microscopy

SHE Standard hydrogen electrode

SVET Scanning vibrating electrode technique

XRD X-ray diffraction

1 Introduction

1.1 Background

Anthropogenic climate change (ACC) is one of the greatest challenges facing society today. While certain industries and political movements choose to wantonly disregard the evidence for the existence and genesis of ACC, recent studies show that 97% of actively publishing climate scientists agree that ACC is operative.¹⁻⁵ Such a resounding consensus is not surprising when looking at the data. For instance, in a study funded by the National Oceanic and Atmospheric Administration (USA) and NASA, ice cores from Greenland and the Arctic were analyzed to investigate the evolution of the earth's atmosphere as a function of time. Each year, as snow accumulates and turns to ice, air bubbles are trapped which contain the prevailing atmosphere of the time. Over hundreds of thousands of years these ice sheets layer on top of one another. By drilling into the ice and extracting cores the composition of these air bubbles can be determined as a function of depth. This allows for the determination of the composition of the atmosphere at specific time points in history. The concentration of CO₂, the most important greenhouse gas, as a function of time is shown in Figure 1.1.⁶ For approximately 400,000 years prior to 1950 a cyclical trend in CO₂ concentration is observable. However, in the last 70 years there is a clear departure from this cycle in the form of a large spike in CO₂ concentration.⁷⁻¹¹ This is a disturbing trend. Heightened levels of CO₂ in the atmosphere contribute to a warming of the earth's surface as shown in Figure 1.2,¹² acidification of oceans, loss of arctic ice mass, increase in sea levels and an increase in severe weather systems across the earth. However, as the effects of ACC become more apparent so does the response of both the public and private sector to mitigate, reduce and where possible, eliminate emissions.

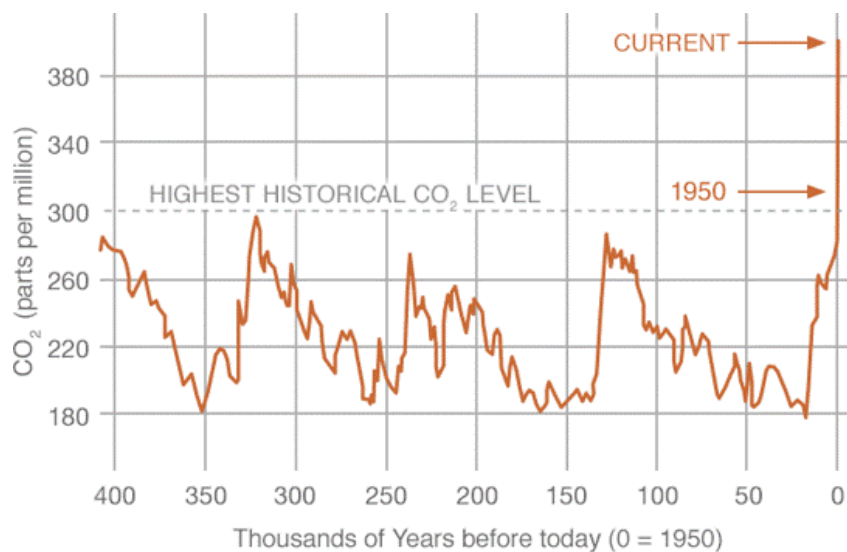
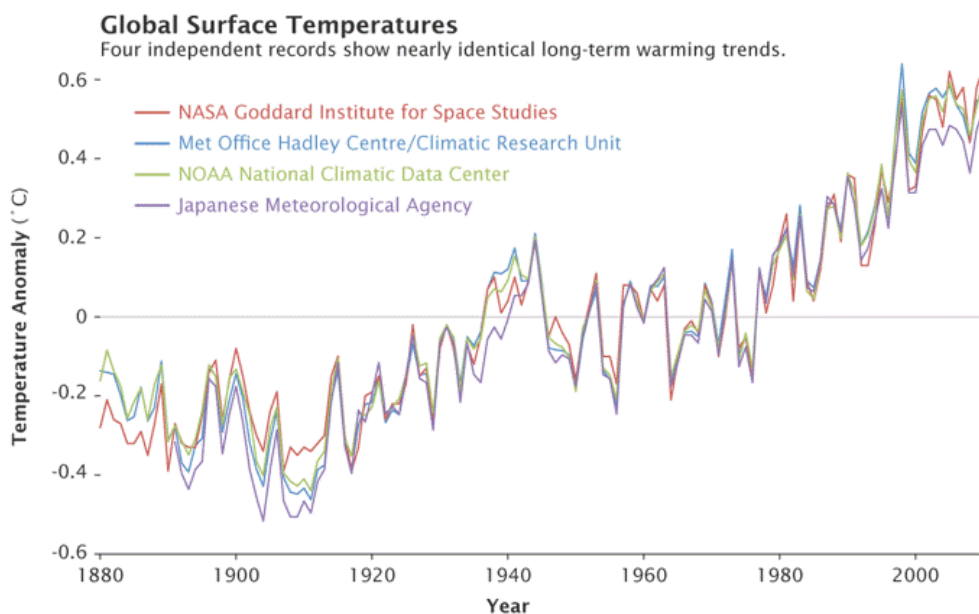


Figure 1.1: Concentration of CO₂ (in ppm) versus time since 1950. Data was gathered by measuring the [CO₂] as a function of depth in ice cores recovered from Greenland and the Arctic. Figure from <https://climate.nasa.gov/vital-signs/carbon-dioxide/>.⁶



Credit: NASA Earth Observatory/Robert Simmon

Data Sources: NASA Goddard Institute for Space Studies, NOAA National Climatic Data Center, Met Office Hadley Centre/Climatic Research Unit, and the Japanese Meteorological Agency.

Figure 1.2: Global surface temperature as a function of year recorded by four independent agencies. Temperatures are given as their deviation from a standard reference point. Figure from <https://climate.nasa.gov/vital-signs/global-temperature/>.¹²

Public responses to ACC range from large scale international agreements such as the Paris Climate Change Agreement which was signed by all but three countries on earth (Syria, Nicaragua and the United States*) to individual tax breaks for citizens who install solar panels on their homes and farms.¹³ Concurrently, many private sector initiatives also exist to combat ACC. For example, General Motors (GM) has committed to reducing the CO₂ emissions of individual vehicles by 20% by 2020.¹⁴ Commitments such as these, should they be met, have the potential to have a significant impact on the rate of emissions. This is particularly true for the transportation sector which is one of the leading sources of emissions in Canada (Figure 1.3)¹⁵ and around the world. In fact, the burning of fossil fuels for ground, air, and marine transportation accounts for 15–25% of total greenhouse gas emissions in regions such as Europe and North America.¹⁶ Given the ubiquity of trains, planes and automobiles in modern society it is unrealistic to expect a large scale paradigm shift in how people transport themselves. Therefore, the most likely answer to vehicle emissions will lie in an advancement of technology.

Two possible avenues exist to help reduce or eliminate emissions from vehicles: (i) improvements in internal combustion engine efficiency or (ii) adoption of alternative fuel sources for vehicle engines. While option (i) sees incremental gains over decades due to advances in engine and drive train technology progress in this area is limited due to thermodynamics, with studies suggesting a bounding maximum efficiency of ~67%.¹⁷ Therefore, for the long-term health of the environment option (ii) is more appealing and

* The United States signed the original agreement under President Barack Obama but later withdrew under the subsequent administration.

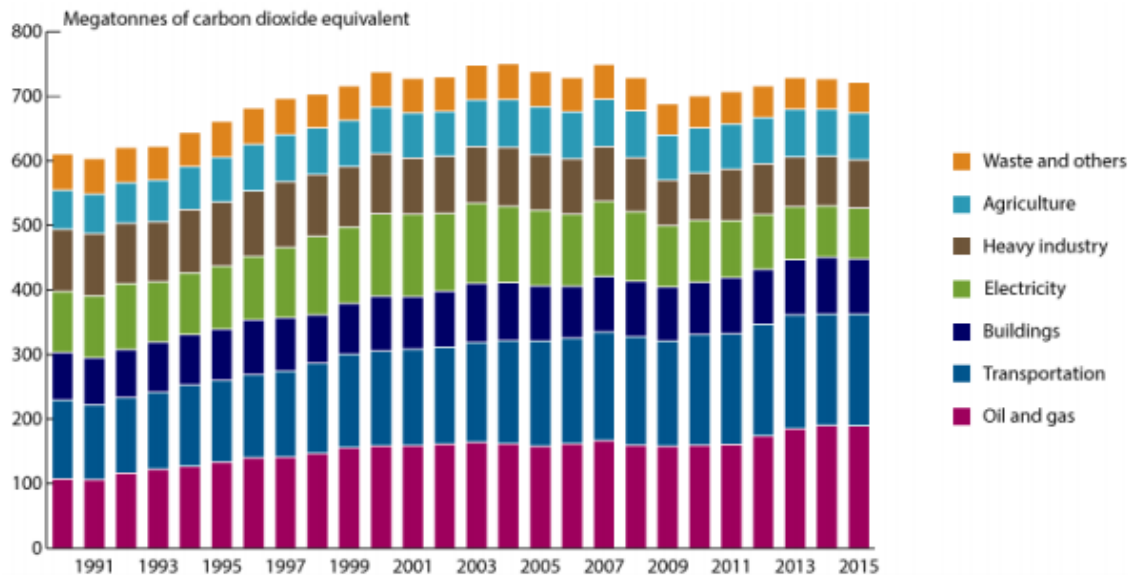


Figure 1.3: Total mass of carbon in megatonnes emitted by different Canadian economic sectors as a function of year. Figure from <https://www.ec.gc.ca/indicateurs-indicators/default.asp?lang=en&n=F60DB708->.¹⁵

the world is slowly catching on. Year-over-year, electric vehicles are grabbing a larger share of the global automobile market with over a million units sold for the first time this year; a number expected to double in less than three years.¹⁸ However, electrical vehicles (and other alternatives) also face challenges with respect to affordability, lack of charging infrastructure and concerns over range limitations.^{19,20} While a transition from fossil fuel burning vehicles to alternatively powered ones seems inevitable, expediting this process and mitigating the emissions of the current fleet is in the best interest of the planet. One way to achieve both goals is through light-weighting of vehicles.

The simplest way to achieve a mass reduction in vehicles is to replace heavy steel components with lighter materials. Figure 1.4 shows how decreasing vehicle weight improves fuel efficiency.²¹ One of the best options for light-weighting is to utilize

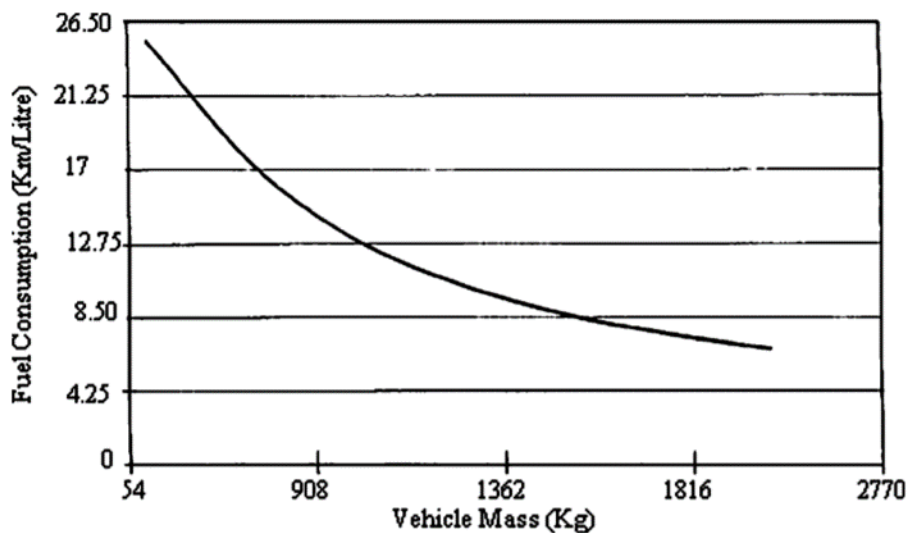


Figure 1.4: The effect of vehicle mass on fuel consumption for an automobile. Note the exponential increase in fuel savings with decreasing vehicle mass. Figure from reference 21.

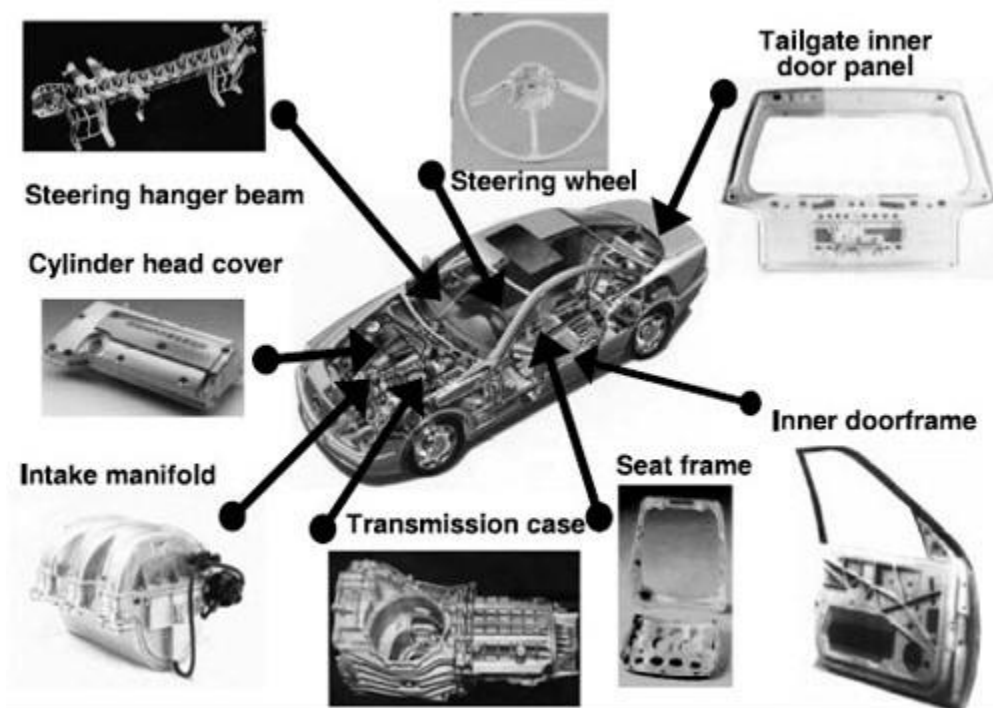


Figure 1.5: Examples of current applications of magnesium alloys in vehicles. Notably, each application occurs on the interior of the vehicle to prevent exposure of the magnesium alloy to the environment. Figure from reference 22.

magnesium alloys which are the lightest of all the engineering metals. Figure 1.5 shows examples of where magnesium alloys are currently being used in vehicles.²² Notably, each application of magnesium occurs on the interior of vehicles, shielded from the environment. This is because magnesium has an “Achilles heel”. Magnesium exhibits extremely high corrosion rates in very mild aqueous immersions. Therefore, before magnesium can see more widespread use in automobiles a solution must be found for this corrosion problem.

1.2 Light-weighting of Vehicles: Magnesium Alloys

The most alluring aspect of magnesium and its alloys with respect to the transportation industry is its extreme lightweight. Mg has a density of 1.74 g/cm^3 . This is much lower than aluminum, titanium or iron which have densities of 2.70, 4.51 and 7.87 g/cm^3 , respectively. Furthermore, magnesium alloys have been shown to exhibit the greatest strength-to-weight ratio of any structural alloy, possess excellent dampening characteristics, are easily machined, nontoxic and are easily cast and formed in a variety of ways.^{21,23} Despite each of these advantages, the uptake of magnesium alloys into the transportation sector has been limited to applications on the interior of vehicles as shown in Figure 1.5. This is because magnesium has a fatal flaw; it corrodes at an extreme rate in aqueous environments.

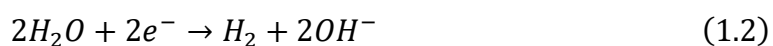
Pure magnesium has poor physical properties (e.g. poor strength and low hardness) and can ignite in air. Therefore, for any practical application magnesium will have to be alloyed. As with any other alloy, there is often a trade off when choosing which and how

much of an alloying element to add. In the case of magnesium, additions such as rare earths or zinc can increase the strength of an alloy but generally have a negative effect on the corrosion resistance of the alloy. Alloying with aluminum can provide strength while increasing corrosion resistance to a point (i.e. too much aluminum can decrease corrosion resistance). Whereas alloying elements such as arsenic have been shown to improve strength and corrosion resistance but render the alloy toxic. However, the immense benefit that could be derived from widespread adoption of magnesium alloys in the transportation industry is driving extensive research efforts to produce a sufficiently corrosion resistant magnesium alloy.

1.3 Fundamentals of Aqueous Corrosion

1.3.1 Thermodynamics of Corrosion

For a material to corrode two complementary interfacial reactions must occur. The first is a metal oxidation which produces a metal cation and some number of electrons depending on the metal being oxidized. This process is illustrated for magnesium in reaction 1.1. In order for this oxidation to proceed the generated electron(s) must be consumed in a reduction reaction. Again, in the case of magnesium, the generated electrons are used in water reduction, shown in reaction 1.2.

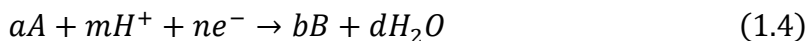


Together, the oxidation and reduction half-reactions form a redox couple.

Since this redox couple involves a charge transfer process, we can define a standard state equilibrium electrochemical potential (E°) given by equation 1.3.

$$\Delta G^\circ = -nFE^\circ \quad (1.3)$$

Here, ΔG° is the change in the standard Gibbs free energy (where a negative value indicates that the reaction is spontaneous), n is the number of electrons transferred, F is the Faraday constant ($96,486 \text{ C}\cdot\text{mol}^{-1}$) and E° is the standard state cell potential (i.e., the activity of all species is $1 \text{ mol}\cdot\text{kg}^{-1}$, all gases have a partial pressure of 1 atm, and the temperature is 25°C). However, in the real-world corrosion commonly does not occur under standard conditions making it necessary to express the potential as a function of these conditions. For the general half-cell reaction, where A and B are generic chemical species and a, m, n, b and d are molar equivalents:



the standard and nonstandard Gibbs free energy change for the overall reaction is given by

$$\Delta G^\circ = (bG_B^\circ + dG_{H_2O}^\circ) - (aG_A^\circ + mG_{H^+}^\circ) \quad (1.5)$$

$$\Delta G = (bG_B + dG_{H_2O}) - (aG_A + mG_{H^+}) \quad (1.6)$$

By taking these relationships together and recognizing equation 1.7 from thermodynamics

$$\Delta G = \Delta G^\circ + RT \ln \left\{ \frac{[B]^b [H_2O]^d}{[A]^a [H^+]^m} \right\} \quad (1.7)$$

equation 1.3 can be used to derive the Nernst equation, 1.8, which describes the equilibrium potential (E^e).

$$E^e = E^\circ - \frac{RT}{nF} \ln \left\{ \frac{[B]^b [H_2O]^d}{[A]^a [H^+]^m} \right\} \quad (1.8)$$

Notably, for generally encountered solutions, the concentration of H₂O is ~1 and concentrations can be used instead of activities. Therefore, by using standard electrochemical potentials and the Nernst equation, it is possible to calculate the equilibrium potential for concentrations beyond the standard state.

These equilibrium potentials can be used to express the driving force for corrosion as the difference between the equilibrium potentials for the anodic and cathodic reactions as shown in equation 1.9.

$$\Delta E = E_{ox/red}^e - E_{M/M^{n+}}^e \quad (1.9)$$

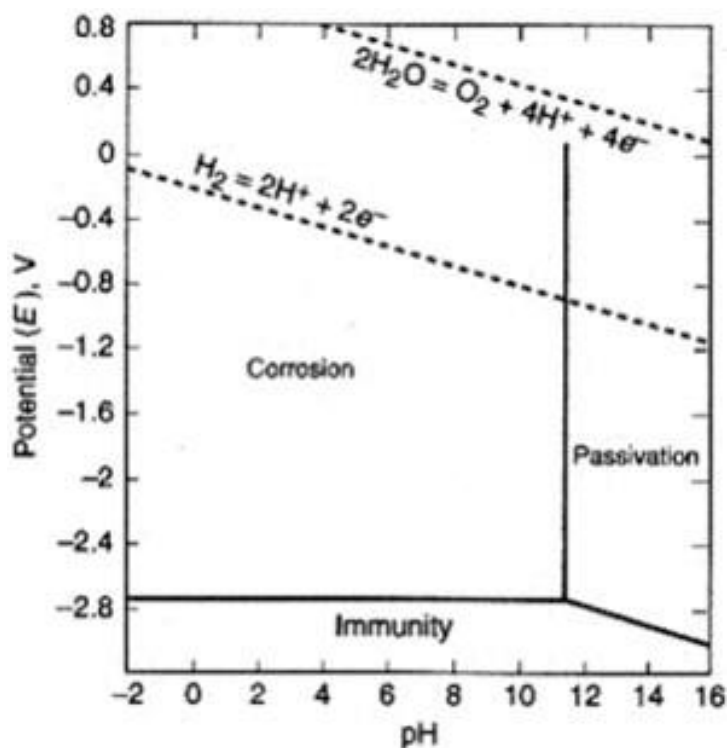
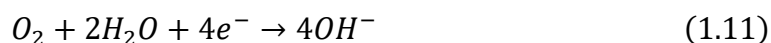
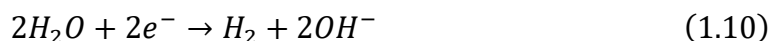


Figure 1.6: Pourbaix diagram for magnesium immersed in water at 25°C and a $[Mg^{2+}] = 10^{-5} \text{ mol/L}$.²⁴

where $E_{ox/red}^e$ and $E_{M/M^{n+}}^e$ are the equilibrium potentials of the reduction and oxidation half-reactions, respectively. For corrosion to proceed (i.e. for a reaction to have a negative ΔG) ΔE must be positive.

Using the Nernst equation and a table of standard potentials it is possible to construct a thermodynamic map of the most stable species for a given pH, potential, temperature and species concentration. Such a map is called a Pourbaix diagram, an example for pure magnesium being shown in Figure 1.6.²⁴ Since we are interested in aqueous corrosion, a logical place to start are the stability limits of water, the two relevant reactions being shown in reactions 1.10 and 1.11.



Writing the Nernst equation for reaction 1.10 and assuming a partial pressure of hydrogen of 1 Pa yields:

$$E^e = E^\circ - \frac{0.059}{2} \log[OH^-]^2 \quad (1.12)$$

which can be simplified to equation 1.13.

$$E^e = E^\circ - 0.059 \cdot pH \quad (1.13)$$

A similar relationship to that in equation 1.13 can be derived for reaction 1.11 where the two differ only in their standard potentials, E° . When plotted these relationships yield two parallel lines on the Pourbaix diagram with a slope of -0.059. These lines are shown as

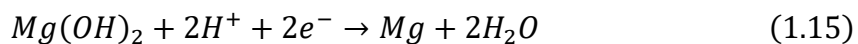
dashed lines in Figure 1.6, with the region between the two lines called the stability region for water. For practical applications of magnesium and its alloys the corrosion potential exhibited by the materials are well below the reversible hydrogen potential (i.e. the lower line of the water stability region) and making water and/or proton reduction viable reduction reactions to support magnesium oxidation. To complete the Pourbaix diagram all possible reactions for magnesium in an aqueous environment must be considered.

For the dissolution of magnesium, equation 1.1, the standard reduction potential is -2.37 V_{SHE} yielding the Nernst equation

$$E^e = -2.37 V - \frac{0.059}{2} \log \left\{ \frac{1}{[Mg^{2+}]} \right\} \quad (1.14)$$

a plot of which produces a straight horizontal line on the Pourbaix diagram whose y-intercept is determined by the $[Mg^{2+}]$. An example of the effect on $[Mg^{2+}]$ on the Pourbaix diagram is illustrated in Figure 1.7,²⁵ where the lines shift to more negative values as $[Mg^{2+}]$ decreases. Below these lines magnesium is stable and will not corrode whereas corrosion proceeds above these potentials. Should the potential and pH fall on the line the processes are in equilibrium for the specific $[Mg^{2+}]$ used in the calculation.

The next important reaction to consider is the direct conversion of magnesium metal to the corrosion product, magnesium hydroxide on contact with water, reaction 1.15, written as a reduction to adhere to convention.



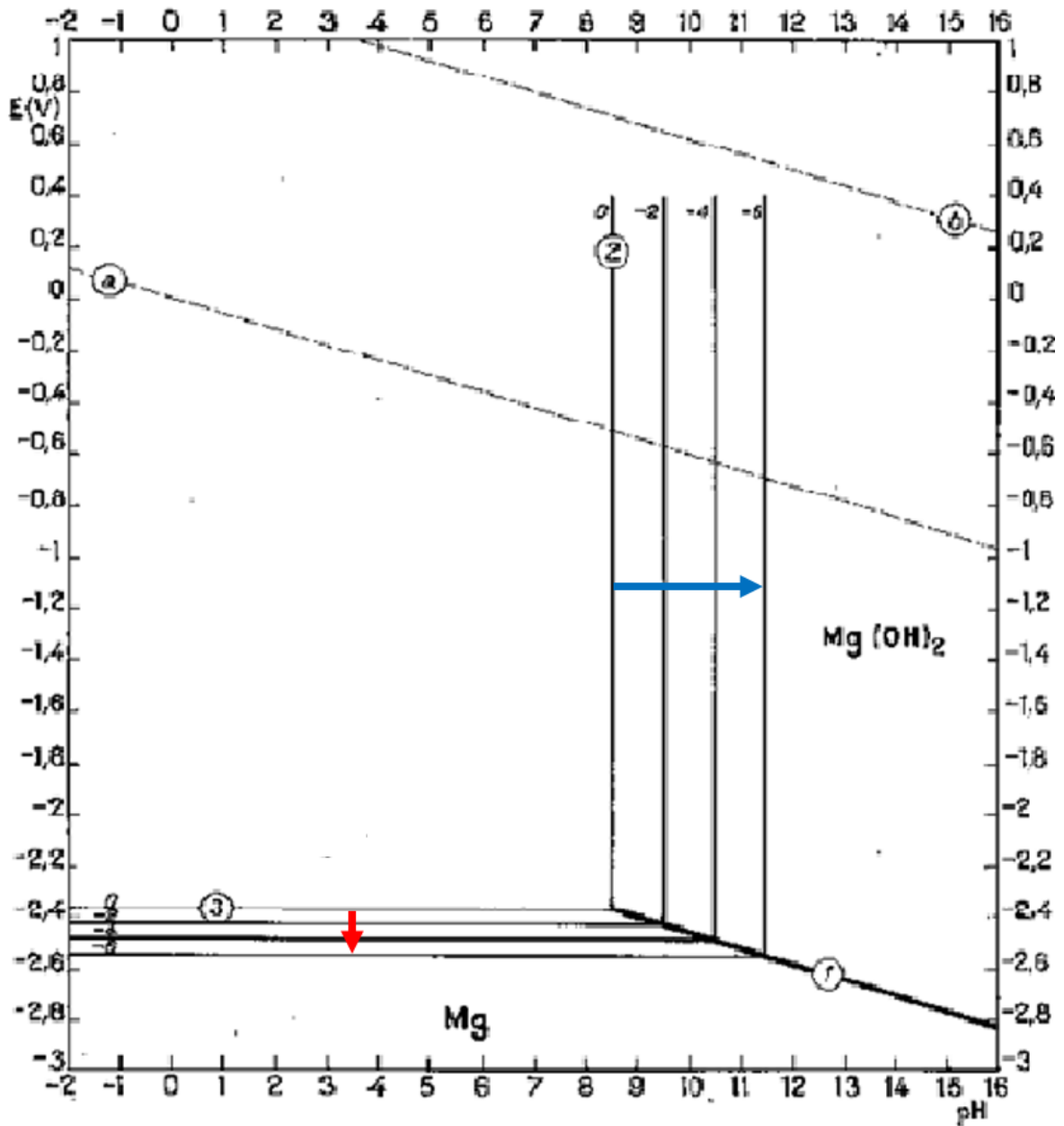


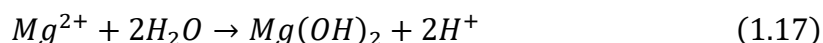
Figure 1.7: Pourbaix diagram for magnesium immersed in water at 25°C. The red arrow indicates the effect of decreasing $[Mg^{2+}]$ and the blue arrow indicates the effect of increasing pH. The numbers associated with the lines are $[Mg^{2+}]$ expressed logarithmically. Figure from reference 25.

The standard potential for this reaction is $-1.86 \text{ V}_{\text{SHE}}$, which when substituted into the Nernst equation yields equation 1.16

$$E^e = -1.86 \text{ V} - 0.059 \log\{[H^+]\} \quad (1.16)$$

and produces the diagonal line with a slope of -0.059 which terminates when it intersects the horizontal line for reaction 1.1.

The potential-pH diagram for pure magnesium is incomplete without the solubility equilibrium between Mg^{2+} and $\text{Mg}(\text{OH})_2$, shown in reaction 1.17



This reaction is chemical not electrochemical and therefore does not depend on the electrochemical potential. The equilibrium for this reaction is governed by the solubility product (K_{sp}) according to equation 1.18.

$$K_{sp} = \frac{[H^+]^2}{[Mg^{2+}]} \quad (1.18)$$

Since the K_{sp} for $\text{Mg}(\text{OH})_2$ is approximately 10^{-11} , the pH which defines this solubility equilibrium depends on the $[\text{Mg}^{2+}]$, and is given by the series of vertical lines in Figure 1.7. On the left side of this line Mg^{2+} will be the stable species whereas $\text{Mg}(\text{OH})_2$ will be the stable species on the right side.

With the basic Pourbaix diagram constructed for pure Mg in an aqueous system, three distinct regions emerge. These regions, indicated in Figure 1.6 are immunity, within

which Mg metal is stable, corrosion, within which Mg^{2+} is stable, and passivation, within which $\text{Mg}(\text{OH})_2$ is the most stable species. This information is invaluable when rationalizing observed phenomena and for selecting materials for an application. However, this is a simplified diagram for a pure magnesium system. Potential-pH diagrams increase in complexity when considering alloyed systems and/or more complicated immersion environments. Additionally, Pourbaix diagrams offer thermodynamic insight only and do not elucidate corrosion kinetics.

1.3.2 Electrochemical Kinetics and Corrosion Kinetics

The coupling of two interfacial redox processes, metal oxidation and oxidant reduction, forms a short circuited galvanic cell. This creates a flow of electrons from the oxidation to the reduction site. This flow of these electrons dictates the rate of corrosion and is termed the corrosion current (I_{CORR}), defined as:

$$I_{CORR} = I_{anode} = -I_{cathode} \quad (1.19)$$

In the event the corrosion current is known, Faraday's law can be used to calculate the amount of material lost,

$$I_{CORR} = \frac{nFm}{Mt} \quad (1.20)$$

Where n is the number of electrons involved in the redox couple, F is Faraday's constant, m is the mass of corroded material in grams, M is the molecular mass of the material in

grams per mole, and t is the duration of corrosion. Despite the simplicity of equation 1.20, the nature of the corrosion process makes the measurement of I_{CORR} nontrivial and thus, a

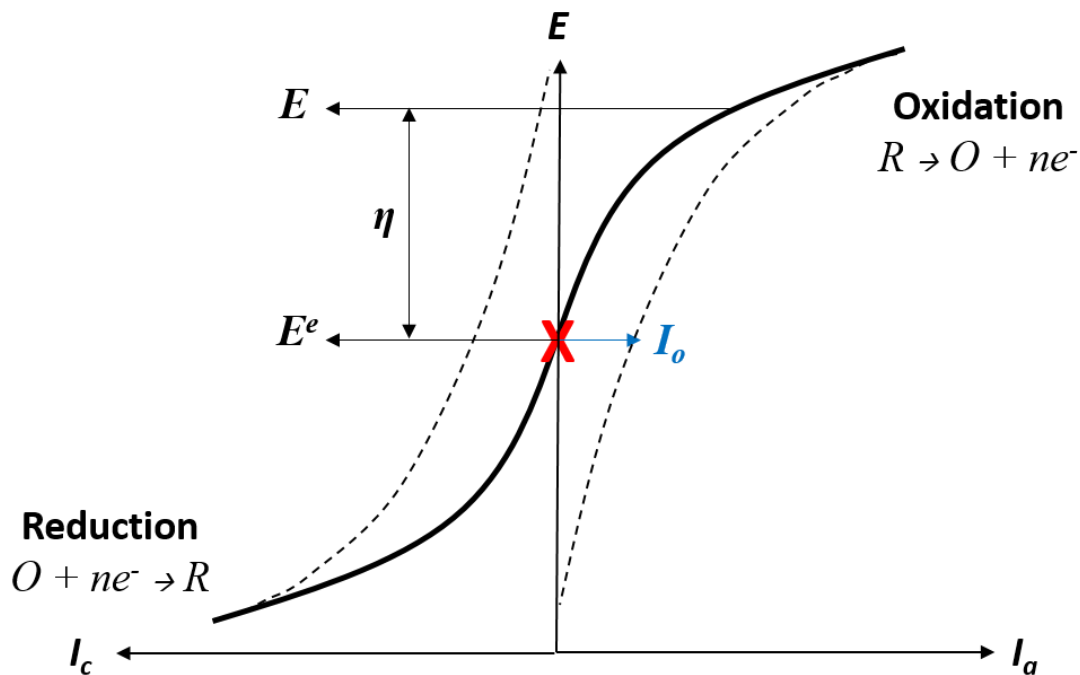


Figure 1.8: Current-potential relationship (solid line) for a generic, reversible electrochemical reaction with anodic and cathodic transfer coefficients equal to 0.5. This process is described by the Butler-Volmer relationship. E is the applied potential, E^e is the equilibrium potential, η is the overpotential and I^o is the exchange current density. The dashed lines show the currents associated with the forward and reverse reactions.

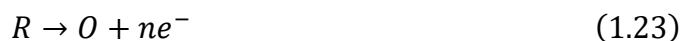
combination of electrochemical theory and shrewd experimental design have discerned various ways to elucidate I_{CORR} .

Since the i - E relationship for a coupled electrochemical process is determined by the individual i - E relationships for the two half-reactions these relationships can be considered separately and added to determine the i - E relationship for the overall corrosion

process. A generic i - E relationship for a reversible electrochemical reaction ($O + ne^- = R$) is shown in Figure 1.8. From the laws of chemical kinetics and Faraday's law we have:

$$\text{Rate} = \frac{i}{nF} = kc \quad (1.21)$$

Where k is the rate constant (assuming a first order reaction) and c is the concentration of the electrochemically active species. Therefore, for the generic cathodic and anodic reactions, 1.22 and 1.23, respectively



recognizing that the current will be proportional to the area of the electrode, the following relationships can be formulated for the current density ($I=i/area$) of the cathodic (1.24) and anodic (1.25) half-reactions.

$$I_c = -nFk_c c_O \quad (1.25)$$

$$I_a = nFk_a c_R \quad (1.26)$$

Since I is equal to the sum of I_c and I_a ,

$$I = nFk_a c_R - nFk_c c_R \quad (1.27)$$

However, since the reactions involved are electrochemical, the rate constants are functions of potential as specified in equations 1.28 and 1.29 for the cathodic and anodic reactions, respectively.

$$k_c = k_c^\circ \cdot \exp\left\{-\frac{\alpha_c nF}{RT} E\right\} \quad (1.28)$$

$$k_a = k_a^\circ \cdot \exp\left\{\frac{\alpha_a nF}{RT} E\right\} \quad (1.29)$$

where k_c° and k_a° are standard electrochemical rate constants (assumed to be equal for simple reversible reactions), α_c and α_a are transfer coefficients (for symmetrical electron transfer reactions, $\alpha_c \sim \alpha_a \sim 0.5$) and E is the potential. Equations 1.28 and 1.29 can be combined to yield:

$$I_c = nF c_O k^\circ \cdot \exp\left\{-\frac{\alpha_c nF}{RT} E\right\} \quad (1.30)$$

$$I_a = nF c_R k^\circ \cdot \exp\left\{\frac{\alpha_a nF}{RT} E\right\} \quad (1.31)$$

Combining equations 1.30 and 1.31 with the Nernst equation and recognizing that, at $E = E^e$, $I_a = -I_c = I_o$, we get the Butler-Volmer equation, 1.32.

$$I = I_o \left[\exp\left\{\frac{\alpha_a nF}{RT} \eta\right\} - \exp\left\{-\frac{\alpha_c nF}{RT} \eta\right\} \right] \quad (1.32)$$

In which η is the overpotential ($\eta = E - E^e$) Where I_o is the exchange current density and is defined by equation 1.33.

$$I_o = nFk^o(c_R)^{\alpha_c}(c_O)^{\alpha_a} \quad (1.33)$$

Equation 1.32 is the Butler-Volmer equation and is depicted graphically for a reversible electrochemical process in Figure 1.8. The solid line represents the net current, I , while the dashed lines show the contributions of the cathodic and anodic processes to the overall current. From Figure 1.8, it can be seen that, for sufficiently large overpotentials, the contribution of one of the two half-reactions dominates the current response, with I becoming equal to either I_a or I_c , depending on the applied overpotential. In this case, taking a large anodic overpotential as an example, the cathodic term in the Butler-Volmer equation becomes negligible and equation 1.32 simplifies to:

$$I = I_a = I_o \left[\exp \left\{ \frac{\alpha_a n F}{RT} \eta \right\} \right] \quad (1.34)$$

This expression can be written logarithmically as shown in equation 1.35.

$$\log I_a = \log I_o + \frac{\alpha_a n F}{RT} \eta \quad (1.35)$$

With a plot of $\log I_a$ vs. η yielding a straight line with a y-intercept corresponding to I_o and a slope given by

$$\beta_a = \frac{2.303RT}{\alpha_a n F} \quad (1.36)$$

where the slope, β_a , is called the anodic Tafel coefficient. A similar process yields the cathodic Tafel coefficient which takes the same form as equation 1.36 but is negative with

α_c substituted for α_a . Such a Tafel relationship holds for a simple, reversible electrochemical reaction.

For a corrosion reaction, a metal oxidation (i.e. dissolution) will couple to a cathodic reaction. In this case, the anodic half of one reaction (metal oxidation) is coupled to the cathodic half of another reaction (oxidant reduction. This involves the polarization of each reaction away from its equilibrium potential toward a common value, the corrosion potential (E_{CORR}), a unique value at which the rates of the anodic and cathodic half-reactions are equal, equation 1.19. This current is the corrosion current described by the Wagner-Traud relationship, Equation 1.37.

$$I = I_{CORR} \left[\exp \left\{ \frac{\alpha_a n F}{RT} (E - E_{CORR}) \right\} - \exp \left\{ \frac{\alpha_c n F}{RT} (E - E_{CORR}) \right\} \right] \quad (1.37)$$

And depicted in Figure 1.9. The blue and red curves represent the i - E relationships for the individual reduction and oxidation half-reactions while the black curve represents the coupled corrosion reaction given by the sum of the currents.

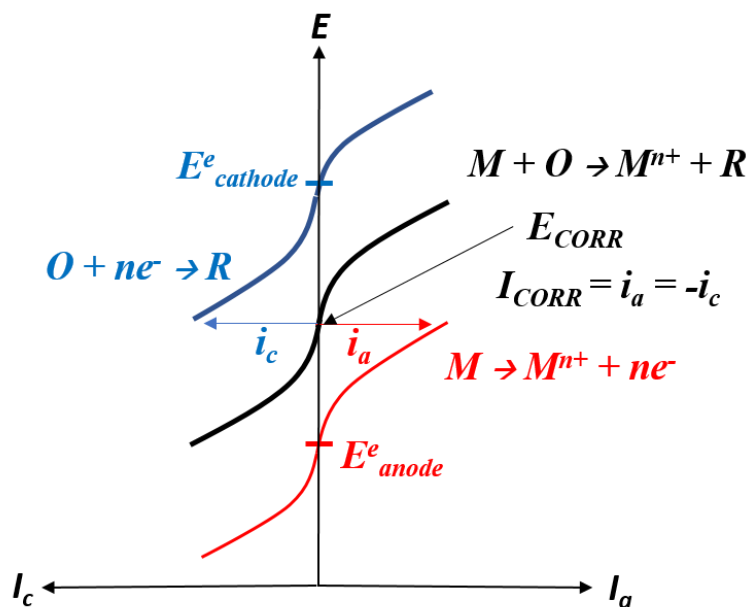
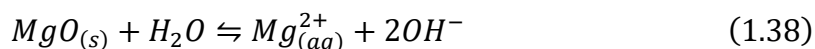


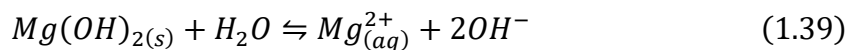
Figure 1.9: (black) Current-potential relationship for a generic metal oxidation coupled to an oxidant reduction where E_{CORR} is the potential at which the current for the cathodic half-reaction equals the current for the anodic half-reaction which equals I_{CORR} . (blue) & (red) Current potential relationship for the oxidant reduction and metal oxidation reactions, respectively.

1.4 Aqueous Corrosion of Magnesium and its Alloys

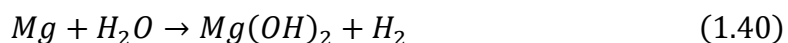
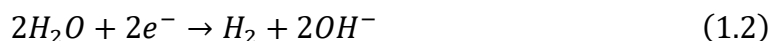
1.4.1 Corrosion of Mg: The Basics

All metals readily form surface oxides upon exposure to air and magnesium is no exception. Thus, in air, the entire surface of magnesium will be covered by a thin (~4 nm) layer of MgO.^{26,27} In humid air, this oxide film can become hydroxylated creating a bilayer structure on the alloy with an outermost layer of Mg(OH)₂.^{28–30} Upon exposure to an aqueous environment both MgO and Mg(OH)₂ are soluble, reactions 1.38 and 1.39, with corresponding K_{sp} values of ~ 10⁻⁶ and 10⁻¹¹.





Owing to this solubility, the air formed oxide/hydroxide of magnesium is not protective (at pH $\sim < 12$, depending $[Mg^{2+}]$) allowing exposure of the magnesium metal surface to the electrolyte and initiating corrosion. The oxidation and reduction half-reactions, shown in equations 1.1, and 1.2 and reproduced here for convenience



Due to the large difference in reduction potentials for the two half-reactions ($E^\circ_{OX} = -2.37$ V_{SHE} vs. $E^\circ_{RED} = -0.83$ V_{SHE}) the driving force for corrosion is large and corrosion would be expected to proceed rapidly. As a result, the local surface pH increases resulting in the precipitation and deposition of brucite ($Mg(OH)_2$) on the metal surface.²⁷ However, this corrosion product deposit is not particularly adherent and is highly porous and provides little protection against on-going corrosion.

1.4.2 Effect of Secondary Phases: Microgalvanic Coupling

Magnesium alloys are only practical engineering materials when alloyed with other elements. However, most elements have poor solubility in magnesium leading to their segregation into secondary phases within the matrix.^{31,32} While these phases can lead to improvements in the physical properties of the alloys, they typically promote the corrosion behaviour of the alloys.³³⁻³⁷ This enhancement in the corrosion rate of the alloy can generally be attributed to the very low reduction potential of magnesium as compared to

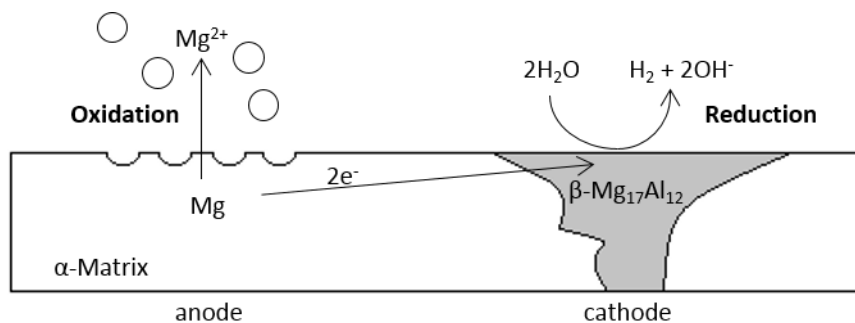


Figure 1.10: Schematic representation of the microgalvanic coupling process occurring on a Mg AM50 alloy. Here, the more noble secondary phase ($\text{Mg}_{17}\text{Al}_{12}$) supports the cathodic reaction while the magnesium matrix is oxidized. The scale of this schematic is on the order of $10\ \mu\text{m}$.

those of the secondary phases. This can generate the formation of microgalvanic couples with the cathodic reaction occurring readily on the secondary phases leading to the enhanced oxidation of the magnesium matrix. Figure 1.10 shows a schematic representation of such a microgalvanic couple between a segregated β -phase ($\text{Mg}_{17}\text{Al}_{12}$) and the matrix of the Mg AM50 alloy.

The effect of having two dissimilar metallic species in electrical contact with one another (i.e. galvanic coupling) on the corrosion kinetics for a metal (M1) connected to a conducting secondary phase (M2) is shown in an Evans diagram in Figure 1.11. The individual, uncoupled $\log I$ - E relationships for M1 and M2 are shown in blue and red, respectively. When uncoupled, each metal corrodes at the rate $I_{\text{CORR}, M1}$ and $I_{\text{CORR}, M2}$. When coupled, the two materials adopt a new potential termed the mixed potential which is shown by $E_{\text{CORR}, \text{Couple}}$ in the diagram. The metal with the lower corrosion potential (M2) will become the anodic material and transfer electrons to the second phase with the higher potential (M1) which, hence, supports the cathodic reaction. The coupled $\log I$ - E

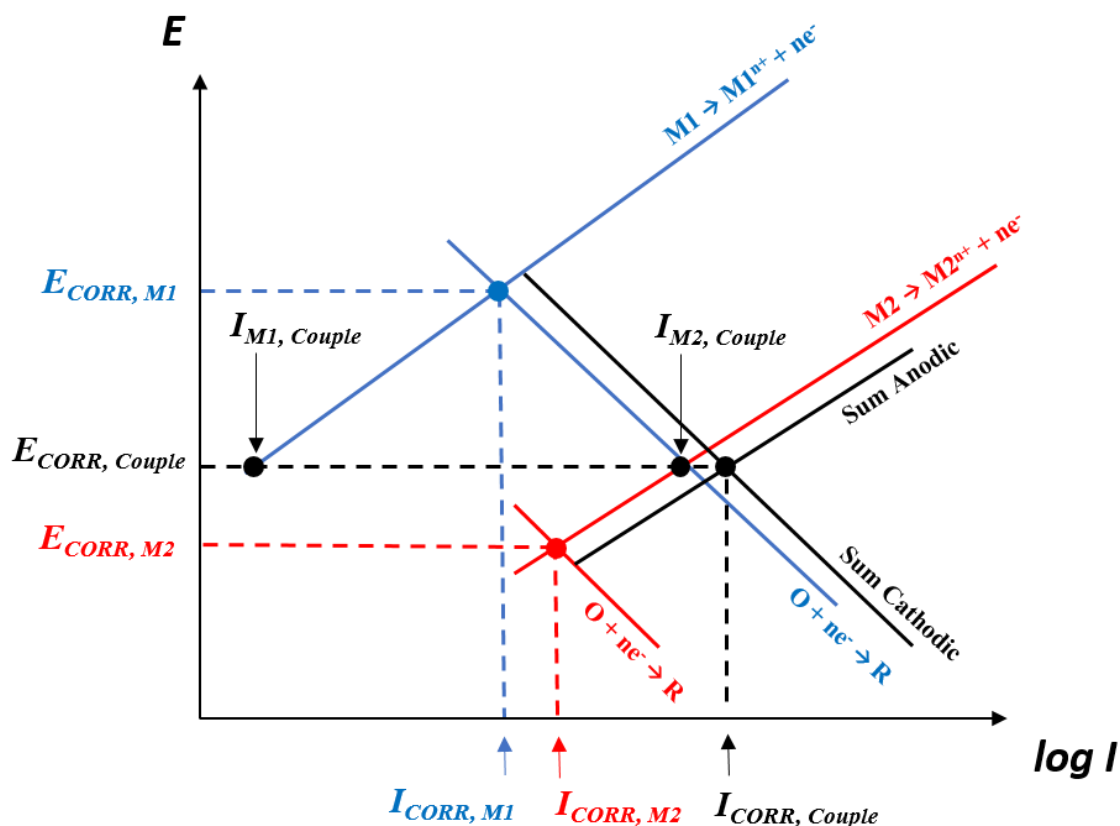


Figure 1.11: Evans diagram illustrating the effect of a galvanic couple on the corrosion kinetics of a noble, uncoupled metal (blue) and an active, uncoupled metal (red). The result of the galvanic couple is illustrated in black.

relationships for the cathodic and anodic branches are shown by black dashed lines and are the sum of the $\log I$ - E relationship for each of the anodic and cathodic process on M1 and M2. Where these two lines intersect is the point where the total cathodic and anodic charges balance for the coupled process. As illustrated, corrosion of the couple proceeds at a rate, $I_{CORR, Couple}$ which is greater than the uncoupled corrosion rate for M2.

1.4.3 Corrosion Morphology

In general, the corrosion product that forms on magnesium alloys is composed of an outer layer of $\text{Mg}(\text{OH})_2$ and an inner layer of MgO .^{38,39} Figure 1.12a and b shows low and high magnification electron micrographs of a corrosion product film formed on the Mg ZEK100 alloy after immersion in a chloride solution for 24 h. The corrosion product forms

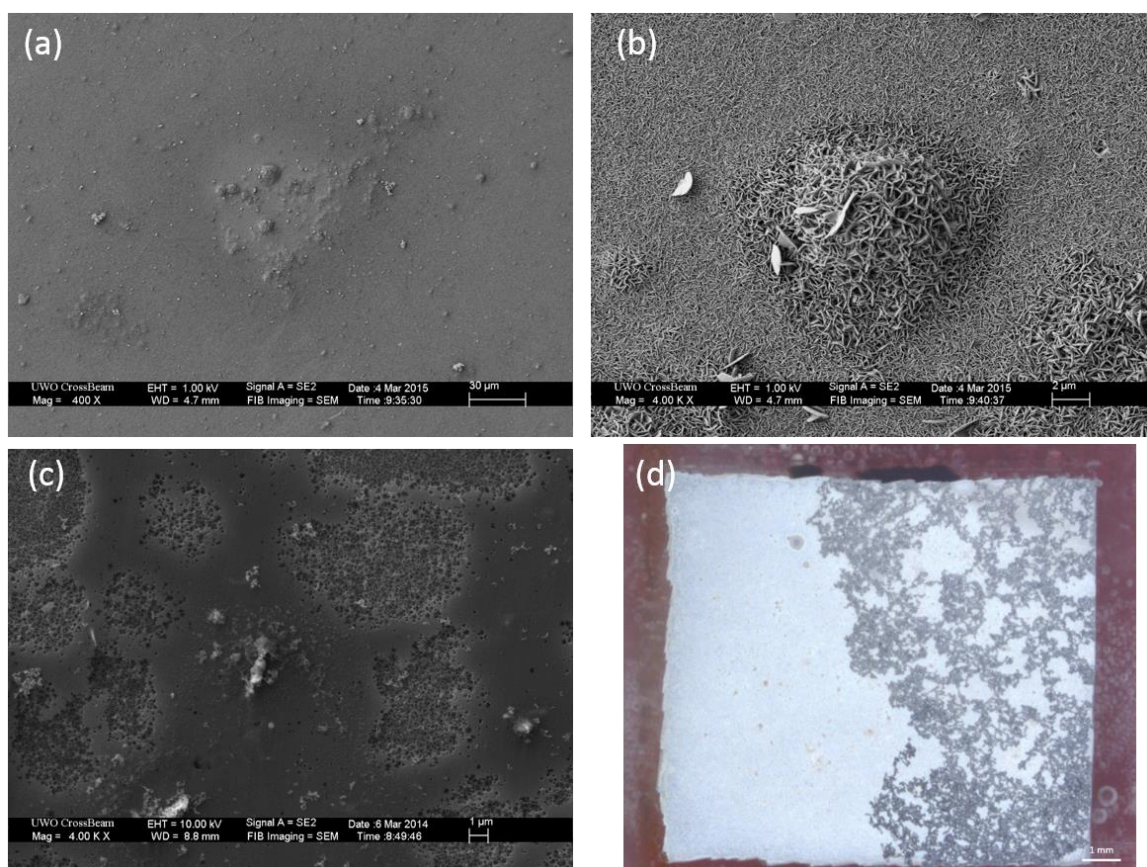


Figure 1.12: (a and b) SEM micrographs of a corroded Mg ZEK100 alloy surface showing the morphology of the general corrosion product and corrosion product domes. (c) SEM micrograph showing the enhanced dissolution of the magnesium matrix compared to regions occupied by secondary microstructures on a Mg AM50 alloy. (d) Optical micrograph showing the morphology of the filiform-like corrosion morphology on a Mg ZEK100 alloy.

as thin platelets which extend outward from the metal surface. In Figure 1.12b the porous nature of this film is evident. Also conspicuous in Figure 1.12 is the presence of several raised areas on the alloy surface. These areas are formed as a consequence of microgalvanic coupling (described in section 1.4.2) and are located over microgalvanically-coupled secondary phases which support the cathodic reaction, water reduction. This leads to the enhanced deposition of $\text{Mg}(\text{OH})_2$ corrosion product as a result of an increase in the local pH. The presence of these corrosion product domes are commonly observed on many different magnesium alloys.^{33,40,41} Their formation is often accompanied by dissolution of the surrounding local α -Mg matrix,^{34,40,42} An example is shown in Figure 1.12c. For alloys containing aluminum or zinc corrosion has been shown to lead to an enriched layer of either Al or Zn at the metal/oxide interface.^{27,43-45} In both cases, the presence of such a layer has been linked with an enhanced corrosion resistance.

Another common morphology of corrosion on both pure and alloyed magnesium is the so-called “filiform-like” corrosion. An example is shown in Figure 1.12d. This morphology is characterized by a laterally propagating corrosion front which leaves behind a black raised deposit of corrosion product. The black nature of this corrosion product is puzzling since $\text{Mg}(\text{OH})_2$ is a white substance. Typically, these filaments only penetrate ~ 20 – 25 μm into the alloy and, as noted above, exhibit an enrichment of Zn at the metal/corrosion product interface.^{43,46} The nature of these filaments and the mechanism of their formation will be discussed in Chapters 5 and 6.

1.4.4 The Anomaly of Anodic Polarization

Despite what appears to be a relatively straightforward corrosion mechanism, magnesium and magnesium alloys exhibit strange behaviour when anodically polarized. As the potential is increased positive to E_{CORR} , there is a corresponding increase in hydrogen evolution from the metal surface. This behaviour is counterintuitive as the hydrogen evolution reaction (HER) is a cathodic reaction and, according to classical electrochemical kinetics, ought to decrease in rate and eventually cease as the potential is made more positive. Historically, this phenomenon was labelled the negative difference effect (NDE) but this terminology is increasingly scarce in the literature with many researchers preferring either “anomalous hydrogen evolution” or “anodic hydrogen evolution”. Semantics aside, understanding the root cause of this behaviour is vital for the successful adoption of magnesium in light-weighting technology since magnesium, due to its low reduction potential, will always be the preferential anode when coupled to other conducting materials.

The first explanation for the NDE was proposed by Petty et al. in 1954.⁴⁷ This work claimed that a unipositive Mg^+ species could exist in solution, oxidize by coupling to water reduction and thus cause a greater than expected amount of hydrogen. This explanation was widely accepted and propagated through the literature for several decades.^{48–53} However, to date, no experimental or spectroscopic evidence is available to unequivocally show that Mg^+ is a viable aqueous species capable of producing the NDE.^{54–58} However, over the last decade the understanding of the corrosion of magnesium and its alloys has been extensively advanced.

Williams et al.^{55,56} utilized the scanning vibrating electrode technique (SVET) to map localized current densities on a corroding Mg surface. Experiments conducted on anodically polarized magnesium revealed that localized anodes traverse the alloy surface leaving behind black corroded areas. These dark areas were shown to exhibit net cathodic behaviour, a process called 'cathodic activation'.^{55,57-60} It was proposed that magnesium oxidation is supported by two cathodic reactions: that occurring on the counter electrode and that occurring on the dark corroded regions on the surface which supported hydrogen evolution. The site of the cathodic reaction occurring in the dark regions has been extensively debated. Various studies attempted to implicate the corrosion product film,^{55,57,60-62} the impurities in the film or at the metal/film interface^{38,63} or on sites were impurities, previously dissolved, have redeposited on the surface.^{64,65} However, measurements of hydrogen gas evolving from anodically polarized samples show that the rate of the cathodic reaction is not a function of the surface area of the dark regions as would be expected for a cathodic activation mechanism.⁶⁶ Rather, the rate of hydrogen evolution is a function of either the area of actively corroding material or the magnitude of the applied anodic potential.

Based on this evidence, Fajardo et al. were able to show an approximately four fold increase in the exchange current density for the HER on magnesium with an increase in applied anodic current.⁶² It was also demonstrated that this increase in exchange current density was associated with regions dominated by the oxidation reaction. This led to the conclusion that the source of the HE was from a co-located anode-cathode couple existing at the advancing corrosion front.

While the mechanistic details of anomalous hydrogen evolution remain to be determined there are some compelling avenues under investigation. The first, recently supported by density functional theory (DFT) modelling hypothesises that a bare magnesium surface will split a water molecule leading to the adsorption of hydroxyl radicals and atomic hydrogen on the metal surface. Subsequently, H_2 is produced via recombination of the atomic hydrogen and oxidation of the $Mg(OH)_{(ads)}$ site.⁶⁷ However, this model does not account for the dynamic nature of the magnesium surface. The second line of thinking proposes that a magnesium hydride species is an important intermediate in the corrosion mechanism.^{46,68–70} Such a scenario is consistent with the aforementioned observations and several other light metal systems exhibit similar behaviour including titanium,^{71,72} aluminum⁷³ and zirconium.⁷⁴ Our evidence supporting this mechanism is presented in Chapters 5 and 6 of this thesis.

1.4.5 Role of Alloying Elements in the Corrosion of Mg Alloys.

As discussed, for magnesium to be of any use in engineering applications it is necessary to alloy it with other elements. A list of common alloying elements along with their impact on magnesium are listed in Table 1.1.^{75–79} In general, alloying elements have low solubility in magnesium which leads to the formation of secondary phases and alloy microstructures which can promote microgalvanic coupling. As with any metal system, the pros and cons of alloying elements must be considered if effective alloys are to be developed for specific applications.

1.4.5.1 Aluminum

Aluminum is one of the most commonly used alloying elements in magnesium alloys because it is cheap and relatively soluble in magnesium. Additions of aluminum increase the strength and decrease the ductility of magnesium alloys. These changes in physical properties are the result of the formation of an aluminum rich β -phase ($\text{Mg}_{17}\text{Al}_{12}$) which has an accompanying eutectic phase extending into the magnesium matrix.^{80,81} In general, it has been shown that adding aluminum to magnesium up to approximately 10 wt% is beneficial for the corrosion resistance of alloys with larger amounts of aluminum leading to enhanced corrosion.⁷⁶ However, the corrosion behaviour of alloys is not solely reliant on the concentration of aluminum (or other alloying elements) in the matrix. Many studies, including those in Chapters 4 and 6 of this thesis, show that the composition, size and distribution of secondary phases plays a key role in determining the corrosion behaviour of an alloy. For example, it is reported that alloys with a more even distribution of aluminum in the magnesium matrix exhibit shallower corrosion penetration than those with a more localized distribution.

1.4.5.2 Zinc

Zinc, the second most common alloying element used in magnesium is frequently added in conjunction with aluminum. As with many other elements, the addition of zinc leads to the formation of secondary phase particles (Mg_xZn_y , where x and y depend on Zn content and the time-temperature history of the alloy) when the zinc content exceeds 1 wt%.³² This produces particles which are more noble than the matrix and lead to enhanced corrosion via microgalvanic coupling. This effect has been shown to increase significantly

with even small increases of zinc content (i.e. from 1 to 3 wt%).⁸²⁻⁸⁴ Often, zinc is incorporated into magnesium alloys along with other alloying elements (e.g. in the AZ, ZE, ZEK series magnesium alloys).

1.4.5.3 Zirconium

Zirconium is typically used in magnesium alloys as a strong grain refiner which imparts favourable mechanical properties. This is because zirconium is not soluble in magnesium and acts as a nucleation site for grains during the crystallization process. While some studies suggest that small additions (i.e. < 0.5 wt%) of zirconium are favourable for corrosion resistance most studies report the opposite.⁸⁵⁻⁸⁷ Zirconium has been shown to have an activation effect on anodic kinetics by destabilizing the corrosion product film. Zirconium particles have also been identified as local cathodes which support oxidation of the matrix in a ZE41 alloy.

1.4.5.4 Rare Earths

Like zirconium, rare earth elements (i.e. Nd, Ce and La) are also added to magnesium as grain refiners. As commonly observed with other alloying elements, the rare earths tend to increase corrosion rate by forming secondary phases and increasing the rate of the cathodic reaction.⁸⁸ Studies suggest that cerium and lanthanum have a more dramatic effect on the corrosion rate than neodymium.⁸⁴ However, when added in conjunction with aluminum or manganese, neodymium will form Al-Nd or Mn-Nd particles which tend to have reduced cathodic reaction rates associated with microgalvanic couples.⁸⁹ It has been suggested that rare earths scavenge impurity levels of Fe. The resulting RE-Fe particles are

less noble than iron alone and thus, serve to reduce the corrosion rate of the magnesium matrix.

Table1.2: List of alloying elements common to magnesium alloys and their influence on alloy properties.

Alloying Element	Code	Influence	Reference
Aluminum	A	Improve castability, precipitation hardness, corrosion resistance	80, 81
Calcium	X	Improves creep resistance, grain refiner	83, 84
Manganese	M	Scavenge impurities	81
Rare Earths	E	Improve creep resistance, castability, age hardening and grain refiner	83, 85
Silicon	S	Improve creep resistance	83
Strontium	J	Improve creep resistance	84
Yttrium	W	Improve tensile properties, grain refiner	83
Zinc	Z	Improve ductility and castability	81
Zirconium	K	Scavenges impurities and grain refiner	80, 87

1.4.6 Effects of Microstructure on Magnesium Corrosion

Because the solubility of most alloying elements is low, most magnesium alloys exhibit secondary (or more) microstructures. On one hand, these microstructures can help improve various physical characteristics of the alloys while on the other they often decrease the corrosion resistance. However, it is not easy to predict precisely what effect the composition, size or distribution of a specific microstructure will have on corrosion behaviour. Further, these effects are complicated by the microstructural features of the magnesium matrix itself where features such as grain size have been shown to have a

significant influence on corrosion.⁹⁰ This section offers a brief review of the effects of microstructure on the corrosion performance of alloys relevant to this thesis.

1.4.6.1 Grain Size

Casting procedure has a pronounced effect on the grain size of magnesium alloys.^{91,92} Frequently, smaller grain sizes are correlated with a decrease in the corrosion rate of an alloy.⁹³ Examples of this trend have been shown for magnesium AZ31,⁹⁴⁻⁹⁷ AZ91^{93,98} and ZK60.⁹⁹ Typically, the enhancement of corrosion resistance is attributed to the formation of a better corrosion product layer which is promoted by a more evenly dispersed secondary phase network. While studies on pure magnesium reinforce this trend it is difficult to decouple the combined effect of grain size and chemical distribution in alloys.

1.4.6.2 Al-Mn Intermetallics

Manganese is often added to magnesium alloys as a scavenger for impurities such as iron and copper. In aluminum containing alloys, this can lead to the presence of small intermetallic particles (IMPs) (e.g. Al-Mn-Fe or Al-Mn-Cu) distributed throughout the magnesium matrix. As with other secondary microstructures, these IMPs are more noble than the matrix and therefore act as cathodes. In fact, these IMPs were shown to have a more positive Volta potential than the $Mg_{17}Al_{12}$ β -phase in the AZ80 alloy.¹⁰⁰ This would suggest that in this case, the IMPs are more efficient cathodes than the β -phase. Typically, following corrosion, these IMPs collect corrosion product domes indicating their function as a cathode. However, differences in the amount of $Mg(OH)_2$ deposition suggest that some IMPs are better cathodes than others. This difference has been attributed to the amount of

impurities contained in the IMP (i.e. a higher impurity level produces a better cathode).^{34,41,44,76,98,101–103}

1.4.6.3 β -phase

Above 3 wt%, Al will precipitate in the magnesium matrix to produce a β -phase ($\text{Mg}_{17}\text{Al}_{12}$).³² The presence of this β -phase increases the strength of the alloy and its castability.⁷⁵ However, this phase has been reported to have both a detrimental^{104,105} and positive^{44,103} effects on the corrosion rates of alloys. In studies which show a detrimental effect, the β -phase is claimed to be an efficient cathode supporting magnesium oxidation. Increases in corrosion resistance are attributed to formation of a fine aluminum enriched surface layer at the metal/oxide interface. However, the effectiveness of such a layer as a corrosion barrier has been shown to be a function of the distribution of the β -phase in the alloy; with a more even distribution leading to a greater corrosion resistance.^{40,44,106} The influence of the distribution of this β -phase is explored in Chapter 4.

1.5 Scope of Thesis

The goals of this research are to investigate the effects of changes in the microstructure (i.e. composition, distribution and size) of lightweight alloys on their overall corrosion behaviour and to contribute to the fundamental understanding of the magnesium corrosion mechanism. While the main focus is on magnesium alloys, Chapter 3 focuses on the role of magnesium as an alloying element in another lightweight material, aluminum. Specifically, the effect of small additions (1 – 2 wt%) of magnesium to alloys used in brazing sheet materials on the localized corrosion behaviour of the alloy are investigated.

This research combines bulk electrochemical (i.e. E_{CORR} , PDP) and microscopy (SEM) with localized techniques (EDX and SECM) to assess the corrosion behaviour.

Chapter 4 focuses on a well characterized class of magnesium alloys, the AM series. The specific focus is on the role of the size and distribution of microstructural features on the corrosion properties of the alloy. Standard electrochemical techniques are utilized (i.e. E_{CORR} and EIS) in conjunction with optical and electron microscopy. A range of chloride containing aqueous and non-aqueous electrolytes are investigated to interrogate the nature of microgalvanic coupling and how it is influenced by the alloy microstructure and the composition of the exposure environment.

Chapters 5 and 6 are companion studies which interrogate the underlying mechanism of magnesium alloy corrosion. In Chapter 5, electrochemical and physical evidence is presented to support the role of a magnesium hydride intermediate in magnesium corrosion. The electrochemical and physical measurements are compared with recent literature to propose a mechanism consistent with the observable phenomena. With this in mind, Chapter 6 investigates the effect of alloy cooling rate on the corrosion behaviour of a Mg ZEK100 alloy. Again, the work utilizes a range of electrochemical (E_{CORR} and PDP) and microscopic (optical, electron and confocal microscopy) techniques which support the findings of Chapter 5 and relate the changes in corrosion behaviour to the nature of the corrosion product film.

1.6 References

- (1) Cook, J.; Nuccitelli, D.; Green, S. A.; Richardson, M.; Winkler, B.; Painting, R.; Way, R.; Peter Jacobs; Skuce, A. Quantifying the Consensus on Anthropogenic Global Warming in the Scientific Literature. *Environ. Res. Lett.* **2013**, *8* (2), 024024.
- (2) Cook, J.; Oreskes, N.; Doran, P. T.; Anderegg, W. R. L.; Verheggen, B.; Maibach, E. W.; Carlton, J. S.; Lewandowsky, S.; Skuce, A. G.; Green, S. A.; et al. Consensus on Consensus: A Synthesis of Consensus Estimates on Human-Caused Global Warming. *Environ. Res. Lett.* **2016**, *11* (4), 048002.
- (3) Anderegg, W. R. L.; Prall, J. W.; Harold, J.; Schneider, S. H. Expert Credibility in Climate Change. *Proc. Natl. Acad. Sci. U. S. A.* **2010**, *107* (27), 12107–12109.
- (4) Doran, P. T.; Zimmerman, M. K. Examining the Scientific Consensus on Climate Change. *Eos Trans. Am. Geophys. Union* **2009**, *90* (3), 22–23.
- (5) Oreskes, N. The Scientific Consensus on Climate Change. *Science* **2004**, *306* (5702), 1686.
- (6) Change, N. G. C. Carbon dioxide concentration | NASA Global Climate Change <https://climate.nasa.gov/vital-signs/carbon-dioxide> (accessed Sep 24, 2018).
- (7) Brook, E. J.; Buizert, C. Antarctic and Global Climate History Viewed from Ice Cores. *Nature* **2018**, *558* (7709), 200–208.
- (8) Buizert, C.; Keisling, B. A.; Box, J. E.; He, F.; Carlson, A. E.; Sinclair, G.; DeConto, R. M. Greenland-Wide Seasonal Temperatures During the Last Deglaciation. *Geophys. Res. Lett.* **2018**, *45* (4), 1905–1914.
- (9) Cole-Dai, J.; Peterson, K. M.; Kennedy, J. A.; Cox, T. S.; Ferris, D. G. Evidence of Influence of Human Activities and Volcanic Eruptions on Environmental Perchlorate from a 300-Year Greenland Ice Core Record. *Environ. Sci. Technol.* **2018**, *52* (15), 8373–8380.
- (10) Prokopiou, M.; Sapart, C. J.; Rosen, J.; Sperlich, P.; Blunier, T.; Brook, E.; Wal, R. S. W. van de; Röckmann, T. Changes in the isotopic signature of atmospheric nitrous oxide and its global average source during the last three millennia. *J. Geophys. Res. Atmospheres* *0* (ja).
- (11) Winski, D.; Osterberg, E.; Kreutz, K.; Wake, C.; Ferris, D.; Campbell, S.; Baum, M.; Bailey, A.; Birkel, S.; Introne, D.; et al. A 400-Year Ice Core Melt Layer Record of Summertime Warming in the Alaska Range. *J. Geophys. Res. Atmospheres* **2018**, *123* (7), 3594–3611.
- (12) Change, N. G. C. Global surface temperature | NASA Global Climate Change <https://climate.nasa.gov/vital-signs/global-temperature> (accessed Sep 24, 2018).
- (13) Solar Power Incentives, Rebates, And Tax Credits (Canada 2018) <https://solarpanelpower.ca/rebates-incentives-tax-credits-canada/> (accessed Sep 4, 2018).
- (14) GM to Cut Vehicle Weight ‘Up to 15%’ by 2017 - Environmental Leader <https://www.environmentalleader.com/2013/03/gm-to-cut-vehicle-weight-up-to-15-by-2017/> (accessed Sep 4, 2018).
- (15) Government of Canada, E. and C. C. C. Environment and Climate Change Canada - Environmental Indicators - Greenhouse Gas Emissions by Canadian Economic Sector <https://www.ec.gc.ca/indicateurs-indicators/default.asp?lang=en&n=F60DB708>- (accessed Sep 24, 2018).

- (16) Meinshausen, M.; Meinshausen, N.; Hare, W.; Raper, S. C. B.; Frieler, K.; Knutti, R.; Frame, D. J.; Allen, M. R. Greenhouse-Gas Emission Targets for Limiting Global Warming to 2 °C. *Nature* **2009**, *458*, 1158.
- (17) Caton, J. A. Maximum Efficiencies for Internal Combustion Engines: Thermodynamic Limitations. *Int. J. Engine Res.* **2017**, 1468087417737700.
- (18) Global Electric Vehicle Market Looks To Power Up In 2018 <https://www.forbes.com/sites/sarwantsingh/2018/04/03/global-electric-vehicle-market-looks-to-fire-on-all-motors-in-2018/#425bad742927> (accessed Sep 5, 2018).
- (19) March 17, jim motavalli M.; 2010; Pm, 1:21. Seven Barriers to the Electric Car <https://www.cbsnews.com/news/seven-barriers-to-the-electric-car/> (accessed Sep 5, 2018).
- (20) The Hurdles For Electric Cars <https://www.forbes.com/2010/03/24/fuel-batteries-subsidies-technology-ecotech-electric-vehicles.html#2d4d241b7ba8> (accessed Sep 5, 2018).
- (21) Kulekci, M. Magnesium and Its Alloys Applications in Automotive Industry. *Int. J. Adv. Manuf. Technol.* **2008**, *39* (9–10), 851–865.
- (22) Automotive Uses of Magnesium Alloys: Part One :: Total Materia Article <https://www.totalmateria.com/page.aspx?ID=CheckArticle&site=ktn&NM=246> (accessed Sep 24, 2018).
- (23) Abbott, T. B. Magnesium: Industrial and Research Developments Over the Last 15 Years. *Corrosion* **2015**, *71* (2), 120–127.
- (24) Pourbaix, M. *Atlas of Electrochemical Equilibria in Aqueous Solutions*, 2nd English ed.; National Association of Corrosion Engineers: Houston, Texas, 1974.
- (25) Salahshoor, M.; Guo, Y.; Salahshoor, M.; Guo, Y. Biodegradable Orthopedic Magnesium-Calcium (MgCa) Alloys, Processing, and Corrosion Performance. *Materials* **2012**, *5* (1), 135–155.
- (26) Splinter, S. J.; McIntyre, N. S. The Initial Interaction of Water Vapour with Mg–Al Alloy Surfaces at Room Temperature. *Surf. Sci.* **1994**, *314* (2), 157–171.
- (27) Nordlien, J. H.; Ono, S.; Masuko, N.; Nisancioglu, K. Morphology and Structure of Oxide Films Formed on Magnesium by Exposure to Air and Water. *J. Electrochem. Soc.* **1995**, *142* (10), 3320–3322.
- (28) Refson, K.; Wogelius, R. A.; Fraser, D. G.; Payne, M. C.; Lee, M. H.; Milman, V. Water Chemisorption and Reconstruction of the MgO Surface. *Phys. Rev. B* **1995**, *52* (15), 10823–10826.
- (29) Włodarczyk, R.; Sierka, M.; Kwapien, K.; Sauer, J.; Carrasco, E.; Aumer, A.; Gomes, J. F.; Sterrer, M.; Freund, H.-J. Structures of the Ordered Water Monolayer on MgO(001). *J. Phys. Chem. C* **2011**, *115* (14), 6764–6774.
- (30) Hydration Structures of MgO, CaO, and SrO (001) Surfaces - The Journal of Physical Chemistry C (ACS Publications) <https://pubs.acs.org/doi/abs/10.1021/acs.jpcc.6b07434> (accessed Sep 24, 2018).
- (31) Avedesian, M. M.; Baker, H. *Magnesium and Magnesium Alloys*; ASM Specialty Handbook; 1999.
- (32) Pekguleryuz, M. O.; Kainer, K.; Kaya, A. A. *Fundamentals of Magnesium Alloy Metallurgy*; Elsevier, 2013.

- (33) Asmussen, R. M.; Binns, W. J.; Jakupi, P.; Shoesmith, D. The Influence of Microstructure on the Corrosion of Magnesium Alloy ZEK100. *Corrosion* **2015**, *71* (2), 242–254.
- (34) Asmussen, R. M.; Binns, W. J.; Jakupi, P.; Dauphin-Ducharme, P.; Tefashe, U. M.; Mauzeroll, J.; Shoesmith, D. Reducing the Corrosion Rate of Magnesium Alloys Using Ethylene Glycol for Advanced Electrochemical Imaging. *Corros. Sci.* **2015**, *93*, 70–79.
- (35) Deshpande, K. B. Effect of Aluminium Spacer on Galvanic Corrosion between Magnesium and Mild Steel Using Numerical Model and SVET Experiments. *Corros. Sci.* **2012**, *62* (Complete), 184–191.
- (36) Lacroix, L.; Blanc, C.; Pébère, N.; Tribollet, B.; Vivier, V. Localized Approach to Galvanic Coupling in an Aluminum–Magnesium System. *J. Electrochem. Soc.* **2009**, *156* (8), C259–C265.
- (37) Deshpande, K. B. Experimental Investigation of Galvanic Corrosion: Comparison between SVET and Immersion Techniques. *Corros. Sci.* **2010**, *52* (9), 2819–2826.
- (38) Taheri, M.; Kish, J. R.; Birbilis, N.; Danaie, M.; McNally, E. A.; McDermid, J. R. Towards a Physical Description for the Origin of Enhanced Catalytic Activity of Corroding Magnesium Surfaces. *Electrochimica Acta* **2014**, *116* (Complete), 396–403.
- (39) Taheri, M.; Phillips, R. C.; Kish, J. R.; Botton, G. A. Analysis of the Surface Film Formed on Mg by Exposure to Water Using a FIB Cross-Section and STEM–EDS. *Corros. Sci.* **2012**, *59* (Complete), 222–228.
- (40) Asmussen, R. M.; Binns, W. J.; Jakupi, P.; Shoesmith, D. Microstructural Effects on Corrosion of AM50 Magnesium Alloys. *J. Electrochem. Soc.* **2014**, *161* (10), C501–C508.
- (41) Asmussen, R. M.; Binns, W. J.; Partovi-Nia, R.; Jakupi, P.; Shoesmith, D. W. The Stability of Aluminum–Manganese Intermetallic Phases under the Microgalvanic Coupling Conditions Anticipated in Magnesium Alloys: The Stability of Aluminum–Manganese Intermetallic Phases. *Mater. Corros.* **2016**, *67* (1), 39–50.
- (42) Neil, W. C.; Forsyth, M.; Howlett, P. C.; Hutchinson, C. R.; Hinton, B. R. W. Corrosion of Magnesium Alloy ZE41 – The Role of Microstructural Features. *Corros. Sci.* **2009**, *51* (2), 387–394.
- (43) Cano, Z. P.; Danaie, M.; Kish, J. R.; McDermid, J. R.; Botton, G. A.; Williams, G. Physical Characterization of Cathodically-Activated Corrosion Filaments on Magnesium Alloy AZ31B. *Corrosion* **2015**, *71* (2), 146–159.
- (44) Danaie, M.; Asmussen, R. M.; Jakupi, P.; Shoesmith, D. W.; Botton, G. A. The Role of Aluminum Distribution on the Local Corrosion Resistance of the Microstructure in a Sand-Cast AM50 Alloy. *Corros. Sci.* **2013**, *77*, 151–163.
- (45) Rossouw, D.; Fu, D.; Leonard, D. N.; Brady, M. P.; Botton, G. A.; Kish, J. R. Characterization of Localized Filament Corrosion Products at the Anodic Head on a Model Mg–Zn–Zr Alloy Surface. *Corrosion* **2017**, *73* (5), 518–525.
- (46) Binns, W.; Zargarzadah, F.; Dehnavi, V.; Chen, Jian; Noel, J.; Shoesmith, D. Physical and Electrochemical Evidence for the Role of a Mg Hydride Species in Mg Alloy Corrosion. *Corrosion* **2018**.

- (47) Petty, R. L.; Davidson, A. W.; Kleinberg, J. The Anodic Oxidation of Magnesium Metal: Evidence for the Existence of Unipositive Magnesium^{1,2}. *J. Am. Chem. Soc.* **1954**, *76* (2), 363–366.
- (48) Atrens, A.; Dietzel, W. The Negative Difference Effect and Unipositive Mg⁺. *Adv. Eng. Mater.* **2007**, *9* (4), 292–297.
- (49) Song, G.; Atrens, A.; Stjohn, D.; Nairn, J.; Li, Y. The Electrochemical Corrosion of Pure Magnesium in 1 N NaCl. *Corros. Sci.* **1997**, *39* (5), 855–875.
- (50) Song, G.; Atrens, A.; John, D. S.; Wu, X.; Nairn, J. The Anodic Dissolution of Magnesium in Chloride and Sulphate Solutions. *Corros. Sci.* **1997**, *39* (10), 1981–2004.
- (51) Song, G.; Atrens, A.; Wu, X.; Zhang, B. Corrosion Behaviour of AZ21, AZ501 and AZ91 in Sodium Chloride. *Corros. Sci.* **1998**, *40* (10), 1769–1791.
- (52) Song, G. L. *Corrosion of Magnesium Alloys*; Elsevier, 2011.
- (53) Tunold, R.; Holtan, H.; Berge, M.-B. H.; Lasson, A.; Steen-Hansen, R. The Corrosion of Magnesium in Aqueous Solution Containing Chloride Ions. *Corros. Sci.* **1977**, *17* (4), 353–365.
- (54) Samaniego, A.; Hurley, B. L.; Frankel, G. S. On the Evidence for Univalent Mg. *J. Electroanal. Chem.* **2015**, *737*, 123–128.
- (55) Williams, G.; Birbilis, N.; McMurray, H. N. The Source of Hydrogen Evolved from a Magnesium Anode. *Electrochem. Commun.* **2013**, *36* (Supplement C), 1–5.
- (56) Williams, G.; McMurray, H. N. Localized Corrosion of Magnesium in Chloride-Containing Electrolyte Studied by a Scanning Vibrating Electrode Technique. *J. Electrochem. Soc.* **2008**, *155* (7), C340–C349.
- (57) Curioni, M. The Behaviour of Magnesium during Free Corrosion and Potentiodynamic Polarization Investigated by Real-Time Hydrogen Measurement and Optical Imaging. *Electrochimica Acta* **2014**, *120* (Supplement C), 284–292.
- (58) Fajardo, S.; Frankel, G. S. Effect of Impurities on the Enhanced Catalytic Activity for Hydrogen Evolution in High Purity Magnesium. *Electrochimica Acta* **2015**, *165*, 255–267.
- (59) Birbilis, N.; King, A. D.; Thomas, S.; Frankel, G. S.; Scully, J. R. Evidence for Enhanced Catalytic Activity of Magnesium Arising from Anodic Dissolution. *Electrochimica Acta* **2014**, *132* (Supplement C), 277–283.
- (60) Salleh, S. H.; Thomas, S.; Yuwono, J. A.; Venkatesan, K.; Birbilis, N. Enhanced Hydrogen Evolution on Mg (OH)₂ Covered Mg Surfaces. *Electrochimica Acta* **2015**, *161* (Supplement C), 144–152.
- (61) Curioni, M.; Scenini, F.; Monetta, T.; Bellucci, F. Correlation between Electrochemical Impedance Measurements and Corrosion Rate of Magnesium Investigated by Real-Time Hydrogen Measurement and Optical Imaging. *Electrochimica Acta* **2015**, *166*, 372–384.
- (62) Fajardo, S.; Frankel, G. S. Effect of Impurities on the Enhanced Catalytic Activity for Hydrogen Evolution in High Purity Magnesium. *Electrochimica Acta* **2015**, *165* (Supplement C), 255–267.
- (63) Cain, T.; Madden, S. B.; Birbilis, N.; Scully, J. R. Evidence of the Enrichment of Transition Metal Elements on Corroding Magnesium Surfaces Using Rutherford Backscattering Spectrometry. *J. Electrochem. Soc.* **2015**, *162* (6), C228–C237.

- (64) Höche, D.; Blawert, C.; Lamaka, S. V.; Scharnagl, N.; Mendis, C.; Zheludkevich, M. L. The Effect of Iron Re-Deposition on the Corrosion of Impurity-Containing Magnesium. *Phys. Chem. Chem. Phys.* **2015**, *18* (2), 1279–1291.
- (65) Lamaka, S. V.; Höche, D.; Petrauskas, R. P.; Blawert, C.; Zheludkevich, M. L. A New Concept for Corrosion Inhibition of Magnesium: Suppression of Iron Re-Deposition. *Electrochem. Commun.* **2016**, *62*, 5–8.
- (66) Fajardo, S.; Glover, C. F.; Williams, G.; Frankel, G. S. The Source of Anodic Hydrogen Evolution on Ultra High Purity Magnesium. *Electrochimica Acta* **2016**, *212* (Supplement C), 510–521.
- (67) Taylor, C. D. A First-Principles Surface Reaction Kinetic Model for Hydrogen Evolution under Cathodic and Anodic Conditions on Magnesium. *J. Electrochem. Soc.* **2016**, *163* (9), C602–C608.
- (68) Chen, J.; Wang, J.; Han, E.; Dong, J.; Ke, W. States and Transport of Hydrogen in the Corrosion Process of an AZ91 Magnesium Alloy in Aqueous Solution. *Corros. Sci.* **2008**, *50* (5), 1292–1305.
- (69) Chen, J.; Dong, J.; Wang, J.; Han, E.; Ke, W. Effect of Magnesium Hydride on the Corrosion Behavior of an AZ91 Magnesium Alloy in Sodium Chloride Solution. *Corros. Sci.* **2008**, *50* (12), 3610–3614.
- (70) Buggio, D.; Trueba, M.; Trasatti, S. P. Corrosion of Mg Alloy in the Presence of Ammonium Ion. Evidence of Hydride Sub-Products. *Corros. Sci.* **2016**, *104* (Supplement C), 173–186.
- (71) Yan, L.; Ramamurthy, S.; Noël, J. J.; Shoesmith, D. W. Hydrogen Absorption into Alpha Titanium in Acidic Solutions. *Electrochimica Acta* **2006**, *52* (3), 1169–1181.
- (72) He, X.; Shoesmith, D. W.; Noel, J. J. Crevice Corrosion of Grade-12 Titanium. *J. ASTM Int.* *5* (8), 14.
- (73) Adhikari, S.; Hebert, K. R. Participation of Aluminum Hydride in the Anodic Dissolution of Aluminum in Alkaline Solutions. *J. Electrochem. Soc.* **2008**, *155* (5), C189.
- (74) Malka, I. E.; Bystrzycki, J.; Płociński, T.; Czujko, T. Microstructure and Hydrogen Storage Capacity of Magnesium Hydride with Zirconium and Niobium Fluoride Additives after Cyclic Loading. *J. Alloys Compd.* **2011**, *509*, S616–S620.
- (75) Polmear, I. *Light Alloys: From Traditional Alloys to Nanocrystals*; Elsevier, 2005.
- (76) Song, G. Recent Progress in Corrosion and Protection of Magnesium Alloys. *Adv. Eng. Mater.* **2005**, *7* (7), 563–586.
- (77) Pekguleryuz, M. O.; Kaya, A. A. Creep Resistant Magnesium Alloys for Powertrain Applications. *Adv. Eng. Mater.* **2003**, *5* (12), 866–878.
- (78) Luo, A. A. Recent Magnesium Alloy Development for Elevated Temperature Applications. *Int. Mater. Rev.* **2004**, *49* (1), 13–30.
- (79) Atrens, A.; Winzer, N.; Dietzel, W.; Srinivasan, P. B.; Song, G.-L. 8 - Stress Corrosion Cracking (SCC) of Magnesium (Mg) Alloys. In *Corrosion of Magnesium Alloys*; Song, G., Ed.; Woodhead Publishing Series in Metals and Surface Engineering; Woodhead Publishing, 2011; pp 299–364.
- (80) Liu, M.; Uggowitzer, P. J.; Nagasekhar, A. V.; Schmutz, P.; Easton, M.; Song, G.-L.; Atrens, A. Calculated Phase Diagrams and the Corrosion of Die-Cast Mg–Al Alloys. *Corros. Sci.* **2009**, *51* (3), 602–619.

- (81) Mathieu, S.; Rapin, C.; Steinmetz, J.; Steinmetz, P. A Corrosion Study of the Main Constituent Phases of AZ91 Magnesium Alloys. *Corros. Sci.* **2003**, *45* (12), 2741–2755.
- (82) Kirkland, N.; Staiger, M.; Nisbet, D.; Davies, C.; Birbilis, N. Performance-Driven Design of Biocompatible Mg Alloys. *JOM* **2011**, *63* (6), 28–34.
- (83) Makar, G. L.; Kruger, J. Corrosion Studies of Rapidly Solidified Magnesium Alloys. *J. Electrochem. Soc.* **1990**, *137* (2), 414–421.
- (84) Corrosion of Magnesium Alloys: The Role of Alloying. *Int. Mater. Rev.* **2015**, *60* (3), 169–194.
- (85) Sun, M.; Wu, G.; Wang, W.; Ding, W. Effect of Zr on the Microstructure, Mechanical Properties and Corrosion Resistance of Mg–10Gd–3Y Magnesium Alloy. *Mater. Sci. Eng. A* **2009**, *523* (1), 145–151.
- (86) Gandel, D. S.; Easton, M. A.; Gibson, M. A.; Abbott, T.; Birbilis, N. The Influence of Zirconium Additions on the Corrosion of Magnesium. *Corros. Sci.* **2014**, *81*, 27–35.
- (87) Gandel, D. s.; Easton, M. a.; Gibson, M. a.; Birbilis, N. Influence of Mn and Zr on the Corrosion of Al-Free Mg Alloys: Part 2—Impact of Mn and Zr on Mg Alloy Electrochemistry and Corrosion. *Corrosion* **2013**, *69* (8), 744–751.
- (88) Birbilis, N.; Easton, M. A.; Sudholz, A. D.; Zhu, S. M.; Gibson, M. A. On the Corrosion of Binary Magnesium-Rare Earth Alloys. *Corros. Sci.* **2009**, *51* (3), 683–689.
- (89) Arrabal, R.; Pardo, A.; Merino, M. C.; Mohedano, M.; Casajús, P.; Paucar, K.; Garcés, G. Effect of Nd on the Corrosion Behaviour of AM50 and AZ91D Magnesium Alloys in 3.5wt.% NaCl Solution. *Corros. Sci.* **2012**, *55*, 301–312.
- (90) op't Hoog, C.; Birbilis, N.; Estrin, Y. Corrosion of Pure Mg as a Function of Grain Size and Processing Route. *Adv. Eng. Mater.* **2008**, *10* (6), 579–582.
- (91) Nagasekhar, A. V.; Easton, M. A.; Cáceres, C. H. Solute Content and the Grain Microstructure of High Pressure Diecast Magnesium–Aluminium Alloys. *Adv. Eng. Mater.* **2009**, *11* (11), 912–919.
- (92) Bowles, A.; Kazuhiro, N.; Dargusch, M.; Davidson, C.; Griffiths, J. Grain Size Measurements in Mg-Al High Pressure Die Castings Using Electron Back-Scattered Diffraction (EBSD). *Mater. Trans.* **2004**, *45* (11), 3114–3119.
- (93) Ralston, K. D.; Birbilis, N. Effect of Grain Size on Corrosion : A Review. *Corrosion* **2010**, *66* (7), 075005–075013.
- (94) Liao, J.; Hotta, M.; Yamamoto, N. Corrosion Behavior of Fine-Grained AZ31B Magnesium Alloy. *Corros. Sci.* **2012**, *61*, 208–214.
- (95) Alvarez-Lopez, M.; Pereda, M. D.; del Valle, J. A.; Fernandez-Lorenzo, M.; Garcia-Alonso, M. C.; Ruano, O. A.; Escudero, M. L. Corrosion Behaviour of AZ31 Magnesium Alloy with Different Grain Sizes in Simulated Biological Fluids. *Acta Biomater.* **2010**, *6* (5), 1763–1771.
- (96) Aung, N. N.; Zhou, W. Effect of Grain Size and Twins on Corrosion Behaviour of AZ31B Magnesium Alloy. *Corros. Sci.* **2010**, *52* (2), 589–594.
- (97) Liao, J.; Hotta, M.; Motoda, S.; Shinohara, T. Atmospheric Corrosion of Two Field-Exposed AZ31B Magnesium Alloys with Different Grain Size. *Corros. Sci.* **2013**, *71* (Complete), 53–61.

- (98) Ballerini, G.; Bardi, U.; Bignucolo, R.; Ceraolo, G. About Some Corrosion Mechanisms of AZ91D Magnesium Alloy. *Corros. Sci.* **2005**, *47* (9), 2173–2184.
- (99) Orlov, D.; Ralston, K. D.; Birbilis, N.; Estrin, Y. Enhanced Corrosion Resistance of Mg Alloy ZK60 after Processing by Integrated Extrusion and Equal Channel Angular Pressing. *Acta Mater.* **2011**, *59* (15), 6176–6186.
- (100) Andreatta, F.; Apachitei, I.; Kodentsov, A. A.; Dzwonczyk, J.; Duszczak, J. Volta Potential of Second Phase Particles in Extruded AZ80 Magnesium Alloy. *Electrochimica Acta* **2006**, *51* (17), 3551–3557.
- (101) Pardo, A.; Merino, M. C.; Coy, A. E.; Arrabal, R.; Viejo, F.; Matykina, E. Corrosion Behaviour of Magnesium/Aluminium Alloys in 3.5wt.% NaCl. *Corros. Sci.* **2008**, *50* (3), 823–834.
- (102) Matsubara, H.; Ichige, Y.; Fujita, K.; Nishiyama, H.; Hodouchi, K. Effect of Impurity Fe on Corrosion Behavior of AM50 and AM60 Magnesium Alloys. *Corros. Sci.* **2013**, *66* (Complete), 203–210.
- (103) Ma, Y.; Zhang, J.; Yang, M. Research on Microstructure and Alloy Phases of AM50 Magnesium Alloy. *J. Alloys Compd.* **2009**, *470* (1–2), 515–521.
- (104) Song, G.; Bowles, A. L.; StJohn, D. H. Corrosion Resistance of Aged Die Cast Magnesium Alloy AZ91D. *Mater. Sci. Eng. A* **2004**, *366* (1), 74–86.
- (105) Zhao, M.-C.; Liu, M.; Song, G.; Atrens, A. Influence of the β -Phase Morphology on the Corrosion of the Mg Alloy AZ91. *Corros. Sci.* **2008**, *50* (7), 1939–1953.
- (106) Zhang, T.; Shao, Y.; Meng, G.; Cui, Z.; Wang, F. Corrosion of Hot Extrusion AZ91 Magnesium Alloy: I-Relation between the Microstructure and Corrosion Behavior. *Corros. Sci.* **2011**, *53* (5), 1960–1968.

2 Experimental

This chapter introduces the fundamental aspects of the experimental and analytical techniques employed in the research described in this thesis. Emphasis is placed on generic descriptions of the instrumentation and underlying scientific theories which govern each technique. Specific functionalities related to the work herein are discussed. However, this is not intended to be an exhaustive account of the capabilities of each technique or instrument. For more details, should the reader be so inclined, please see the references cited throughout.

2.1 Materials and Material Preparation

2.1.1 Al Alloys

Three novel Al alloys based on the AA3xxx Al-Mn-Cu system containing various amounts of Mg content (i.e. from 0.11 to 2.06 wt%) were provided by CanmetMATERIALS, Hamilton, ON. The alloy nomenclature and corresponding elemental compositions are shown in Table 2.1. The alloys were provided in as-cold rolled sheets with dimensions of 300 x 300 x 2 mm³. Samples, 10 x 10 mm², were cut and cold mounted in Struers Epofix® epoxy resin and ground successively with P800 and P2400 grit SiC grinding paper using a 1:1 ethanol-to-isopropanol mixture as lubricant. The final polishing step utilized a Struers MasterTex® polishing cloth with a 3 µm diamond abrasive. Samples were polished unidirectionally for each step and rotated 90° for the subsequent step. Following polishing, samples were immersed in anhydrous (99.5%) ethanol and sonicated for 1 min prior to being dried in an Ar stream. This process produced

a scratch free mirror finish which was suitable for microscopic and electrochemical analysis.

Table 3.1: Compositions of the three Al alloys investigated.

Alloy	Mn	Fe	Cu	Si	Mg
A005	1.5	0.25	0.5	0.1	0.11
A002	1.5	0.25	0.5	0.1	1.0
A004	1.5	0.25	0.5	0.1	2.06

2.1.2 Mg Alloys

A central theme of this thesis is the effect of composition and the size and distribution of metallurgical features on the corrosion of Mg alloys. To investigate this phenomenon two different Mg alloys were chosen: AM50 and ZEK100. For the AM50 alloy three different alloy casting methods were explored: sand, graphite and die casting. Wedge cast and a rolled sheet alloy were investigated for the ZEK100 alloy.

2.1.2.1 Mg AM50 Alloys

Mg AM50 alloys were received from General Motors, USA. The three different casts had nominally identical compositions of 4.9 % Al and 0.5% Mn by weight. Trace impurities such as Fe and Cu are also present. The sand and graphite cast ingots were cylindrical in shape with a 5 cm diameter and a height of 30 cm. Samples were machined into 1 cm³ cubes from the center of the ingots to ensure that cooling rates for each sample from the same cast were identical. Die cast Mg AM50 was received in 3 mm thick sheets

that were cut and machined into 1 x 1 cm² samples. All samples were tapped on one face to allow a stainless-steel rod to be threaded into the sample, to allow electrical connection to external circuitry. Samples were then cold mounted in Struers Epofix® epoxy resin and allowed to set for 12 h. All samples were polished to a mirror finish prior to testing. Polishing was performed with a 1:1 ethanol-to-isopropanol lubricant on 800, 1200 and 4000 grit SiC polishing pads, successively. This was followed by polishing with a 3 µm diamond abrasive on a Struers DP-Dur® pad. Samples were rinsed with anhydrous ethanol (99.5%) and sonicated for 1 min. The final polishing step was performed with a 1:1 0.04 µm colloidal silica-to-ethylene glycol suspension on a Struers OP-Chem® polishing pad. Once polished, samples were again sonicated in anhydrous ethanol for 1 min before drying under an Ar stream.

2.1.2.2 Mg ZEK100 Alloys

Two Mg ZEK100 alloys with nominally identical compositions (1.33Zn-0.30Zr-0.17Nd-Bal.Mg (wt%)) were investigated. The first, was a Mg ZEK100F sheet alloy with F referring to the alloy in the as-formed condition. Alloys with a 1.5 mm thickness were received as 30 x 30 cm² sheets and cut into 1 x 1 cm² samples. Samples were tapped, mounted and polished according to the procedure described in section 2.1.2.1. The second

alloy investigated was a wedge cast Mg ZEK100 alloy fabricated by CanmetMATERIALS,

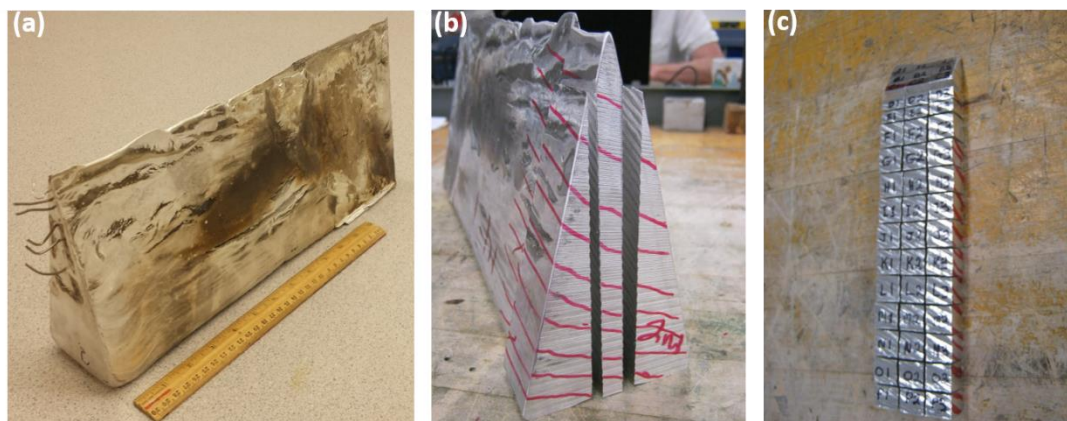


Figure 2.1: (a) Mg ZEK100 wedge cast ingot, with a 30 cm ruler as a reference scale, and series of six thermocouples attached to one end. (b) End view of the Mg ZEK100 wedge cast with 5 cm of the end removed to cut out the thermocouples. A 1 cm thick portion was sectioned down the center line to create samples with gradients in cooling rate. (c) Final samples are labelled alphabetically with sample A being taken from the narrow tip of the wedge cast.

Hamilton, Figure 2.1a. The wedge had a height of 15.5 cm, a width at the base of 7 cm and a length of 39.5 cm. Triangular coupons were prepared by cutting each ingot into 1 cm sections, Figure 2.1b and c. Samples were cut at various distances from the tip of the cast and labelled alphabetically with section A being closest to the wedge tip as shown in Figure 1c. Section A was produced by cutting the ingot 0.64 cm from the tip to produce a sample with a surface area of 0.125 cm^2 . Section B was produced by cutting the ingot 0.5 cm below section A to yield a sample with a surface area of 0.375 cm^2 . Similarly, section C was produced by cutting the ingot 0.5 cm below section B and had a surface area of 0.5 cm^2 . Sections D-E were each cut to a height of 0.5 cm (surface area of 1 cm^2) and sections F-M to a height of 1 cm (surface area of 1 cm^2). Samples were tapped, mounted and polished according to the procedure described in section 2.1.2.1.

2.2 Chromic Acid Treatment

Following corrosion experiments the alloy surface was covered by a mixed MgO/Mg(OH)₂ corrosion product film. To investigate the nature of the alloy surface (e.g. the corrosion morphology or corrosion penetration depth) it is necessary to remove this

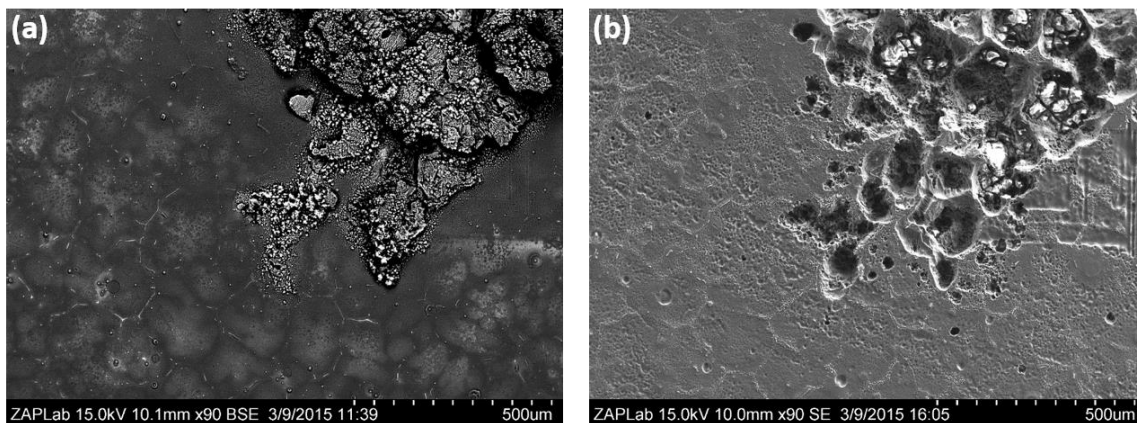


Figure 2.2: Scanning electron micrographs of a corroded Mg ZEK100 wedge cast alloy (a) before and (b) after a chromic acid treatment to remove the Mg(OH)₂ corrosion product.

film. This was done using the ASTM G 1-90 standard procedure, “Standard Practice for Preparing, Cleaning, and Evaluating Corrosion Test Specimens”.¹ This method involves immersing the corroded material in a chemical solution to dissolve the corrosion products thereby exposing the metal surface. This etchant comprised 200 g of CrO₃, 10 g of AgNO₃ and 20 g of Ba(NO₃)₂ in 1000 mL of deionised water. Samples were immersed in the solution and agitated until bubbles ceased to be liberated from the surface. Typically, this method required approximately 1 min of immersion. Upon removal from the etchant samples were rinsed with anhydrous ethanol (99.5%) and dried under an Ar gas stream.

Figure 2.2a and b show scanning electron micrographs of a surface of a Mg sample both before and after chromic acid treatment, respectively.

2.3 Microscopy

2.3.1 Optical Microscopy

Optical microscopy, also called light microscopy, is a widely used technique. Although invented in the 1590's by Zacharias Jansen, a Dutch spectacle maker, the microscope was not employed as an experimental tool until the late 1600's when Anton van Leeuwenhoek was able to create a lens capable of 270x magnification.² Nowadays, particularly in materials and corrosion science, optical microscopy is invaluable for investigating the microstructures of different metals and other materials.

2.3.1.1 Optical Principles

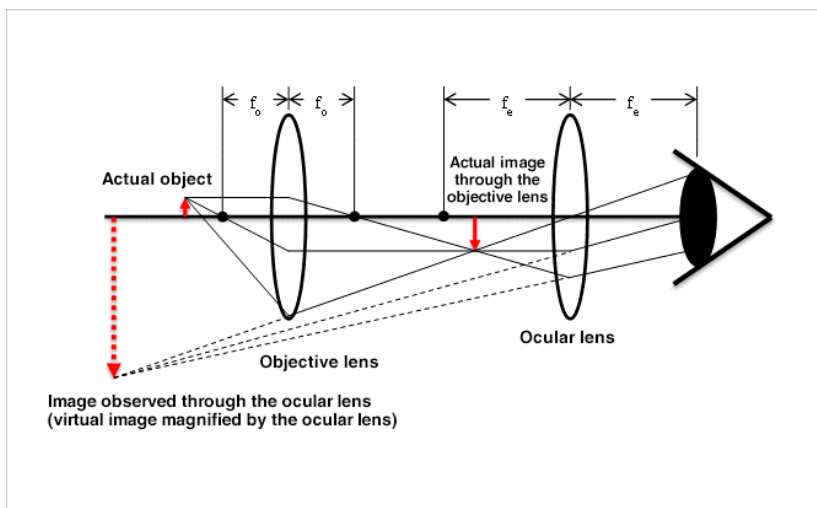


Figure 2.3: Schematic illustration of the basic optical principles of image formation and magnification in an optical microscope. The theoretical focal lengths for the objective and ocular lens are indicated by f_o and f_e , respectively.

The three basic features of optical microscopy are image formation, magnification and resolution. A schematic illustration of the process of image formation is shown in Fig. 2.3. The sample is placed at position A, between one and two focal lengths from the objective lens. A focal length is the distance from the middle of the lens to the point at which it focuses light, as illustrated by f_o and f_e in Figure 2.3. Light from the object passes through the optical lens and becomes focused at point B. This forms a magnified, inverted image of the object, the primary image. Finally, the light rays emanating from the primary image converge on the ocular lens revealing a real, magnified image, point C. This real image can then be passed through an eyepiece to form a virtual image which can be seen by the eye or be recorded electronically on a computer screen.

The magnification of a microscope (M) can be calculated by utilizing linear optics, equation 2.1.³

$$M = \frac{v - f}{f} \quad (2.1)$$

Where f is the focal length of the lens and v is the distance between the image and the lens. Clearly, higher magnification microscopes will have shorter focal lengths. For compound microscopes (i.e. microscopes which employ a series of lenses), the magnification can be calculated by multiplying the magnification of the objective lens by that of the ocular lens. For Figure 2.3, this takes the form of equation 2.2.

$$M = M_o M_e = \frac{(v_o - f_o)(v_e - f_e)}{f_o f_e} \quad (2.2)$$

Similarly, when an eyepiece is used, the total magnification of the microscope will be the magnification of the objective lens multiplied by the eyepiece magnification.

The final feature, resolution, refers to the minimum distance between two points or objects which allows the points to be recognized as distinct. The resolution (R) of a microscope is determined by the refractive index of the medium between the object and the objective lens (μ) and the half-angle of the cone of light entering the objective (α) where the product of $\mu \sin \alpha$ is called the numerical aperture (NA). This relationship is demonstrated by Equation 2.3.

$$R = \frac{0.61\lambda}{\mu \sin \alpha} \quad (2.3)$$

It follows from Equation 2.3 that microscopes which utilize shorter wavelengths of light and possess larger NA s will achieve the greatest resolution.

2.3.1.2 Experimental Details

In the studies presented in this thesis, optical microscopy was used to characterize corroded Mg alloy surfaces following immersion in various electrolytes both prior to and following chromic acid treatment as described in section 2.2. All studies were performed using a Zeiss LUMAR stereomicroscope. This instrument utilizes reflected light from the sample surface. This mode of operation is ideal for metallic surfaces which readily reflect light even following prolonged corrosion. Only relatively low-resolution micrographs were acquired with magnifications ranging from 10x to 120x. This range of magnification was ideal for characterizing macroscopic corrosion morphologies. When required, higher magnification images were acquired with a scanning electron microscope (SEM).

2.3.2 Scanning Electron Microscopy

Owing to its simple experimental procedures, relatively low cost and highly customizable features, SEM has become an indispensable tool in corrosion science, materials science and many other fields of scientific research. Developed in 1938, the SEM can achieve significantly greater magnification and resolution than conventional optical microscopes. Furthermore, SEM allows for qualitative and semi-quantitative chemical analysis of specimens.⁴ The following sections explain the fundamental aspects of SEM along with the various complementary techniques in the studies described in this thesis.

2.3.2.1 Instrumentation

As shown in Figure 2.4, an SEM consists of an electron gun, electromagnetic lenses (in series), and various apertures and detectors. The electron gun generates a high energy electron beam which will ultimately interact with the sample to yield an image. Because the energy of the electrons govern the wavelength of the beam and the wavelength of the beam factors significantly in the resolution of the microscope (Equation 2.3), the acceleration voltage of the electron gun, which determines the energy of the electrons, goes a long way in determining the resolution of the microscope. Two types of electron source exist for SEM: a thermionic emission gun (TEG) and a field emission gun (FEG). In a TEG system, either a tungsten filament or a lanthanum hexaboride filament serves as the cathode. In both cases the filament is heated by the passage of an electrical current which provides electrons with sufficient kinetic energy to leave the filament thereby creating an electron beam. For FEG electron sources, a very high electric field is applied to a metal surface (typically tungsten) which is tapered into a very fine tip. The electric field pulls the

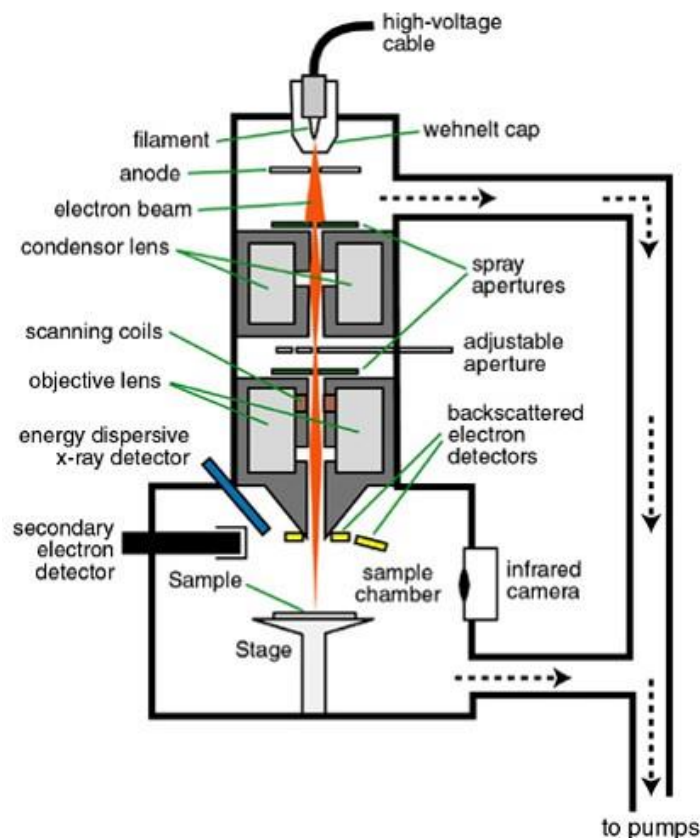


Figure 2.4: Schematic of a scanning electron microscope (SEM).

electrons from the metal to generate the beam. FEG systems are capable of generating electron beams 10^4 times more intense than tungsten TEG systems and 10^2 times more intense than lanthanum hexaboride TEG systems.^{3,4} Except when indicated otherwise, TEG electron sources were utilized in this work since high resolution was not required.

Like light microscopes, an SEM requires a series of lenses to manipulate the electron beam. However, since glass will block the path of electrons, SEM systems take advantage of the charge on the electron by using electromagnetic lenses. Electromagnetic lenses are discs with a hole in the middle through which the electrons pass. The lens contains a solenoid and generates an intense magnetic field which is concentrated in the

opening of the disc. By controlling the current which passes through the solenoid this magnetic field is easily managed and the electrons assume a helical path which can be manipulated to achieve the desired result. As shown in Figure 2.4, two types of electromagnetic lens are utilized; a condenser lens which is closest to the electron gun and an optical lens which is downstream from the electron gun. By changing the distance at which the electron beam converges prior to entering the objective lens, the condenser lens controls the initial spot size of the electron beam whereas the main purpose of the objective lens is to focus the beam onto the sample.

Sitting above and below each lens are adjustable apertures. Apertures are strips of metal with holes of various sizes. The aperture can be moved in and out to select for various beam diameters which are permitted to pass through. The aperture also serves to block any off-axis or off-energy electrons from reaching the sample. After passing through each lens and aperture the electron beam interacts with the sample to produce electrons and x-rays which can be used for image formation and chemical analyses.

2.3.2.2 Electron-Specimen Interactions

When an incident beam of high-energy electrons is focused on a specimen they interact with atoms within the sample. This leads to scattering of the incident electrons just below the surface of the sample. The shape of the trajectory of the electrons within the sample will depend on several factors such as the accelerating voltage and the sample density but typically this produces a pear-shaped pattern as depicted in Figure 2.5.^{3,4} Within this interaction volume, various kinds of electrons and x-rays can be generated, emitted and detected by the SEM. In the research in this thesis, secondary electrons (SE) and

backscattered electrons (BSE) were utilized for sample imaging. Characteristic X-rays were also utilized and are discussed in section 2.3.3.1.

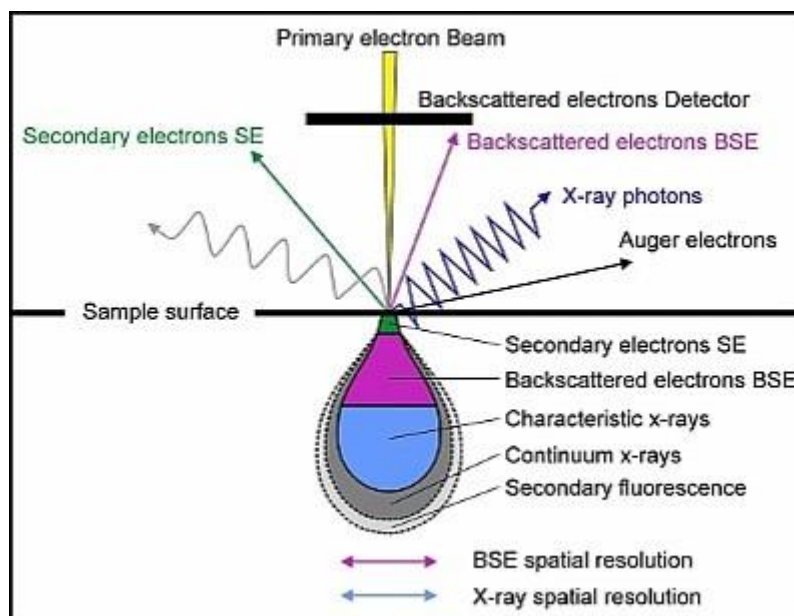


Figure 2.5: Diagram showing the interaction volume of a primary electron beam with a sample and the possible outputs resulting from electron-specimen interactions.

The main difference between SEs and BSEs is the type of scattering which produces them. SEs are the result of inelastic scattering and possess energies on the order of a few keV. Because these SEs are relatively low in energy they can only escape from the near surface region (i.e. from depths up to approximately 50 nm). By contrast, BSEs are generated by elastic scattering with energies similar to that of the incident beam. This means that BSEs produced deeper in the interaction volume (i.e. approximately 300 nm) have sufficient energy to escape the sample and reach the detector. The relative depths from which each kind of electron can be generated are summarized in Figure 2.5. Because these electrons have different energies and origins they can be utilized to extract different information about the sample.

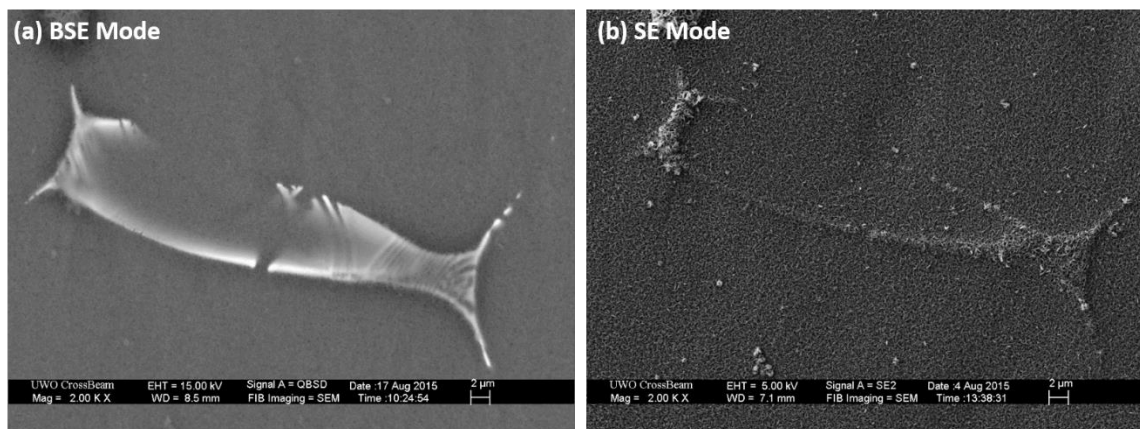


Figure 2.6: SEM micrographs recorded on the same microstructural feature of a Mg ZEK100 alloy. (a) is recorded utilizing the BSE mode which is sensitive to compositional differences. Here, the white regions correspond to a Zn-rich secondary phase and the dark areas the Mg matrix. (b) is recorded utilizing the SE mode which is sensitive to topographical features. The fine needle-like corrosion product layer is clearly visible.

The difference between micrographs recorded with SEs and BSEs is demonstrated in Figure 2.6a and b, respectively. Both micrographs were recorded on a Mg ZEK100 wedge cast sample exposed to a 0.16 wt% NaCl solution for 24 h. This juxtaposition underscores the fact that SEs are most useful for investigating topographic contrast while BSEs are better indicators of the contrast in chemical composition between features.

Topographical information arises from two possible effects: the trajectory effect and the electron number effect. The trajectory effect is a result of the position of the SE detector in the SEM. When an interface is parallel to the detector, or nearly so, more of the SEs released reach the detector as compared to surfaces which are orthogonal to the detector. When more electrons reach the detector, a more intense signal is recorded making these areas appear brighter in the resultant micrograph. The electron number effect is a result of the shape of various surface features. When the interaction volume of the incident electron beam occurs near edges of surface features more SEs can escape from the sample.

This increases the number of electrons that reach the detector yielding a more intense signal from these locations. Both effects are visible in Figure 2.6a. It is worth re-emphasizing the fact that SEs arise from the shallowest region of the interaction volume which makes this analysis ideal for investigating the surface of specimens. For Mg alloys, the fine needle morphology of the $\text{Mg}(\text{OH})_2$ corrosion product is best appreciated in SE mode. Such fine surface features are not appreciable in BSE mode, as demonstrated by Figure 2.6b.

For BSEs, differences in chemical composition are easily detectable. This is because the ability of BSEs to escape from a certain chemical phase is dependent upon the atomic number of the atoms which the phase comprises. This relationship is characterized by the backscatter coefficient (η) which is the ratio of the number of BSEs escaping from the specimen (η_{BSE}) to the number of incident electrons (η_i), Equation 2.4.

$$\eta = \frac{\eta_{BSE}}{\eta_i} \quad (2.4)$$

Because η scales with atomic number monotonically, the larger the difference in atomic number between atoms, the greater the BSE yield and therefore the contrast between the two phases. This is demonstrated by the bright spots in Figure 2.6b which are Zr intermetallic particles (atomic number 40) embedded in the $\text{Mg}(\text{OH})_2$ corrosion product (largest atomic number is 12).

2.3.3 Energy Dispersive X-ray Spectroscopy

Energy dispersive X-ray spectroscopy (EDX) is referred to by various abbreviations throughout the literature including: EDX, EDS, EDXS or XEDS. Throughout this thesis the EDX abbreviation is used. EDX is a technique which is easily

incorporated into an SEM by including an X-ray detector in the sample chamber. By collecting characteristic X-rays which are generated by the interaction of incident electrons with the sample this technique can spatially resolve elemental compositions of specimens and correlate the results with SEM micrographs. The source of characteristic X-rays from within the interaction volume is shown in Figure 2.5. Although semi-quantitative, EDX is an extremely valuable tool in many scientific disciplines owing to its straightforward application and relatively low cost.

2.3.3.1 Characteristic X-rays

When atoms are irradiated by high-energy beams the core electrons of the atom may interact with the incident beam. If the incident beam, in this case an electron, is of sufficiently high energy it can displace the core electron from its orbital. The ejection of this electron leaves the atom ionized and in a high-energy excited state. To relieve this excitation, an electron from a higher orbital will relax to take the place of the emitted

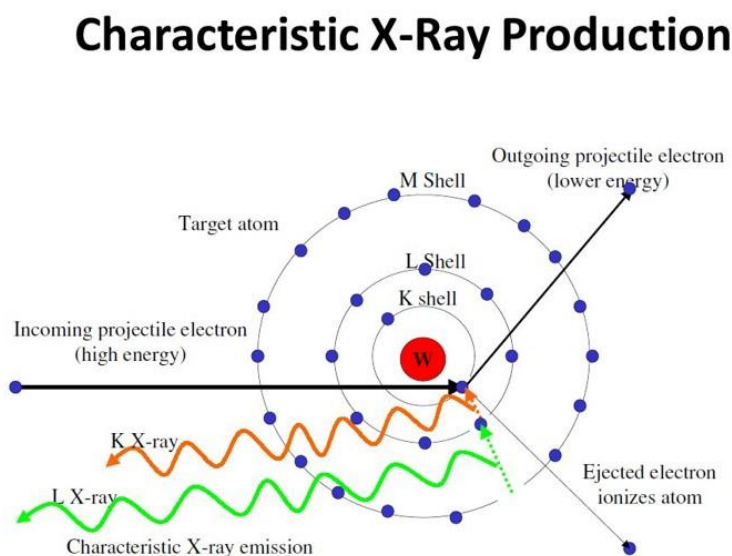


Figure 2.7: Diagram demonstrating the production of characteristic X-rays. An incident electron expels an electron from its orbit causing an electron from a higher orbital to relax to fill the void with the excess energy emitted as an X-ray.

electron. As a result, the atom will emit either an X-ray photon, called a characteristic X-ray or another free electron, called an Auger electron. The process leading to the emission of characteristic X-rays is illustrated in Figure 2.7. The energy of the characteristic X-ray is equal to the energy difference between the emitted electron and the electron which takes its place and is dependent upon the atomic number of the atom. Thus, it can be used to identify the presence of an element in a given sample. The relationship between the wavelength of characteristic X-rays (λ) and the atomic number (Z) is given by Moseley's Law, equation 2.5.

$$\lambda = \frac{B}{(Z - \sigma)^2} \quad (2.5)$$

Where B and σ are constants which depend on the specific shells from which each electron originates.

As characteristic X-rays are emitted by the sample they are collected by the EDX detector which produces a spectrum of signal intensity versus energy where the signal intensity is proportional to the quantity of the element present and the energy identifies the source of the characteristic X-ray. An example of a spectrum recorded on an Al sample is shown in Figure 2.8a. As the electron beam is rastered across the sample surface a spectrum can be recorded for each pixel in the field of view producing a map of the elemental distribution in the analyzed area, as shown in Figure 2.8b. In this way, morphology and topography revealed by SEM can be correlated to elemental composition.

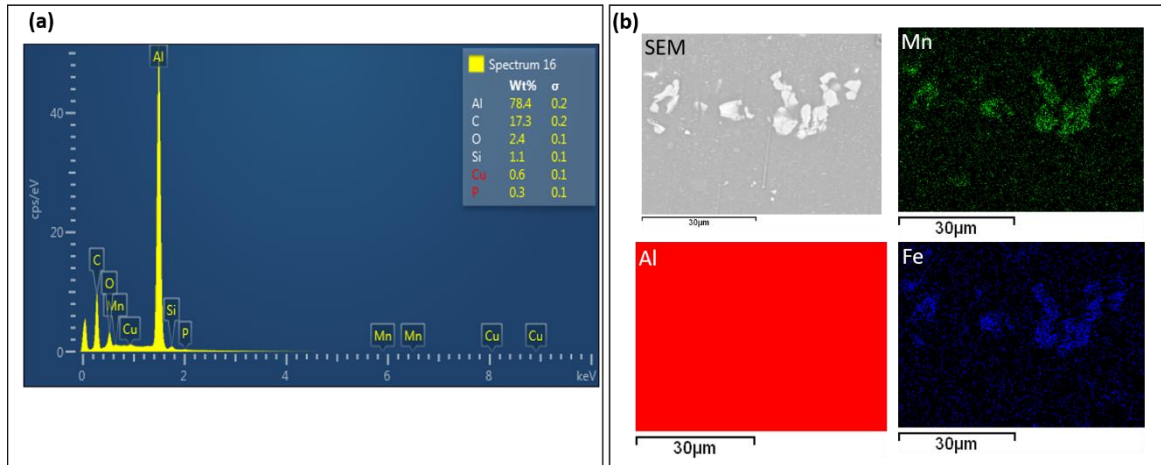


Figure 2.8: (a) EDX spectrum recorded on an Al A005 sample showing the measured counts versus the x-ray energy. (b) EDX maps recorded on the same sample showing the correlation between the SEM micrograph and the elemental composition of Mn, Fe and Al.

2.3.4 Focused Ion Beam (FIB) Cross Sectioning

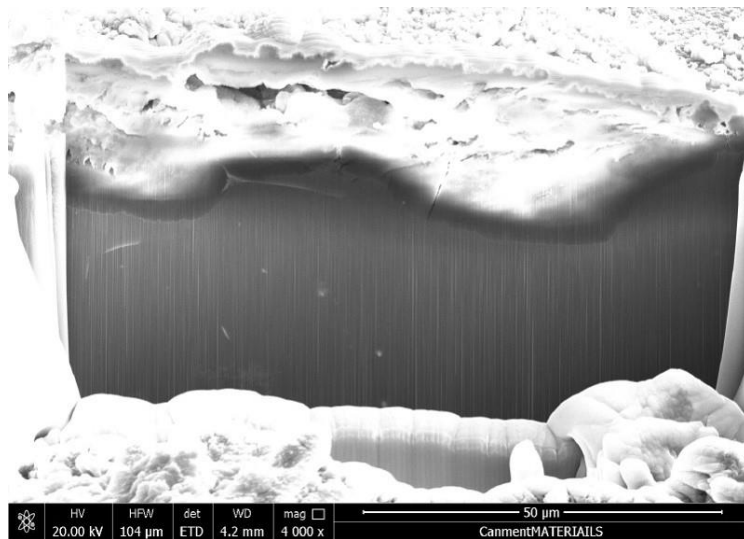


Figure 2.9: FIB cross-section of a Mg ZEK100 wedge cast alloy corroded for 24 h in 0.16 wt% NaCl solution. Fine vertical lines are a result of the FIB bombardment process.

A Focused Ion Beam (FIB) can be used in conjunction with SEM and EDX. A FIB is used to make fine cuts into samples to prepare them for subsequent analysis using

analytical techniques such as SEM, EDX, transmission electron microscopy (TEM) or atom probe tomography (APT). The sample surface is bombarded by heavy atoms to mill away atoms from the sample. In the research described in this thesis, FIB is used to create cross-sections to visualize corrosion product films on corroded surfaces, as shown in Figure 2.9. Commonly, as is the case in this project, a Ga-ion beam is utilized to make FIB cuts. To create the beam, solid Ga is melted and the liquid flows to the tip of a fine W needle in the presence of a strong electric field. Like the electron sources mentioned in section 2.3.2.1, this causes Ga^+ ions to be ejected forming a Ga^+ beam which is accelerated toward the sample surface. When the ion beam reaches the surface elastic collisions cause atoms from the sample to be ejected, thereby cutting into the sample.

2.3.5 Electron Backscatter Diffraction

Electron Backscatter Diffraction (EBSD) can provide quantitative information on the crystallographic nature of various materials. Material properties such as grain size, grain orientation and the overall microstructural texture are readily elucidated provided that the sample has been fine polished to a sufficient degree. This is of great interest with respect to corrosion science as corrosion often proceeds preferentially on certain crystallographic orientations or within grain boundaries among other reasons.

2.3.5.1 EBSD Theory

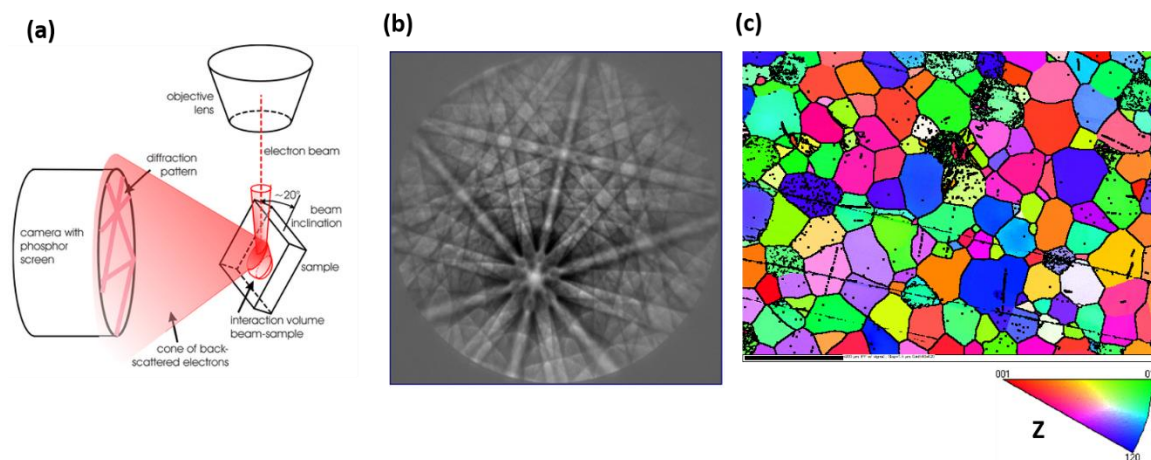


Figure 2.10: (a) Schematic illustration of the EBSD experimental setup. (b) Image showing the Kikuchi bands produced as a result of the electron diffraction process which is recorded on a phosphor screen. Software analyses the Kikuchi bands to extract a myriad of information about the sample including crystallographic structure and grain boundary properties. (c) A map of the crystallographic orientation of grains in a Mg ZEK100 wedge cast alloy. The inverse pole figure at the bottom of the map shows the relationship between grain colour and orientation with respect to the surface normal.

EBSD positions a finely polished sample at an angle of around 20° to the incident electron beam. Such an angle allows many backscattered electrons to escape from the sample and be collected at the detector, which in this case is a phosphor screen. This arrangement is shown in Figure 2.10a. When the primary electron beam impinges on the surface of the sample it interacts with the crystal lattice and diffracts. BSEs originating from various depths of the atomic layers will exit the sample with different path lengths depending on the physical arrangement of the crystal lattice. This leads to constructive and destructive interference, creating an electron backscatter pattern (EBSP) which produces bands of intensity called Kikuchi bands, as shown in Figure 2.10b. The EBSP is a function of the crystal under investigation, the orientation of the crystal in space, the wavelength of

the incident beam and the proximity of the phosphor screen to the sample.⁵ By measuring the relative positions of the Kikuchi bands combined with *a priori* knowledge about the phases present, specialized software deduces the crystal phase and orientation based on a best fit method. By repeating this process across the entire field of view maps of crystallographic orientation can be produced as shown in Figure 2.10c. The colours of the map relate to the various Miller indices of crystals according to the inverse pole figure at the bottom of the map.

2.3.6 Confocal Laser Scanning Microscopy

Confocal Laser Scanning Microscopy (CLSM) is an optical technique which produces three-dimensional (3D) images by scanning through the various focal planes of a sample. By utilizing a high-intensity laser this instrument can image very small areas (compared to a conventional optical microscope) and stitch them together to produce a high-resolution image for a relatively large field of view.

2.3.6.1 Optical Principles

The optical principles for a CLSM are best understood by appreciating the optical arrangement of the instrument, as illustrated in Figure 2.11a. A high-intensity laser source emits light to a dichroic mirror which serves as a filter for the laser. The laser is then directed towards scanning mirrors which are responsible for moving the laser in the x and y-planes with great precision. In combination, these mirrors are responsible for rastering the laser beam across the sample surface. Next, the laser passes through an objective lens which focuses it on the sample. Once the light has been reflected, it passes back through

the objective lens through the semitransparent dichroic mirror towards the confocal pinhole aperture and detector. The aperture allows only a small, central portion of the reflected beam to reach the detector and blocks any out of focus light. Because the light reaching the detector is low intensity a photomultiplier tube (PMT) is used to amplify the received signal. By utilizing a sample stage which is mobile in the z-direction consecutive focal planes can be mapped and stacked by computer software. This creates a 3D image of the sample surface and allows quantitative topographical measurements to be made.

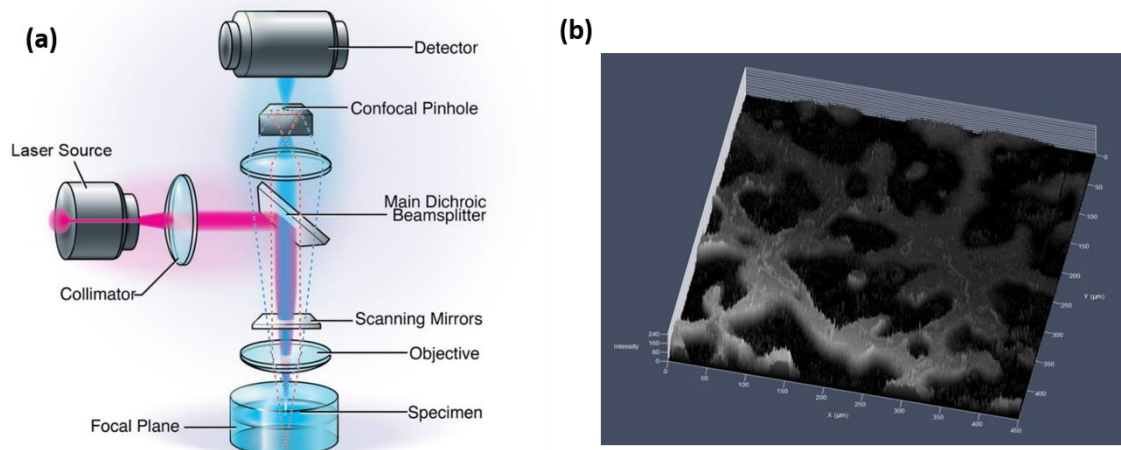


Figure 2.11: (a) Schematic of a CLSM microscope. (b) Sample topographic micrograph produced by CLSM on a Mg AM50 alloy corroded for 96 h in a 1.6 wt% NaCl solution.

2.4 Electrochemical Methods

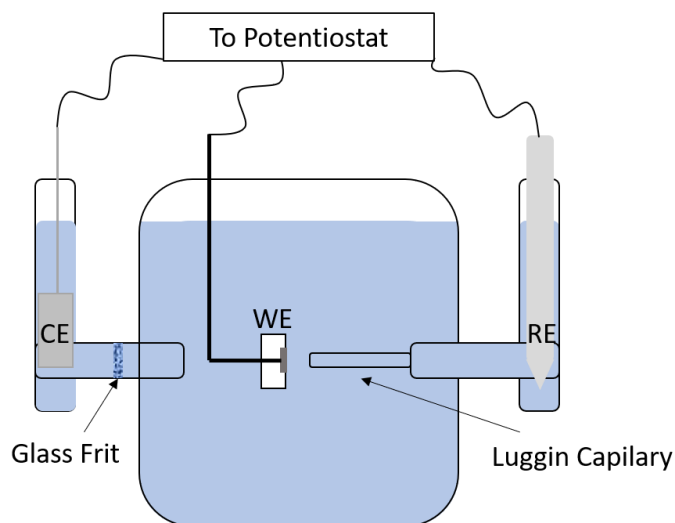
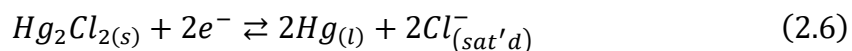
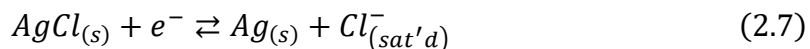


Figure 2.12: Typical three-electrode, three-compartment electrochemical cell used for all electrochemical experiments except for scanning electrochemical microscopy studies. The cell houses a WE, RE and CE (when necessary) in three distinct compartments. Each electrode is connected to a potentiostat via external circuitry.

All electrochemical experiments were performed using a three-electrode cell similar to that depicted in Figure 2.12 which was placed in a Faraday cage to eliminate external noise. In all cases the working electrode (WE) was the alloy of interest, either Al or Mg and prepared as described in section 2.1. The counter electrode (CE) was a Pt flag which was heated until red hot with a Bunsen burner and cooled with deionised water prior to immersion in the electrochemical cell. Two different reference electrodes (RE) were used depending on the immersion environment. In near neutral solutions a commercially available saturated calomel electrode (SCE) was used. This electrode relies on a mercurous chloride equilibrium, equation 2.6, which has an $E^\circ = 0.244 \text{ V}_{\text{NHE}}$.



The electrode consists of Hg_2Cl_2 (i.e. calomel) in contact with a pool of liquid mercury. These components are immersed in a saturated KCl solution, connected to the electrolyte in the main cell via a glass frit and connected to external circuitry through a platinum wire. The second RE, utilized in alkaline solutions, was a homemade Ag/AgCl RE with an $E^\circ = 0.222 \text{ V}_{\text{NHE}}$. This RE relies on equilibrium 2.7 and



consists of a AgCl coated silver wire immersed in a saturated KCl solution connected to the main cell electrolyte via a glass frit and connected to external circuitry through the Ag wire.

Each electrode occupies a different compartment of the cell with the CE and RE being immersed in the arms of the cell which are connected to the main compartment containing the WE, Figure 2.12. The CE compartment is connected through a glass frit which avoids mixing of electrolyte between the two compartments. This is necessary when polarizing the WE as the compensating electrochemical process occurring at the CE can generate contaminating chemical species. The RE compartment terminates in a Luggin capillary the tip of which approaches the WE. The tip of the Luggin capillary serves as the “sensing” end of the RE and therefore allows the electrolyte potential to be monitored close to the WE.

2.4.1 Corrosion Potential

The corrosion potential (E_{CORR}) is the measured potential difference between the Mg or Al WE and the RE when there is no external potential or current applied to the system. Therefore, in these experiments a CE is not required and not present in the electrochemical cell. The thermodynamic driving force for corrosion is the difference in equilibrium potentials (E°) between the metal oxidation reaction and the oxidant reduction reaction. Corrosion occurs at E_{CORR} , the unique potential at which the rates of the metal oxidation and oxidant reduction reactions are equal; i.e., the current for the cathodic reaction (i_c) equals the current for the anodic reaction (i_a). This situation is illustrated in Figure 2.13.

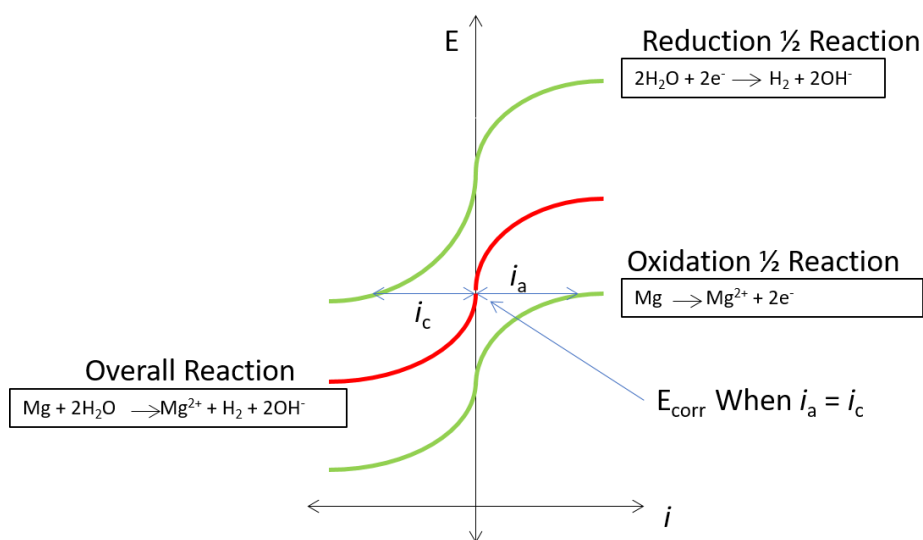


Figure 2.13: Diagram illustrating the concept of a corrosion potential. The two green curves represent the current-potential relationship for the two half-reactions, water reduction and Mg oxidation. The red curve represents the current-potential relationship of the coupled half-reactions, i.e. the corrosion reaction. The E_{CORR} occurs when the rate of the anodic reaction equals the rate of the cathodic reaction.

2.4.2 Potentiodynamic Polarization

Potentiodynamic polarization (PDP) experiments require the passage of current between the WE and the CE. By using a potentiostat, the potential of the WE can be controlled to accelerate or decelerate the half-reaction of interest on the WE surface. By applying more positive potentials (with respect to E_{CORR}) to the WE the anodic reaction can be accelerated, and, conversely, applying more negative potentials (with respect to E_{CORR}) will accelerate the cathodic reaction on the WE. In either scenario the compensating current is either consumed (for negative applied potentials) or generated (for positive applied potentials) at the CE. By measuring the current which passes through the potentiostat plots of current versus potential can be obtained. Of course, the above description is simplified and holds for ideal systems only. Corroding surfaces are dynamic and have rapidly evolving surfaces, particularly when large magnitude polarization or sweep rates are applied. The synergistic effects of these processes will impact the measured current making PDP curves powerful tools for investigating electrochemical and corrosion phenomena.

2.4.3 Electrochemical Impedance Spectroscopy

Electrochemical impedance spectroscopy (EIS) is a widely used technique in electrochemistry and corrosion science as it provides a means to investigate the properties of corroding interfaces. EIS experiments use the same experimental arrangement as PDP experiments. In EIS a small amplitude (i.e. ± 10 mV) sinusoidal potential wave is applied to the WE over a range of frequencies. In response, the output alternating current (AC)

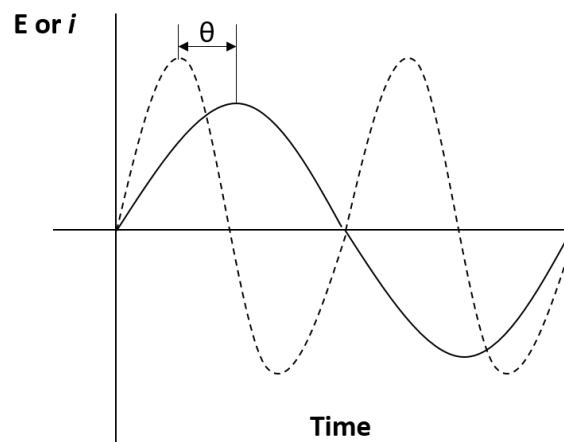


Figure 2.14: Diagram showing the relationship between the input potential (dashed line) and the output current (solid line) response for an EIS experiment. The phase shift between the potential and current waves is shown by θ .

wave exhibits characteristics (e.g. phase shift or amplitude) which vary as a function of frequency and can be used to characterize the properties of the corroding interface. This scenario is depicted in Figure 2.14 where the dashed line is the potential input, the solid line is the current response and θ is the phase shift between the two waves. In this thesis the potential perturbation was applied exclusively around the E_{CORR} but this does not have to be the case.

As shown, both the potential input and current response exhibit a sinusoidal waveform and can therefore be represented by typical wave equations. Equation 2.8 and 2.9 show these relationships for potential ($E(t)$) and current ($I(t)$), respectively as a function of time.

$$E(t) = E_o \sin \omega t \quad (2.8)$$

$$I(t) = I_o \sin(\omega t + \theta) \quad (2.9)$$

E_o and I_o are the amplitude of the potential and current, respectively, ω is the angular frequency of the wave and θ is the phase shift between the two waves. For a direct current

(DC) system, Ohm's Law (Equation 2.10) shows that the ratio of potential and current is equal to the resistance (R) of the system. An analogous relationship exists for an AC system where the resistance term is replaced by impedance (Z), Equation 2.11.

$$E = iR \text{ or } R = \frac{E}{i} \quad (2.10)$$

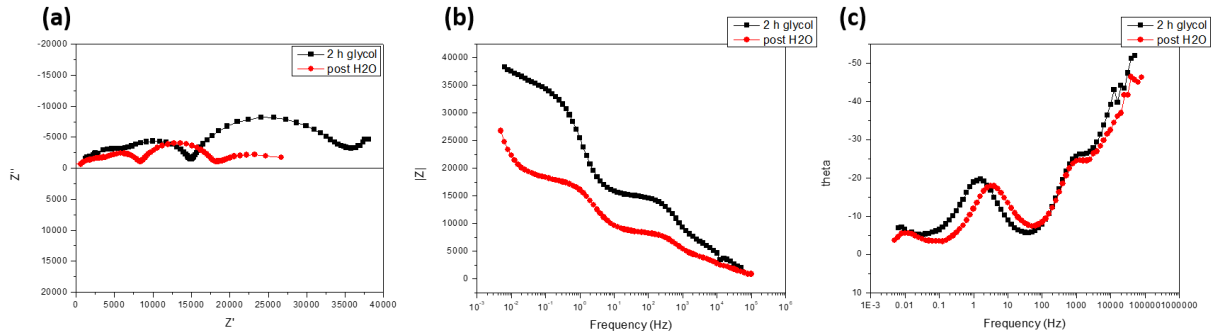


Figure 2.15: (a) Nyquist plot showing the imaginary impedance (Z'') versus the real impedance (Z') for a Mg AM50 sample immersed in ethylene glycol before and after the addition of H_2O . The corresponding Bode plots for the magnitude of impedance ($|Z|$) versus frequency and the phase angle (theta) versus frequency are shown in (b) and (c), respectively.

$$Z(\omega t) = \frac{E_o \sin \omega t}{I_o \sin(\omega t + \theta)} \quad (2.11)$$

Mathematically this impedance can be separated into both a real (Z') and an imaginary (Z'') component, Equation 2.12. Note that in electrochemistry the imaginary unit is represented by j rather than i to avoid confusion with current.

$$Z(\omega t) = Z'(\omega t) + jZ''(\omega t) \quad (2.12)$$

The resistance of the system is expressed by the real component of the impedance while the capacitance (c) is expressed by the imaginary component, Equation 2.13.

$$Z = R + j \frac{1}{\omega c} \quad (2.13)$$

Impedance data can be plotted as either a Nyquist plot or as Bode Plots. Generic examples of these are shown in Figure 2.15. Nyquist plots graph the imaginary impedance on the y-axis against the real impedance on the x-axis. The two types of Bode plots used are also shown in Figure 2.15b and c. The first plots the magnitude of the impedance response ($|Z|$) versus the frequency (f) of the input potential while the second plots the phase shift versus the frequency. By fitting EIS spectra to equivalent electrical circuits whose components (i.e. resistors, capacitors and inductors) are based on a physical model of the corroding interface, various physical parameters such polarization resistance (R_p) and surface film capacitance can be extracted.

2.4.4 Scanning Electrochemical Microscopy

Scanning electrochemical microscopy (SECM) involves bringing an ultramicroelectrode (UME) near (i.e. on the order of the UME diameter) to a substrate of interest. UME's can have diameters of tens of micrometers down to the nanometer scale and are typically made of noble metals encased in a glass sheath. By controlling the bias at the UME tip, the current for a selected electrochemical process (e.g. oxidation of H_2) can be measured. By rastering the UME across the substrate surface, it is possible to create maps of localized current density as a function of UME position.

2.4.4.1 SECM Theory: Feedback Mode

Although SECM can be operated in several modes, the research described in this thesis utilized the feedback mode. For more information on other applications of SECM the reader is referred to references.⁶ The fundamental principle of the feedback mode is

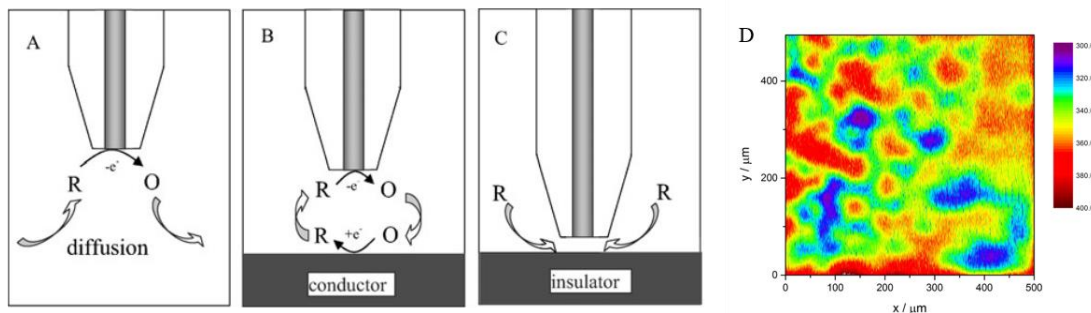


Figure 2.16: Diagrams showing electrochemical responses for an UME that is (a) far away from a substrate (b) close to a conducting substrate and (c) close to an insulating substrate. (d) sample data output from an SECM experiment showing cathodic (blue) and anodic (red) behavior.

demonstrated in Figure 2.16. When the UME is far away from the substrate the situation shown in Figure 2.16a prevails and the current measured is governed by the radial diffusion of the species R to the UME surface. This current ($i_{T,\infty}$) is given by equation 2.14

$$i_{T,\infty} = 4nFDca \quad (2.14)$$

where n is the number of electrons involved in the reaction, F is the Faraday constant, D is the diffusion coefficient of species R, c is the concentration of species R and a is the radius of the electrode. As the tip is brought close to the substrate the behaviour of the system becomes influenced by the electrochemical properties of the substrate. If the substrate is conducting, Figure 2.16b, the oxidized species, O, generated at the UME can be reduced back to the reduced species, R, at the substrate establishing a positive feedback loop. Therefore, as the tip is brought closer to a conducting surface the measured current at the UME will increase as the oxidized species consumed at the substrate is regenerated. If the substrate is an insulator there is no regeneration of the reduced species. As the tip is brought closer to the substrate, access to the UME by R is blocked and the measured current

decreases. Figure 2.16d shows an example of an SECM map recorded on an Mg AM50 sample.

2.4.4.2 SECM Instrumentation

A schematic of an SECM instrument is shown in Figure 2.17. The electrochemical cell is a small (i.e. 50 mL) glass cell in which the sample sits on the bottom of the cell facing upwards. The UME, the WE in the schematic, is secured to a piezo system which can move in a stepwise manner in the x, y and z directions and connected to a potentiostat. Also connected to the potentiostat and placed in the electrolyte are both a CE, typically a small Pt wire and a RE. However, in this work a quasi-reference electrode (i.e. 5 mm silver wire) was used as both the RE and the CE.

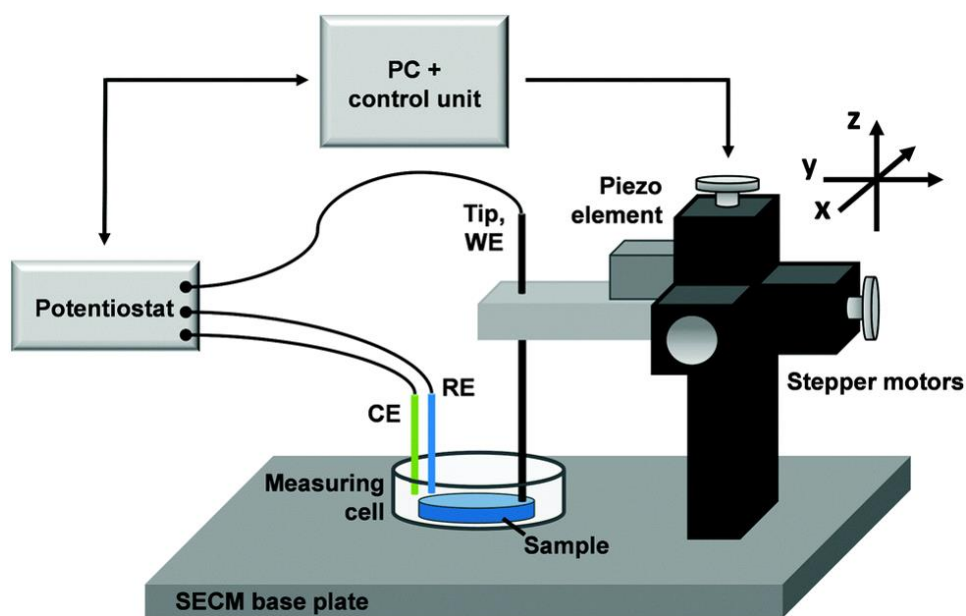


Figure 2.17: Schematic of a simple SECM instrument. Note, in this thesis a pseudo RE electrode was used to perform the CE and RE roles simultaneously rather than the separate CE and RE shown in the figure.

2.5 X-ray Diffractometry

The most common way to probe the crystallographic structures of materials is by using X-ray diffraction (XRD). XRD was first discovered in 1912 and has since become one of the most widely used tools for materials science research.⁷ This technique identifies chemical compounds based on their arrangement in space rather than by their chemical composition. By fitting diffraction patterns of real samples to those of known compounds, XRD reveals both the crystallographic structure of a material as well as the chemical composition.

2.5.1 Diffraction Principles

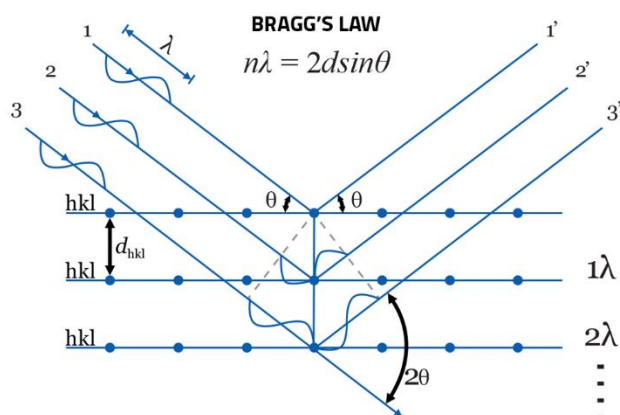


Figure 2.18: Diagram illustrating the XRD diffraction phenomenon and the mathematical relationship between wave length and lattice spacing (Bragg's Law).

As with EBSD, XRD is based on the constructive and destructive interference of X-rays which have been diffracted by atoms. This diffraction phenomenon is shown in Figure 2.18. When incident light or x-ray waves share a wavelength and travel in the same

direction they can combine to either amplify or cancel each other. Complete constructive interference is achieved when two waves have a phase difference of $n\lambda$, where n is an integer and λ is the wavelength. Conversely, complete destructive interference is achieved when the phase difference between the two waves is $n\lambda/2$. In Figure 2.18, two in-phase incident X-rays are diffracted by adjacent atomic layers of a material. Because the two waves travel different distances the diffracted X-rays have a phase difference which is proportional to the crystallographic structure of the material. This relationship is known as Bragg's Law, equation 2.15,

$$n\lambda = 2d \sin \theta \quad (2.15)$$

where θ is the incident angle of the X-rays and d is the spacing between the parallel interatomic layers. Once the spacing of interatomic layers is known it is possible to determine the crystallographic structure of the material. For example, when the system is cubic the relationship between the interatomic spacing and the Miller indices is given by equation 2.16 and the relationship between the diffraction pattern and the lattice parameter is given by equation 2.17.

$$d = \frac{a}{\sqrt{h^2 + k^2 + l^2}} \quad (2.16)$$

$$\sin^2 \theta = \frac{\lambda^2}{4a^2} (h^2 + k^2 + l^2) \quad (2.17)$$

Similar relationships exist for other crystal types which allow the crystallographic elucidation of any crystal phase. For work carried out in this thesis, XRD results should be considered as a surface averaged response in that no attempt was made to single out a certain phase.

2.5.2 Instrumentation

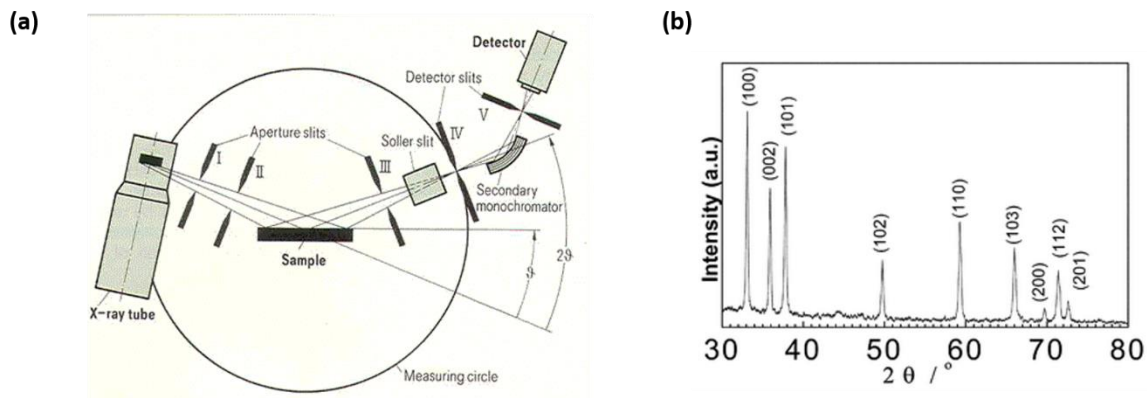


Figure 2.19: (a) Schematic showing the instrumental setup for a typical XRD experiment. In this case the detector rotates around the Measuring circle and the intensity of the diffracted x-rays is measured as a function of the angle of the detector, 2θ . (b) Sample output from an XRD experiment with the corresponding Miller indices of the crystal which cause each peak.

Figure 2.19a shows the basic setup for a typical XRD instrument. X-ray radiation is generated at the X-ray tube and directed toward the sample. The beam passes through several apertures and Collimator slits to create a highly collimated beam. In our case, the sample was a rolled sheet Mg ZEK100F alloy in both the as-polished and cathodically charged state. Following diffraction, X-rays pass through more apertures before reaching the detector. Most commonly, XRD instruments utilize a system where the incident beam remains stationary and the detector travels circumferentially recording the signal intensity as a function of 2θ , where θ is the angle between the incident beam and the crystallographic plane which generates the signal. An example of an XRD spectrum is shown in Figure 2.19b, the Miller indices of the plane which generate the signal being indicated on the spectrum. Once acquired, the spectrum can be cross referenced to a large database of known samples to positively identify which phases are present in the sample.

2.6 Dynamic Secondary Ion Mass Spectrometry

Dynamic Secondary Ion Mass Spectrometry (SIMS) discerns the chemical composition of samples based on the mass of ions that are sputtered from the sample surface. This technique is particularly useful as it can produce maps of chemical composition as a function of depth up to tens of micrometers. An additional benefit of this technique is the extreme sensitivity that can be achieved with respect to mass resolution. SIMS is capable of discerning between isotopes of the same element making it ideal for isotopic labelling studies. Moreover, unlike techniques which rely on Auger transitions or characteristic X-ray emissions, SIMS can analyze samples for the entire periodic table.

2.6.1 Dynamic SIMS Principles

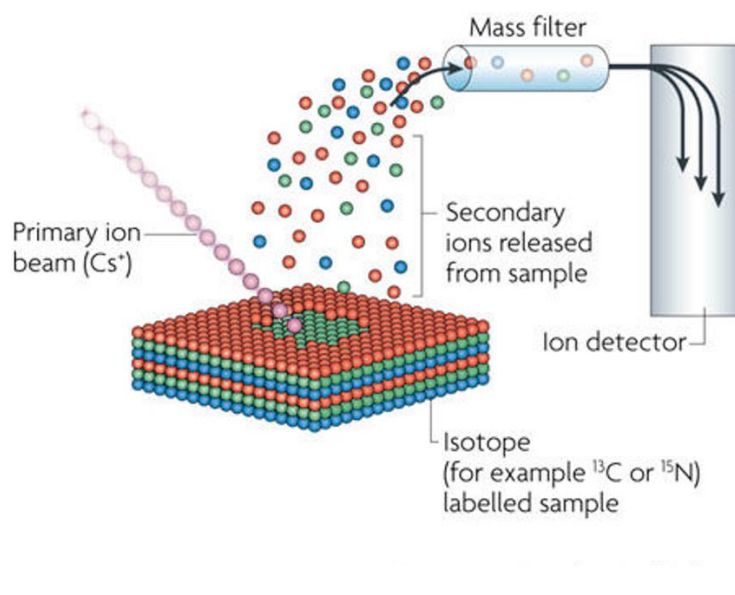


Figure 2.20: Schematic illustrating the basic principles of dynamic SIMS.

Dynamic SIMS is a destructive analytical technique in that it relies on the release of ions from the sample surface. This release is caused by accelerating a high energy ion beam toward the sample surface. These ions constitute the primary ion beam. A Cs^+ primary ion beam was used in the study in this thesis. When this ion beam impacts the surface, it sputters atoms from the surface as secondary ions which are then accelerated to the mass filter and then the detector. This process is depicted in Figure 2.20. Secondary ion generation is a complicated process and a full description is beyond the scope of this work, the reader is referred references for more information.^{3,8} What is important is that only a small percentage of secondary particles will be analyzed by the detector (i.e. approximately 1% of the total secondary particles). This secondary ion yield or secondary ion current (I_m) is influenced by several factors including the primary ion flux (I_p), the sputter yield (Y_m), the ionization probability (α^+), the fractional concentration of species m in the surface layer (θ_m) and the transmission of the detection system (η). The relationship between these parameters is given by Equation 2.18.

$$I_m = I_p Y_m \alpha^+ \theta_m \eta \quad (2.18)$$

The wide variability of secondary ionic currents between different samples makes quantitative SIMS difficult and therefore, only qualitative conclusions are drawn from the SIMS data in this project.

2.6.1.1 Instrumentation

The two main components of the SIMS instrument include the primary ion source and the mass analyzer. The primary ion source creates a beam of high energy ions which bombard the sample surface and generate secondary ions. These secondary ions proceed to the mass analyzer, in this case a quadrupole mass analyzer, which selects certain ions based

on their mass-to-charge ratio (m/z). To ensure that both the primary and secondary ions utilized in SIMS have true trajectories and remain unimpeded through the instrument an ultra-high vacuum environment must be maintained throughout the entire SIMS instrument.

As mentioned above, the primary ion source for the SIMS instrument used in this work generates a beam of Cs^+ ions. This primary ion beam is produced by a surface ionization source which heats Cs metal that has been adsorbed onto a metal which possesses a high work function. In this case, the ionization potential of the Cs is less than the work function of the substrate which causes a migration of electrons from the adsorbed Cs to the substrate. By creating an electric field around the source Cs^+ ions are extracted, and a primary ion beam produced.

A schematic of a quadrupole mass analyzer is shown in Figure 2.21. The analyzer utilizes four parallel cylindrical rods through which the secondary ions pass (e.g. red and

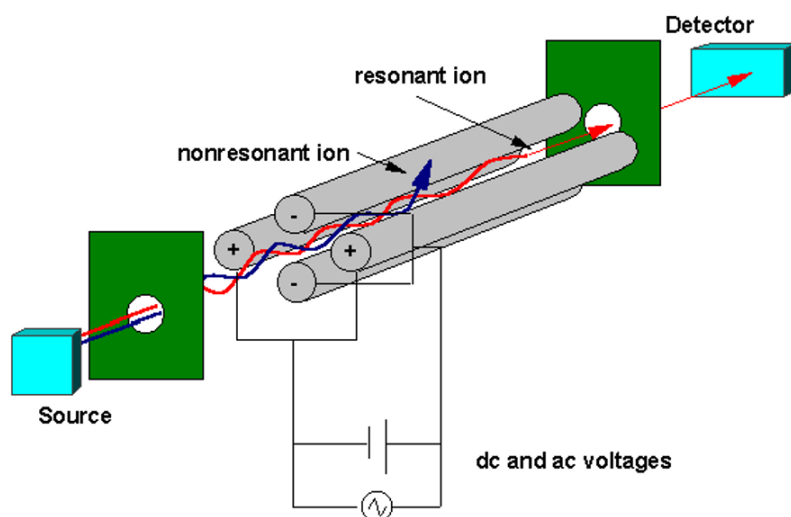


Figure 2.21: Schematic of a quadrupole mass analyzer employed in dynamic SIMS experiments. Secondary ions from the source enter and pass through the quadrupole where they are separated based on their m/z ratio before striking the detector.

blue lines in Figure 2.21). By passing both an AC and DC current through the rods an oscillating electric field is produced in the secondary ion path. By manipulating the frequency of the AC, the trajectory of the secondary ions can be controlled with great sensitivity. In this manner the analyzer can select ions with a specific m/z while other ions are deflected and do not reach the detector. This process creates a spectrum of signal intensity versus m/z and can achieve isotopic resolution. By equipping the primary ion source with an X-Y deflector (i.e. rastering the primary beam) and recording a series of spectra across the sample surface a spatially resolved map can be created for any isotope of interest. By repeating this analysis as a function of time, a depth profile can be created to gain chemical insight as a function of depth. This combination of isotopic resolution with depth profiling capabilities make SIMS a powerful investigative tool.

2.7 References

- (1) ASTM, “Standard Test Methods for Chemical Analysis of Cuprous Oxide and Copper Pigments” (ASTM International, 2013).
- (2) “A Complete Microscope History - Who Invented the Microscope?” (n.d.), <http://www.history-of-the-microscope.org/history-of-the-microscope-who-invented-the-microscope.php> (Accessed: Feb. 19, 2018).
- (3) Leng, Y., *Materials Characterization Introduction to Microscopic and Spectroscopic Methods*, 1st ed. (Singapore: Wiley, 2008).
- (4) Bard, A.J., and M.V. Mirkin, *Scanning Electrochemical Microscopy*, 2nd ed. (Florida: Taylor and Francis, 2012).
- (5) Maitland, T., and S. Sitzman, *Electron Backscatter Diffraction (EBSD) Technique and Materials Characterization Examples* (Springer Berlin, 2007).
- (6) “Scanning Electron Microscopy (SEM) - Helmholtz-Zentrum Dresden-Rossendorf, HZDR” (n.d.), <https://www.hzdr.de/db/Cms?pNid=67> (Feb. 24, 2018).
- (7) Design, F., “X-Ray Diffraction,” VEQTER - Residual Stress Experts (n.d.), <http://www.veqter.co.uk/residual-stress-measurement/x-ray-diffraction> (Dec. 14, 2017).
- (8) Yu, M.L., *Nuclear Instruments and Methods in Physics Research Section B: Beam Interactions with Materials and Atoms* **1986** 15, pp. 151–158.

3 The Effect of Mg Content on the Corrosion Behaviour of Al-Mn-Cu-Mg Alloys for Automotive Heat Exchanger Brazing Sheets

3.1 Introduction

Brazing sheets are sandwich-like alloys composed of a core alloy, which provides strength, and one or more clad alloy(s) exploited for joining purposes. Al brazing sheet alloys have been utilized in automotive heat exchangers since the 1970's and were initially designed for use below 150 °C. However, if these alloys could maintain the required strength at temperatures up to 300 °C they would become candidates for use in supercharger and turbocharger technologies designed to increase fuel economy. Contemporary core alloys are based on the commercial AA3xxx Al-Mn-Cu system which benefits from the strong solid solution hardening effects of both Mn and Cu.^{1,2} However, addition of either Mn or Cu beyond their solubility limits would yield diminishing returns on alloy strength and, possibly corrosion performance, due to the precipitation of secondary phases.³⁻⁶ Previous work done at CANMETMaterials, Hamilton, has shown, that increasing the Mg content up to 2.06 wt% can provide the required yield strength of ≥ 60 MPa at in-service temperatures due to strong solution hardening.⁷ However, what effect, if any, increasing Mg content exerts on the corrosion behaviour of these alloys is presently unknown and is the focus of this study.

The Al-Mn-Cu system is susceptible to microgalvanic corrosion due to the presence of intermetallic particles (IPs) throughout the Al matrix.⁸⁻¹⁰ These particles are expected to behave as cathodes which support the reduction of O₂ or H⁺ in an acidic environment leading to the dissolution of the matrix and eventually to pit formation. Local probe techniques such as scanning electrochemical microscopy (SECM) have proven particularly

useful for the study of localized corrosion.¹¹⁻¹⁵ SECM has been applied in conjunction with energy dispersive x-ray spectroscopy (EDX) to correlate cathodic activity with the location of Cu-rich IPs in an Al alloy.^{16,17} A similar approach is adopted here with hydroquinone (HQ) utilized as a redox mediator in tip-generation substrate-collection mode in order to map the localized cathodic activity of three Al alloys with increasing Mg content from 0.11 to 2.06 wt%. The resulting electrochemical maps are correlated with elemental maps in order to determine the local cathodic activity as a function of microstructure.

3.2 Experimental

3.2.1 Material Preparation

Materials were received in the as-cold rolled condition from CanmetMATERIALS in Hamilton, Ontario, Canada. Samples were cut from the supplied sheets into 1 x 1 x 0.2 cm³ specimens and a stainless steel rod soldered to one face to allow for electrical connection to external circuitry. Samples were then cold mounted in Struers Epofix[®] clear epoxy resin and ground successively with P800 and P2400 SiC grinding paper while being lubricated with a 1:1 ethanol-to-isopropanol mixture. The final polishing step was performed with a 3 μm diamond abrasive on a Struers MasterTex[®] polishing cloth until a mirror finish was achieved. Finally, samples were sonicated in anhydrous ethanol for 1 min and dried in an Ar_(g) stream.

3.2.2 Bulk Electrochemical Experiments

Corrosion potential (E_{CORR}) and potentiodynamic polarization (PDP) experiments were conducted in a three-electrode electrochemical cell with the reference electrode connected to the main cell body via a Luggin capillary. The Al alloys served as the working electrode with a saturated calomel electrode (SCE) and a Pt plate as the reference and counter electrodes, respectively. Following various periods of immersion at E_{CORR} , PDP experiments were initiated at $-100 \text{ mV vs } E_{\text{CORR}}$ and the potential scanned at $0.1667 \text{ mV}\cdot\text{s}^{-1}$ in the anodic direction to a final potential of -0.5 V vs SCE . All experiments were performed using either a Solartron 1287 potentiostat or a Solartron 1480 multistat with the cell in a grounded Faraday cage to minimize external noise. Solutions for these and other experiments consisted of either 0.6 M NaCl (reagent grade, 99% assay) and 0.1 M acetic acid (Caledon Laboratories Ltd.) or 0.06 M NaCl and 0.1 M acetic acid prepared with Type 1 ($18.2 \text{ M}\Omega\cdot\text{cm}$) MilliQ[®] water. Acetic acid being used to dissolve the native passive oxide.

3.2.3 SECM Arrangement

SECM was performed using a Uniscan SECM 270 instrument coupled to a Uniscan PG580R bipotentiostat. Current was recorded by positioning a Pt ultramicroelectrode (UME) with a $10 \mu\text{m}$ tip diameter over the alloy surface immersed in a $0.06 \text{ M NaCl} + 0.1 \text{ M}$ acetic acid solution containing 1 mM HQ (Sigma-Aldrich Co.). The reduction in chloride concentration by an order of magnitude from the proposed 0.6 M NaCl reflects the need to minimize changes in surface topography in order to attain lucid electrochemical

maps. If corrosion processes produce protruding features (i.e. corrosion product deposits) which exceed the tip-to-substrate separation, they can cause electrical contact between the probe and substrate and/or damage the UME. Moreover, since the UME current is strongly dependent on the tip-to-substrate separation, differences in local electrochemical activity can only be reliably determined if topographical variations remain negligible or can be corrected for. Since the SECM instrument used in this study does not contain a topographical correction module, altering the immersion environment is a simple alternative which reduces the development of topographical variations. A Ag/AgCl quasi-reference electrode comprising a 5.0 mm diameter Ag wire (99.99% pure; annealed), supplied by Goodfellow Cambridge Ltd., was employed to record electrochemical data. Prior to experimentation, the performance of the UME was examined using cyclic voltammetry (CV) and the potential required to achieve a steady state UME current identified. Chronoamperometry was used to monitor the stability of the steady state current over the time period of a typical mapping experiment during which the selected imaging potential (800 mV vs Ag/AgCl) was applied.

Probe approach curves (PAC) measuring the tip current for HQ oxidation were performed at an approach speed of $3 \mu\text{m}\cdot\text{s}^{-1}$ in order to position the UME at a known distance (d) of approximately $5 \mu\text{m}$ from the substrate surface. Currents measured during PAC experiments are normalized to the current measured in the bulk solution ($i_{T\infty}$) beyond any influence of the substrate (normalized current = $i_T/i_{T\infty}$), while the distance of the UME from the substrate is normalized to the radius (r) of the UME (normalized distance = d/r). The UME tip was polarized at the imaging potential and rastered at $5 \mu\text{m}\cdot\text{s}^{-1}$ over a region of interest (ROI). ROIs of $120 \times 120 \mu\text{m}$ were mapped at various time intervals to determine

the change in current response with surface location as a function of time. Prior to recording each map fresh electrolyte was pipetted into the SECM sample holder and removed upon completion of the map to be replaced with electrolyte not containing the mediator. This was done throughout the experiment to minimize any effect of the organic mediator on the corrosion of the alloys.

3.3 Results

3.3.1 Microstructure

The compositions of the three Al alloys, (A005, A002 and A004) investigated are listed in Table 3.1. Each alloy contains similar amounts of Mn, Fe, Cu and Si, while the Mg content increases from 0.11 to 1.00 to 2.06 wt% for the A005, A002 and A004 alloys, respectively. Figure 3.1 shows SEM micrographs, collected in BSE mode and prior to immersion, recorded on the polished Al A004 alloy. White precipitates, likely an $\text{Al}_6(\text{Fe},\text{Mn})$ phase,⁷ appear in clusters within horizontal bands throughout the Al matrix (grey area), clearly indicating the rolling direction of the alloy, Figure 3.1A. Figure 3.1B shows one such cluster of precipitates at a higher magnification. These particles are irregular in shape and it is possible they are

Table 4.1: Chemical compositions of each Al alloy in wt%. Compositions were supplied by CANMETMaterials, Hamilton, Ontario, Canada.

Alloy	Mn	Fe	Cu	Si	Mg
A005	1.5	0.25	0.5	0.1	0.11
A002	1.5	0.25	0.5	0.1	1.0
A004	1.5	0.25	0.5	0.1	2.06

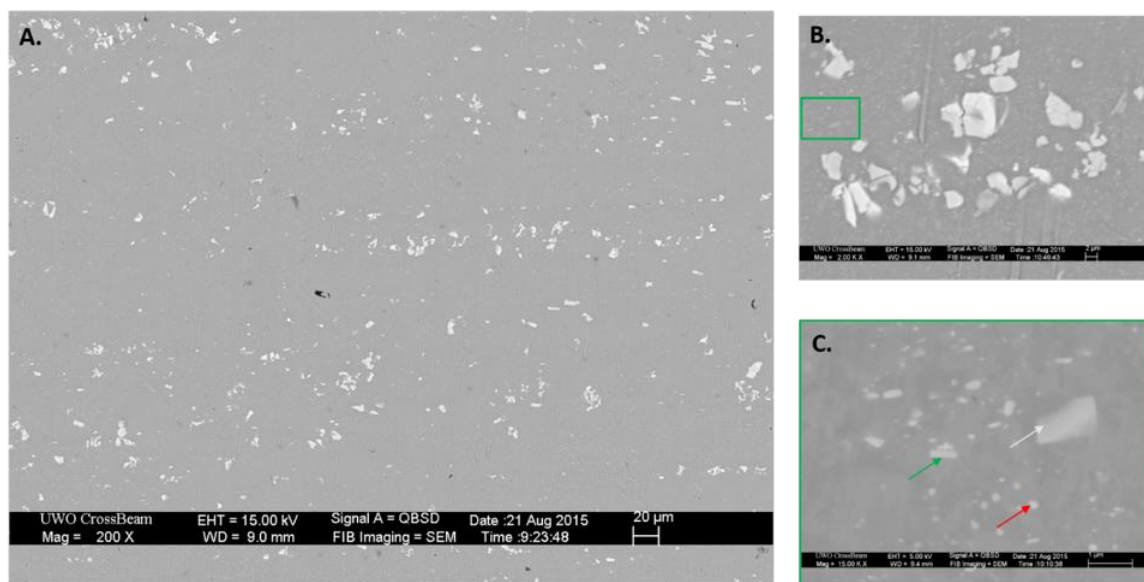


Figure 3.1: SEM micrographs of a polished Al A004 (2.06% Mg) surface. A. Low magnification micrograph showing the general microstructure of the alloy which is representative of the A002 and A005 alloys as well. B. High magnification image of alloy A004 detailing the coarse microstructure ($d > 1\ \mu\text{m}$), likely $\text{Al}_6(\text{Fe},\text{Mn})$ particles. C. High magnification image of the highlighted area in B showing the fine dispersoid particles ($d < 1\ \mu\text{m}$).

fragments from a larger particle fractured during the rolling process. Closer inspection of the image in Figure 3.1B reveals the presence of a finer microstructure ($d < 1\ \mu\text{m}$) throughout the matrix in addition to the coarse ($d > 1\ \mu\text{m}$) IPs. A higher magnification micrograph of the area within the green box in Figure 3.1B is shown in Figure 3.1C. These small features possess rod-like (green arrow), circular (red arrow) and irregular morphologies (white arrow) and appear to be evenly distributed throughout the Al matrix.

Elemental analysis was performed using SEM EDX on both the coarse (Figure 3.2) and fine (Figure 3.3 and 3.4) particles. No appreciable difference exists between the three alloys with respect to the elemental composition of either the coarse or fine particles. Figures 3.2A, B and C show SEM micrographs taken in BSE mode and the corresponding

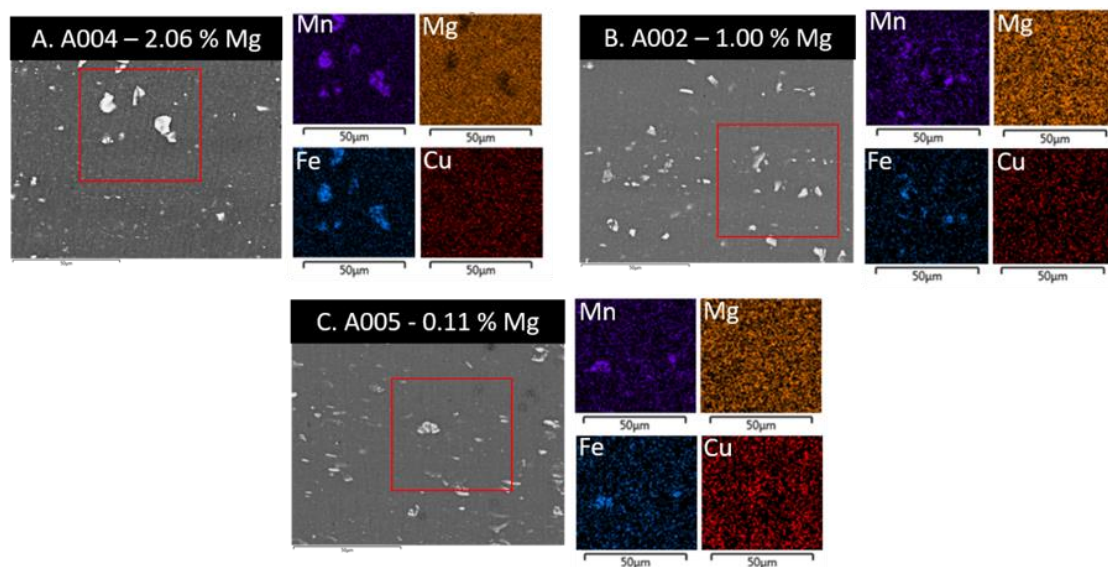


Figure 3.2: SEM micrographs and corresponding EDX analyses of the coarse microstructures present in A. A004 – 2.06 wt% Mg, B. A002 – 1.00 wt% Mg and C. A005 – 0.11 wt% Mg alloys. Red boxes indicate the regions chosen for EDX analysis. In all three alloys, coarse particles are enriched in Fe (blue maps) and Mn (purple maps) indicating that they are likely $Al_6(Fe,Mn)$. Mg (orange maps) and Cu (red maps) show no enrichment of either alloying element indicating that they are dissolved in solid solution.

elemental maps for A004 (2.06% Mg), A002 (1.00% Mg) and A005 (0.11% Mg), respectively. The coarse particles are enriched in Fe and Mn and are likely an $Al_6(Fe,Mn)$ phase, although the stoichiometry is uncertain. Elemental maps for Mg and Cu show no enrichment in the coarse particles, both elements being dissolved within the matrix. This is expected since Mg is highly soluble in Al while Cu, at 0.5 wt%, is at its solubility limit for Al.

Figure 3.3A shows a high resolution SEM BSE image for the A005 alloy with the corresponding elemental maps for Fe, Mn and Cu shown in Figure 3.3B, C and D, respectively. The SEM micrograph shows many different fine dispersoid particles with rod shaped, circular and irregular morphologies. The rod-like particle (indicated with the white

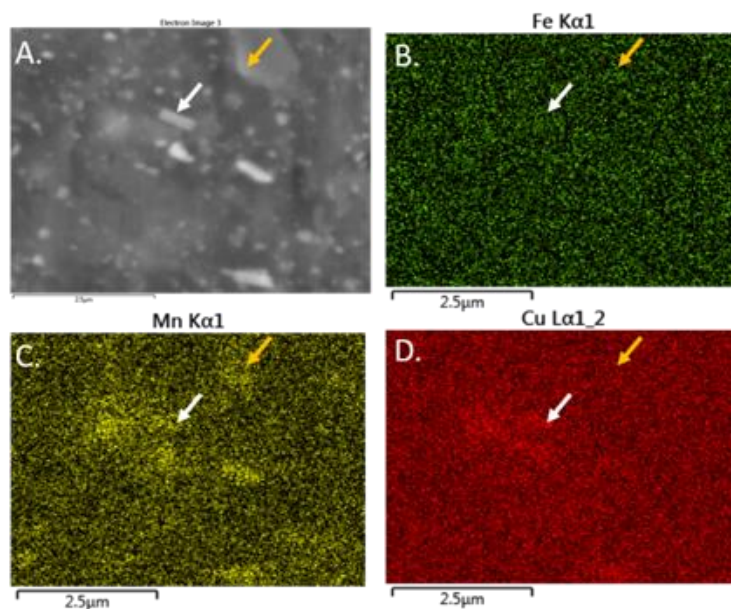


Figure 3.3: A SEM micrograph recorded in BSE mode and the corresponding elemental maps for B. Fe; C. Mn and D; Cu for the A005 (0.11% Mg) alloy. These maps indicate that the fine dispersoid particles have various compositions in addition to Al, Fe and Mn.

arrow) shows enrichment in Mn and Cu but no enrichment in Fe indicating its distinction from the coarse particles. Only Mn enrichment is detected for the irregular particle (indicated with the orange arrow) confirming the diversity of compositions of the fine particles. Similarly, Figure 3.4A shows an SEM BSE micrograph of the A004 (2.06% Mg) alloy with the corresponding EDX spectra, Figures 3.4B and 3.4C. Here, the rod-like particle (indicated by the red arrow) is enriched in Cu and Mn, spectrum B, consistent with the analyses of similar particles in the A005 (0.11% Mg) alloy, Figure 3.3. Furthermore, the circular particle (indicated by the green arrow) shows an accumulation of Si. Both Figures 3.3 and 3.4 demonstrate the extensive variety in compositions and stoichiometries of the fine dispersoid microstructures.

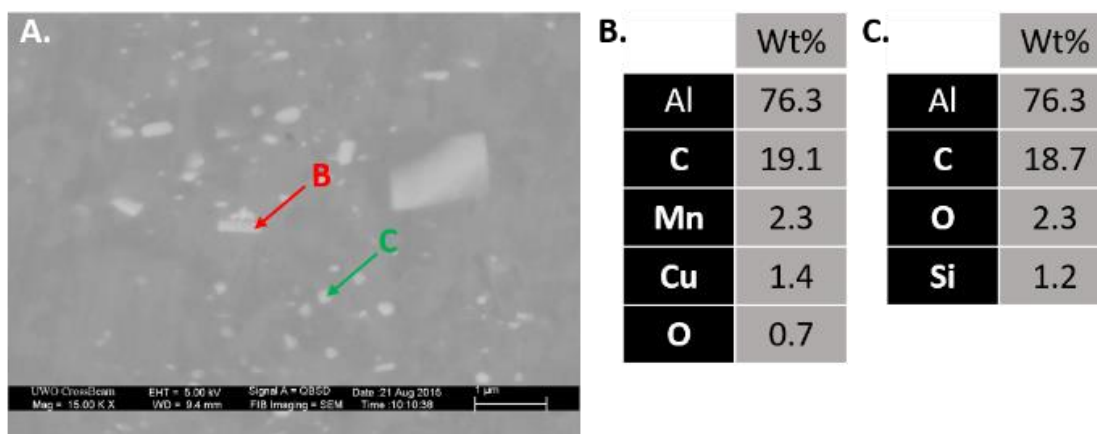


Figure 3.4: A. SEM micrograph recorded in BSE mode and the corresponding elemental analysis, B and C, generated from EDX spot analysis on alloy A004 (2.06% Mg). Spectrum B shows slight Cu enrichment in the indicated particle while spectrum C shows slight Si enrichment in the indicated particle.

3.3.2 Electrochemistry and Corrosion Experiments

Each alloy was immersed in a solution containing 0.6 M NaCl and 0.1 M acetic acid (pH ~ 3.2) for 96 h and the corrosion morphology analyzed using SEM BSE, Figure 3.5. Each alloy exhibits a similar corrosion morphology, characterized by a high number density of pits covering the entire surface of the alloys. Additionally, large columns of corrosion products extend outward from the surface of the alloys, as indicated, by the white arrows for alloys A004 (2.06% Mg), A002 (1.00% Mg) and A005 (0.11% Mg) in Figure 3.5A, B and C, respectively. Each column of corrosion product serves as the focal point for a series of concentric circles of corrosion products which extend up to 100 μm laterally. Although each alloy exhibits similar types of corrosion damage, there appears to be a difference in behaviour as the Mg content decreases; the concentric corrosion behaviour

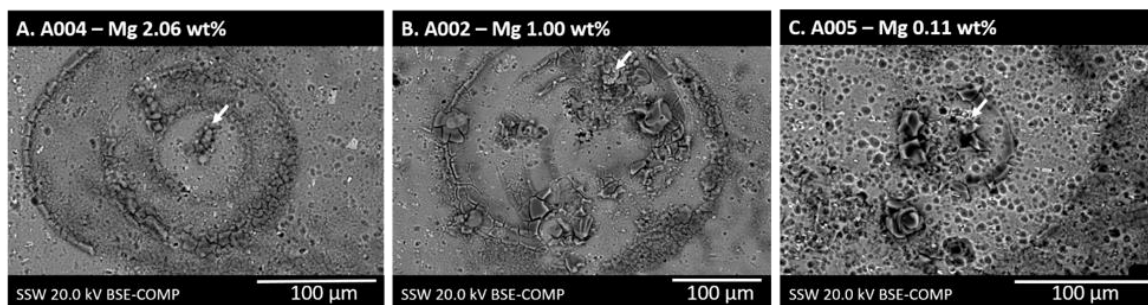


Figure 3.5: SEM BSE micrographs of A. A004 (2.06% Mg); B. A002(1.00% Mg); and C. A005 (0.11% Mg) following immersion in a 0.6 M NaCl + 0.1 M acetic acid solution (pH ~ 3.2) for 96 h. Each specimen exhibits extensive corrosion damage indicated by the high number density of pitting sites. Columns of corrosion products protrude from large pitting sites as indicated with a white arrow.

being more marked at the high Mg content than at the low one. By contrast, the low Mg alloy exhibits less concentric behaviour but a much higher density of localized small pits. Also for the alloys with high Mg content the number of “large” corroded areas is much higher than for the low Mg alloys. This combination of the extensive damage penetrating into the alloy surface and the deposition of corrosion products protruding from the surface introduces significant topographic variations making the acquisition and interpretation of SECM data difficult, as discussed in section 3.2.4. To minimize these effects subsequent experiments were performed in a less aggressive electrolyte containing 0.06 M NaCl + 0.1 M acetic acid.

The E_{CORR} behaviour of each alloy over a 96 h immersion period in 0.06 M NaCl and 0.1 M acetic acid is displayed in Figure 3.6. Figure 3.6A shows the E_{CORR} for the full immersion period while Figures 3.6B, C and D show sections recorded for the first 6 h, 10 to 20 h and 80 to 90 h, respectively. Figure 3.6A indicates little difference in corrosion behaviour between the three alloys over the 96 h immersion period. Increasing the Mg

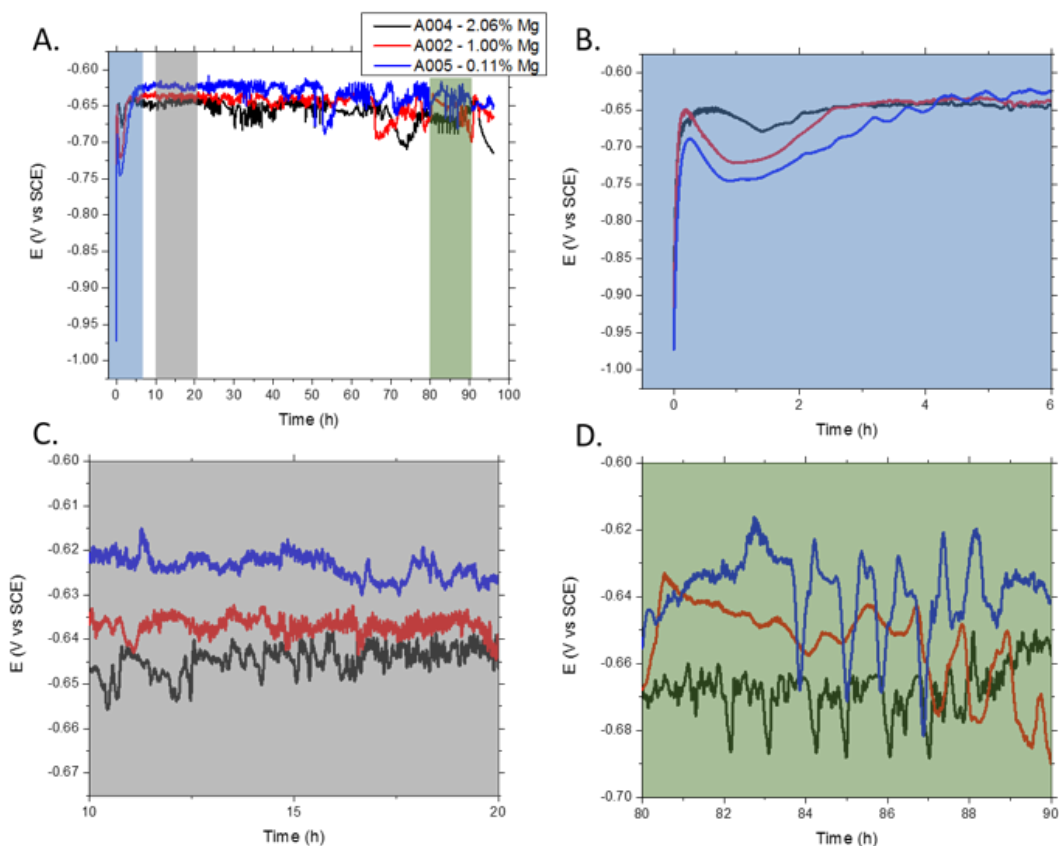


Figure 3.6: A. E_{CORR} measurements recorded for 96 h in a 0.06 M NaCl + 0.1 M acetic acid solution for the A004 (2.06% Mg), A002 (1.00% Mg) and A005 (0.11% Mg) Al alloys. B, Magnification of A showing similar E_{CORR} behaviour for each alloy during the first 6 h of immersion. C, Magnification of the 10 to 20 h period in A, E_{CORR} correlates with Mg content with greater Mg concentration leading to lower E_{CORR} values. D, Magnification of the 80 to 90 h period in A. Fluctuations in E_{CORR} increase with time with A005 exhibiting the greatest change in potential during potential transients.

content lowers the average E_{CORR} of the alloy slightly while the magnitude of the potential transients increases with time for the three alloys. Initially, all three alloys show similar behaviour with a rapid increase in E_{CORR} followed by a slight decrease before recovery to approximately -0.65 V vs SCE at 4 h, Figure 3.6B. Notably, the length of time required for the transient to recover is greatest for the low Mg alloy and shortest for the high Mg alloy. These transients likely reflect the chemical dissolution of the air-formed passive oxide

layer, a process which is expected in acidic media.¹⁸ As time progresses, the E_{CORR} evolves from relatively stable, Figure 3.6C, to exhibiting sharp negative transients consistent with pitting, Figure 3.6D, as exhibited in the microscopy, Figure 3.5. To investigate the evolution of the corrosion kinetics with time, PDP experiments were performed following various lengths of immersion at the open circuit condition.

Figure 3.7A, B and C show PDP curves for each alloy following immersion for 0.5, 24 and 48 h, respectively. In all cases, the cathodic branch of the polarization curves reveal consistent Tafel slopes and current densities not particularly dependent on Mg content. With prolonged immersion times there is a slight increase in the cathodic current densities indicating an acceleration of cathodic kinetics with time. This increase in cathodic current could be attributable to the depassivation of local cathodes as a result of the dissolution of the $Al_2O_3 \cdot H_2O$ passive film with time.

Anodic polarization following a short 0.5 h of immersion, however, shows a difference in the active/passive behaviour between the low and high Mg alloys, Figure 3.7A. The two high Mg alloys are active at the E_{CORR} as evidenced by the rapid increase in current density for small increases in anodic overpotential. The low Mg alloy (A005) however exhibits passive behaviour for applied potentials up to 75 mV above E_{CORR} before activating at the breakdown potential (E_b), Figure 3.7. After 24h immersion, all three alloys exhibit similar E_{CORR} values and develop a passive region which is marginally wider for the low Mg alloy and smallest for the high Mg alloy, Figure 3.7B. Extending the immersion period to 48h, Figure 3.7C, leads to a widening of the passive region especially for the two alloys with higher Mg content, consistent with a general establishment of a passive surface, but one undergoing metastable pitting events, as indicated by the onset of negative-going

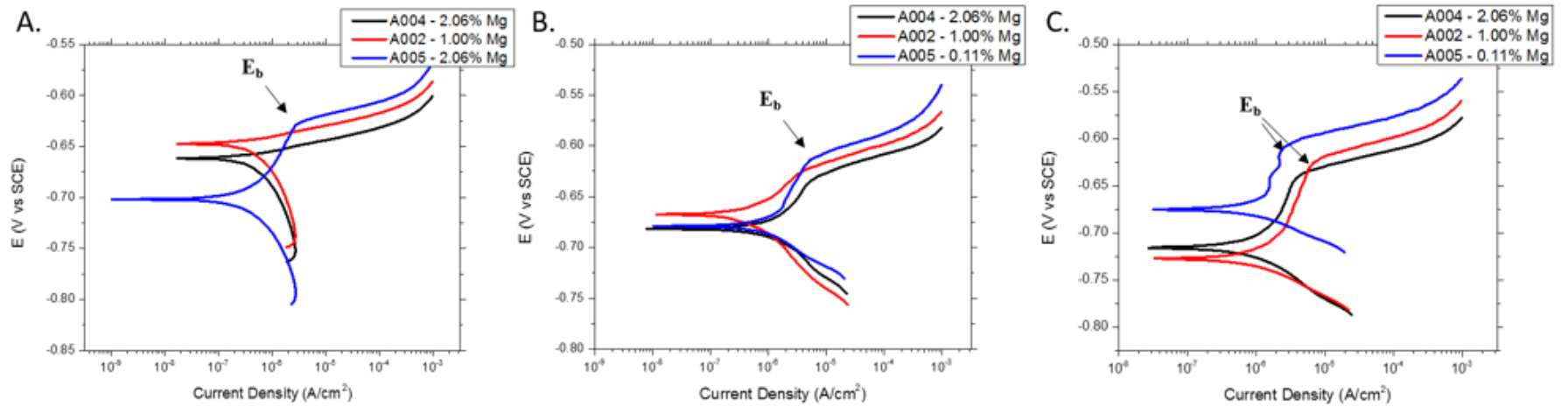


Figure 3.7: PDP scans for alloys A004 (2.06% Mg), A002 (1.00% Mg) and A005 (0.11% Mg) recorded in a 0.06 M NaCl + 0.1 M acetic acid solution following A. 0.5 h, B. 24 h and C. 48 h immersion at open circuit.

transients after this duration of exposure, Figure 3.6A. For all three exposure periods, E_b is the most positive for the low Mg alloy and the most negative for the high Mg alloy. The narrower passive region for the low Mg alloy (i.e., $E_b - E_{\text{corr}}$) could account for the higher density of shallow pits observed on this alloy, Figure 3.5C, while the more negative E_{CORR} values for the two alloys with higher Mg content (consistent with the behaviour in Figure 3.6) suggest a breakdown event on these two alloys leads to a more active behaviour within a breakdown site.

3.3.3 SECM

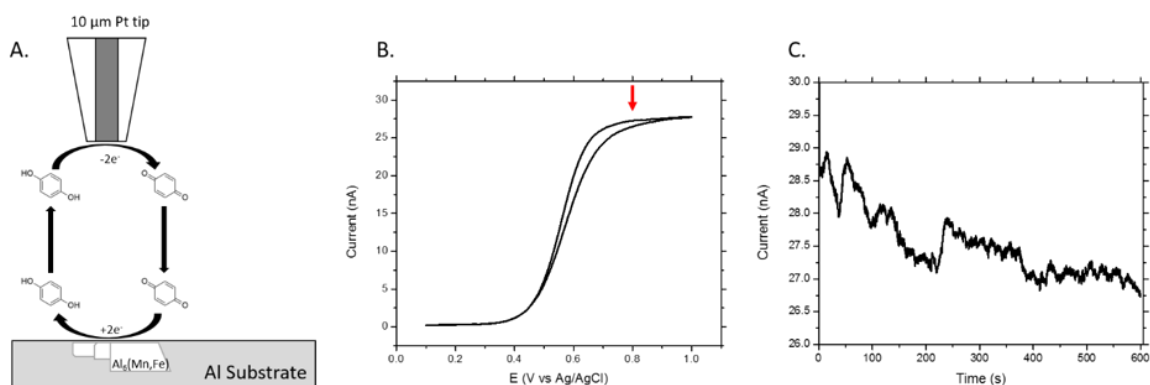


Figure 3.8: A. Schematic of the feedback loop utilized in the SECM instrument. The mediator, HQ is oxidized to Q at the 10 μm Pt tip and diffuses to the alloy surface to be reduced at a cathodic site. Q then diffuses back to the Pt tip and is reoxidized. B. CV recorded at the Pt microelectrode in bulk solution. The CV shows a steady-state current plateau where the current is transport limited. The red arrow indicates the imaging potential of 0.800 V vs Ag/AgCl chosen for SECM experiments. C. Chronoamperometric curve recorded at the 10 μm Pt tip in bulk solution for 600 s; the length of an SECM mapping experiment.

SECM experiments utilized the arrangement depicted in Figure 3.8A. The mediator, HQ was chosen based on studies by Jensen et al. who demonstrated its utility as a probe for the reductive electron transfer reaction in Al systems.¹⁶ As illustrated in Figure

3.8A, the quinone (Q) is generated at the Pt UME, diffuses to the Al substrate where it acts as a cathodic reagent and is reduced back to HQ which is then reoxidized at the Pt UME establishing the feedback loop. To confirm the suitability of HQ as a redox mediator, cyclic voltammetry and chronoamperometry were performed, Figures 3.8B and C, respectively. The CV was recorded at the Pt UME in a bulk solution containing 0.06 M NaCl + 0.1 M acetic acid containing 1 mM HQ. A steady state transport-controlled current was achieved between 0.7 and 1.0 V, with the red arrow indicating the chosen imaging potential of 0.8 V vs Ag/AgCl. Chronoamperometry measurements were performed to confirm that the current at the UME remained constant throughout the duration of an SECM experiment, Figure 3.8C. The UME was held at the imaging potential for 600s to replicate the time required to record one SECM map. The change in current over this period was ~ -3 nA which is an order of magnitude smaller than the current measured in the bulk solution, ~ 30 nA, validating that the SECM measurements were representative of the cathodic behaviour on the substrate.

Figure 3.9A, B and C show PACs performed in a 0.06 M NaCl + 0.1 M acetic acid solution containing 1 mM HQ at various open circuit exposure intervals up to 24 h for alloy A004 (2.06% Mg), A002 (1.00% Mg) and A005 (0.11% Mg), respectively. Each alloy behaves similarly, exhibiting a negative feedback response during the initial stages of immersion before eventually switching to positive feedback at longer times. The two high Mg alloys maintain an insulating response up to 4h before the surface becomes reactive for the generation of HQ while the low Mg alloy exhibits positive feedback after only ~ 4 h of immersion. As suggested by the early transients observed in E_{CORR} measurements, Figure 3.6B, the short term response of each alloy is likely governed by the stability/instability of

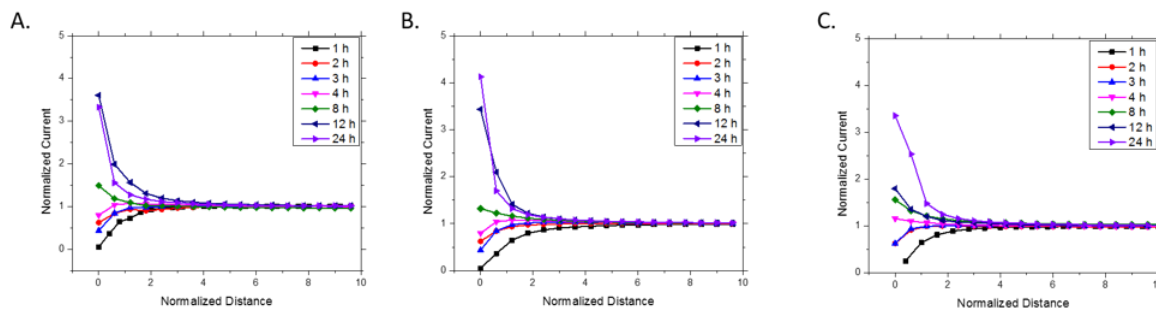


Figure 3.9: PACs recorded in a 0.06 M NaCl + 0.1 M acetic acid solution containing 1 mM hydroquinone after 1, 2, 3, 4, 8, 12 and 24 h of open circuit exposure for alloys A. A004 (2.06% Mg), B. A002 (1.00% Mg) and C. A005 (0.11% Mg). Initially, each alloy exhibits negative feedback indicating insulating behaviour before evolving to increasingly positive feedback with time indication greater reactivity towards the reduction of hydroquinone. Each PAC was initiated 200 μm from the alloy surface.

the native passive oxide, negative feedback arising at short times when the reduction of Q is blocked. As the $\text{Al}_2\text{O}_3 \cdot \text{H}_2\text{O}$ film dissolves, reduction of the redox mediator on the substrate becomes possible leading to the formation of HQ at the substrate surface and the generation of positive feedback in the PAC. Although the low Mg alloy becomes active more readily than the two high Mg alloys the normalized currents exhibited beyond 8 h of immersion are greatest for the high Mg alloys. This implies that, in the long term (i.e. ≥ 12 h) when the major E_{CORR} transients occur the demand for cathodic current is highest on the high Mg alloys.

Using a PAC the UME tip was positioned $\sim 5 \mu\text{m}$ above the Al substrate before each map was recorded. Figure 3.10A, B, C, E, F and G shows SECM maps recorded at the same location on the A004 alloy following 12, 24, 36, 48, 60 and 72 h of exposure to solution along with the corresponding Fe EDX map, D and the SEM BSE micrograph, H, recorded on completion of the experiment. Regions producing enhanced current at the

UME tip appear as blue areas in the maps while low current areas appear as red. Following 12 h of immersion, Figure 3.10A, several cathodic hot spots appear in the SECM map but do not necessarily correlate with the location of the coarse $\text{Al}_6(\text{Fe},\text{Mn})$ particles, three of which are numbered 1, 2 and 3 (as indicated with the purple, white and green arrows, respectively). As the immersion time progresses particles 1 and 2 begin to exhibit cathodic behaviour. Current values recorded at particle 1 are: 45, 45, 62, 87, 87 and 58 nA, for 12, 24, 36, 48, 60 and 72 h, respectively. By comparison, for the same immersion times the current values recorded for particle 2 are: 45, 66, 5, 45, 90 and 86 nA. In general terms the cathodic current at both locations increases throughout the experiment before decreasing after 72h (by 29 nA for particle 1 but only 4nA for particle 2). The current of only 5 nA for particle 2 after 36h of immersion appears anomalous given that subsequent measurements indicate cathodic activity. A possibility is that this location was temporarily blocked by a H_2 bubble formed as a consequence of the simultaneous reduction of H^+ at this location.

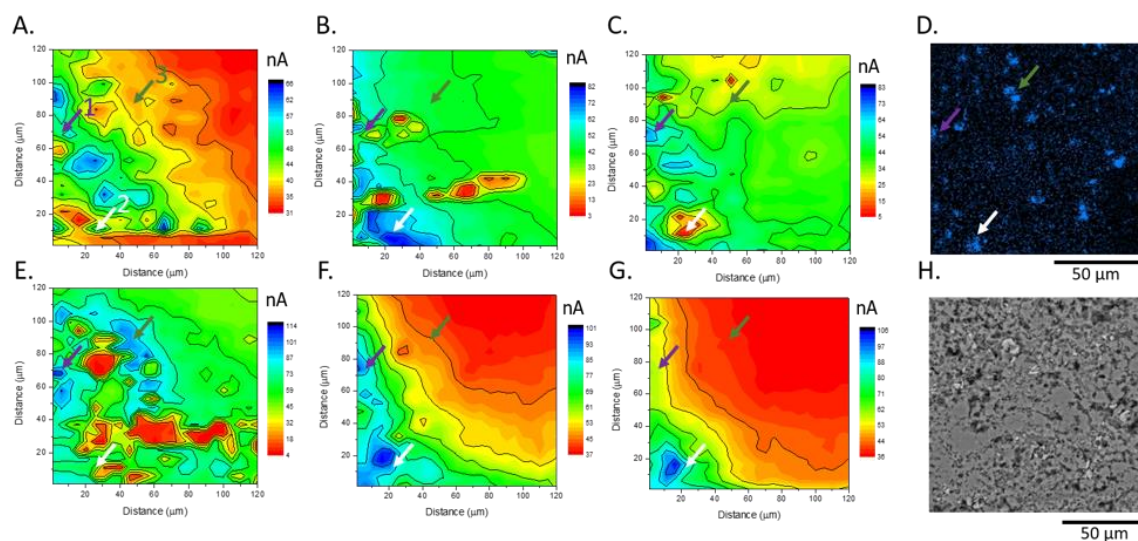


Figure 3.10: A, B, C, E, F and E are SECM maps of the same region recorded after 12, 24, 36, 48, 60 and 72 h of immersion in a 0.06 M NaCl + 0.1 M acetic acid containing 1 mM HQ solution using alloy A004 (2.06% Mg) as the substrate. D and H are the EDX analysis for Fe and the corresponding SEM BSE micrograph of the same region analyzed with SECM. Purple, green and white arrows indicate the locations of $\text{Al}_6(\text{Fe},\text{Mn})$ coarse particles.

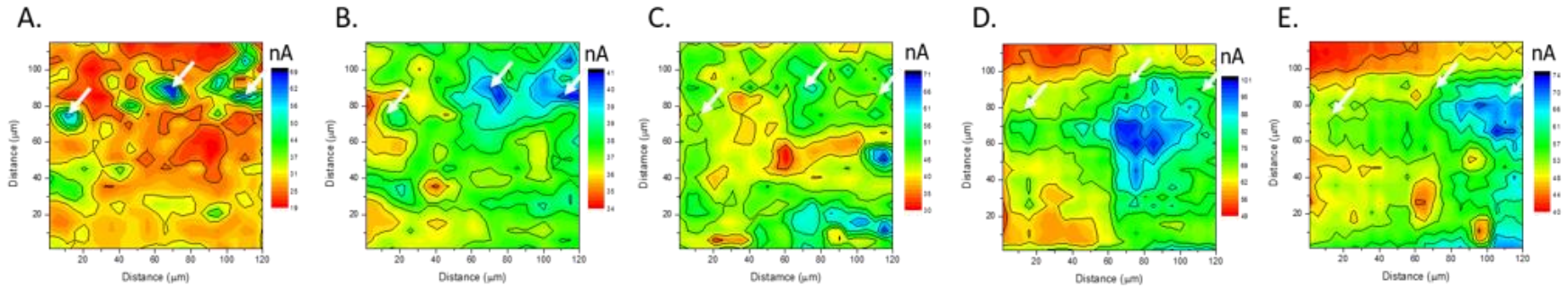


Figure 3.11: A, B, C, D and E are SECM maps of the same region recorded after 4, 8, 12, 24 and 36 h of immersion in a 0.06 M NaCl + 0.1 M acetic acid solution containing 1 mM HQ using alloy A002 (1.00% Mg) as the substrate, respectively. White arrows indicate the location of Al₆(Fe,Mn) coarse particles.

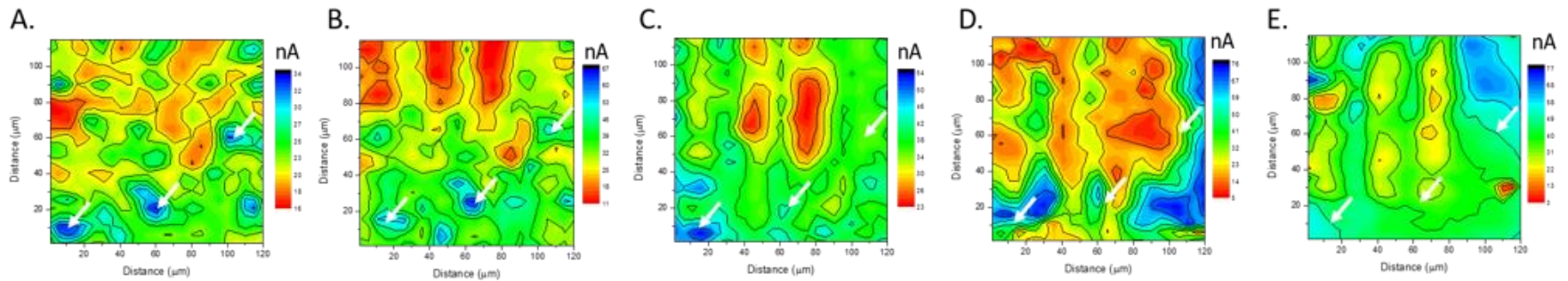


Figure 3.12: A, B, C, D and E are SECM maps of the same region recorded after 4, 8, 12, 24 and 36 h of immersion in a 0.06 M NaCl + 0.1 M acetic acid solution containing 1 mM HQ using alloy A005 (0.11% Mg) as the substrate, respectively. White arrows indicate the location of Al₆(Fe,Mn) coarse particles.

Unlike particles 1 and 2, particle 3 only temporarily exhibits cathodic behaviour, apparently remaining dormant for the first 36 h of immersion with currents being only slightly higher than those measured in the bulk solution, ~ 30 nA. Beyond 48 h the behaviour at this location becomes difficult to interpret the maps recorded after 60 to 72 h showing a large area on which the current is very low extending across the map towards the bottom left corner. The SEM BSE image, Figure 3.10H, shows that extensive damage accumulated in this area possibly rendering the mapping unreliable. Alternatively, as the micrograph in Figure 3.5A shows, and the electrochemical evidence in Figure 3.7 supports, it is possible this indicates the general repassivation of extensive areas of the surface. In an attempt to avoid these complications, especially to minimize the influence of changes in topography, SECM analyses on alloys A002 and A005 were limited to 36 h of immersion.

SECM maps recorded following 4, 8, 12, 24 and 36 h of immersion are shown in Figure 3.11 A-E for alloy A002 (1.00% Mg) and in Figure 3.12 A-E for alloy A005 (0.11% Mg). Both alloys exhibit several cathodic hot spots corresponding to the location of coarse ($\text{Al}_6(\text{Fe},\text{Mn})$) particles following 4 h of immersion. However, the currents recorded on A002 (1.00% Mg), 69 nA at the maximum, are twice as high as those measured on the cathodic sites located on alloy A005 (0.11% Mg). One reason for this could be a difference in tip-to-substrate distance between the two experiments. Although the tip is estimated to be 5 μm from the alloy surface the estimated error is high at ± 3 μm . The exponential dependence of current on tip height when in close proximity to the surface could induce such an error. Regardless, the trend of cathodic activity remains consistent between both alloys. White arrows indicate the position of the strongest cathodes following the initial scan (after 4h) for both alloys. In both cases, these sites remain the most active cathodes up to 8 h of immersion before being replaced by new cathodic sites after 12 h. It is important

to note that maps recorded after 12 h show these original hot spots remain active cathodes but are no longer the most active. This trend persists up to 36 h of immersion. Cathodic sites appearing in the maps recorded following 24 and 36 h are much larger than those revealed during shorter immersion times and do not correlate with coarse, Fe and Mn-rich microstructures.

An SEM BSE micrograph of the ROI mapped by SECM on alloy A002 (1.00% Mg) (Figure 3.11) is presented in Figure 3.13. Many damage sites, which appear to penetrate significantly into the alloy, exist across the surface, and contain coarse microstructures (e.g., bottom right corner) suggesting they acted as cathodes that supported anodic dissolution of the surrounding matrix. Other damage sites (bottom center) simply appear to be voids, although it is possible particles were dislodged from these locations. Large areas of the surface remain apparently undamaged as would be expected from the electrochemical data showing the development of an expanded passive region in the polarization scans, Figure 3.7.

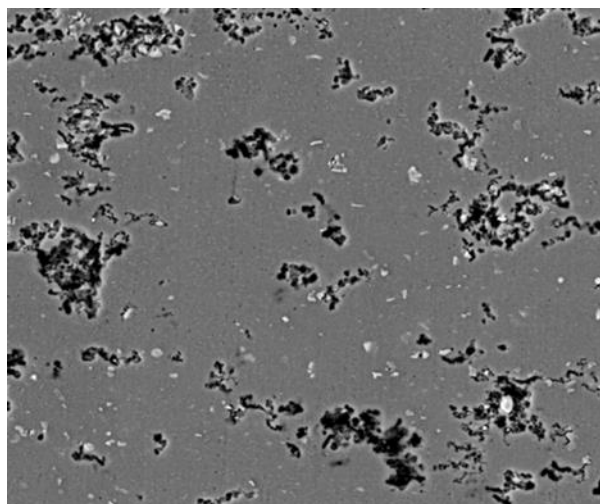


Figure 3.113: SEM BSE image of alloy A002 (1.00% Mg) following the SECM experiments shown in Figure 11. Large topographical variations are present across the entire alloy surface.

3.4 Discussion

On first immersion the alloys would be covered by an air-formed oxide which, if it endured, would maintain passivity. However, as indicated by the Pourbaix diagram¹⁸, the oxide present is unstable in the acidic solution used and would be expected to chemically dissolve. The decrease in E_{CORR} in the first 0.5 to 1 h (Figure 3.6B) could reflect this dissolution process as the alloys attempted to become active. The recovery in E_{CORR} could then indicate an attempt to repassivate and/or the “switching on” of the microgalvanically coupled cathodes once depassivated anodic locations became available. If these early transients in E_{CORR} do indicate the switching on of the microgalvanically coupled cathodes then the differences in their size and duration indicates this occurs more rapidly as the Mg content increases. The PACs (Figure 3.9) support this claim, the change from negative to positive feedback occurring over a similar time interval.

The PDP scans (Figure 3.7) also show that after 0.5 h the two high Mg alloys are active at the E_{CORR} while the low Mg alloy remains passive. Microscopy (Figures 3.1 to 3.4) shows little difference between the number density of either the coarse or fine particulates for the three alloys. Therefore, the differences in alloy behaviour cannot be attributed to the availability of microgalvanic cathodes, suggesting the key difference is the Mg content of the matrix. If so, the more rapid activation of microgalvanic cathodes as the Mg content increased could be attributed to an enhanced anodic reactivity of the activated sites. Once these early transients are complete, the eventual development of transient events in E_{CORR} (Figure 3.6) and the widened passive region observed in the PDP scans (Figure 3.7) indicate an unstable surface with the micrographs in Figure 3.5 showing this can be attributed to periodic pitting events.

These transient events are too infrequent to account for the large number of minor pits, especially on the low Mg A005 (0.11% Mg) alloy, Figure 3.5C. Consequently, they almost certainly represent the larger events leading to more substantial corrosion product deposits. One possible explanation for why the low Mg alloy doesn't generate the same number or area of large breakdown sites could be that enhanced reactivity of the Al matrices with higher Mg content allows more rapid anodic dissolution and hence more corrosion damage at these sites. Enhanced anodic reactivity appears to be confined to the local region around the microgalvanically-coupled cathodes and the extent of its propagation may be limited by a number of features: the kinetics of H_2 reduction on the large particle surfaces is slow and/or the cathodic reduction of other available oxidants besides HQ (i.e. O_2 and H^+) leads to local increases in pH and the deposition of corrosion product thereby limiting the overall propagation to the local area around the particle or particle cluster. Although the transients in E_{CORR} (beyond 30 h (Figure 3.6)) do not reflect the activation/repassivation events observed microgalvanically, it is possible that the wide distribution of small pits reflects metastable pitting events at these locations which would present defects in the generally passive surface.

The SECM maps (Figures 3.10, 3.11 and 3.12) show that the $Al_6(Fe,Mn)$ coarse particles do act as microgalvanically-coupled cathodes but perhaps not exclusively. With time, the cathodic sites shift to different locations, some of which are not associated with any identifiable elemental enrichment. These shifts in location of highly active cathodic sites on the alloy surface does not necessarily involve the loss of cathodic activity at previously functioning sites. The reasons for these shifts in cathodic activity is not immediately obvious but several possibilities exist. First, as a result of anodic dissolution of the Al matrix, previously buried IPs, both coarse and fine, would be exposed with time

and could function as cathodes seen in the SECM maps as new cathodic locations. Second, Al-Mn-Cu systems exhibit dynamic behaviour in acidic salt solutions and as noted by other authors Cu-rich phases in alloy AA2024 (sometimes referred to as the S phase) exhibit time dependent behaviour. These and other Cu-rich IPs are known to electrochemically dissolve via dealloying.^{8,16,19} Yoon et al. demonstrated that dealloyed S phase particles can catalyze O₂ reduction and can also release Cu ions at potentials well below the reversible potential as estimated from the Nernst equation.⁸ Once dissolved, Cu ions can electrochemically plate elsewhere on the alloy surface generating active cathodes. Our studies show the presence of fine Cu-rich IPs, Figure 3.3 and 3.4 as well as the presence of cathodic activity which does not correlate with coarse Al₆(Fe,Mn) particles, Figures 3.10 to 3.12. This possible role of Cu on the distribution of cathodes on the alloys studied remains to be further investigated. Third, as demonstrated in Figure 3.13, the development of surface topography remains a significant barrier to clearly defining the influence of Mg on the cathodic kinetics of these Al alloys. A similar study conducted for shorter immersion times would drastically reduce the height variations present on the surface and could facilitate the development of a better understanding of the corrosion processes.

3.5 Conclusions and Future Work

Microscopic analyses show all three alloys contain irregular Al₆(Fe,Mn) coarse particles and a large number of fine dispersoid particles distributed throughout the matrix. The composition of these particles vary with some being enriched in Cu and Mn while others show an accumulation of Si. The Mg is dissolved within the matrix. On first exposure

to the acidic saline solution all three alloys attempt to depassivate a process which activates the coarse $\text{Al}_6(\text{Fe},\text{Mn})$ particles which SECM shows then function as microgalvanically coupled cathodes. This leads to the accumulation of localized damage on the alloy surfaces with the major damage locations being most commonly located around the cathodes. A high density of small pits is also formed. It is possible these are due to metastable pitting events initiated at the location of the fine dispersoid particles. As corrosion progresses the initially activated cathodes may become dormant possibly due to the accumulation of corrosion product deposits while others exhibited delayed activation. The major effect of the Mg content is on the anodic reactivity of the Al matrix which is increased as the Mg content is increased. This leads to a difference in the distribution of corrosion damage. At a high Mg content activation of the matrix leads to extensive localized corrosion indicated by sites at which corrosion penetrates into the alloy leading to significant Al_2O_3 corrosion product deposits. At a low Mg content the decreased reactivity of the Al matrix limits the propagation of these locations. This is accompanied by a higher density of the metastable pitting event possibly occurring at the fine particle sites.

3.6 References

- (1) Marshal, G.J., Bolingbroke, R.K., Gray, A., Microstructural control in an aluminum core alloy for brazing sheet applications, *Metall. Trans.* 24A: 1935-1942, 1993.
- (2) Marshal, G.J., Flemming, A.J.E., Gray, A., R. Llewellyn, Development of Al-Mn-Cu-Mg brazing sheet core alloys for automotive heat exchanger units for service at high temperatures, 4th International Conference on Aluminum and Alloys, Atlanta, USA, vol 1, 467-474, September 1994.
- (3) L.F. Mondolfo, *Aluminum Alloys: Structure and Properties*, Butterworths, London (1976).
- (4) C. Blanc, B. Lavelle, G. Mankowski, The role of precipitates enriched with copper on the susceptibility to pitting corrosion to the 2024 aluminum alloy, *Corros. Sci.*, **1997**, 39, 495.
- (5) T.J. Warner, M.P. Schmidt, F. Sommer, D. Bellot, Characterization of corrosion initiation on 2024 aluminum alloy by atomic force microscopy, *Z. Metallkd.*, **1995**, 86, 494.
- (6) G.S. Chen, M. Gao, R.P. Wei, Microconstituent induced pitting corrosion in aluminum alloy 2024-T3, *Corros. Sci.*, **1996**, 52, 8.
- (7) Development of Al-Mn-Cu-Mg Brazing Sheet Core Alloys for Automotive Heat Exchanger Units for Service at High Temperatures, 2015-01-XXXX.
- (8) Y. Yoon, R.G. Buchheit, Dissolution behaviour of Al₂CuMg (S phase) in chloride and chromate conversion coatings, *J. Electrochem. Soc.*, **2006**, 153, B151 (2006).
- (9) R.G. Buchheit, R.P. Grant, P.F. Hlava, B. McKenzie, G.L. Zender, Local dissolution phenomena associated with S phase (Al₂CuMg) particles in aluminum alloy 2024-T3, *J. Electrochem. Soc.*, **1997**, 144, 2621.
- (10) K. Sieradzki and N. Dimitrov, in *Localized Corrosion*, Proceedings of the Corrosion/2001 Research Topical Symposium, Houston, TX, p. 293 (2001).
- (11) D.O. Wipf, Initiation and study of localized corrosion by scanning electrochemical microscopy, *Colloids Surf.*, **1994**, 93, 251 (1994).
- (12) J.W. Still, D.O. Wipf, Breakdown of the Fe passive layer by use of the scanning electrochemical microscope, *J. Electrochem. Soc.*, **1997**, 144, 2657.
- (13) C.H. Paik, H.S. White, R.C. Alkire, Visualization and characterization of electroactive defects in the native oxide film on aluminum, *J. Phys. Chem. B*, **2000**, 147, 3691.
- (14) I. Serebrennikova, H.S. White, Scanning electrochemical microscopy measurement of ferrous ion fluxes during localized corrosion of steel, *Electrochem. Solid-State Lett.*, 2000, 4, 4120.
- (15) I. Serebrennikova, S. Lee, H.S. White, Visualization and characterization of electroactive defects on the native oxide film on aluminum, *Faraday Discuss.*, **2002**, 121, 199.

- (16) M.B. Jensen, A. Guerard, D.E. Tallman, G.P. Bierwagen, Studies of electron transfer at aluminum alloy surfaces by scanning electrochemical microscopy, *J. Electrochem. Soc.*, **2008**, 155, C324-C332.
- (17) J.C. Seegmiller, D.A. Buttry, A SECM study of heterogeneous redox activity at AA2024 surfaces, *J. Electrochem. Soc.*, **2003**, 150, (9) B413-B418.
- (18) M. Pourbaix, *Atlas of Electrochemical Equilibria in Aqueous Solutions*, p. 172, NACE International, Houston (1974).
- (19) K. Kowal, J. Deluccia, J.Y. Josefowicz, C. Laird, G.C. Farrington, In situ atomic force microscopy observations of the corrosion behaviour of aluminum-copper alloys, *J. Electrochem. Soc.*, **1996**, 143, 2471.

4 Impedance Study on the Effect of Casting Procedure on the Corrosion Behaviour of Mg AM50 Alloy

4.1 Introduction

Owing to their lightweight and good strength-to-weight ratio Mg alloys have the potential to significantly reduce the weight of automobiles and therefore, reduce emissions from internal combustion engines and improve the range of electrical vehicles. However, Mg alloys see limited use in automotive applications due to their fast corrosion rates upon exposure to aqueous environments.¹⁻⁴ Such extreme corrosion rates are a result of the high activity of Mg metal which leads to enhanced corrosion due to the microgalvanic coupling of the α -Mg matrix to more noble secondary microstructures.⁵⁻⁹ However, there are a select few alloying elements which have been shown to reduce Mg corrosion rates in spite of also forming secondary microstructures. The most common of these alloying elements is Al.

In addition to reduced corrosion rates as compared to pure Mg,¹⁰⁻¹⁴ Mg-Al alloys have the added benefit of possessing superior mechanical properties.^{15,16} However, Mg-Al alloys do exhibit the segregation of secondary microstructures leaving them prone to microgalvanic corrosion. The commercial Mg AM50 alloy contains both a Mg₁₇Al₁₂ β -phase which is surrounded by an Al-rich eutectic phase and Al-Mn intermetallic particles (IMPs).¹⁷ Both secondary microstructures have been shown to act as cathodes which support the corrosion of the α -Mg matrix and therefore their size,^{18,19} distribution^{20,21} and morphology²⁰ can affect their electrochemical behaviour. Since each of the aforementioned microstructural features can be controlled by the manufacturing process of the AM50 alloy, this is an ideal target to optimize the corrosion behaviour of each alloy for a particular environment.

In a previous study we investigated the effect of casting procedure (sand cast vs. graphite cast vs. die cast) on the corrosion of the Mg AM50 alloy in a solution containing a high chloride ion concentration (0.3 M). This study showed that the die cast (DC) alloy exhibited the greatest corrosion resistance followed by the graphite cast (GC) and then the sand cast (SC) alloy.⁵ This order in corrosion resistance was attributed to the presence of a more uniform Al network which results from fast cooling of the alloy melt. At the high chloride concentration used the influence of the exposure environment was the dominant influence on corrosion. In the study presented here the immersion environment, both the chloride concentration and the solvent, have been varied and the corrosion behaviour followed by electrochemical impedance spectroscopy (EIS) in an attempt to gain additional insight on the role of microstructure and the size and distribution of secondary phases. However, while the acquisition of EIS data is relatively simple, its proper interpretation to reach meaningful conclusions is non-trivial.

Many studies exist in the literature which report and interpret Mg and Mg alloy corrosion behaviour via EIS. Depending on the immersion conditions, a typical response contains either one or two capacitive loops in the high and mid-frequency range followed by a pseudo-inductive response in the low frequency range. Disconcertingly, the preponderance of these studies disregard the low frequency response due to the pseudo-inductive behaviour. Typically, conclusions regarding the corrosion resistance of an alloy are based on the charge transfer resistance (R_{CT}) as defined by the value of the real impedance (Z') when the imaginary impedance (Z'') approaches zero. However, while R_{CT} does, to some extent, represent the general resistivity of the alloy surface it occurs in the mid to low-frequency domain and therefore does not faithfully satisfy the condition of

approaching the direct current conditions (i.e. frequency $\rightarrow 0$) required to determine the polarization resistance (R_p), the key parameter from which the corrosion rate should be calculated.²² Therefore, studies which omit the inductive response overestimate the corrosion resistance, and its inclusion has been shown to yield corrosion rates which match well with other analysis techniques (e.g. mass loss, H_2 collection and inductively coupled plasma optical emission spectrometry) for Mg^{23,24} and Mg AZ31B.²⁵

In the following analysis the EIS proposed for pure Mg by King et al.^{23,24} and validated for the Mg AZ31B alloy by Bland et al.²⁵ has been applied to the three Mg AM50 alloys with different casting methods to interrogate the role of microstructure size and distribution on the corrosion processes of the alloys. Our goal was to examine how the casting process affected the alloy microstructure and how this influenced the corrosion behaviour.

4.2 Experimental

4.2.1 Materials and Preparation

The Mg AM50 alloys were received from General Motors (USA) and had nominally identical compositions comprising 4.9 wt% Al, 0.4 wt% Mn with the balance being Mg. This was confirmed by inductively coupled plasma mass spectrometry (ICP-MS). The three different methods employed in alloy fabrication were sand (SC), graphite (GC) and die casting (DC). Both the sand and graphite casting methods produced cylindrical ingots approximately 30 cm in length and 3 cm in diameter. Cubic samples measuring 1 x 1 x 1 cm³ were machined from the center portion of the ingots to ensure that all samples had a

uniform cooling rate (typical cooling rates being on the order of 10^1 - 10^3 K/s). DC samples were received in sheets with a thickness of 3 mm. Samples were cut with dimensions of 1 x 1 cm². All samples were tapped on one side to allow for electrical connection to external electrochemical circuitry.

Prior to both electrochemical and microscopic experiments, samples were cold mounted in Struers Epofix® epoxy resin and hand polished to a mirror finish. Samples were ground successively with 800, 2400 and 4000 grit SiC polishing pads with anhydrous ethanol as a lubricant. Fine polishing employed a Struers 3 µm diamond paste on a DP-Dur polishing pad followed by a 1:1 colloidal silica (0.04 µm) to ethylene glycol mixture on an OP-Chem pad. Following polishing, samples were sonicated in anhydrous ethanol for 1 min and dried in an Ar gas stream.

4.2.2 Electrochemical Experiments

Corrosion potential (E_{CORR}) and EIS measurements were conducted in a conventional three-electrode cell with a saturated calomel reference electrode (SCE), Mg AM50 as the working electrode and, when necessary, a Pt flag as the counter electrode. Electrolytes were prepared with Type 1 water (18 MΩ·cm) or as received reagent grade ethylene glycol and reagent grade NaCl. Notably, no attempt was made to quantify the water content of the ethylene glycol. Experiments were conducted at room temperature (23 ± 2 °C) inside a grounded Faraday cage to minimize interference from external electrical noise.

A Solartron 1287 potentiostat connected to a Solartron 1255 Frequency response analyzer (FRA) running Corrware and ZPlot software were used for all electrochemical measurements. Prior to each experiment the potentiostat and FRA were tested with a dummy cell over a frequency range of 10^4 – 10^{-1} Hz. Impedance measurements utilized a

sinusoidal input potential wave of ± 10 mV around the E_{CORR} over a frequency range of 10^5 to 10^{-3} Hz with 11 data points per decade. All impedance data were subjected to a Kramers-Kronig test and only data with $< 1\%$ residual were accepted. Equivalent electrical circuit fitting was done using ZView software. All equivalent circuit elements exhibited a percentage error of $\leq 5\%$.

4.2.3 Microscopy

All samples analyzed microscopically were prepared according to the procedure described in section 4.2.1. Scanning electron microscopy (SEM) used either a Zeiss LEO 1540XB FIB/SEM or a Hitachi SU3500 Variable Pressure SEM combined with an Oxford Aztec X-Max50 SDD X-ray analyzer.

4.3 Results

4.3.1 Material Characterization

Figure 4.1 shows SEM backscattered electron (BSE) micrographs and the corresponding EDX elemental maps for Mg, Al and Mn for the SC (a-d), GC (e-h) and DC (i-l) Mg AM50 alloys, respectively. Notably, the scale bar for the DC sample is an order of magnitude smaller than for the SC and GC samples. For each alloy, the white areas in the micrographs indicate the locations of Al-Mn intermetallic particles (IMPs), the gray areas correspond to $\text{Mg}_{17}\text{Al}_{12}$ β -phase with the light gray background corresponding to the α -Mg matrix.^{5,17} Additionally, previous high resolution surface analysis shows that a eutectic Al phase extends from the β -phase into the α -Mg matrix.¹⁷

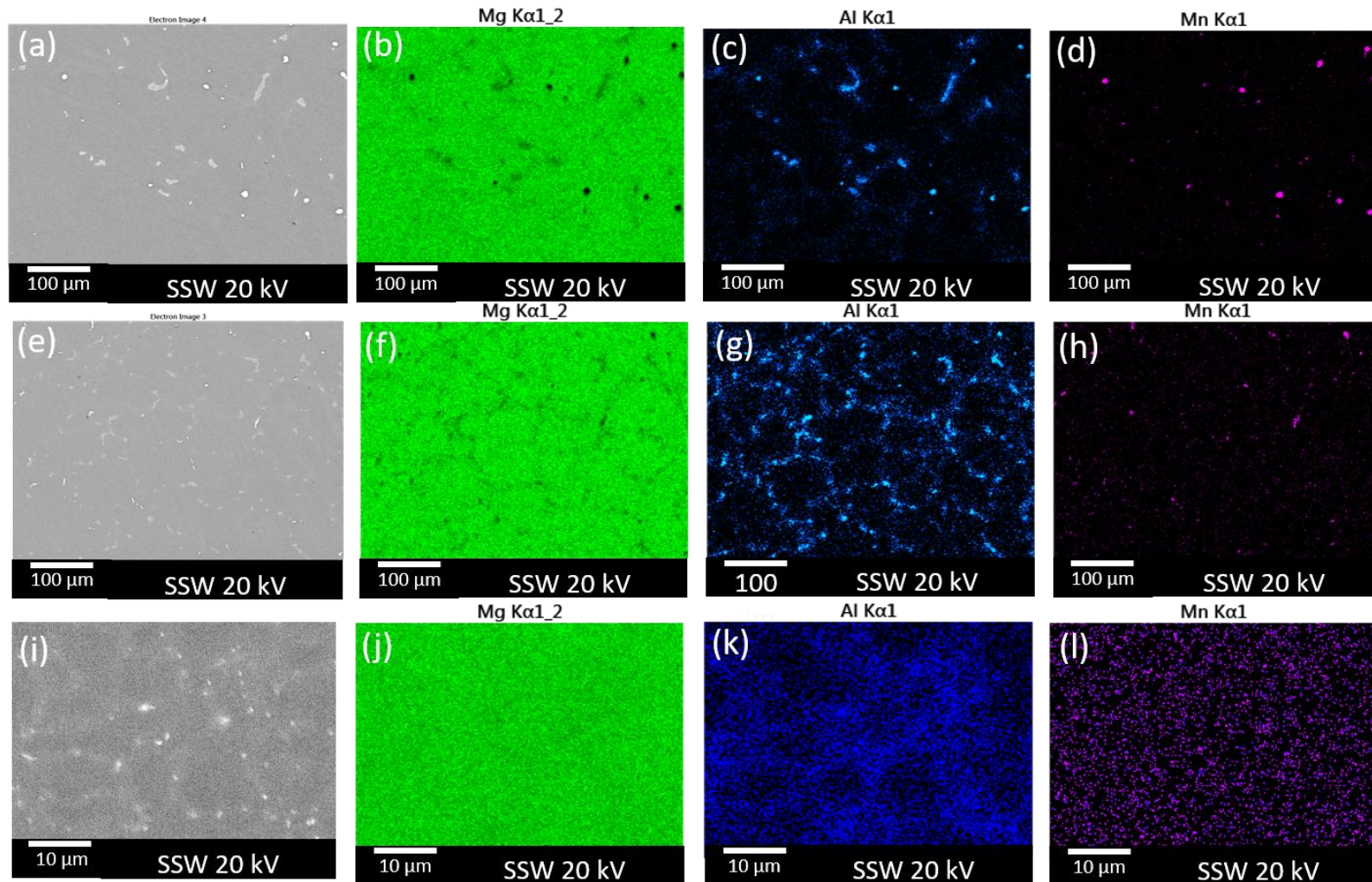


Figure 4.1: (a, e and i) SEM BSE micrographs of as-polished sand, graphite and die cast Mg AM50 alloy. The corresponding EDX elemental maps for Mg, Al and Mn are shown for the sand cast (b, c and d) graphite cast (f, g and h) and die cast (j, k and l), respectively. The white regions in the SEM micrographs correspond to Al-Mn intermetallics, the gray areas correspond to $\text{Mg}_{17}\text{Al}_{12}$ β -phase and the dark gray corresponds to the α -Mg matrix.

While the composition of the alloys is independent of casting technique, the size and distribution of the β -phase and Al-Mn IMPs are not. As is visible in Figure 1, the largest and most localized distribution of the secondary phases occurs for the SC alloy, followed by the GC alloy, with the smallest and most even distribution of phases and elements exhibited by the DC alloy. This difference in microstructure can be attributed to the difference in cooling rate of the alloys for each casting technique^{1,18,26} with the rate of cooling increasing in the order SC < GC < DC. Significantly, as demonstrated by the Al EDX maps, Figure 1 (c, g and k) this results in discontinuous islands of β -phase in the SC alloy and a continuous Al network of β -phase linked by eutectic Al and a solid solution of Al in the GC and DC alloys. The distribution of Al is the most disperse for the DC alloy. Additionally, the Al-Mn IMPs exhibit a very similar size and distribution in the SC and GC alloys while they are finer and more evenly dispersed in the DC alloy.

4.3.2 Electrochemical Experiments

4.3.2.1 E_{CORR} Measurements

The E_{CORR} values for each alloy when immersed in NaCl solutions with concentrations of 0.3, 0.03 and 0.003 M NaCl for 24 h, are shown in Figure 4.2 (a-c). For the high chloride concentration, the E_{CORR} values are a function of cooling rate with the DC alloy exhibiting the most noble value followed by the GC and the SC alloys. For all three alloys, E_{CORR} fluctuates over a range of ~20 mV with the frequency being higher for the DC and GC alloys. This behaviour indicates an influence of microstructure on the corrosion behaviour.

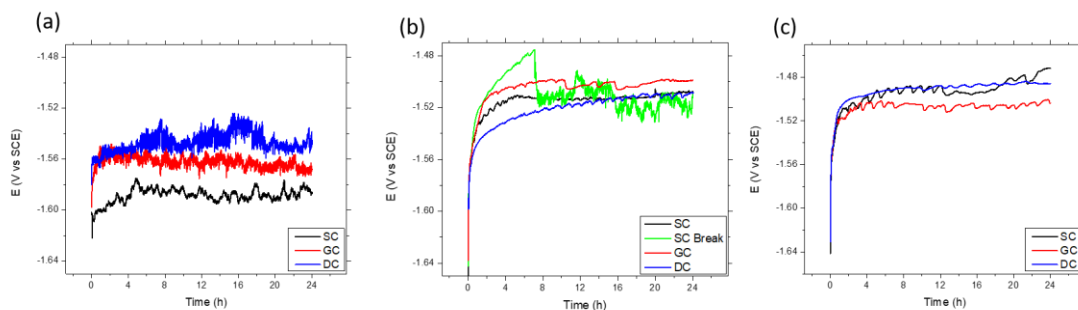


Figure 4.2: E_{CORR} measurements recorded on a sand cast (SC), graphite cast (GC) and die cast (DC) Mg AM50 alloys in (a) 0.3 M NaCl solution, (b) 0.03 M NaCl solution and (c) 0.003 M NaCl solution for 24 h. Note, at 0.03 M NaCl the SC alloy exhibits two types of behaviour; one is characterized by a smooth increase and plateau (black) while the other experiences a sudden breakdown and onset of fluctuations (green).

When the chloride concentration is reduced to 0.03 M NaCl, Fig. 4.2b, the E_{CORR} values are more positive and less dependent on alloy type than at the higher concentration suggesting a decreased role for the microstructure. In general, the values are more stable than at the higher concentration. However, during some immersions, the E_{CORR} for the SC alloy reaches a more positive value before experiencing a rapid decrease of ~ 40 mV. While the length of time for this to occur varies (between 8 and 12 h in four repeats of this experiment) this behaviour is exhibited in roughly half of the experiments performed. Similar behaviour has been observed on a Mg ZEK100 alloy (see chapter 6) and was correlated with the initiation and subsequent propagation of dark corrosion filaments across the alloy surface. Unlike the high chloride case, in 0.03 M NaCl solution, the overall E_{CORR} behaviour of each alloy (when a breakdown does not occur) becomes more similar with respect to the oscillation magnitude and frequency as well as the average value in the long-term. As the $[Cl^-]$ is decreased further to 0.003 M, the E_{CORR} behaviour of each alloy becomes very similar in both form and magnitude with the average E_{CORR} value differing by only ~ 40 mV between the three casts.

4.3.2.2 Impedance as a Function of Immersion Time and Chloride Concentration

Impedance measurements conducted on the SC, GC and DC alloys in 0.3 M NaCl are shown in Figures 4.3(a-c), (d-f) and (g-i), respectively. In each case an impedance spectrum was recorded following 10, 20 and 30 h of immersion in the same electrolyte with data being represented by symbols and the corresponding electrical equivalent circuit fit as a solid line (section 4.3.2.3 (below)). For the SC alloy, the Nyquist plot (Fig. 4.3a) is fitted to an equivalent circuit with a single time constant, although close inspection of the spectra suggests a better fit could be obtained with the addition of a second time constant for lower frequencies. There is little change in the impedance response with respect to time with the exception of the magnitude of the frequency independent impedance modulus (i.e. plateau) at ~ 1 Hz shown, Fig 4.3b. This feature is indicative of the polarization resistance of the alloy. For this alloy, the magnitude of impedance as the low frequency limit is approached decreases from about $1,700 \Omega \cdot \text{cm}^2$ at 10 h to approximately $1,200 \Omega \cdot \text{cm}^2$ at 30 h of immersion indicating only a minor increase in corrosion rate with exposure time. A similar response is observed for the GC alloy over the 30h immersion period. As for the SC alloy a single time constant equivalent circuit was used to fit the data, although, as for the SC alloy, a second time constant would have improved the fit at lower frequencies. For this alloy the magnitude of the impedance at the low frequency limit decreases from $\sim 2 \text{ k}\Omega \cdot \text{cm}^2$ (10 h) to $\sim 1.6 \text{ k}\Omega \cdot \text{cm}^2$ at 30 h. This indicates the corrosion resistance of this alloy is marginally $>$ than that for the SC alloy. However, both sets of measurements were terminated at a relatively high frequency (~ 1 Hz) making it likely that these impedance values overestimate the corrosion resistance of the alloy surface.

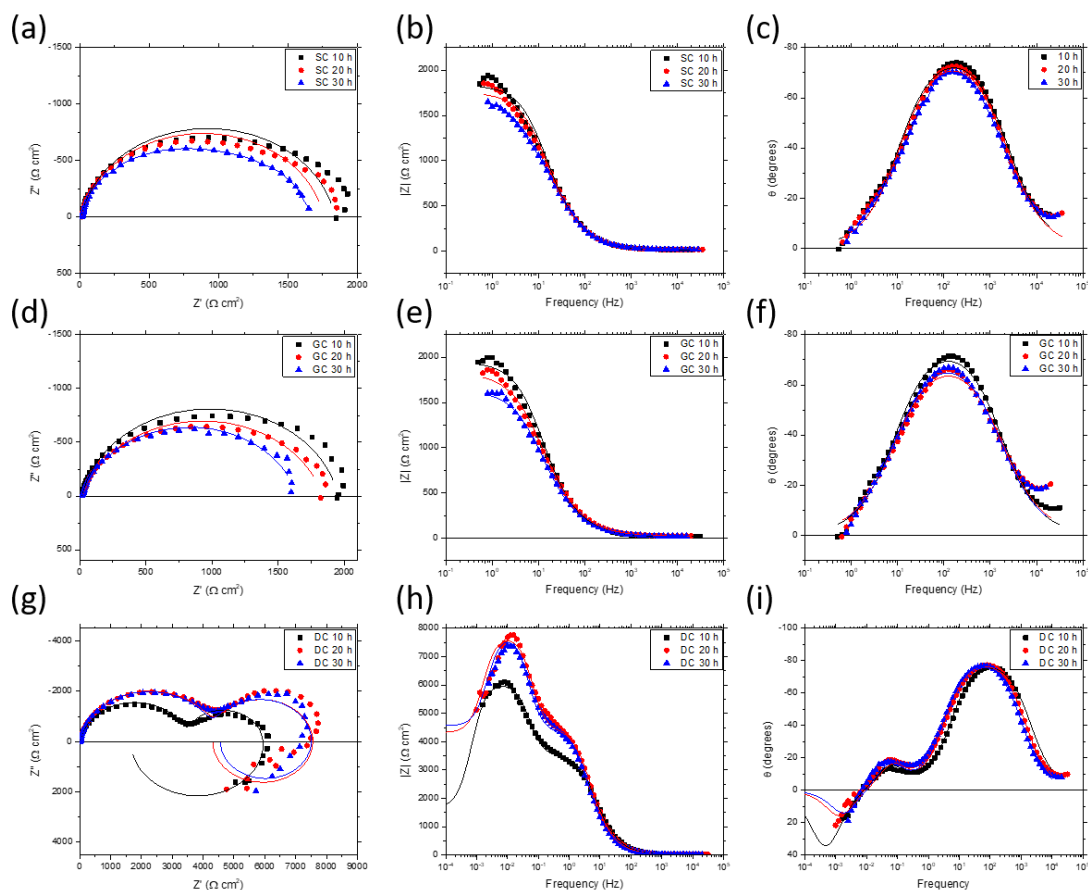


Figure 4.3: (a, d and g) Nyquist plots recorded for a SC, GC and DC Mg AM50 alloy, respectively, with the corresponding impedance modulus (b, e and h) and phase angle plots (c, f and i) following 10, 20 and 30 h of immersion in a 0.3 M NaCl solution. Recorded data points are indicated with symbols while the equivalent electrical circuit fit is indicated with a solid line.

In stark contrast, the DC alloy exhibits a very different impedance response than the SC and GC alloys. The Nyquist plot obtained in 0.3 M NaCl, Figure 4.3g, exhibits two capacitive loops in the high and mid-frequency range with a pronounced pseudo-inductive response in the low frequency domain. Comparison of the spectra for the three alloys shows that the second capacitive loop observed for this alloy occurs in the same frequency range within which a second response is vaguely visible for the SC and GC alloys, 10 to 10^{-2} Hz,

Figure 4.3. The spectra were fit to an equivalent circuit with two R/C components and a low frequency inductive element. As indicated in Fig 4.3 (g to i) this fit is only partially successful, most likely due to the minimal amount of poor quality data available to define the inductive loop. For the DC alloy the impedances are generally significantly higher than for the other two alloys and the trend with time is to larger impedances which is the opposite to that observed for the other two alloys. Both capacitive loops increase in size over the first 10 h of exposure and the R_P values obtained from the low frequency intercept of the spectra increase from a value close to those observed for the other two alloys ($\sim 1500 \Omega \cdot \text{cm}^2$) to a much higher value of $\sim 4600 \Omega \cdot \text{cm}^2$ after 20h. Extending the exposure period to 30 h then has only a marginal further effect on either the size of the two capacitive loops or the R_P value. These trends indicate that while the corrosion rates of the SC and GC alloys increase slightly with time the corrosion rate of the DC alloy decreases.

Similar impedance measurements recorded at an intermediate $[\text{Cl}^-]$ (i.e. 0.03 M) are shown for the SC (in the absence of a breakdown in E_{CORR}), GC and DC alloys in Fig. 4.4(a-c), (d-f) and (g-i), respectively. Each alloy exhibits high and mid-frequency capacitive loops and a pseudo-inductive response in the low frequency domain. Qualitatively, with respect to their own time evolution, each alloy behaves very similarly over a frequency range of 10^4 to 10^0 Hz, which is most evident in the impedance magnitude plots, Fig. 4.4b, e and h. Below 1 Hz, the diameter of the mid-frequency capacitive loop increases with time for all three alloys (Fig. 4.4a, d and g) as does the impedance magnitude. For each alloy, the lower limit frequency impedance value (i.e. $R_P + R_S$) increases with time indicating an increase in corrosion resistance (generally R_S is extremely small and $R_P + R_S \rightarrow R_P$). At each interval the order of this impedance is $\text{SC} > \text{GC} > \text{DC}$,

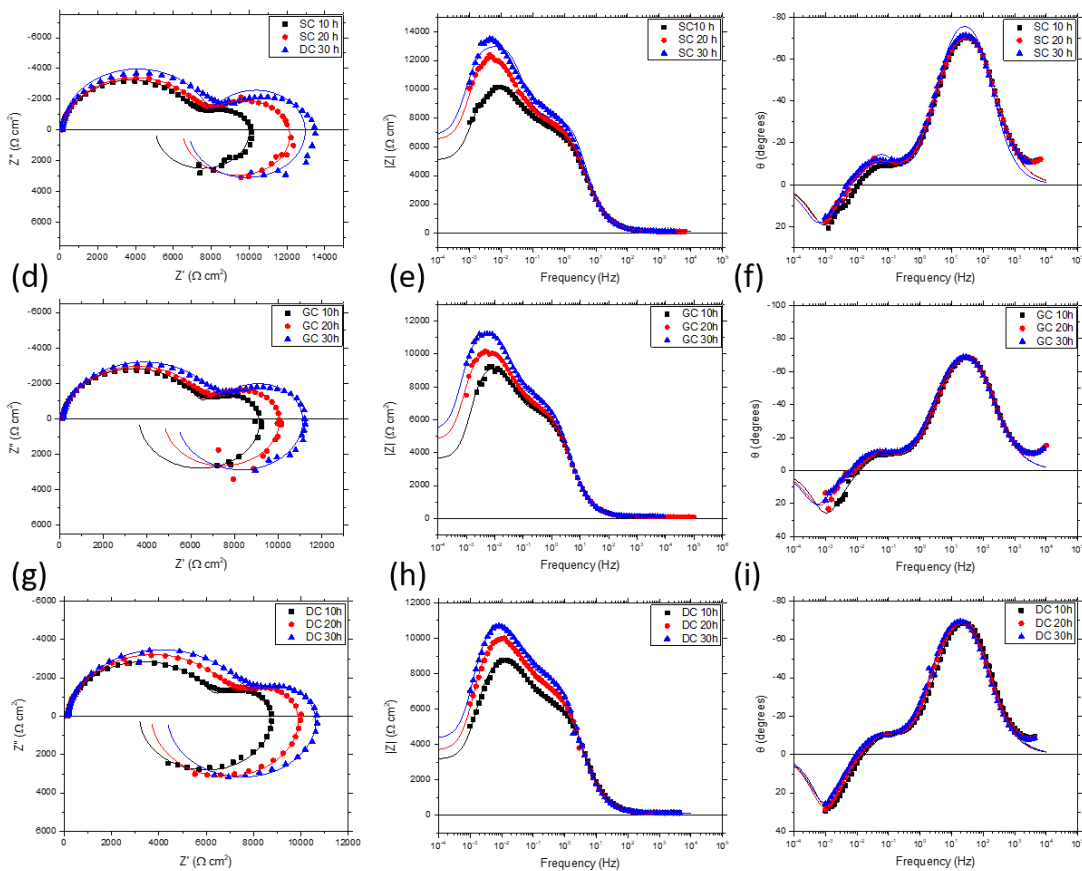


Figure 4.4: (a, d and g) Nyquist plots recorded for a SC, GC and DC Mg AM50 alloy, respectively, with the corresponding impedance modulus (b, e and h) and phase angle plots (c, f and i) following 10, 20 and 30 h of immersion in a 0.03 M NaCl solution. Recorded data points are indicated with symbols while the equivalent electrical circuit fit is indicated with a solid line.

which is an inversion of the trend seen at the high $[Cl^-]$. The similarity in behaviour between the three alloys demonstrates that the influence of microstructure is much less important than at the higher $[Cl^-]$.

As shown above, at the intermediate $[Cl^-]$ the SC alloy can exhibit two distinct behaviours as evidenced by the E_{CORR} and Nyquist plots for each scenario, Fig. 4.5. If E_{CORR} rises to a stable value slightly greater than $-1.5V$, then the impedance behaviour is that

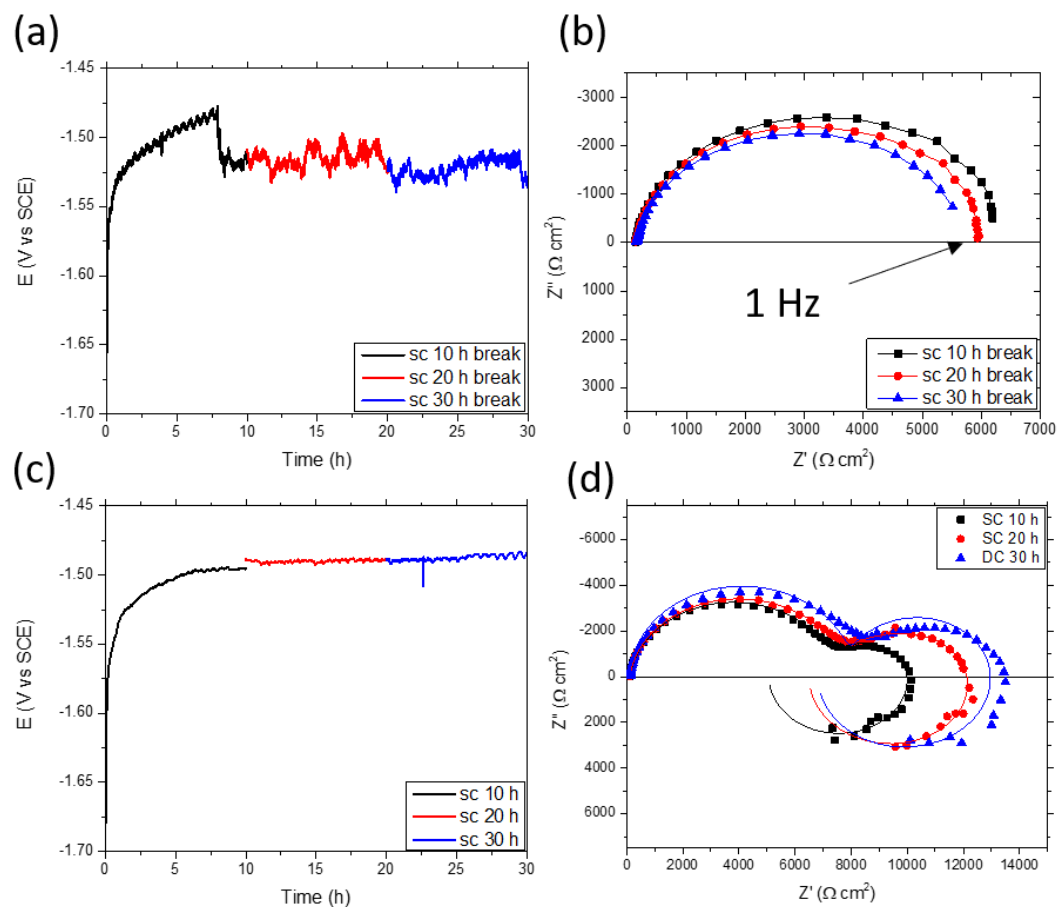


Figure 4.5: (a and c) E_{CORR} measurements recorded on the SC alloy in 0.03 M NaCl solution and the corresponding Nyquist plots (b and d) recorded following 10, 20 and 30 h of immersion.

observed in Figure 4.4. However, if, after an initial rise to this potential range, E_{CORR} suddenly decreases, then the impedance response relapses to that observed at the higher $[\text{Cl}^-]$ although the impedance values are significantly higher at the lower $[\text{Cl}^-]$. These two scenarios are compared in Fig 4.5. This behaviour can be attributed to a breakdown of a surface oxide/hydroxide grown at short exposure times when E_{CORR} suddenly decreases with corrosion subsequently occurring at these breakdown sites. This explanation is

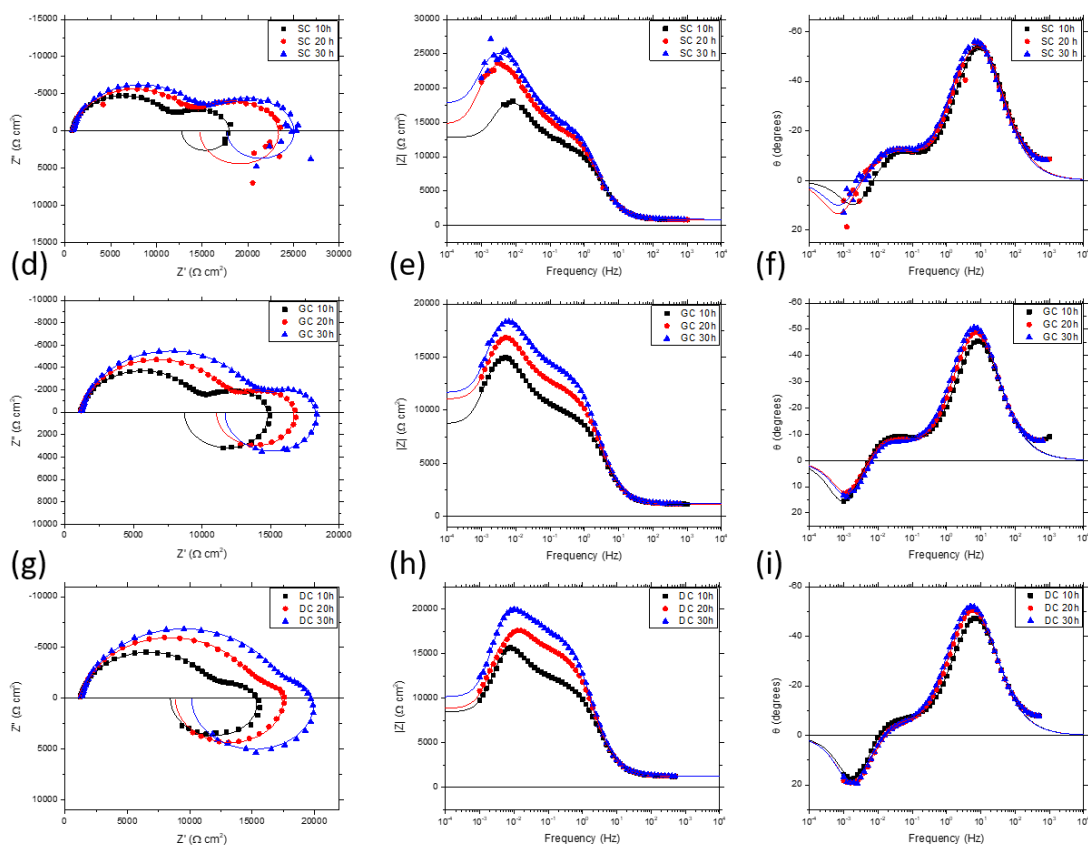


Figure 4.6: (a, d and g) Nyquist plots recorded for a SC, GC and DC Mg AM50 alloy, respectively, with the corresponding impedance modulus (b, e and h) and phase angle plots (c, f and i) following 10, 20 and 30 h of immersion in a 0.003 M NaCl solution. Recorded data points are indicated with symbols while the equivalent electrical circuit fit is indicated with a solid line.

supported by the observation that the impedance increases with time if the film remains intact, Fig 4.5 (d) but decreases with time if film fracture occurs, Fig 4.5 (b).

Impedance data collected in the 0.003 M chloride solution for the SC, GC and DC alloys are shown in Fig. 4.6(a-c), (d-f) and (g-i), respectively. As observed at the intermediate $[Cl^-]$, each alloy exhibits high and mid frequency capacitive loops and a low frequency pseudo-inductive signal although the overall impedance values are higher. However, the three alloys exhibit different behaviour with respect to the diameter of the

mid frequency capacitive loop relative to the high frequency capacitive loop, Fig. 4.6a, d and g for the SC, GC and DC alloys, respectively. For the SC alloy, the diameter of this capacitive loop increases with time and becomes comparable to the size of the high frequency loop over 30 h. By comparison, the diameter of the mid frequency loops for the GC and DC alloys remain unchanged or decrease slightly with time and are significantly smaller than the high frequency loop. Similarly, the trend of increasing R_P+R_S values with time is observed for each alloy. Another similarity to the intermediate $[Cl^-]$ experiments is the order of the low frequency impedance modulus which is $SC > GC > DC$. However, the SC alloy exhibits significantly higher impedance values than the GC or DC alloys.

4.3.2.3 Equivalent Electrical Circuit Fitting

The impedance spectra obtained can be fitted to one of the two electrical equivalent circuits shown in Figure 4.7.^{25,27} When only a single capacitive response is observed the spectra were fitted to the circuit in Fig 4.7(a). When two capacitive responses and a low frequency inductive response are observed the spectra are fitted to the circuit shown in Fig 4.7(b). Impedance behaviour which could be fitted using the circuit in Fig 4.7(a) is always observed for the SC and GC alloys at high $[Cl^-]$ and sometimes for only the Sc alloy at intermediate $[Cl^-]$. Although in these cases the fits to the data at low frequencies could possibly have been improved by including a second time constant, its influence would be minor. It is also worth noting that the noisy corrosion behaviour clearly indicated in the E_{CORR} measurements (Fig. 4.2(a)), precluded the measurement of meaningful data below a frequency of 10^{-1} Hz. As a consequence, inductive behaviour at lower frequencies may

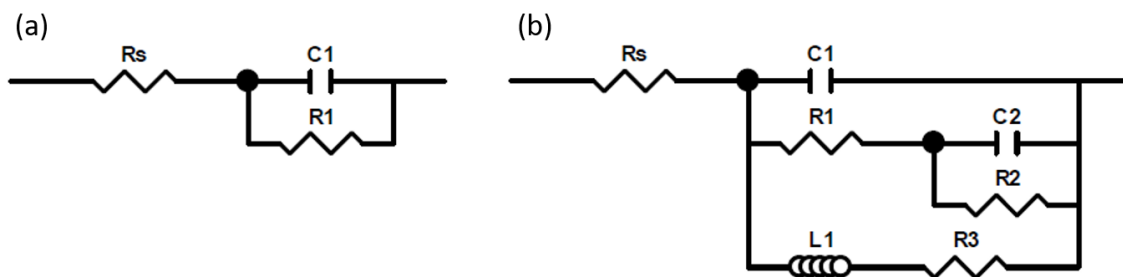


Figure 4.7: Equivalent electrical circuits used to fit impedance data which exhibited (a) a single time constant response and (b) a two time constant response. In some cases, a constant phase element was used instead of a capacitor to more faithfully fit the data. In these cases the exponent is ≥ 0.9 .

have been missed. Given the low impedances, the R_1/C_1 combination can be taken as a measurement of the interfacial charge transfer process with minimal interference from any surface films.

Based on published arguments^{25,28,29} the elements in the circuit in Figure 4.7(b) can be assigned to the following processes. The high frequency response (R_1/C_1) can be attributed to the interfacial charge transfer process. The mid-frequency response (R_2/C_2) can be assigned to the contribution from mass transport processes within a corrosion product layer and the inductive response (R_3/L_1) to relaxation processes involving adsorbed species such as $Mg(OH)_{ads}^+$ and $MgOH_{ads}$ on the corroding Mg surface.

Although the equivalent circuits show only capacitances, in some cases constant phase elements (CPE) were required to faithfully fit the spectra. When used the value of the CPE exponent was always > 0.9 allowing values to be treated as capacitances (for which the exponent = 1). The values for each circuit element for the three alloys in all experiments are shown in Table 4.1. Values of the polarization resistance (R_p) were calculated using equations 1 and 2 for the single (Fig 4.7 (a)) and multiple (Fig 4.7(b)) equivalent circuits, respectively.

Table 5.1: Equivalent electrical circuit element values for SC, GC and DC Mg AM50 alloys immersed in 0.3, 0.03 and 0.003 M NaCl solution for 10, 20 and 30 h.

SC	0.3 M NaCl			0.03 M NaCl			0.003 M NaCl		
	10 h	20 h	30 h	10 h	20 h	30 h	10 h	20 h	30 h
R_s (Ω)	13.39	14.44	16.02	111.5	114.7	128	796	825.2	862.7
C1 (μF)	12.17*	12.93*	14.26*	9.01*	8.71*	6.11*	9.32*	9.80*	9.61*
R1(Ω)	1823	1743	1573	7,373	7,601	7,951	11,244	13,488	14,669
C2 (μF)	-	-	-	1,146.8	782.6	763.5	618.0*	545.3*	530.0*
R2 (Ω)	-	-	-	2,635	5,118	5019	9,084	10,731	10,906
L1 (L)	-	-	-	2.36x10 ⁶	3.44x10 ⁶	4.80x10 ⁶	2.29x10 ⁶	9.15x10 ⁶	1.25x10 ⁷
R3 (Ω)	-	-	-	9,858	12,836	13,818	38,052	32,849	49,673

GC	0.3 M NaCl			0.03 M NaCl			0.003 M NaCl		
	10 h	20 h	30 h	10 h	20 h	30 h	10 h	20 h	30 h
R_s (Ω)	17.62	21.38	19.15	113.3	115.5	118.5	1,142	1,169	1,194
C1 (μF)	14.7*	19.52*	20.43*	10.46*	10.67*	10.96*	10.25*	9.56*	9.40*
R1(Ω)	1,937	1,817	1,626	6,542	6,856	7,460	8,918	11,098	12,924
C2 (μF)	-	-	-	1,298.0	1,152.1	1,152.9	1,022.8*	1,031.5*	1,104*
R2 (Ω)	-	-	-	2657	3190	3,673	5,907	5,972	5,379
L1 (L)	-	-	-	1.35x10 ⁶	3.08x10 ⁶	4.25x10 ⁶	3.39x10 ⁶	3.64x10 ⁶	4.00x10 ⁶
R3 (Ω)	-	-	-	5,716	8,678	10,059	15,474	23,442	24,474

DC	0.3 M NaCl			0.03 M NaCl			0.003 M NaCl		
	10 h	20 h	30 h	10 h	20 h	30 h	10 h	20 h	30 h
R_s (Ω)	14.72	18.99	18.99	125.9	131.5	137.4	1,222	1,266	1,290
C1 (μF)	11.81*	15.20*	15.25*	11.02*	12.17*	12.68*	10.39*	10.05*	9.90*
R1(Ω)	3,540	4,445	4,448	6,401	7,273	7,906	10,970	14,395	16,476
C2 (μF)	1,430.6	1,128.1	1,113.1	1,027.6	1,215.8	1,326.5	1,222.5*	2,024.7*	1,855.9
R2 (Ω)	2,452	3,262	3,260	2,332	2,650	2,762	4,595	2,143	2,795
L1 (L)	1.46x10 ⁶	1.20x10 ⁶	1.20x10 ⁶	1.02x10 ⁶	1.50x10 ⁶	1.87x10 ⁶	1.62x10 ⁶	1.92x10 ⁶	2.22x10 ⁶
R3 (Ω)	2,277	11,068	11,074	4,689	5,529	6,979	13,525	14,034	16,407

* Indicates a value that was produced with a CPE

$$\frac{1}{R_p} = \frac{1}{R_1} \quad (1)$$

$$\frac{1}{R_p} = \frac{1}{R_1 + R_2} + \frac{1}{R_3} \quad (2)$$

The R_p values for the SC, GC and DC alloys are plotted as a function of $[Cl^-]$ and exposure time in Fig. 4.8a, b and c, respectively. Note that the scale of the z-axis (i.e. R_p)

is the same in all three plots to facilitate comparison between the three casts. In all cases, R_p (which is inversely proportional to the corrosion rate) increases with a decrease in $[Cl^-]$, as expected.²⁷ This is also true for increases in immersion time at lower $[Cl^-]$ although the influence is much more muted than that of $[Cl^-]$.

A comparison between the three casts, reveals that the R_p is highly dependent on both the casting procedure and the $[Cl^-]$. At the high $[Cl^-]$ the order of decreasing corrosion resistance is $DC > GC > SC$ while at intermediate and low concentrations this order becomes inverted. Furthermore, the difference in R_p between the three casts increases as $[Cl^-]$ decreases, with the SC alloy being approximately twice as corrosion resistant as the DC alloy in 0.003 M NaCl. Additionally, the sensitivity of R_p to changes in $[Cl^-]$ is also dictated by the casting technique, and hence the alloy microstructure with the SC alloy exhibiting the largest increase in R_p with decreasing $[Cl^-]$.

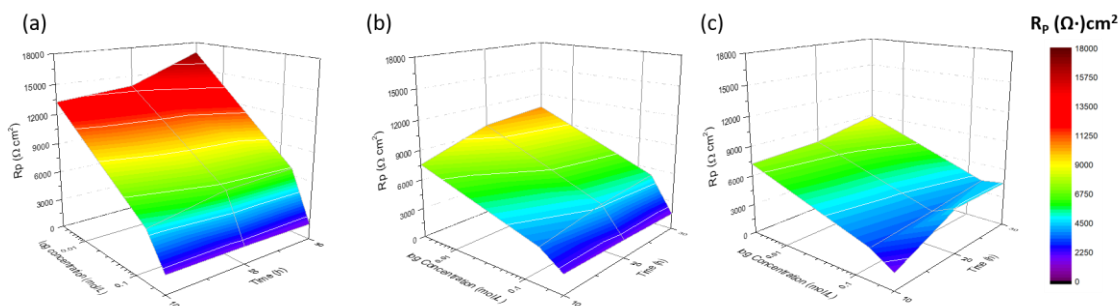


Figure 4.8: Impedance derived polarization resistance (R_p) as a function of $[Cl^-]$ (0.003 – 0.3 M) and time for a (a) SC, (b) GC and (c) DC Mg AM50 alloy. Each plot is constructed on the same axes scale for comparison. R_p values are colour coded according to the scale at the right.

4.3.2.4 Electrochemistry in Ethylene Glycol

Previously, we have demonstrated that, while the mechanism of Mg AM50 corrosion is basically the same in ethylene glycol (EG) as it is in aqueous solution, the rate is greatly reduced.⁸ This enables the individual features of the corrosion process to be more clearly separated. In the previous study, the various casts were exposed for 24h to an EG solution containing 0.003 M NaCl.

E_{CORR} measurements in aqueous solution and EG are shown in Fig 4.9. As previously observed for the SC alloy, the values measured in EG are ~ 300 mV more positive than those measured in aqueous solution. Again, as demonstrated previously, this reflects a significant decrease in corrosion rate. However, while the switch from aqueous conditions to EG has a major influence on corrosion rate, the differences in E_{CORR} between the three casts is minimal.

EIS measurements were also performed in EG containing 0.003 M NaCl, the Nyquist plots following 30 h of exposure being shown in Fig. 4.10. When the spectra are compared to those measured in aqueous solution (Fig. 4.6), there are capacitative responses

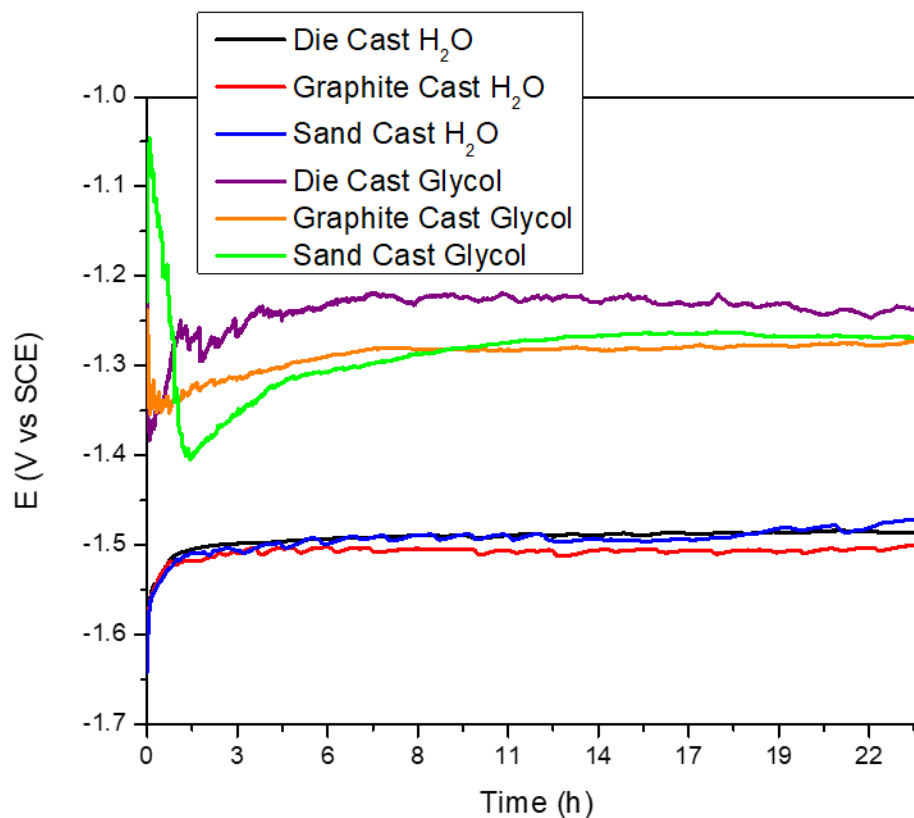


Figure 4.9: E_{CORR} measurements recorded for sand, graphite and die cast Mg AM50 alloys in an aqueous and ethylene glycol solvent, both containing 0.003 M NaCl.

but no inductive response. The response at high frequency has been tentatively ascribed to the dielectric properties of the solvent and/or the cell geometry. The two additional capacitive responses can be attributed to the same processes which occur in aqueous solution. Thus, the intermediate response can be assigned to the interfacial charge transfer process (R_1/C_1) and the lower frequency response to the transport properties of the MgO/Mg(OH)₂ corrosion product layer. The absence of any low frequency inductive response can be attributed to both the protectiveness of the corrosion product and the inability to stabilize the adsorbed species ($Mg(OH)_{ads}^+/MgOH_{ads}$) in a solution with limited H₂O content

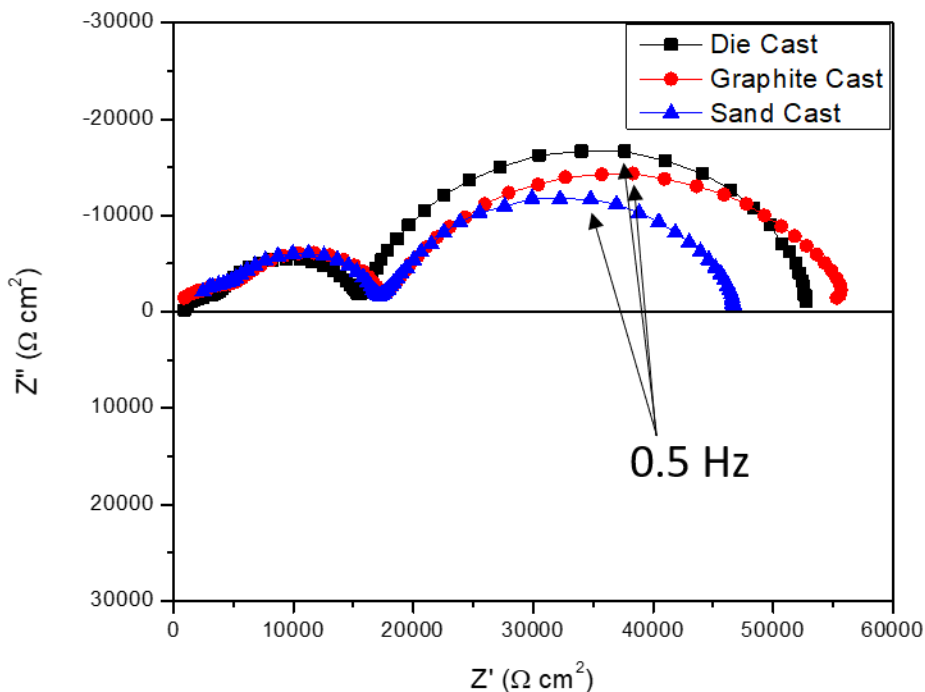


Figure 4.10: Nyquist plots for sand, graphite and die cast Mg AM50 alloys recorded in ethylene glycol containing 0.003 M NaCl following 30 h of immersion.

The intercept of the mid-frequency capacitive response is in the 16 to 18 $\text{k}\Omega\cdot\text{cm}^2$ range which is only slightly higher than the values obtained in aqueous solution at this $[\text{Cl}^-]$, Fig. 4.6, suggesting the kinetics of the interfacial charge transfer process are only slightly slower in the EG solution. By contrast, the mid-frequency capacitive loop, which is indicative of the film properties, in particular its ability to suppress the transport of Mg^{2+} yields a considerably higher value of R_p (47 to 55 $\text{k}\Omega\cdot\text{cm}^2$) compared to the values obtained in aqueous solution (6 to 9 $\text{k}\Omega\cdot\text{cm}^2$).

This is not surprising since the hydration of Mg^{2+} would be expected to be suppressed by the limited availability of H_2O . These results demonstrate that while the amount of H_2O may be restricted, it is sufficient to maintain the interfacial corrosion

process consistent with our previous observation⁸ that the interfacial reaction of the SC alloy is very sensitive to the H₂O content of the EG. While the R_P value appears slightly dependent on the alloy cast, a more extensive investigation is required to demonstrate whether or not this difference is real. However, our previous study⁸ demonstrated that H₂O present in the EG is preferentially reduced on Al-Mn IMPs as indicated by the accumulation of Mg(OH)₂ deposits at these locations. While microgalvanic coupling of these IMPs to the Mg matrix would be severely restricted by the low ionic strength in the present experiment, it would be most efficient on the SC alloy.

4.4 Discussion

The goal of this project is to investigate the effect of casting procedure on the corrosion of the Mg AM50 alloy. Since the application of EIS to study the corrosion of Mg and its alloys is well documented²³⁻²⁵, this technique is used to extract R_P values for each alloy as a function of [Cl⁻], exposure time and the nature of the electrolyte solvent. R_P was chosen since this parameter can be used to calculate the corrosion rate using the Stern-Geary relationship, Equation (3),

$$i_{CORR} = \frac{\beta_a \beta_c}{2.303 R_P (\beta_a \beta_c)} \quad (3)$$

providing the Tafel slopes (β_a and β_c) for the anodic and cathodic reactions, respectively, are known. However, determining meaningful Tafel slopes for Mg corrosion is difficult and, as a result, a wide range of β values is available throughout the literature. Their use would lead to large variations in i_{CORR} values.³⁰ As a consequence of these uncertainties, we have compared corrosion rates based on the R_P values themselves.

In high $[Cl^-]$, the combination of a decrease in E_{CORR} (Fig. 4.2(a)) with an increase in corrosion rate (decrease in R_P , Fig. 4.8) as the alloy microstructure coarsens (i.e. from DC to GC to SC) indicates control of the corrosion rate by the rate of the cathodic reaction (H_2O reduction) as the segregation of IMPs and β -phase occurred (as indicated by the micrographs and EDX spectra, Fig. 4.1). The SC and GC alloys have effectively the same corrosion rates, as indicated by the almost identical R_P values. This similarity suggests that the low density of larger Al-Mn IMPs present in the SC alloy provides a more efficient microgalvanic system than a high grain boundary density of the $Mg_{17}Al_{12}$ β -phase present in the GC alloy. The DC alloy exhibits the highest corrosion resistance in high $[Cl^-]$ which increases slightly with exposure time. The EIS response indicates that this increase with time can be attributed to the improved protective properties of the oxide/hydroxide film. Given the more uniform distribution of Al in the DC alloy, a likely explanation for the improved film resistance is the accumulation of Al at the Mg/oxide interface, a feature demonstrated to enhance corrosion resistance.^{5,17}

As the $[Cl^-]$ is decreased, the corrosion rate sequence inverts to the order $SC < GC < DC$ indicating a decrease in the efficiency of microgalvanic corrosion. Furthermore, as the extent of segregation to first β -phase (GC) and then Al-Mn IMPs (SC) increases the sensitivity of the rate to $[Cl^-]$ also increases with the range of R_P values exhibited for the SC alloy becoming approximately twice as large as those exhibited by the DC and GC alloys over the same $[Cl^-]$ range. This confirms that the nature and distribution of microgalvanically-coupled cathodes is a significant determinant of corrosion resistance. The importance of these cathodes is further emphasized by the measurements in EG, which

demonstrated that by limiting the concentration of the cathodic reagent (H_2O), the effects of microgalvanic coupling could be effectively neutralized.

The EIS results offer a tenable explanation for the apparent increased importance of microgalvanic coupling as $[\text{Cl}^-]$ decreases, an observation which appears counter-intuitive since the range of galvanic coupling would be reduced. As the $[\text{Cl}^-]$ decreases, the increase in size of the two capacitive responses in the EIS spectra with time indicates that the dominant influence on corrosion behaviour is the microgalvanic re-enforcement of the oxide growth process. The increase in film resistance, indicated by the increase in R_2 (Table 4.1) also leads to an increase in charge transfer resistance (R_1 in Table 4.1) demonstrating that the improved quality of the oxide/hydroxide film leads to an enhanced suppression of the interfacial charge transfer process. That the protectiveness of the film increases with exposure time reflects the less aggressive effect of Cl^- at lower $[\text{Cl}^-]$. The importance of film properties in suppressing the corrosion rate is confirmed by the very large increase in film resistance on switching to an EG solution.

4.5 Conclusions

The microstructure of the AM50 alloy is very dependent on the cooling rate during casting. When the alloy is rapidly cooled by die casting segregation into secondary phases is minor with the Al and Mn contents remaining widespread. A decrease in cooling rate using graphite casting leads to the formation of $\text{Mg}_{17}\text{Al}_{12}$ β -phase evenly distributed along grain boundaries with some Al retained in a eutectic phase extending into the Mg matrix

from the grain boundaries. A further decrease in cooling rate using sand casting leads to extensive segregation of Al and Mn into widely distributed intermetallic particles.

In concentrated chloride solutions, when the formation of an oxide/hydroxide film offers minimal protection, microgalvanic corrosion is more effectively driven by microgalvanic coupling of the Al-Mn intermetallic particles to the α -Mg matrix than to the β -phase. For the rapidly cooled die cast alloy, some protection of the matrix is afforded by the film. This protection may be a result of the accumulation of the uniformly distributed Al to form a protective layer at the oxide/alloy interface.

At low chloride concentrations the corrosion rate of the rapidly cooled SC alloy becomes significantly greater than that of the more slowly cooled alloys. This can be attributed to the microgalvanically re-enforced formation of a more protective film.

4.6 References

- (1) Avedesian, M. M.; Baker, H. *Magnesium and Magnesium Alloys*; ASM Specialty Handbook; 1999.
- (2) Abbott, T. B. Magnesium: Industrial and Research Developments Over the Last 15 Years. *Corrosion* **2015**, *71* (2), 120–127. <https://doi.org/10.5006/1474>.
- (3) Eliezer, D.; Aghion, E.; Froes, F. H. (Sam). Magnesium Science, Technology and Applications. *Adv. Perform. Mater.* **1998**, *5* (3), 201–212. <https://doi.org/10.1023/A:1008682415141>.
- (4) Esmaily, M.; Svensson, J. E.; Fajardo, S.; Birbilis, N.; Frankel, G. S.; Virtanen, S.; Arrabal, R.; Thomas, S.; Johansson, L. G. Fundamentals and Advances in Magnesium Alloy Corrosion. *Prog. Mater. Sci.* **2017**, *89*, 92–193. <https://doi.org/10.1016/j.pmatsci.2017.04.011>.
- (5) Asmussen, R. M.; Binns, W. J.; Jakupi, P.; Shoesmith, D. Microstructural Effects on Corrosion of AM50 Magnesium Alloys. *J. Electrochem. Soc.* **2014**, *161* (10), C501–C508.
- (6) Ma, Y.; Zhang, J.; Yang, M. Research on Microstructure and Alloy Phases of AM50 Magnesium Alloy. *J. Alloys Compd.* **2009**, *470* (1–2), 515–521. <https://doi.org/10.1016/j.jallcom.2008.03.047>.
- (7) Neil, W. C.; Forsyth, M.; Howlett, P. C.; Hutchinson, C. R.; Hinton, B. R. W. Corrosion of Magnesium Alloy ZE41 – The Role of Microstructural Features. *Corros. Sci.* **2009**, *51* (2), 387–394. <https://doi.org/10.1016/j.corsci.2008.11.005>.
- (8) Asmussen, R. M.; Binns, W. J.; Jakupi, P.; Dauphin-Ducharme, P.; Tefashe, U. M.; Mauzeroll, J.; Shoesmith, D. Reducing the Corrosion Rate of Magnesium Alloys Using Ethylene Glycol for Advanced Electrochemical Imaging. *Corros. Sci.* **2015**, *93*, 70–79. <https://doi.org/10.1016/j.corsci.2015.01.011>.
- (9) Song, G. L. *Corrosion of Magnesium Alloys*; Elsevier, 2011.
- (10) Lindström, R.; Svensson, J.-E.; Johansson, L.-G. The Influence of Carbon Dioxide on the Atmospheric Corrosion of Some Magnesium Alloys in the Presence of NaCl. *J. Electrochem. Soc.* **2002**, *149* (4), B103–B107. <https://doi.org/10.1149/1.1452115>.
- (11) Nordlien, J. H.; Nisancioglu, K.; Ono, S.; Masuko, N. Morphology and Structure of Water-Formed Oxides on Ternary MgAl Alloys. *J. Electrochem. Soc.* **1997**, *144* (2), 461–466. <https://doi.org/10.1149/1.1837432>.
- (12) Volovitch, P.; Serdechnova, M.; Ogle, K. Aqueous Corrosion of Mg-Al Binary Alloys: Roles of Al and Mg. *Corrosion* **2012**, *68* (6), 557–570. <https://doi.org/10.5006/i0010-9312-68-6-557>.
- (13) Liu, M.; Uggowitzer, P. J.; Nagasekhar, A. V.; Schmutz, P.; Easton, M.; Song, G.-L.; Atrens, A. Calculated Phase Diagrams and the Corrosion of Die-Cast Mg–Al Alloys. *Corros. Sci.* **2009**, *51* (3), 602–619. <https://doi.org/10.1016/j.corsci.2008.12.015>.
- (14) Cheng, Y.; Qin, T.; Wang, H.; Zhang, Z. Comparison of Corrosion Behaviors of AZ31, AZ91, AM60 and ZK60 Magnesium Alloys. *Trans. Nonferrous Met. Soc. China* **2009**, *19* (3), 517–524. [https://doi.org/10.1016/S1003-6326\(08\)60305-2](https://doi.org/10.1016/S1003-6326(08)60305-2).
- (15) Ballerini, G.; Bardi, U.; Bignucolo, R.; Ceraolo, G. About Some Corrosion Mechanisms of AZ91D Magnesium Alloy. *Corros. Sci.* **2005**, *47* (9), 2173–2184. <https://doi.org/10.1016/j.corsci.2004.09.018>.

- (16) Südholz, A. D.; Birbilis, N.; Bettles, C. J.; Gibson, M. A. Corrosion Behaviour of Mg-Alloy AZ91E with Atypical Alloying Additions. *J. Alloys Compd.* **2009**, *471* (1), 109–115. <https://doi.org/10.1016/j.jallcom.2008.03.128>.
- (17) Danaie, M.; Asmussen, R. M.; Jakupi, P.; Shoesmith, D. W.; Botton, G. A. The Role of Aluminum Distribution on the Local Corrosion Resistance of the Microstructure in a Sand-Cast AM50 Alloy. *Corros. Sci.* **2013**, *77*, 151–163. <https://doi.org/10.1016/j.corsci.2013.07.038>.
- (18) Aung, N. N.; Zhou, W. Effect of Grain Size and Twins on Corrosion Behaviour of AZ31B Magnesium Alloy. *Corros. Sci.* **2010**, *52* (2), 589–594. <https://doi.org/10.1016/j.corsci.2009.10.018>.
- (19) Ralston, K. D.; Birbilis, N. Effect of Grain Size on Corrosion : A Review. *Corrosion* **2010**, *66* (7), 075005–075013.
- (20) Zhao, M.-C.; Liu, M.; Song, G.; Atrens, A. Influence of the β -Phase Morphology on the Corrosion of the Mg Alloy AZ91. *Corros. Sci.* **2008**, *50* (7), 1939–1953. <https://doi.org/10.1016/j.corsci.2008.04.010>.
- (21) Zhang, T.; Shao, Y.; Meng, G.; Cui, Z.; Wang, F. Corrosion of Hot Extrusion AZ91 Magnesium Alloy: I-Relation between the Microstructure and Corrosion Behavior. *Corros. Sci.* **2011**, *53* (5), 1960–1968. <https://doi.org/10.1016/j.corsci.2011.02.015>.
- (22) Scully, J. R. Polarization Resistance Method for Determination of Instantaneous Corrosion Rates. *Corrosion* **2000**, *56* (2), 199–218. <https://doi.org/10.5006/1.3280536>.
- (23) King, A. D.; Birbilis, N.; Scully, J. R. Accurate Electrochemical Measurement of Magnesium Corrosion Rates; a Combined Impedance, Mass-Loss and Hydrogen Collection Study. *Electrochimica Acta* **2014**, *121*, 394–406. <https://doi.org/10.1016/j.electacta.2013.12.124>.
- (24) Shkirskiy, V.; King, A. D.; Gharbi, O.; Volovitch, P.; Scully, J. R.; Ogle, K.; Birbilis, N. Revisiting the Electrochemical Impedance Spectroscopy of Magnesium with Online Inductively Coupled Plasma Atomic Emission Spectroscopy. *ChemPhysChem* **2014**, *16* (3), 536–539. <https://doi.org/10.1002/cphc.201402666>.
- (25) Bland, L. G.; King, A. D.; Birbilis, N.; Scully, J. R. Assessing the Corrosion of Commercially Pure Magnesium and Commercial AZ31B by Electrochemical Impedance, Mass-Loss, Hydrogen Collection, and Inductively Coupled Plasma Optical Emission Spectrometry Solution Analysis. *Corrosion* **2015**, *71* (2), 128–145. <https://doi.org/10.5006/1419>.
- (26) Zhang, J.; Fan, Z.; Wang, Y. Q.; Zhou, B. L. Effect of Cooling Rate on the Microstructure of Hypereutectic Al-Mg₂Si Alloys. *J. Mater. Sci. Lett.* **2000**, *19* (20), 1825–1828. <https://doi.org/10.1023/A:1006702709371>.
- (27) Liu, W.; Cao, F.; Chen, A.; Chang, L.; Zhang, J.; Cao, C. Effect of Chloride Ion Concentration on Electrochemical Behavior and Corrosion Product of AM60 Magnesium Alloy in Aqueous Solutions. *Corrosion* **2012**, *68* (4), 045001–1. <https://doi.org/10.5006/0010-9312-68-4-2>.
- (28) Pebere, N.; Riera, C.; Dabosi, F. Investigation of Magnesium Corrosion in Aerated Sodium Sulfate Solution by Electrochemical Impedance Spectroscopy. *Electrochimica Acta* **1990**, *35* (2), 555–561. [https://doi.org/10.1016/0013-4686\(90\)87043-2](https://doi.org/10.1016/0013-4686(90)87043-2).

- (29) Baril, G.; Blanc, C.; Pébère, N. AC Impedance Spectroscopy in Characterizing Time-Dependent Corrosion of AZ91 and AM50 Magnesium Alloys Characterization with Respect to Their Microstructures. *J. Electrochem. Soc.* **2001**, *148* (12), B489–B496. <https://doi.org/10.1149/1.1415722>.
- (30) Kirkland, N. T.; Birbilis, N.; Staiger, M. P. Assessing the Corrosion of Biodegradable Magnesium Implants: A Critical Review of Current Methodologies and Their Limitations. *Acta Biomater.* **2012**, *8* (3), 925–936. <https://doi.org/10.1016/j.actbio.2011.11.014>.

5 Physical and Electrochemical Evidence for the Role of a Mg Hydride Species in Mg Alloy Corrosion

5.1 Introduction

Despite extensive research, the fundamental corrosion mechanisms which underpin the initiation and propagation of the so-called “filiform-like” corrosion morphology seen on Mg and its alloys remain elusive. Much of the mystery surrounding Mg corrosion is attributable to its unexpected behaviour upon anodic polarization which leads to an increase in H₂ evolution with increasing anodic polarization. Historically, this phenomenon has been termed the negative difference effect (NDE) but has most recently been referred to as “anodic hydrogen evolution”. Regardless of terminology, this behaviour is diametrically opposed to the expected behaviour. Attempts to explain the NDE reach back to 1954 when Petty et al. proposed that a unipositive Mg⁺ species could account for the NDE and, thus, Mg oxidation.¹ This hypothesis was eventually adopted to explain the corrosion of Mg and its alloys.²⁻⁷ More recently, the unipositive explanation has been shown to be untenable, with no experimental or spectroscopic evidence available to demonstrate the existence of Mg⁺⁸⁻¹¹ except as a possible short-lived intermediate in the overall anodic dissolution process.

Using the scanning vibrating electrode technique (SVET) to map localized current densities on a corroding Mg surface, Williams et al.^{8,9} revealed that the advancing head of filiform-like corrosion was associated with anodic activity, while active cathodic sites were generated in its wake. This process was labelled “cathodic activation” and has been investigated and invoked extensively as the dominant mechanism for Mg corrosion.¹⁰⁻¹³ However, Fajardo et al. recently showed that topographical variations arising as a result of

the filiform-like corrosion limit the ability of the SVET to capture all the localized current associated with the filiform head. They demonstrated that the cathodic current densities measured by SVET grossly underestimated the true current calculated via gravimetric H₂ collection during anodic polarization.^{14,15} Furthermore, these studies indicated that most of the corrosion current (i_{CORR}) flowed between anode/cathode couples co-located at the advancing filiform head.

Concurrently, via H₂ collection and the judicious selection of immersion environment, several authors have proposed that a Mg hydride may be an important intermediate in the process of Mg corrosion.¹⁶⁻¹⁸ Thermodynamic calculations show that MgH₂ can exist at the corrosion potentials (E_{CORR}) encountered during Mg corrosion over the whole accessible pH range (0-14)¹⁷, although it would be expected to be unstable in H₂O via decomposition to Mg(OH)₂. In addition, studies on other light metals show that hydride plays a key role in their anodic dissolution. Using secondary ion mass spectrometry (SIMS), Adhikari and Hebert¹⁹ demonstrated the formation of AlH₃ during corrosion of Al in alkaline solutions and claimed that the anodic dissolution of the metal proceeded via a hydride surface layer, since passivation by oxide was prevented in this pH range. Similarly, hydrides were shown to be formed on crevice corroding Ti surfaces; i.e., under acidic conditions when passivation was prevented.^{20,21} Experiments in simulated crevice environments (low pH – high chloride) show that hydride formation on Ti strongly catalyzed H⁺ reduction to H₂ leading to the conversion of the surface from a metal one dominantly supporting anodic metal dissolution to a hydride-covered surface dominantly supporting the cathodic reduction of protons.²² Consequently, if the formation of a metastable hydride can be demonstrated during Mg corrosion it would offer a clear

explanation for anodic hydrogen formation while simultaneously satisfying the requirement that the anode/cathode couple be co-located. In this paper we demonstrate the formation of Mg hydride (MgH_2) and link its occurrence to the filiform-like corrosion of Mg alloys.

5.2 Experimental Procedure

5.2.1 Materials and Material Preparation

Two Mg ZEK100 alloys with different casting and processing, but nominally identical compositions (1.33Zn-0.30Zr-0.17Nd-Bal.Mg (wt%)), were used in this study. The first, a sheet alloy in F temper (as formed), supplied by General Motors (USA) with a thickness of 1.5 mm was used in electrochemical, X-ray diffraction (XRD), in situ monitoring, optical microscopy and scanning electron microscopy (SEM) experiments. The second alloy was a 0.5 cm section cut from the thin end of a wedge cast Mg ZEK100 alloy supplied by CanmetMATERIALS, Canada. Details on wedge casting are widely available in the literature^{23,24}. In brief, wedge casting is a process whereby a molten alloy is poured into a mold with the shape of an inverted isosceles triangle or wedge. As a consequence of the change in thickness of the mold there exists a gradient in the cooling rate and therefore the microstructure of the alloy as a function of position within the wedge. This wedge cast alloy was chosen for its relatively large grain size compared to the rolled alloy, which made it ideal for Dynamic Secondary Ion Mass Spectrometry (SIMS) analyses.

Mg ZEK100 F sheets were cut into 1 x 1 cm² samples and one face was tapped to enable connection to a threaded stainless steel rod for electrical connection to external circuitry. Samples for electrochemical and in situ monitoring experiments were mounted

in Struers EpoFix® epoxy and ground successively with 800, 2400 and 4000 grit SiC paper utilizing a 1:1 ethanol-to-isopropanol lubricant. Following grinding, samples were placed in a bath of anhydrous 99.5% ethanol and sonicated for ~ 1 min. Finally, samples were dried under an Ar stream and stored in a vacuum desiccator until needed. Samples for XRD and SIMS analyses were prepared in a similar manner, with two additional polishing steps. The first step utilized a 3 μm diamond abrasive applied to a Struers DP-DUR® pad, followed by sonication in anhydrous ethanol. The final step applied a 1:1 ethylene glycol-to-0.04 μm colloidal silica abrasive to a Struers OP-Chem® polishing cloth, followed by sonication in anhydrous ethanol and drying under an Ar stream, before being stored in a vacuum desiccator. The additional polishing steps were required for reliable XRD and SIMS analyses.

5.2.2 Electrochemical Experiments

Electrochemical experiments were performed in a conventional three-electrode cell, with the Mg alloy serving as the working electrode, a Pt flag as the counter electrode and a Ag/AgCl in saturated KCl reference electrode. Cathodic pre-treatments consisted of galvanostatic polarization at -5 mA/cm^2 for periods of 1, 2 and 3 hours in 0.1 M NaOH (reagent grade, 99% assay) prepared with Type-1 water ($18 \text{ M}\Omega \cdot \text{cm}^2$) at ambient temperature ($\sim 22.5 \text{ }^\circ\text{C}$) yielding a solution pH of 13. This electrolyte was selected to minimize the extent of film formation on the alloy surface thereby maximizing the extent of water reduction to promote hydride formation. The electrolyte was stirred vigorously to release H_2 bubbles from the electrode surface. Anodic polarization scans were conducted on either as-polished or pretreated samples in the same environment, with fresh electrolyte,

using a Solartron® 1287 potentiostat. Following charging, but prior to anodic polarization scans, specimens were hand-polished for ~10 s with a 3 μm anhydrous diamond paste (Struers®) to remove a thin MgO/Mg(OH)_2 film. Samples were then immersed in fresh electrolyte (0.1 M NaOH) at E_{CORR} for 5 min before anodic polarization scans commenced. The working electrode potential was increased from E_{CORR} at a rate of 10 mV/min until a potential of +750 mV vs E_{CORR} was reached.

5.2.3 X-ray Diffraction Analysis

XRD analysis was performed on both as-polished and pretreated Mg ZEK100 F. Pretreated samples were analyzed in a glancing angle configuration. The pretreated samples were subjected to cathodic galvanostatic treatment as described in section 2.2 for 1 h. Samples were quickly rinsed with ethanol and dried in Ar before insertion into the X-ray diffractometer. XRD analysis was conducted using an Inel CPS 120 Diffractometer with a $\text{Cu K}\alpha$ X-ray radiation source running ACQ and Match software.

5.2.4 Scanning Electron (SEM) and Optical Microscopy

SEM was performed with a LEO (Zeiss) 1540XB instrument using secondary and backscattered electrons as indicated throughout. A beam energy of 10 keV was used for energy dispersive (X-ray) analyses. A Zeiss stereo Discovery (V8) optical microscope was used to capture optical images.

5.2.5 Dynamic Secondary Ion Mass Spectrometry

SIMS analysis was performed on as-polished, cathodically pretreated and naturally corroded wedge cast specimens. Each experiment was conducted on three different areas of each sample to ensure that observations were consistent and reproducible. As-polished samples were fine polished using the procedure described in section 2.1 prior to SIMS analysis. Pretreated samples were subjected to the same cathodic treatment as described for the XRD experiments (section 2.3) but in 0.1 M NaOH made with D₂O. Similarly, naturally corroded samples were immersed in a 0.03 M NaCl solution made with D₂O for 36 h. The use of D₂O generated a greater signal-to-noise ratio in SIMS analyses compared to immersion in H₂O and allowed for discrimination between H, which is naturally occurring from a number of sources, and D, which could only originate from the electrolyte. Pretreated samples were analyzed directly following the cathodic pretreatment. Naturally corroded samples were immediately submerged in liquid N₂ for two minutes to prevent degradation of any hydride as a result of H₂O exposure. Subsequently, each sample was fine polished for approximately 30 s with anhydrous 3 μm diamond paste to remove the general surface hydroxide. This exposed the underlying metal surface to optimize the sputtering capability of the SIMS instrument. A modified CAMECA IMS-3e ion microscope was used, with a 5.5 eV Cs⁺ ion beam rastered over a 250 x 250 μm² area of the surface to collect secondary ions within a 150 μm diameter spot for imaging. The spatial and depth resolution of this instrument are approximately 1 μm and 6 nm, respectively.

5.2.6 In situ Corrosion Monitoring

In situ monitoring was performed with a Samsung Galaxy S6 cellular phone camera. Mg ZEK100 F samples, both as-polished and cathodically pretreated, were quickly rinsed with ethanol and dried in Ar following preparation and then immersed in a 0.03 M NaCl solution mixed with Type-1 water ($18 \text{ M}\Omega \cdot \text{cm}^2$). The camera recorded the corrosion processes from above for 30 min.

5.3 Results

5.3.1 Electrochemical Characterization of As-polished and Cathodically Pretreated Mg ZEK100 F

Fig. 5.1a shows anodic polarization curves recorded on the Mg ZEK100 F sheet alloy in 0.1 M NaOH for an as-polished specimen and specimens subjected to cathodic treatment for periods of 1, 2 and 3 hours. A magnification of the area within the box in Fig. 1a is shown in Fig. 1b. The as-polished specimen exhibited a typical active-to-passive transition over the potential range from the E_{CORR} to approximately $-1.2 \text{ V}_{\text{Ag}/\text{AgCl}}$, followed by an approximately constant anodic current density as the overpotential increased. This was consistent with passive behaviour and expected based on the Pourbaix diagram for the Mg system at $\text{pH} = 13$.²⁵

Cathodically charged specimens showed different behaviour, Fig. 1(a and b). The E_{CORR} prevailing prior to polarization was significantly more positive ($\sim -1.5 \text{ V}_{\text{Ag}/\text{AgCl}}$) than that observed on the freshly polished specimens. A similar shift in E_{CORR} during corrosion experiments on the AZ31 alloy was shown by SVET to be accompanied by an increase in

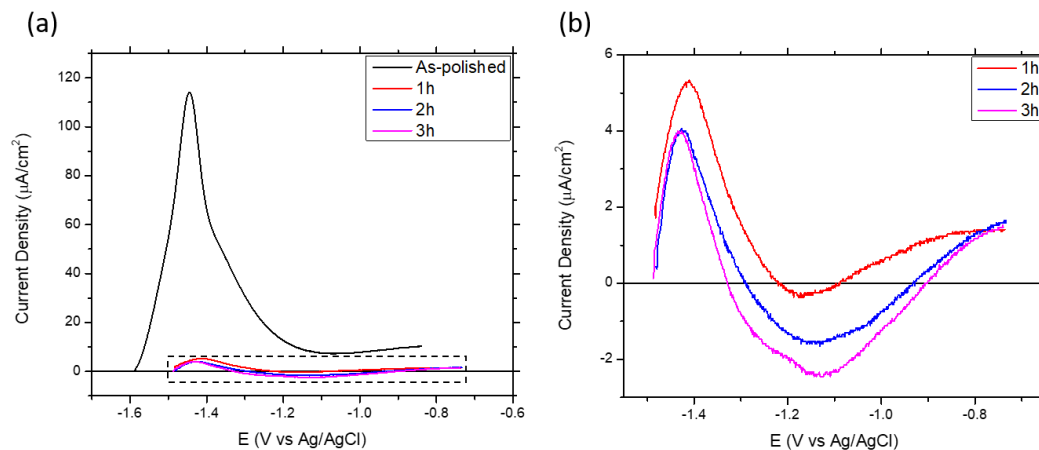


Figure 5.1: (a) Anodic polarization scans performed on rolled Mg ZEK100 sheet alloy in 0.1 M NaOH for an as-polished and galvanostatically treated specimens. Galvanostatic treatment consisted of $-5 \text{ mA}/\text{cm}^2$ in 0.1 M NaOH for various intervals. (b) shows the area indicated in (a) in greater detail.

the area of the surface functioning as an activated cathode.²⁶ On anodic polarization, only a shallow active/passive transition was observed with a peak current ~ 23 times lower than observed on the as-polished specimen. A further increase in potential led to a switch in the polarity of the current, i.e., the observation of cathodic current densities. On further increasing the potential, an anodic current was re-established. The presence of this negative current window, observed as the potential was made more positive, indicated that the cathodic pre-treatment activated the alloy surface for H_2O reduction to H_2 . Furthermore, as the duration of the cathodic pre-treatment was increased, both the width of the cathodic window and the maximum value of the cathodic current increased, accompanied by a decrease in the maximum anodic current observed at lower potentials, Fig. 1b. These results showed the magnitude of the NDE was amplified by increasing the total amount of cathodic charge passed during the pre-treatment. This behaviour is similar to the polarity switch observed on Ti exposed to acidic conditions, when it was demonstrated that active

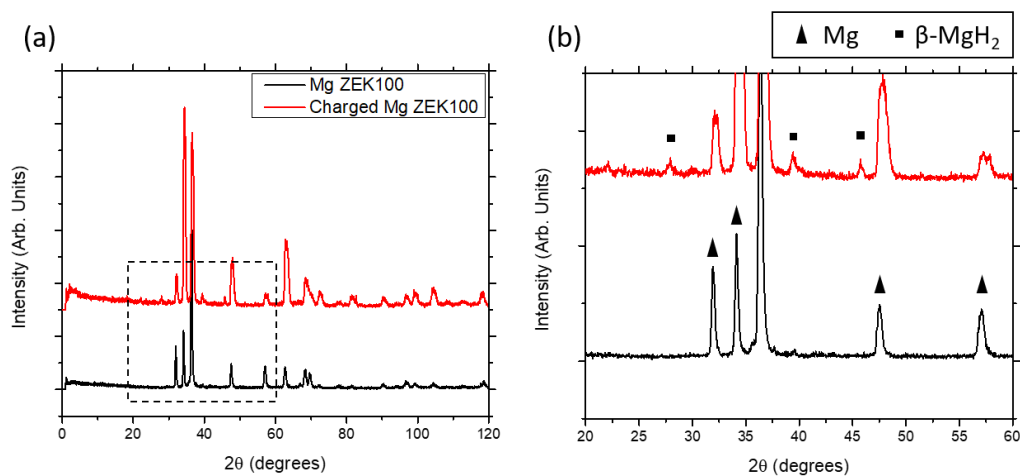


Figure 5.2: (a) XRD spectra recorded on an as-polished Mg ZEK100 sheet specimen (black) and the same alloy pre-treated at -5 mA/cm^2 for 2 h. (b) Higher magnification image of the black box shown in (a).

anodically dissolving metal sites coexisted with hydrided locations which supported cathodic current,²² and that the formation of the hydrided surface converted surface locations initially dominated by anodic dissolution to sites which dominantly supported H^+ reduction to H_2 .

5.3.2 Physical Characterization of Cathodically Pretreated Alloys

To confirm whether or not the formation of hydride can account for this behaviour, XRD analyses were performed on both charged and uncharged Mg ZEK100 F specimens. XRD spectra recorded on as-polished and cathodically-charged (1 h) ZEK100 F specimens are shown in Fig. 5.2a. The area within the box in Fig. 5.2a is magnified in Fig. 5.2b. Both spectra exhibited peaks at 2θ values corresponding to those expected for Mg metal (indicated by triangles). The spectrum recorded on the charged specimen contained additional peaks, which are clearly visible in Fig. 5.2b (indicated by squares). These small

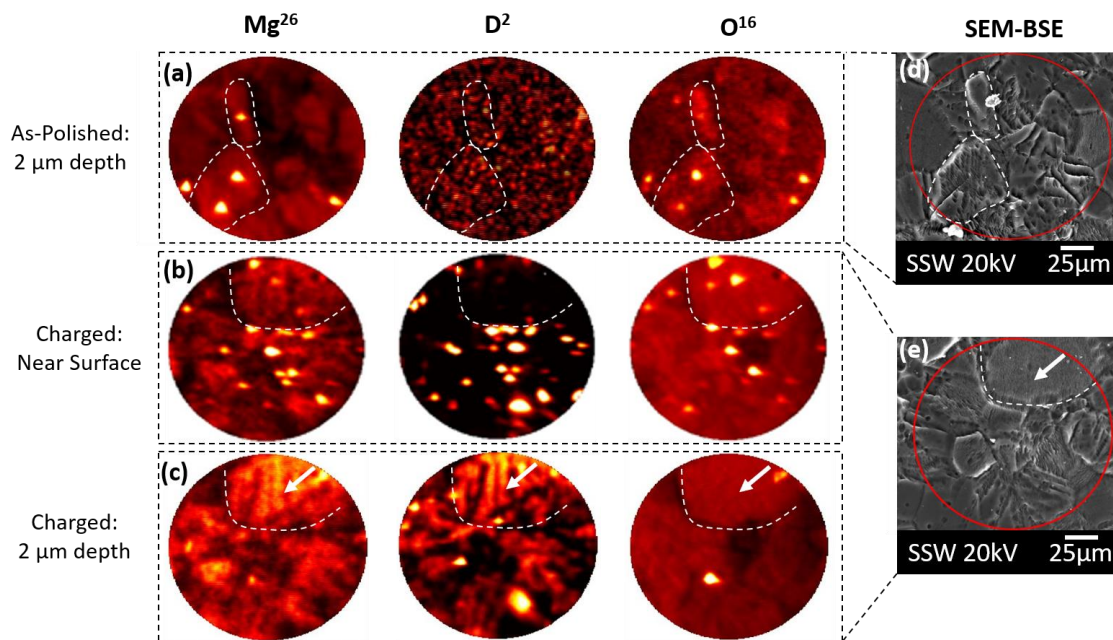


Figure 5.3: (a) Dynamic SIMS isotopic maps for Mg²⁶, D² and O¹⁶ ~2 μm below the surface of an as-polished, wedge cast Mg ZEK100 specimen with the corresponding post-SIMS SEM micrograph, (d). Similar elemental maps are shown for a sample charged for 1 h in 0.1 M NaOH made with D₂O in the (b) near surface region and (c) ~2 μm below the surface with the corresponding post-SIMS SEM micrograph in (e). Dashed white lines indicate the corresponding grain boundary in each image.

but significant peaks appear at 2θ values expected for MgH₂ (JCPDS 04-013-2314), demonstrating the presence of MgH₂, consistent with our claim that its presence was responsible for the cathodic activity observed under anodic polarization, Fig. 5.1. The detection of hydride was also consistent with the increase in duration and magnitude of the current in the cathodic current window with increasing cathodic charge in the pre-treatment, since the extent of MgH₂ formation would rely on the duration of surface exposure to the products of water reduction (in particular atomic H).

To locate the MgH₂, SIMS imaging was used to yield elemental maps as a function of sputter depth. Maps for ²⁶Mg, ²D and ¹⁶O, recorded after sputtering 2 μm from the surface of the as-polished wedge cast Mg ZEK100 specimen, are shown in Fig. 5.3a, and

the corresponding SEM-BSE images of the sputtered surface in Fig. 5.3d. The ^{26}Mg isotope was preferred to the more abundant ^{24}Mg to avoid overlap with C_2^+ peaks, which have the same mass-to-charge ratio as $^{24}\text{Mg}^+$. ^2D was chosen for its diminutive natural abundance (0.015 %) to ensure a high signal-to-noise ratio, unachievable with the ubiquitous ^1H isotope. As shown in Fig. 5.3a, an as-polished specimen exhibited a low background ^2D signal while the ^{26}Mg and ^{16}O maps correlated with the grain structure of the alloy shown by the SEM micrograph. Corresponding grain boundaries are indicated with dashed white lines. Similar analyses were performed on a pre-charged specimen after minimal sputtering (to reveal the near surface region), Fig 5.3b, and after removal of 2 μm of the surface, Fig 5.3c and Fig 5.3e. In the near-surface region, each isotope exhibited several intense regions, which generally corresponded with each other, indicating the presence of $\text{Mg}(\text{OD})_2$ on the surface of the alloy. Approximately 2 μm below the surface a different picture emerged, Fig 5.3c and 5.3e. Maps for ^{26}Mg and ^2D showed a close correspondence, particularly in the regions which produced the most intense signal, one such area being indicated with white arrows. Conversely, the intensity of the ^{16}O signal remained uniform, except for two small bright spots. This indicated that, at this depth, striations of MgD_2 existed, localized within grains which coexist within a more homogeneously distributed $\text{MgO}/\text{Mg}(\text{OD})_2$ film.

5.3.3 In situ Monitoring of Corrosion

To determine the effect of the hydride on corrosion, an as-polished specimen and a charged sample were monitored, in situ, during immersion in the chloride solution. Fig. 5.4 shows images of the Mg ZEK100 F sheet alloy, recorded in situ, following 0.5, 1, 3, 5 and 20 min of immersion on a specimen subjected to cathodic charging for 1 h, a-e, and for an

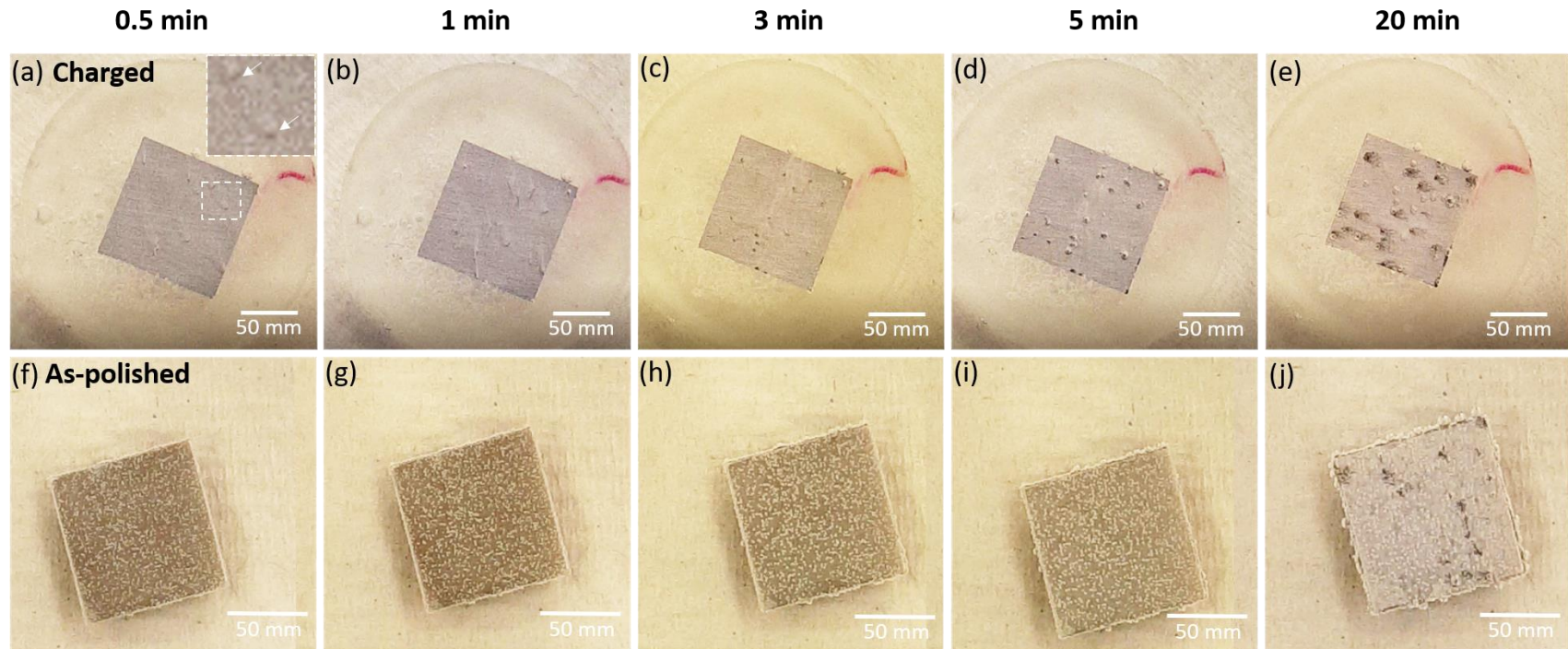


Figure 5.4: *In-situ* images recorded for a sample subjected to 1 h cathodic pre-treatment and immersed in 0.03 M NaCl for (a) 0.5, (b) 1, (c) 3, (d) 5 and (e) 20 min. The inset in (a) shows the area indicated with a dashed white line in greater detail and the arrows show black initiation sites for filiform-like corrosion. (f-j) show the corresponding images for an as-polished Mg ZEK100 sheet alloy in the same immersion environment at identical intervals.

as-polished specimen, f-j. Immediately upon immersion, the charged specimen evolved fine streams of H_2 from small black regions on the surface, Fig. 5.4a. Following 1 min of immersion the black regions increased in size and number, while rapidly and constantly evolving gas at their margins. After 3 min of immersion the blackened regions increased in size and remained the only visible sites for H_2 evolution. As time progressed, 5 and 20 min, large gas bubbles collected on the interior of the black regions, while the advancing front was the location of the rapid release of a fine stream of bubbles. Conversely, when exposed to the same environment, the as-polished specimen behaved very differently. In contrast to the charged specimens, no intense localized H_2 evolution was observed from black regions. Rather, hydrogen bubbles collected at cathodic sites across the alloy surface. Up to 5 min of immersion caused little change in the alloy surface, except for a gradual whitening due to the formation of a $Mg(OH)_2$ film. After ~10 min of immersion (not shown) the as-polished specimen began to behave similarly to the charged specimen by developing several dark regions which exhibited intense H_2 evolution along their leading edge. Following 20 min of immersion the typical filiform-like morphology was exhibited, Fig. 5.4j.

To confirm that corrosion proceeds in a filiform-like manner and to compare the corrosion morphology of the as-polished and pretreated samples post-immersion, optical and SEM microscopy were performed on the samples following in situ monitoring, Figure 5.5. Optical micrographs of the pretreated and as-polished samples following immersion are shown in Fig. 5.5a and 5.5c, respectively, revealing the presence of long, black corrosion filaments. SEM micrographs of the same samples, Fig. 5.5b and 5.5d, confirm the existence of corrosion filaments filled with corrosion products, as observed in previous

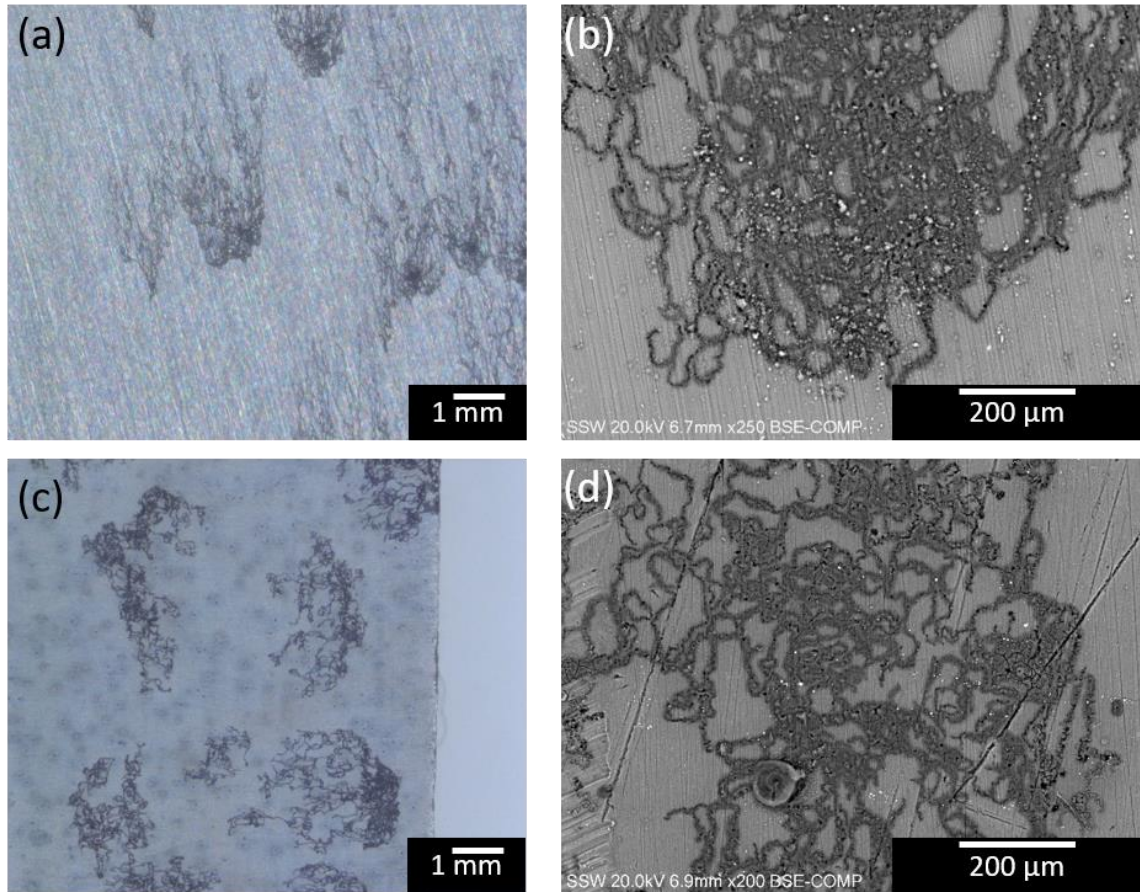


Figure 5.5: (a) Optical and (b) SEM micrographs of the filiform-like corrosion which occurred on a sample subjected to 1 h cathodic pre-treatment and immersed in 0.03 M NaCl for 30 min. (c) and (d) are a similar set of micrographs showing a similar filiform-like corrosion occurring on an as-polished Mg ZEK100 F sample in 0.03 M NaCl for 30 min.

studies conducted on Mg ZEK100 F, other Mg alloys and pure Mg^{11,27-30}, confirming that the general form of corrosion is not dictated by alloy content or the presence of secondary phases. Interestingly, despite the specimens being immersed in a NaCl solution for the same length of time, the optical micrograph of the pretreated sample shows that polishing lines persisted on the uncorroded regions while the as-polished sample exhibited a white surface layer, most likely Mg(OH)₂. This suggests that a much thicker corrosion product layer persisted on the as-polished sample compared to the pretreated sample following immersion. Speculatively, we suggest that this corrosion product film growth period, which

preceded the onset of filiform-like corrosion at open circuit, facilitated the formation of hydrides. However, more extensive physical characterization of the metal/film interface is required to substantiate such a claim. This is currently underway.

5.3.4 Physical Characterization of Mg ZEK100 Corroded at E_{CORR}

To this point, ZEK100 alloys were polarized cathodically in alkaline solution to maximize the extent of hydride production, thereby facilitating electrochemical and physical characterization. To investigate whether hydride formation occurs under natural corrosion conditions (at E_{CORR}), wedge cast Mg ZEK100 samples were immersed in the chloride solution made with D_2O for 36 h. In this solution filiform-like corrosion initiates and propagates.

Two separate areas of the filiform corrosion morphology were analyzed by dynamic SIMS. The first was an “aged” section of the filament (terminology coined by Cano et al. to designate a filament section which had been in contact with solution for an extended period of time as opposed to the filament tip, which is transient).²⁹ In our case, aged refers to a section which was significantly displaced (i.e., > 2 mm) from the tip of a corrosion filament. Isotopic maps for ^2D , ^{16}O , ^{26}Mg and ^{64}Zn , recorded with dynamic SIMS, for an aged filament are shown in Figure 5.6. White dashed lines indicate the outer edges of the corrosion filament (i.e., the filament occupies the central portion of the field of view) at the alloy surface prior to sputtering.

Following minimal sputtering of $\sim 2 \mu\text{m}$, there was a strong correlation between the ^2D , ^{16}O , and ^{26}Mg signals outside of the corrosion filament on the uncorroded metal surface, indicating the presence of a $\text{Mg}(\text{OD})_2$ film. Likely, this is a remnant of the hydroxide

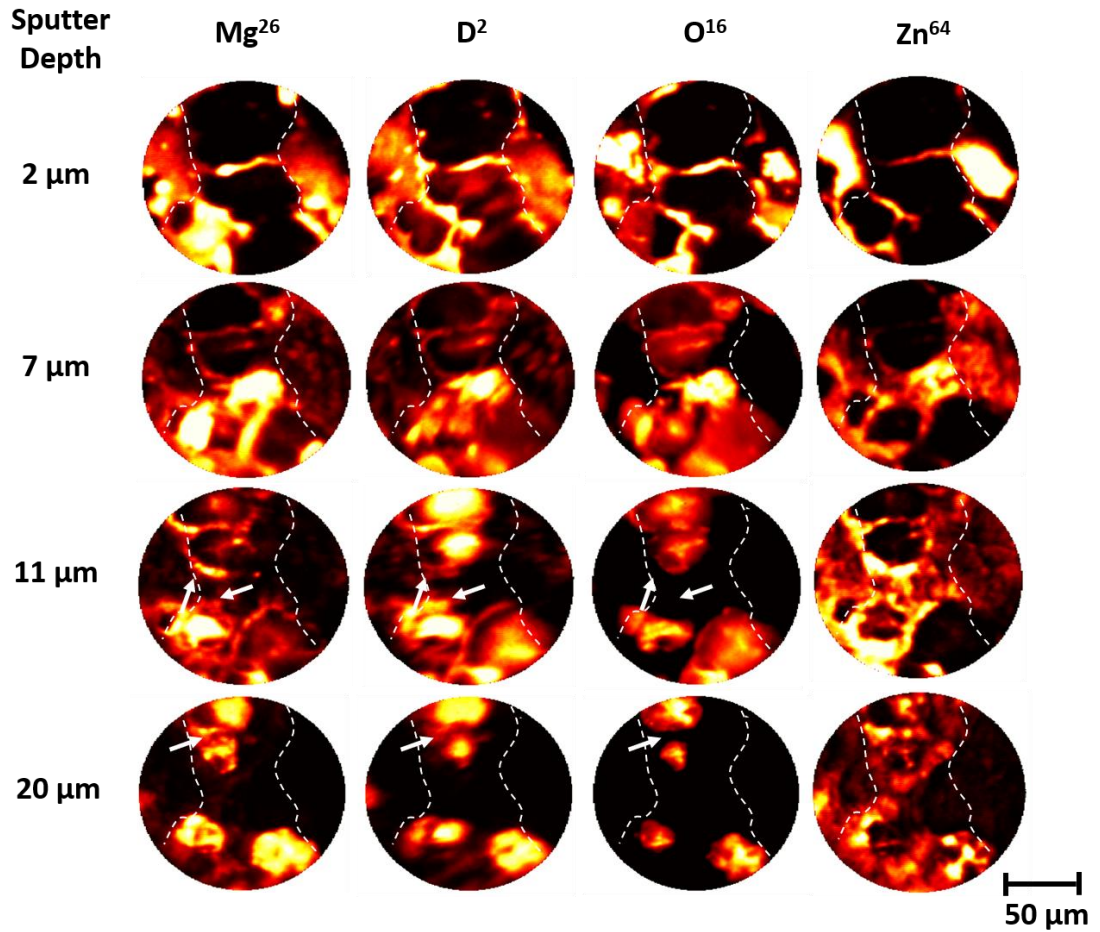


Figure 5.6: Dynamic SIMS elemental maps for Mg^{26} , D^2 , O^{16} and Zn^{64} at approximately 2, 7, 11 and 20 μm depth of an aged corrosion filament formed on a wedge cast Mg ZEK100 alloy during free corrosion in a 0.03 M NaCl solution made with D_2O . The area contained by the dashed white lines indicates the location of the corrosion filament.

formed on the surface of the alloy following the brief polishing which preceded the SIMS analysis. At this depth, the strong localized ^{64}Zn signals can be attributed to the presence of the Zn-rich T-phase ($\text{Mg}_7\text{Zn}_3\text{Nd}$),^{31,32} which decorates the alloy grain boundaries, Figure 5.7. Much of the corrosion filament interior yielded little signal except for a few intense regions which correlate well for each of the four isotopes analyzed. Given that Zn segregates into the grain boundaries of this alloy, these signals likely demarcate Mg grains.

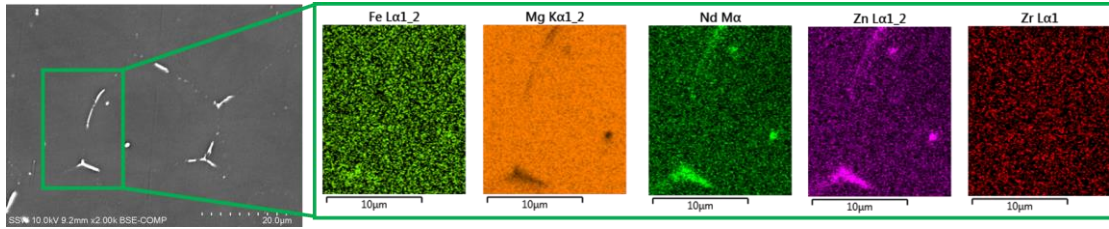


Figure 5.7: SEM micrograph and corresponding EDX elemental maps recorded on a polished Mg ZEK100 wedge cast alloy. The image shows that a Zn and Nd-rich phase segregates to grain boundaries.

At a sputtering depth of $\sim 7 \mu\text{m}$, ^2D , ^{16}O and ^{26}Mg signals generally correlate with one another on the interior of the corrosion filament, again consistent with the presence of hydroxide. Outside of the corrosion filament, however, ^2D is visible and correlates with ^{26}Mg at locations where no ^{16}O signal is exhibited. At this depth, the ^{64}Zn signal is more disperse, and could indicate the presence of a thin Zn-enriched layer which has been shown to form on an AZ31 alloy with similar Zn content.²⁹ A similarly enriched Al layer has been shown to form at the alloy/oxide interface on the AM50 alloy³³. At sputtering depths of ~ 11 and $20 \mu\text{m}$, the ^{16}O signal diminishes and becomes more localized, indicating that the SIMS analysis has nearly reached the bottom of the corrosion filament. For the most part, ^2D and ^{26}Mg exhibit a similar trend and coexist with ^{16}O , but not exclusively. Various regions at both depths (one such region indicated with white arrows) are enriched in both ^2D and ^{26}Mg but devoid of ^{16}O , indicating the presence of a hydride. Notably, areas rich in ^2D and ^{26}Mg occur at the margins of ^{16}O enrichment. Given the rough topography which occurs at the filament/base metal interface, this suggests that a phase rich in ^2D lies below the hydroxide present in the filament. To confirm that the sputtering process had reached the bottom of the corrosion filament, the crater created by the dynamic SIMS analysis was imaged by SEM and mapped by EDX.

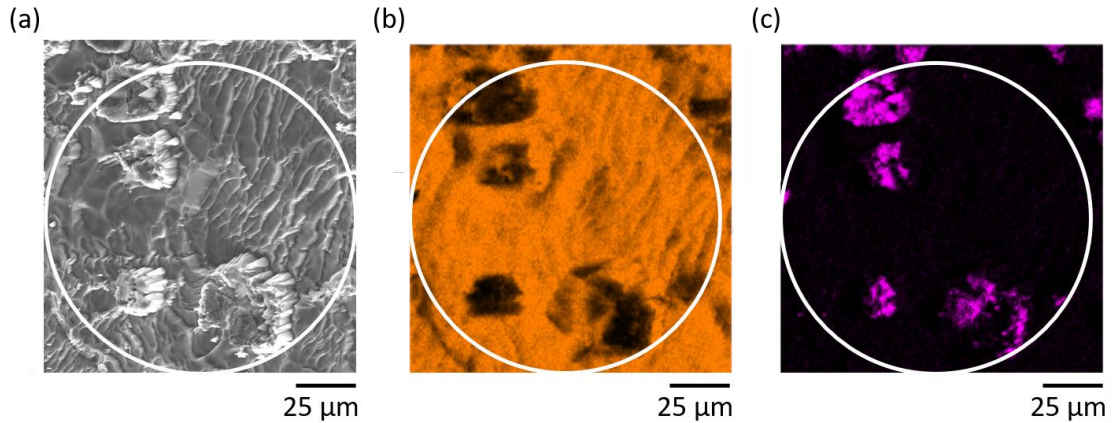


Figure 5.8: (a) SEM micrograph of the crater left after dynamic SIMS analysis of an aged corrosion filament shown in Figure 6. (b) and (c) are the corresponding EDX elemental maps for Mg and O, respectively.

Figure 5.8a shows a SEM micrograph, recorded in secondary electron mode, of the area analyzed with dynamic SIMS, along with the corresponding EDX maps for Mg and O, Figure 8b and c, respectively. Small features visible in the SEM micrograph correspond with the O elemental map and occur in the same pattern as the ^{16}O maps recorded by SIMS at approximately 20 μm depth. The morphology and occurrence of O are indicators of the hydroxide, which occupies corrosion filaments. This, combined with the fact that most of the crater exhibits a strong Mg signal, indicates that the base metal underneath most of the corrosion filament has been exposed. A similar SIMS analysis was conducted on a filament tip.

Figure 5.9 shows SIMS isotopic maps for ^2D , ^{26}Mg , ^{16}O and ^{64}Zn as a function of the approximate sputter depth, recorded at the leading edge of a corrosion filament. The location of the original position of the filament edge is indicated by the ^{16}O signal. After sputtering to a depth of $\sim 6 \mu\text{m}$ there is a strong correlation between the ^2D , ^{26}Mg and ^{64}Zn signals at the margins of the filament tip where no ^{16}O signal is observed. Outside of the

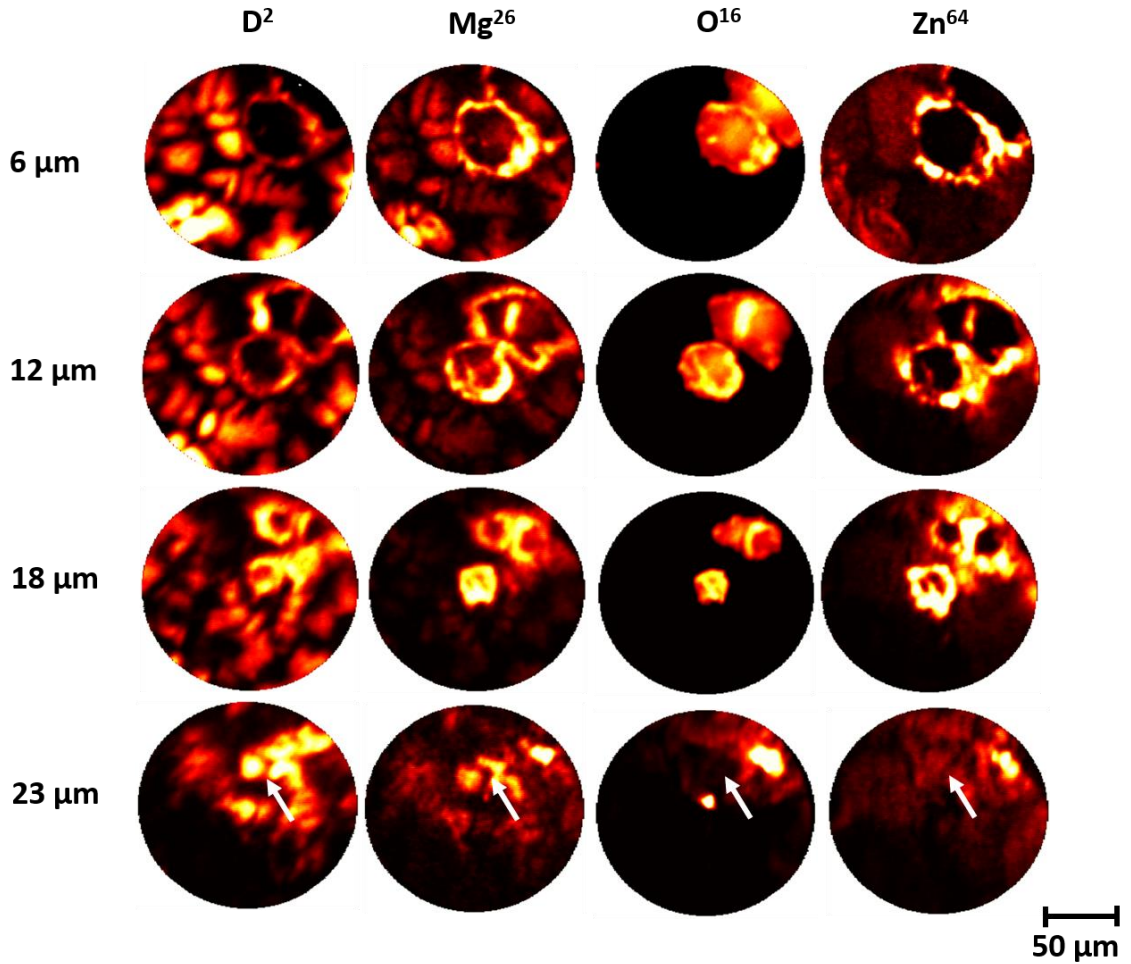


Figure 5.9: Dynamic SIMS isotopic maps for Mg^{26} , D^2 , O^{16} and Zn^{64} at approximately 6, 12, 18 and 23 μm depth of the leading edge of a corrosion filament formed on a wedge cast Mg ZEK100 alloy during free corrosion in a 0.03 M NaCl solution made with D_2O . The position of the original filament tip is clearly indicated by the O^{16} signal.

filament, striations of ^2D and ^{26}Mg , unassociated with ^{64}Zn , exist in various orientations, possibly dictated by the crystallographic orientation of the alloy. A similar distribution and correlation of the same isotopes is observed for samples subjected to a cathodic pre-treatment, Figure 5.3. No ^{16}O signal is present outside of the filament. ^{64}Zn is concentrated at the edges of the propagating filiform front. The coincident enhancement of the ^{26}Mg signal indicates the coexistence of these two elements, which probably enhanced their

sputtering efficiency. The observation of a ^2D signal associated with these locations indicates that the Zn-containing T-phase is hydrided.

Inside of the corrosion filament there is a strong, relatively uniform ^{16}O signal due to the presence of the hydroxide. At sputter depths of ~ 12 and $18\ \mu\text{m}$, similar trends are observable: coexistence of striated ^2D and ^{26}Mg enrichment outside, and ahead of, the corrosion filament; intense enrichment of ^2D , ^{26}Mg and ^{64}Zn at the margins of the corrosion filament confirming hydriding of the T-phase; and a strong, relatively uniform ^{16}O signal on the interior of the filament. At the deepest point of analysis, $\sim 23\ \mu\text{m}$, there is a strong correlation between the ^2D and ^{26}Mg signals at locations where no signal exists for ^{16}O or ^{64}Zn , as indicated by the white arrows. Again, similar to SIMS analysis conducted on the aged filament, this indicates that a phase rich in ^2D and ^{26}Mg lies below the hydroxide which occupies the corrosion filament.

To confirm the presence of hydride at the base of the filament, depth profiles were recorded with dynamic SIMS. Figure 5.10 shows depth profiles recorded on a separate corrosion filament tip from the same sample analyzed to produce Figure 9. During the first $15\ \mu\text{m}$ of depth profiling each isotope analyzed exhibits a similar decreasing signal, with transients being attributable to oxygen-enhanced ion yields.^{34,35} However, at about 16 to $20\ \mu\text{m}$ depth, the approximate thickness of a corrosion filament, there is a large increase in the ^2D signal, indicating its enrichment at the alloy/corrosion product interface. A similar, but much lower magnitude, increase is seen for the ^{16}O signal, while no such increase is observed for the ^{26}Mg . Neither the ^{16}O nor ^{26}Mg behaviour is unexpected, given that a dense MgO phase has been shown to exist at the bottom of such corrosion filaments, and at this depth, ^{26}Mg ions from the matrix will dominate the overall ^{26}Mg ion yield. These

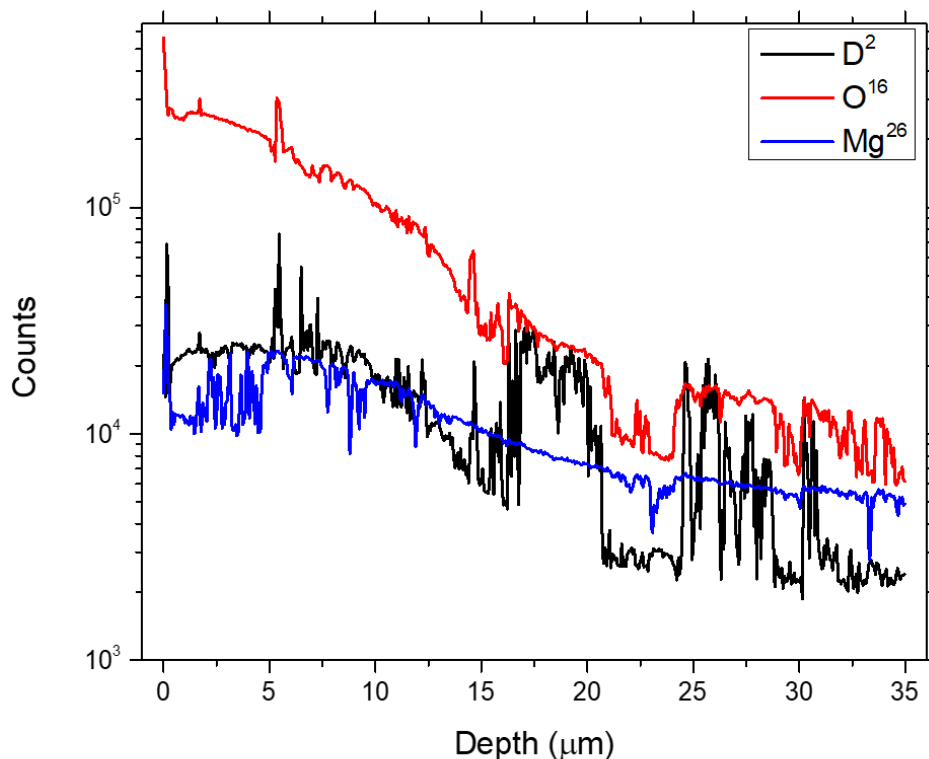


Figure 5.10: Dynamic SIMS depth profiles for Mg^{26} , D^2 and O^{16} recorded on a wedge cast Mg ZEK100 alloy specimen corroded in 0.03 M NaCl solution made with D_2O for 36 h.

observations are consistent with similar SIMS depth profiles recorded on the corroded AZ31B and E717 alloys which showed H/D signals at depths indicating the association of H/D with the substrate alloy, although the possibility of hydride formation was not discussed.³⁶

5.4 Discussion

To date, the dominant foci in attempts to explain the NDE have been on the properties of corrosion product films and the influence of alloy impurities,^{11,13} the nature

of the anodic head of the corrosion filaments,^{14,15} and the interaction between water and the Mg surface.³⁷ While previously proposed,¹⁶⁻¹⁸ the possible influence of hydride has been generally ignored. This study demonstrates that hydride is widespread and formed on the alloy studied (ZEK100) either electrochemically by the application of a cathodic current or naturally under corrosion conditions. SIMS analyses confirm the presence of hydrides at the base of mature corroded filaments (Fig 5.6), at the leading edge of propagating filaments (Fig 5.9 and Fig 5.10), on the alloy surface immediately in front of a corroding filament (Fig 5.9) and on the surface of the Zn-containing T-phase distributed along alloy grain boundaries (fig 5.9). In addition, it has been shown that the formation of MgH_2 leads to a switch from anodic to cathodic current as the applied potential is made more positive (Fig 5.1), the essential feature of the NDE. That such a switch in current can be attributed to the presence of hydride and its ability to catalyze H^+ reduction to H_2 has been previously demonstrated on the similar light metal, Ti.²⁰⁻²²

It is not surprising that MgH_2 would form, since thermodynamic calculations demonstrate its formation is favourable over the whole pH range (0-14)^{17,38} and the potential range within which the E_{CORR} on Mg is generally observed. Under electrochemical conditions (the application of a cathodic current in our case), H_2O would be rapidly reduced to produce H atoms on the Mg surface leading to both the formation of hydride and the evolution of H_2 . The mechanism of this process has been studied in detail on Ti.²⁰⁻²²

Recently, Taylor³⁷ proposed a first-principles surface reaction kinetic model for H_2 evolution on Mg, in an attempt to simulate the electrochemical response of a Mg surface under both cathodic and anodic polarization. The first step in the proposed mechanism involves the dissociation of H_2O to produce adsorbed atomic H and an associated adsorbed OH,



followed by the recombination of H atoms to produce H₂.



In the subsequent reaction steps proposed, this mechanism overlooks the probability that H_{ads} will simultaneously lead to hydride formation, as demonstrated previously for the similar light metals Ti and Al, and demonstrated in this study.^{19,22}

The generation of atomic H on Mg surfaces has been shown to be the first step in introducing stored H in Mg alloys³⁹, a process that can be improved, i.e., H absorption catalyzed, by doping the metal matrix with rare earths and transition metals, both of which are common alloying elements in Mg alloys, including Mg ZEK100.^{40,41} This introduces a second route for hydride formation and the catalysis of H₂ production, via the microgalvanic coupling of noble secondary phases, a well demonstrated process on the ZEK100²⁷ and other Mg alloys.^{29,31,42} As demonstrated in this study, the Zn- and rare earth-containing T-phase, which decorates the alloy grain boundaries is hydrided, a feature which would promote its activity as a coupled cathode. Inspection of the filament head shows that the hydrided T-phase tends to surround the corroding grain. Such a distribution of hydrided catalytic cathodes could explain the grain-sized features which define the shape of the propagating filaments. The ability of hydrided and microgalvanically coupled intermetallic phases to catalyze H⁺ reduction leading to H₂ formation has been demonstrated for Ti₂Ni within a Ti matrix.²¹

While the first step in the mechanism proposed by Taylor, reaction 1, involves the possible formation of Mg^+ , solid evidence exists to demonstrate that Mg dissolves as Mg^{2+} .⁴³⁻⁴⁹ This would be expected in the case of a chemically formed hydride



followed by its decomposition in H_2O to form soluble Mg^{2+} and H_2



and the deposition of $\text{Mg}(\text{OH})_2$ on the Mg surface in the locally alkaline solution. This mechanism would be consistent with that proposed by Chen et al.,¹⁷ based on a combination of electrochemical and H_2 collection measurements conducted under “anodic” conditions. That the corrosion of Mg proceeds in this manner is strongly supported by the observation that H_2 evolution is predominantly observed on black areas of the surface, since many hydrides have been observed to be black.⁵⁰⁻⁵² Consistent with the results in this study, Curioni et al.¹⁰ observed that high cathodic activity was observed at the black locations propagating across the surface. Their subsequent conversion would then lead to the formation of the white $\text{Mg}(\text{OH})_2$ which we observed.

It has been claimed that the surface species catalyzing H_2 evolution is the corrosion product, $\text{Mg}(\text{OH})_2$.^{8,10,11,13,29,53} Scanning electrochemical microscopy was used to demonstrate that the rate of H_2 evolution on surfaces artificially covered with $\text{Mg}(\text{OH})_2$ was 4 to 6 times faster than on a pristine Mg surface. Additionally, polarization techniques have shown an enhanced catalytic activity for H_2 evolution is observed on a previously dissolved Mg surface.^{12,13} However, it is highly unlikely that electron transport through a

large band gap hydroxide like $\text{Mg}(\text{OH})_2$ could catalyze the proton reduction reaction required to produce H_2 .

The conductivity of $\text{Mg}(\text{OH})_2$ (as the mineral brucite) has been shown to be extremely low with ionic (not electronic) conduction only being possible when the solid contains H_2O ; i.e., when it is porous or permeated with wet grain boundaries.⁵⁴ Some authors have proposed that noble metal intermetallic phases or impurities retained within the deposited hydroxide film could provide the cathodes required to couple to the substrate anode.^{9,29,55} However, the insulating nature of the hydroxide would interrupt any electrical pathways between these features and the anodic sites.

Since $\text{Mg}(\text{OH})_2$ is insulating, it is more likely that its dominant role is to provide a degree of protection to the underlying hydride but with sufficient porosity to allow access of H_2O to the hydride surface, maintaining its function as a H_2 -producing cathode. The non-protective nature of $\text{Mg}(\text{OH})_2$ films is well characterized.⁵⁶ That H_2 is produced at the alloy surface was demonstrated on the AM50 alloy.³³ In that case, microgalvanically-coupled phases, similar to the T-phase present in ZEK100, acted as H_2 -producing cathodes and accumulated domes of $\text{Mg}(\text{OH})_2$. Periodically these domes collapsed and then reformed as a consequence of the internal H_2 pressure generated by H_2 production on the surface of the secondary phase. Similarly, in the context of filiform-like corrosion of Mg alloys, Melia et al.⁵⁷ have shown that corrosion filaments on Mg AZ31B can propagate briefly without observing H_2 evolution at the filiform front, thus indicating H_2 build up underneath the intact oxide-hydroxide film of the matrix. This feature of hydride formation leading to the catalysis of $\text{H}_2\text{O}/\text{H}^+$ reduction is commonly observed on light metals when passivity is avoided; e.g., Al in alkaline solutions¹⁹ and Ti in acidic solutions.²²

Detailed studies have shown that the anomalous production of H₂ is associated with regions of the surface dominated by the anodic dissolution reaction^{14,15,56} as first demonstrated by Williams et al.⁸ and clearly observed in this study. This was confirmed by an analysis of the possible contributions to H₂ production; (i) anodic formation, (ii) catalysis by the film: (iii) as a consequence of the presence of impurities. This study ruled out the possible contribution of the film as expected (above) and demonstrated that impurities were not essential. This provides direct evidence that the primary source of H₂ was associated with the anode and could only be explained by a change in properties of the corroding surface. To account for the magnitude of the effect, Fajardo et al.¹¹ calculated that an increase in exchange current for the cathodic reaction of 4 orders of magnitude was required. A similar major increase in the kinetics of H₂ evolution was achieved on a Ti surface after electrochemical conversion to hydride.²² The results presented in this paper confirm that this change in surface properties can be attributed to the formation of a surface hydride both directly on the alloy surface and on the microgalvanically-coupled T-phase present in the ZEK100 alloy. The alternative explanation proposed by these authors, that the anomalous production of H₂ can be attributed to a severe distortion of the charge transfer coefficients associated with the anodic and cathodic reactions seems speculative and unsupported by convincing experimental evidence.⁵⁸

Figure 5.11 attempts to summarize our observations schematically. The contribution of the hydride secondary phase is not included for clarity, and because its contribution is an addendum to, not an essential feature, of the influence of hydrides. The tendency for corrosion to propagate in a filiform morphology and for the corrosion penetration depth within the filament to be limited can then be explained by the coupling

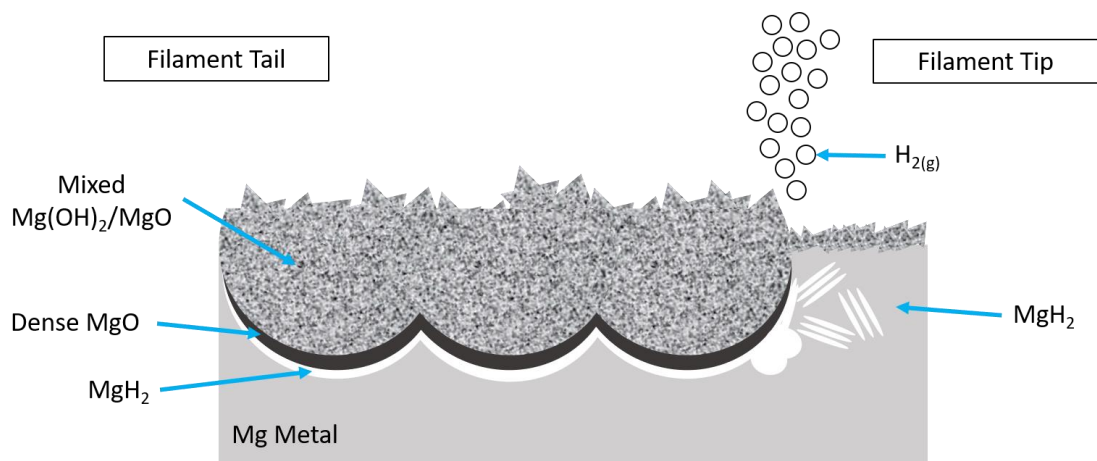


Figure 5.11: Physical model of a corrosion filament occurring on a Mg ZEK100 alloy based on SIMS isotopic mapping and depth profiles. For scale, the depth of the corrosion filament is on the order of 25 μm .

of the anode and the catalytic hydride cathode at the filiform tip, followed by a suppression of corrosion behind the tip as the MgH_2 is converted to the corrosion-suppressing $\text{Mg}(\text{OH})_2$.

5.5 Conclusions

In this work we examined the role of MgH_2 in generating the filiform-like corrosion morphology exhibited by Mg and its alloys. These hydrides demonstrated an ability to support enhanced cathodic activity, even under the application of anodic polarization, a hallmark of the NDE. Hydrided samples initiated filiform-like corrosion immediately upon immersion in saline solution and exhibited a filiform-like morphology identical to that of as-polished samples. SIMS analysis of samples corroded at E_{CORR} showed the existence of hydrides in aged corrosion filaments, the leading edge of corrosion filaments and on the Mg matrix directly in front of the corrosion filament. These results are consistent with a mechanism whereby a metastable MgH_2 is formed anodically, catalyzes the HER and

degrades by reaction with H_2O , forcing the filiform head to traverse the surface and leave behind a tail of $\text{Mg}(\text{OH})_2$. Although more work is needed to definitively assign a comprehensive corrosion mechanism, the results presented validate the hypothesis that a MgH_2 species is a key species driving the filiform-like corrosion morphology observed on Mg and its alloys.

5.6 References

- (1) Petty, R.L., A.W. Davidson, and J. Kleinberg, *J. Am. Chem. Soc.* 76 (1954): pp. 363–366.
- (2) Song, G.L., *Corrosion of Magnesium Alloys* (Elsevier, 2011).
- (3) Song, G., A. Atrens, X. Wu, and B. Zhang, *Corros. Sci.* 40 (1998): pp. 1769–1791.
- (4) Song, G., A. Atrens, D.S. John, X. Wu, and J. Nairn, *Corros. Sci.* 39 (1997): pp. 1981–2004.
- (5) Song, G., A. Atrens, D. Stjohn, J. Nairn, and Y. Li, *Corros. Sci.* 39 (1997): pp. 855–875.
- (6) Tunold, R., H. Holtan, M.-B.H. Berge, A. Lasson, and R. Steen-Hansen, *Corros. Sci.* 17 (1977): pp. 353–365.
- (7) Atrens, A., and W. Dietzel, *Adv. Eng. Mater.* 9 (2007): pp. 292–297.
- (8) Williams, G., N. Birbilis, and H.N. McMurray, *Electrochem. Commun.* 36 (2013): pp. 1–5.
- (9) Williams, G., and H.N. McMurray, *J. Electrochem. Soc.* 155 (2008): pp. C340–C349.
- (10) Curioni, M., *Electrochimica Acta* 120 (2014): pp. 284–292.
- (11) Fajardo, S., and G.S. Frankel, *Electrochimica Acta* 165 (2015): pp. 255–267.
- (12) Birbilis, N., A.D. King, S. Thomas, G.S. Frankel, and J.R. Scully, *Electrochimica Acta* 132 (2014): pp. 277–283.
- (13) Salleh, S.H., S. Thomas, J.A. Yuwono, K. Venkatesan, and N. Birbilis, *Electrochimica Acta* 161 (2015): pp. 144–152.
- (14) Fajardo, S., C. f. Glover, G. Williams, and G. s. Frankel, *Corrosion* 73 (2017): pp. 482–493.
- (15) Fajardo, S., C.F. Glover, G. Williams, and G.S. Frankel, *Electrochimica Acta* 212 (2016): pp. 510–521.
- (16) Buggio, D., M. Trueba, and S.P. Trasatti, *Corros. Sci.* 104 (2016): pp. 173–186.
- (17) Chen, J., J. Dong, J. Wang, E. Han, and W. Ke, *Corros. Sci.* 50 (2008): pp. 3610–3614.
- (18) Chen, J., J. Wang, E. Han, J. Dong, and W. Ke, *Corros. Sci.* 50 (2008): pp. 1292–1305.
- (19) Adhikari, S., and K.R. Hebert, *J. Electrochem. Soc.* 155 (2008): p. C189.
- (20) Noel, J.J., D.W. Shoesmith, and B.M. Ikeda, “Crevice Corrosion of Alpha Titanium Alloys,” in Proc. Top. Res. Symp. (Houston, Texas: NACE International, 2001), p. 68.
- (21) He, X., D.W. Shoesmith, and J.J. Noel, *J. ASTM Int.* 5 (n.d.): p. 14.
- (22) Yan, L., S. Ramamurthy, J.J. Noël, and D.W. Shoesmith, *Electrochimica Acta* 52 (2006): pp. 1169–1181.
- (23) Zhang, J., Z. Fan, Y.Q. Wang, and B.L. Zhou, *J. Mater. Sci. Lett.* 19 (2000): pp. 1825–1828.
- (24) Hildal, K., N. Sekido, and J.H. Perepezko, *Intermetallics* 14 (2006): pp. 898–902.
- (25) Pourbaix, M., *Atlas of Electrochemical Equilibria in Aqueous Solutions*, 2nd English ed. (Houston, Texas: National Association of Corrosion Engineers, 1974).
- (26) Williams, G., H. ap Llwyd Dafydd, and R. Grace, *Electrochimica Acta* 109 (2013): pp. 489–501.

- (27) Asmussen, R.M., W.J. Binns, P. Jakupi, and D. Shoesmith, *Corrosion* 71 (2015): pp. 242–254.
- (28) Asmussen, R.M., W.J. Binns, P. Jakupi, and D. Shoesmith, *J. Electrochem. Soc.* 161 (2014): pp. C501–C508.
- (29) Cano, Z.P., M. Danaie, J.R. Kish, J.R. McDermid, G.A. Botton, and G. Williams, *Corrosion* 71 (2015): pp. 146–159.
- (30) Bland, L.G., K. Gusieva, and J.R. Scully, *Electrochimica Acta* 227 (2017): pp. 136–151.
- (31) Neil, W.C., M. Forsyth, P.C. Howlett, C.R. Hutchinson, and B.R.W. Hinton, *Corros. Sci.* 51 (2009): pp. 387–394.
- (32) Zhao, M.-C., M. Liu, G.L. Song, and A. Atrens, *Adv. Eng. Mater.* 10 (2008): pp. 104–111.
- (33) Danaie, M., R.M. Asmussen, P. Jakupi, D.W. Shoesmith, and G.A. Botton, *Corros. Sci.* 77 (2013): pp. 151–163.
- (34) Wittmaack, K., and W. Wach, *Nucl. Instrum. Methods Phys. Res.* 191 (1981): pp. 327–334.
- (35) Yu, M.L., *Nucl. Instrum. Methods Phys. Res. Sect. B Beam Interact. Mater. At.* 15 (1986): pp. 151–158.
- (36) Unocic, K.A., H.H. Elsentriecy, M.P. Brady, H.M. Meyer, G.L. Song, M. Fayek, R.A. Meisner, and B. Davis, *J. Electrochem. Soc.* 161 (2014): pp. C302–C311.
- (37) Taylor, C.D., *J. Electrochem. Soc.* 163 (2016): pp. C602–C608.
- (38) PERRAULT, G.G., (n.d.): p. 13.
- (39) Schlapbach, L., and A. Züttel, 414 (2001): p. 6.
- (40) Hanada, N., E. Hirotoishi, T. Ichikawa, E. Akiba, and H. Fujii, *J. Alloys Compd.* 450 (2008): pp. 395–399.
- (41) Malka, I.E., J. Bystrzycki, T. Płociński, and T. Czujko, *J. Alloys Compd.* 509 (2011): pp. S616–S620.
- (42) Asmussen, R.M., W.J. Binns, P. Jakupi, P. Dauphin-Ducharme, U.M. Tefashe, J. Mauzeroll, and D. Shoesmith, *Corros. Sci.* 93 (2015): pp. 70–79.
- (43) Kirkland, N.T., G. Williams, and N. Birbilis, *Corros. Sci.* 65 (2012): pp. 5–9.
- (44) Cain, T., S.B. Madden, N. Birbilis, and J.R. Scully, *J. Electrochem. Soc.* 162 (2015): pp. C228–C237.
- (45) Bender, S., J. Goellner, A. Heyn, and S. Schmigalla, *Mater. Corros.* (2011): p. n/a-n/a.
- (46) Rossrucker, L., A. Samaniego, J.-P. Grote, A.M. Mingers, C.A. Laska, N. Birbilis, G.S. Frankel, and K.J.J. Mayrhofer, *J. Electrochem. Soc.* 162 (2015): pp. C333–C339.
- (47) Rossrucker, L., K.J.J. Mayrhofer, G.S. Frankel, and N. Birbilis, *J. Electrochem. Soc.* 161 (2014): pp. C115–C119.
- (48) Lebouil, S., O. Gharbi, P. Volovitch, and K. Ogle, *Corrosion* 71 (2014): pp. 234–241.
- (49) Swiatowska, J., P. Volovitch, and K. Ogle, *Corros. Sci.* 52 (2010): pp. 2372–2378.
- (50) Le Guyadec, F., X. Génin, J.P. Bayle, O. Dugne, A. Duhart-Barone, and C. Ablitzer, *J. Nucl. Mater.* 396 (2010): pp. 294–302.
- (51) Schefer, J., P. Fischer, W. Hälgl, F. Stucki, L. Schlapbach, J.J. Didisheim, K. Yvon, and A.F. Andresen, *J. Common Met.* 74 (1980): pp. 65–73.

- (52) Rusman, N.A.A., and M. Dahari, *Int. J. Hydrog. Energy* 41 (2016): pp. 12108–12126.
- (53) Curioni, M., F. Scenini, T. Monetta, and F. Bellucci, *Electrochimica Acta* 166 (2015): pp. 372–384.
- (54) Gasc, J., F. Brunet, N. Bagdassarov, and V. Morales-Flórez, *Phys. Chem. Miner.* 38 (2011): pp. 543–556.
- (55) Taheri, M., J.R. Kish, N. Birbilis, M. Danaie, E.A. McNally, and J.R. McDermid, *Electrochimica Acta* 116 (2014): pp. 396–403.
- (56) Esmaily, M., J.E. Svensson, S. Fajardo, N. Birbilis, G.S. Frankel, S. Virtanen, R. Arrabal, S. Thomas, and L.G. Johansson, *Prog. Mater. Sci.* 89 (2017): pp. 92–193.
- (57) Melia, M.A., T.W. Cain, B.F. Briglia, J.R. Scully, and J.M. Fitz-Gerald, *JOM* 69 (2017): pp. 2322–2327.
- (58) Fajardo, S., and G.S. Frankel, *Electrochem. Commun.* 84 (2017): pp. 36–39.

6 The Effect of Cooling Rate on the Corrosion Properties of Mg

ZEK100

6.1 Introduction

Due to their superior strength-to-weight ratio Mg alloys are candidates to replace heavier structural materials such as steels and aluminum in the automotive industry. Inclusion of Mg alloys would achieve significant light-weighting of vehicles leading to decreased fuel consumption and a reduction in the vehicle's carbon footprint. However, widespread adoption of Mg based alloys has been limited to use on the interior of vehicles due to their high corrosion rates.^{1,2} Further complicating the issue, from a manufacturing point of view, are the high production costs and poor low temperature formability associated with many commercial Mg alloys.³⁻⁵ One class of alloys which have shown promise due to their low temperature formability is the Mg-Zn-RE-Zr series.¹ Although these alloys exhibit favourable mechanical properties, their corrosion behaviour has received only minimal attention, although their potential as a biomedical material has been investigated and their corrosion performance compared to that of other alloys.^{1,6-9}

In general, Mg alloys have been shown to be susceptible to microgalvanic corrosion, with oxidation of Mg grains being accelerated via coupling to the reduction of water on more noble secondary phases dispersed throughout the matrix.^{10,11} However, the influence of these microstructural effects, such as the size, shape and distribution of intermetallic particles (IMP) on the corrosion behaviour of Mg alloys remains uncertain. Elucidation of these effects on the corrosion behaviour could lead to the optimization of casting and processing techniques and the production of alloys with an improved corrosion

resistance. Additionally, Mg alloys are known to commonly exhibit a distinct corrosion morphology. This morphology is “filiform-like” and characterized by the propagation of dark corrosion filaments across the alloy surface. A similar form of corrosion has also been observed for pure Mg.¹¹

Considerable attention has been devoted to the study of this unusual propagation morphology,¹⁰⁻¹⁹ which involves the lateral propagation of active anodes across an alloy surface coupled to cathodically activated corroded regions co-located with the anode at filament tips but eventually left behind by the advancing anodes.^{10-12,14,15} Cathodic activation in this manner has been attributed to a number of possible effects:¹¹ (i) the accumulation of impurities (especially Fe) in the corroding surface; (ii) a significant increase in surface area leading to enhanced cathodic evolution of H₂; and (iii) the enrichment in the surface of cathodically active, microgalvanically-coupled noble IMPs. While many of these features may contribute, we recently demonstrated that the dominant process leading to cathodic activation is the formation of MgH₂.¹³

A mechanism involving hydride formation, which has been shown to be catalytic for H⁺/H₂O reduction on other light metals,¹⁶⁻¹⁸ would be consistent with the conclusion by Cano et al.¹⁰ that cathodic activation was due to the direct reaction of Mg with H₂O and with the claim by Fajardo et al.¹⁹ that an increase in exchange current for the cathodic reaction by 4 orders of magnitude was required to account for the magnitude of the effect. In our previous paper the surfaces of both the α -Mg grains and the noble T-phase (Mg₇Zn₃Nd) were hydrided making it feasible that both surfaces could act as cathodically-activated cathodes.¹³

In this study we tailored the microstructural features (i.e. altering the size, shape, composition, and distribution of IMPs) of the alloy using wedge casting. In Mg alloys, it

has been shown that the relatively fast cooling of the narrow wedge tip produces finer grains and less well developed secondary microstructures than the slow cooling thick base.²⁰⁻²² This allowed us to interrogate the influence of microstructure on filiform corrosion without changing the overall composition of the alloy, in a quest to determine the relative importance of the two hydride locations on the filiform process.

6.2 Experimental

6.2.1 Materials

The wedge cast Mg ZEK100 alloy was fabricated by CanmetMaterials Hamilton, Ontario, with a height of 15.5 cm, a width at the base of 7 cm, and a length of 39.5 cm, Figure 6.1(a). Ingots were melted in a resistance furnace using a mild steel crucible and degassed with a CO₂ + 0.5% SF₆ gas mixture. Following removal of surface oxide films, the castings were poured at 730 °C into a water-cooled Cu mold. The increasing thickness from the tip to the top of the cast wedge results in a gradient in the crystallization rate of the alloy on cooling leading to variations in microstructure (Typical cooling rates for the wedge ranging from 10¹-10³ K/s) . A section with a width of 1 cm was cut from the centre of the wedge, as shown in Figure 6.1b. Samples were then cut along the center line of the wedge at various distances from the tip of the cast and labelled alphabetically with section A being closest to the wedge tip, as shown in Figure 6.1c. Section A was produced by cutting the ingot 0.64 cm from the tip to produce a sample with a surface area of 0.125 cm². Section B was produced by cutting the ingot 0.5 cm below section A to yield a sample with

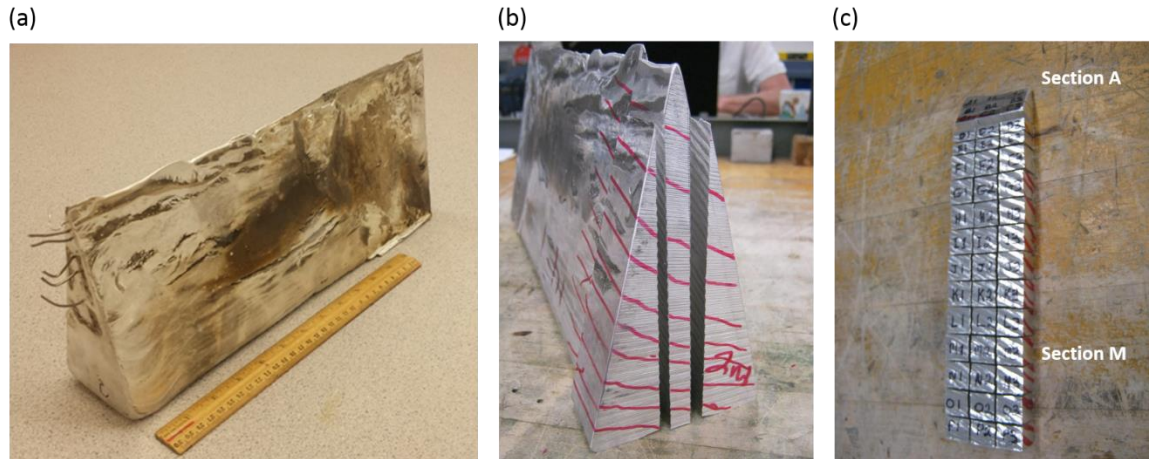


Figure 6.1: (a) Photo of the Mg ZEK100 wedge cast ingot with 30 cm ruler for scale. Thermocouples can be seen sticking out of the left side of the ingot. (b) Image showing the centerline section of the ingot which was used to prepare samples. (c) Final samples cut from the center line of the wedge cast ingot. Samples are labelled alphabetically from the narrow portion of the wedge (Section A) to the thick portion (Section M).

a surface area of 0.375 cm^2 . Similarly, section C was produced by cutting the ingot 0.5 cm below section B and had a surface area of 0.5 cm^2 . Sections D-E were each cut with a height of 0.5 cm (surface area of 1 cm^2) and sections F-M to a height of 1 cm (surface area of 1 cm^2). Below, electrodes and specimens are labelled A to M to designate the section from which they were cut.

The back of each sample was tapped and threaded with a stainless steel rod to enable electrical connection to external circuitry. Samples were mounted in Struers EpoFix™ epoxy resin with a single surface exposed. The electrodes were ground successively with 800, 2400, and 4000 grade silicon carbide papers in a 1:1 ethanol/isopropanol mixture, then on a Struers DP-DUR pad using a $3 \mu\text{m}$ diamond abrasive, and cleaned ultrasonically in anhydrous ethanol. The electrodes were then polished to a mirror finish on a Struers OP-Chem pad using a $0.04 \mu\text{m}$ colloidal silica suspension in ethylene glycol, cleaned

ultrasonically in anhydrous ethanol, and rinsed with a 1:1 ethanol-isopropanol mixture. Finally, samples were dried in an Ar stream.

6.2.2 Electrochemical Measurements

A standard three-compartment, three-electrode cell was used for electrochemical experiments, with a saturated calomel reference electrode (SCE) and, when necessary, a Pt plate counter electrode. Experiments were performed using a Keithly 6514 electrometer to record the corrosion potential (E_{CORR}) and a Solartron 1287 potentiostat to perform potentiodynamic polarization (PDP) scans. All experiments were conducted inside a grounded Faraday cage (to minimize interference from external electrical noise) in a naturally aerated 0.03 M NaCl (reagent grade, 99 % assay) solution prepared with Type 1 water ($18 \text{ M}\Omega \cdot \text{cm}^2$) at ambient temperature ($\sim 25 \text{ }^\circ\text{C}$). PDP scans were initiated at $-0.25 \text{ V vs. } E_{\text{CORR}}$ and scanned in the positive direction at 10 mV/min and terminated at either $+0.25 \text{ V vs. } E_{\text{CORR}}$, or when a current density of 10 mA/cm^2 was reached.

6.2.3 Microscopy

Optical stereo micrographs were collected using a Zeiss Lunar V12 microscope equipped with an Axio 1.1 camera. Scanning electron microscopy (SEM) was performed in either secondary electron (SE) or back-scattered electron (BSE) mode using a LEO 1540 XB SEM/FIB or a Hitachi SU6600 FEG-SEM. X-ray energy dispersive spectroscopy (XEDS) maps were obtained using Quartz One software[®]. Confocal Laser Scanning Microscopy (CLSM) was used to record topographic information following corrosion

product removal and was conducted using a LSM Zeiss 510 Duo confocal microscope running ZEN 2009 software. All micrographs were recorded using a 50x optical lens.

6.2.4 Corrosion Product Removal

Corrosion products were removed using the ASTM G 1-90 standard.²³ This method involved immersing the corroded material in a chemical solution to etch away corrosion products and expose the metal surface. This etchant comprised 200 g of CrO_3 , 10 g of AgNO_3 and 20 g of $\text{Ba}(\text{NO}_3)_2$ in 1000 mL of deionised water. Samples were immersed in the solution and agitated until the release of bubbles from the surface ceased. Typically, this method required approximately 1 min of immersion. Upon removal from the etchant samples were rinsed with anhydrous ethanol (99.5%) and dried under an Ar gas stream.

6.3 Results

6.3.1 Wedge Cast Microstructure

Table 6.1: Inductively coupled plasma mass spectrometry (ICP-MS) elemental

Wedge Section	%Al	%Zn	%Mn	%Fe	%Nd	%Zr	%Mg
A	0.02	1.31	0.02	< 0.01	0.17	0.40	Bal
D	0.02	1.38	0.02	< 0.01	0.19	0.37	Bal
G	0.01	1.32	0.02	< 0.01	0.15	0.36	Bal
M	0.02	1.20	0.02	< 0.01	0.15	0.40	Bal

The elemental compositions of four wedge sections, determined by inductively coupled plasma mass spectrometry (ICP-MS), are shown in Table 6.1. The small

differences in elemental composition throughout the wedge cast demonstrate that the alloy composition was effectively independent of cooling rate or distance from the wedge tip. Elemental compositions for Zn, Nd and Zr ranged from 1.20-1.38%, 0.15-0.19% and 0.36-0.40% by weight, respectively. In addition, trace amounts (i.e., <0.01 wt%) of Si, Cu, Fe and Ni were detected.

Figure 6.2 (a to d) shows SEM images, recorded in the backscatter electron (BSE) mode, on freshly polished surfaces for A, D, G and M. The corresponding EDX maps for Zn and Zr are shown in Figure 6.2 (e to h) and Figure 6.2 (i to l), respectively. Red arrows in Figure 6.2 (a to d) indicate many of these particles are rich in Zn, making them likely to be the Mg_7Zn_3RE T-phase demonstrated to be present in this and the similar ZE41 alloy.² In the alloy used in this study the rare earth is Nd. Green arrows in these images show the locations of the light grey Zr-rich IMPs which reside within grains or exist as long chains along grain boundaries., Figures 6.2 (c) and 6.2(k), and sometimes penetrate into the grains. Commonly, Zr forms IMPs containing Fe in these alloys.²⁴ These microstructural features exist within an α -Mg matrix, which appeared dark grey in the micrographs. While each section of the wedge exhibited all of these features, their size, shape and distribution varied depending on the cooling rate experienced.

The influence of cooling rate on the distribution of Zn throughout the alloy is visible in EDX maps, Figure 6.2 (e to h). Each section appeared to contain equiaxed grains which increased in average size from A to M. A and D, Figure 6.2 (a and b) possess similar microstructures with respect to size, shape and distribution of the T-phase and other IMPs and exhibit a generally uniform distribution of Zn, Figure 6.2(e and f). This indicates that the difference in cooling rate of the alloy in the thinner sections of the wedge has only a minor effect on the crystallization of the alloy. This is likely due to the presence of Zr which

is known to be a strong grain refiner in Mg.^{4,25} In the thicker sections of the wedge, G and M, Figure 6.2 (c and d) respectively, the slower cooling rates overcome the grain refining

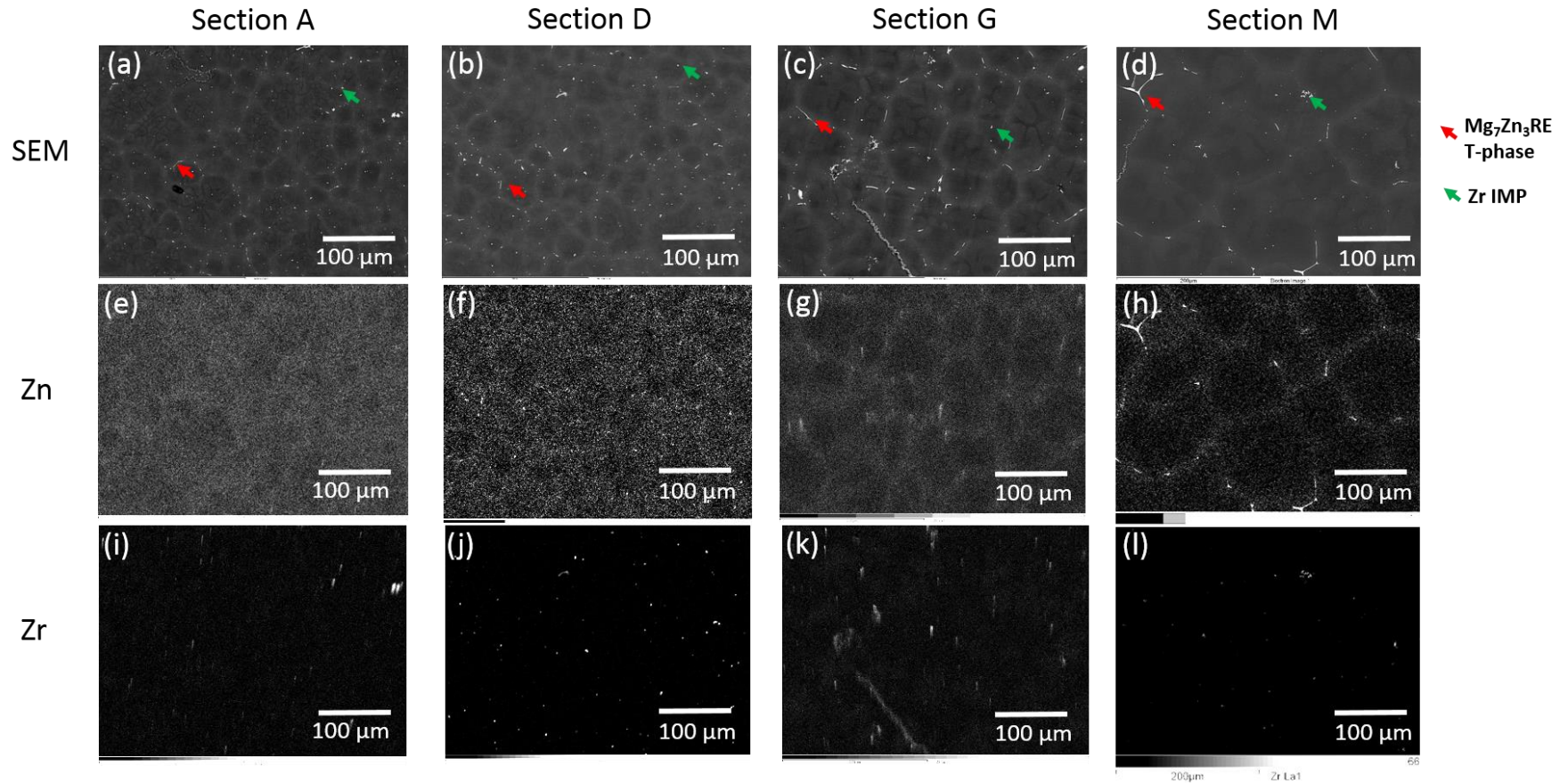


Figure 6.2: (a-d) SEM micrographs recorded in BSE mode for section A, D, G and M of the Mg ZEK100 wedge cast, respectively. A Zn-rich Mg₇Zn₃RE T-phase which segregates in the grain boundaries is indicated with red arrows and Zr-rich intermetallic particles are indicated with green arrows. (e-h) EDX elemental maps for Zn for section A, D, G and M of the alloy. (i-l) the corresponding EDX elemental maps for Zr.

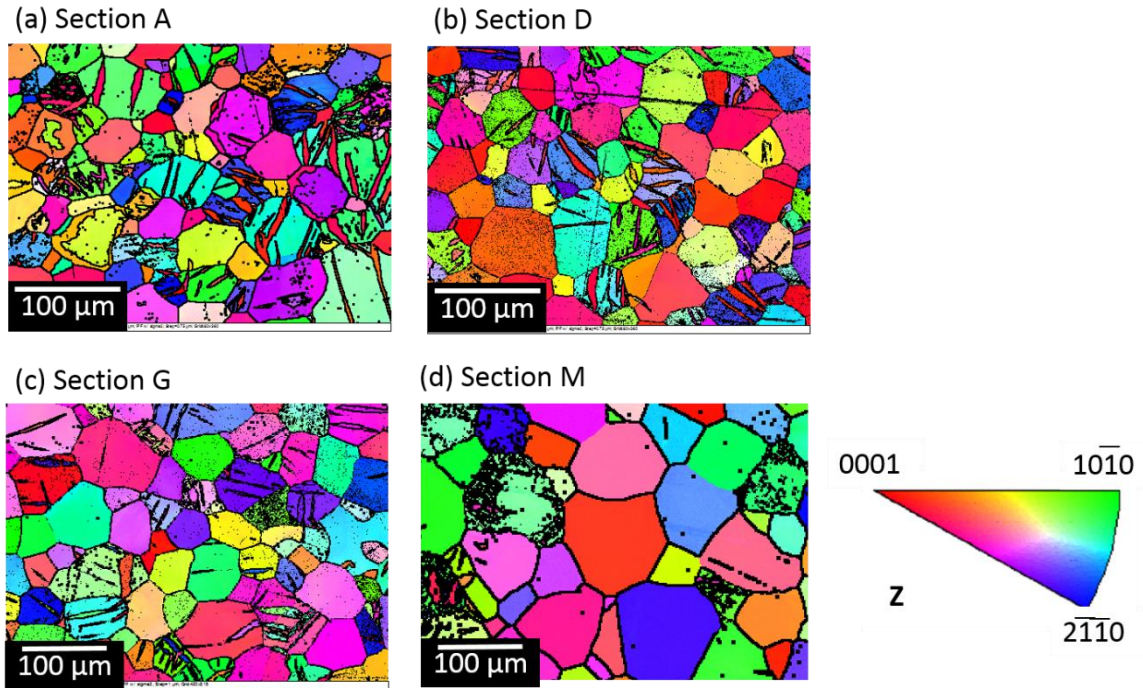


Figure 6.3: (a-d) EBSD crystallographic orientation maps recorded on Mg ZEK100 wedge cast alloy for section A, D, G and M, respectively. The inverse pole figure is in the bottom right and displays the colour code for each hcp Miller indices.

capability of Zr leading to the enhanced precipitation of T-phase in the grain boundaries and a more localized distribution of Zn along grain boundaries. This enhanced Zn content is associated with the visible, but faint, dendritic α -Mg grain fringes, Figure 6.2 (a to d). A similar partial segregation of Al to form IMPs and decorated grain boundaries with a higher matrix Al content was observed for the AM50 alloy.^{26,27}

To confirm the effect of cooling rate on the grain size, specimens were analyzed by EBSD. The grain orientation maps for all four sections are displayed in Figure 6.3 (a to d). The orientations of the grains are colour coded based on the inverse pole figure in Figure 6.3, with black regions corresponding to non-indexed locations. The textures of the sections were independent of cooling rate with close to random crystallographic orientations. For A, D, and G many grains exhibit striations of different orientation most likely due to

dendritic features within each grain., Mg alloys being well known to exhibit dendritic growth.²¹ Conspicuously, the EBSD measurements on M do not exhibit such features despite the clear visibility of dendrites in the SEM micrograph, Figure 6.2d. Most likely this is due to the relatively larger step size used in the analysis of the more coarse material.

Using the linear intercept method, average grain diameters of 29.0, 29.9, 39.8, and 48.4 μm were measured for A, D, G, and M, respectively. As mentioned above, the similar smaller grain sizes observed for A and D can be attributed to the grain refining ability of Zr, which is lost at the slower cooling rates allowing substantial grain growth for G and M.

6.3.2 Electrochemical Behaviour

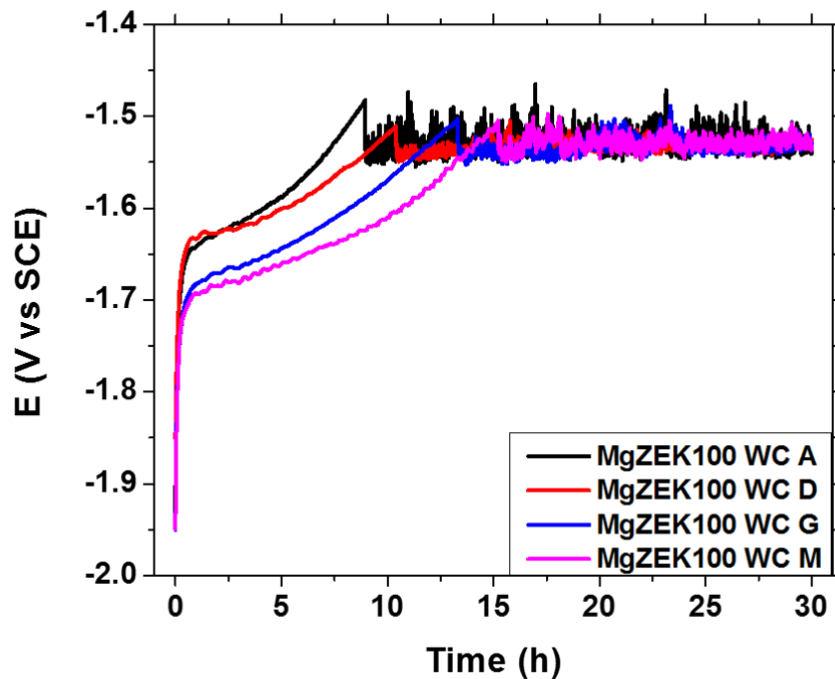


Figure 6.4: E_{CORR} measurements recorded in 0.03 M NaCl solution for section A, D, G and M of a wedge cast Mg ZEK100 alloy for 30 h.

Figure 6.4 shows E_{CORR} measurements recorded on A, D, G and M in 0.03 M NaCl. Each section behaves similarly, exhibiting two distinct stages of behaviour. Stage 1 begins with a rapid increase in E_{CORR} over the first 20 min of immersion followed by a slower increase to $\sim -1.50 \text{ V}_{\text{SCE}}$ until the initiation of stage 2. E_{CORR} increases more rapidly the faster the cooling rate indicating a dependence on alloy microstructure. The time to reach the transition to stage 2 increases from $\sim 7\text{h}$ for A to 15h for M; i.e, with decreasing cooling rate. The transition to stage 2 occurs at approximately the same potential for all sections, with E_{CORR} becoming noisy with fluctuations of $\sim \pm 50 \text{ mV}$ but remaining identical for all sections. This general behaviour was demonstrated to be reproducible by repeating the sequence of experiments 5 times. Similar behaviour was observed for the Zn-containing AZ31 alloy with the duration of stage 1 increasing as the $[\text{Cl}^-]$ of the solution decreased.¹⁴ In the present experiments the $[\text{Cl}^-]$ was identical in all experiments indicating that the duration of stage 1 was dependent on the microstructure dictated by the cooling rate.

E_{CORR} values for all four sections were recorded for exposure periods ranging from 0.5h to 30h, Figure 6.5 (a to d). Immediately following each exposure period, PDP scans were initiated at -0.25 V vs E_{CORR} and scanned in the positive direction, Figure 6.5 (e to h). Over an immersion period of 0.5h, E_{CORR} for each section effectively exhibited an identical response with the spread in values being $< 25 \text{ mV}$. The PDP scans recorded subsequently were also essentially indistinguishable. The cathodic branch of the scan exhibited Tafel behaviour for H_2O reduction, while the anodic branch showed similar behaviour up to $\sim -1.50 \text{ V}_{\text{SCE}}$ when a more dramatic increase in current occurred. This increase was the same for A, D and M but slightly less prominent for G. This increase occurs at the same potential at which the transition from stage 1 to stage 2 is observed in the initial open circuit section of these experiments.

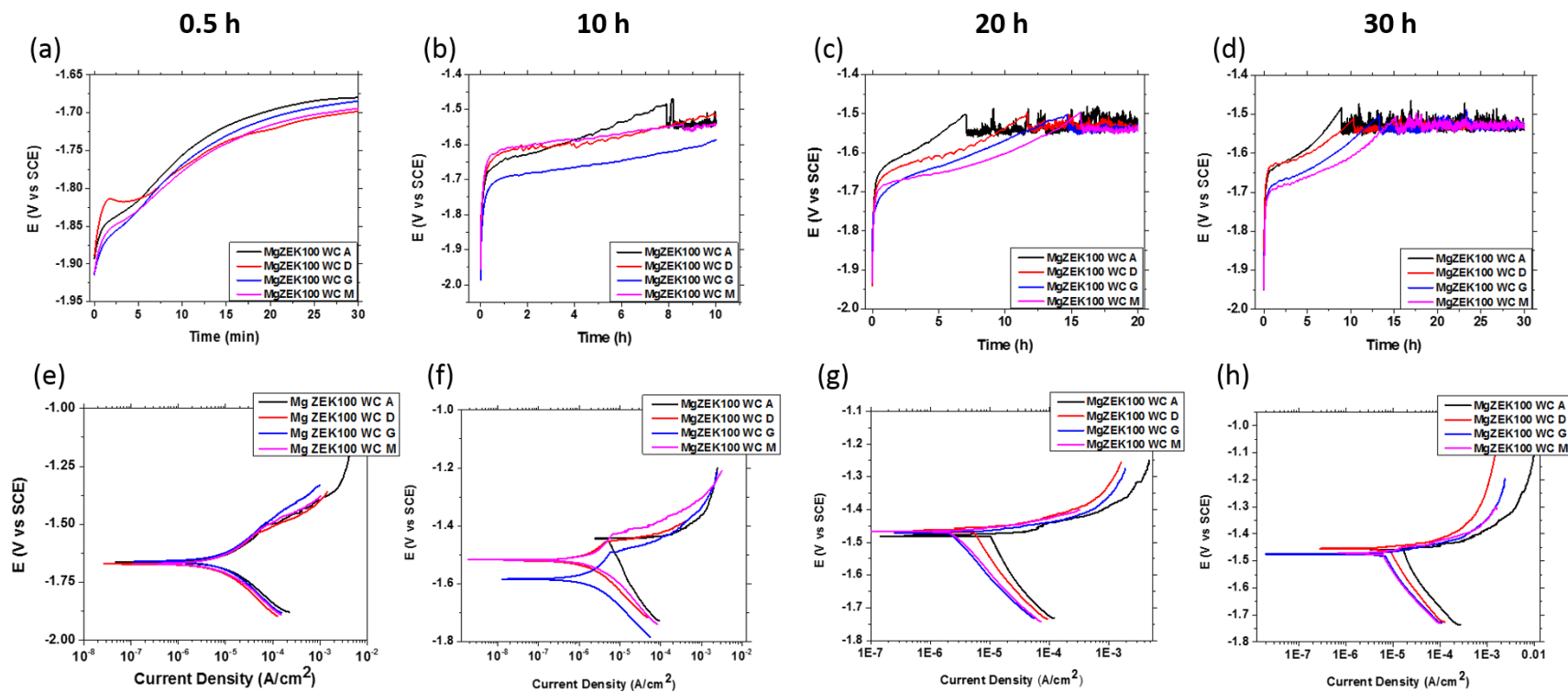


Figure 6.5: (a-d) E_{CORR} measurements recorded for section A, D, G and M of a wedge cast Mg ZEK100 alloy in 0.03 M NaCl for 0.5 (black), 10 (red), 20 (blue) and 30 (pink) h, respectively. (e-h) PDP curves recorded directly following the E_{CORR} measurements in a-d in the same solution. Sections of the wedge have corresponding colours in the E_{CORR} and PDP measurements. PDP scans were initiated -0.25 V vs. SCE and scanned in the positive direction.

Over a 10 h exposure period differences in E_{CORR} for the different specimens become apparent. However, only A underwent the transition from stage 1 to stage 2. In the subsequent PDP scan, the cathodic current for A is markedly higher than that for D, G and M and the increase in anodic current is large and immediate once a net anodic current is established. For D, G and M, which remained in stage 1 after 10 h, a period of low anodic current preceded the eventual step increase at more positive potentials. After 20 and 30 h of exposure all 4 specimens had achieved stage 2 and the rapid increase in anodic current for an applied potential $> -1.5 V_{SCE}$ was apparent for all specimens. The cathodic currents observed were in the order $A > D > G \sim M$ which reflected the length of time a particular specimen had spent in stage 2. These results confirm that the transition from stage 1 to stage 2 under open circuit conditions can be attributed to the breakdown of the film initially grown in stage 1.

The corrosion current densities (I_{CORR}) obtained by extrapolation of the cathodic currents to E_{CORR} are plotted in Figure 6.6. In general, the values obtained for each section show a similar trend with exposure period. There is an initial decrease over the early exposure period, when E_{CORR} is increasing in stage 1, and an increase once the transition to stage 2 has occurred. After the short exposure period of 0.5h the values are very similar, varying only between $\sim 1.08 \mu A.cm^{-2}$ (A) and $0.83 \mu A.cm^{-2}$ (G). After 10 h of exposure the significantly higher rate for A ($0.59 \mu A.cm^{-2}$) compared to the other sections (0.2 to $0.3 \mu A.cm^{-2}$) reflects the fact A has transitioned into stage 2.

As illustrated by the optical micrographs in Figures 6.6b and 6.6c, stage 1 involves the formation of a coherent protective corrosion film, while the transition into stage 2 can be attributed to the initiation of filiform corrosion. This is consistent with the observations

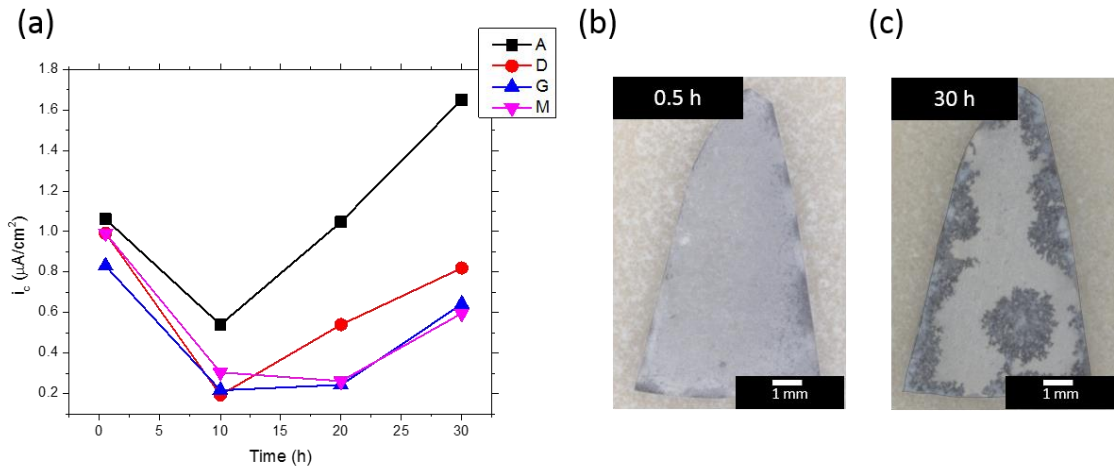


Figure 6.6: (a) Cathodic current densities as a function of immersion time extracted from PDP curves in Figure 5. i_c values were extracted by Tafel analysis of the cathodic branch of the polarization curve extrapolated to the E_{CORR} . Optical micrographs of section A following the PDP analysis conducted in figure 5 following (b) 0.5 and (c) 30 h. The black areas in (c) are the result of filiform-like corrosion.

of Williams et al.¹⁴ who demonstrated that a shift in E_{CORR} to less negative values accompanied by an increase in cathodic current was an indication of the onset of the cathodic activation associated with the filiform process. Thus, the increase in corrosion rate for A in stage 2 reflects the increase in active area as the filiform front progresses. As demonstrated by Williams et al.¹⁴ on the AZ31 alloy, anodic activity is local and non-uniformly distributed. The delay in increase in corrosion rate for G and M can then be attributed to the delay in initiation of filiform corrosion, Figure 6.5, on these sections. While it is tempting to claim the differences in corrosion rate after 30 h of exposure reflect the influence of microstructure on the rate of filiform propagation, it is more likely that they reflect only the active area of the filiform front, the individual current densities remaining the same.

6.3.3 Analysis of Corroded Surfaces

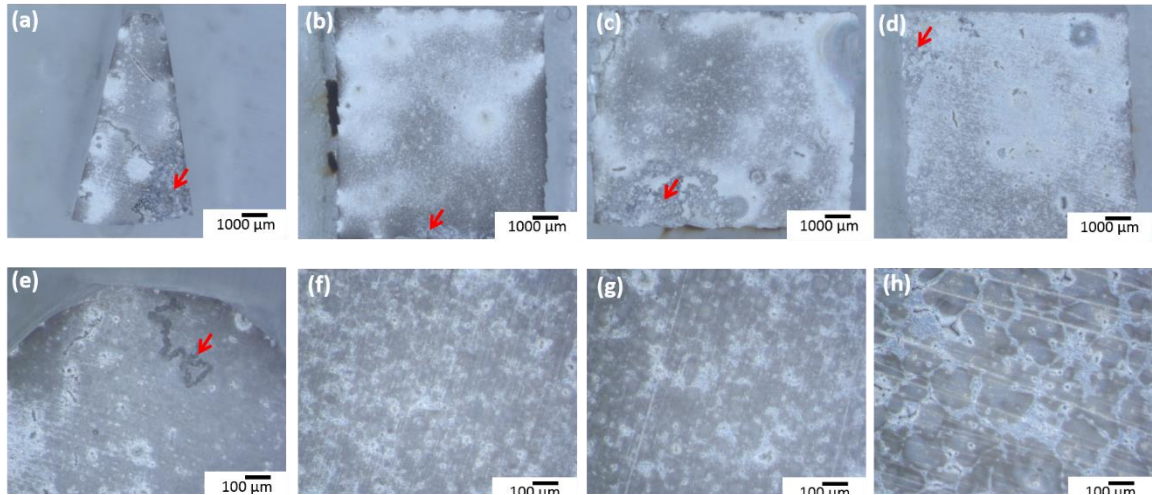


Figure 6.7: Optical micrographs of section A (a & e), section D (b & f), section G (c & g) and section M (d & h) of a Mg ZEK100 wedge cast alloy following 24 h immersion in 0.03 M NaCl solution. Red arrows indicate the locations of the filiform-like corrosion morphology.

Figure 6.7 shows optical micrographs for all four sections recorded at low (a to d) and high (e to h) magnifications, respectively, after 24h of immersion. At low magnification, the sections look very similar with the majority of the surface covered by a light coloured corrosion film. The presence of dark corrosion filaments, indicated by the red arrows, confirms the presence of filiform tracks. At the higher magnification clear differences in the distribution of corrosion becomes apparent clearly indicating that the alloy microstructure has an influence on the general, non-filiform corrosion of the surface. A, Figure 6.7e, exhibits no clearly defined influence of microstructure on the distribution of corrosion. One clear filiform track is indicated by the red arrow. For the other sections the tendency for corrosion to occur preferentially along the grain boundaries increases in the order D to G, and especially to M, Figure 6.7 (f to h). This behaviour can be attributed

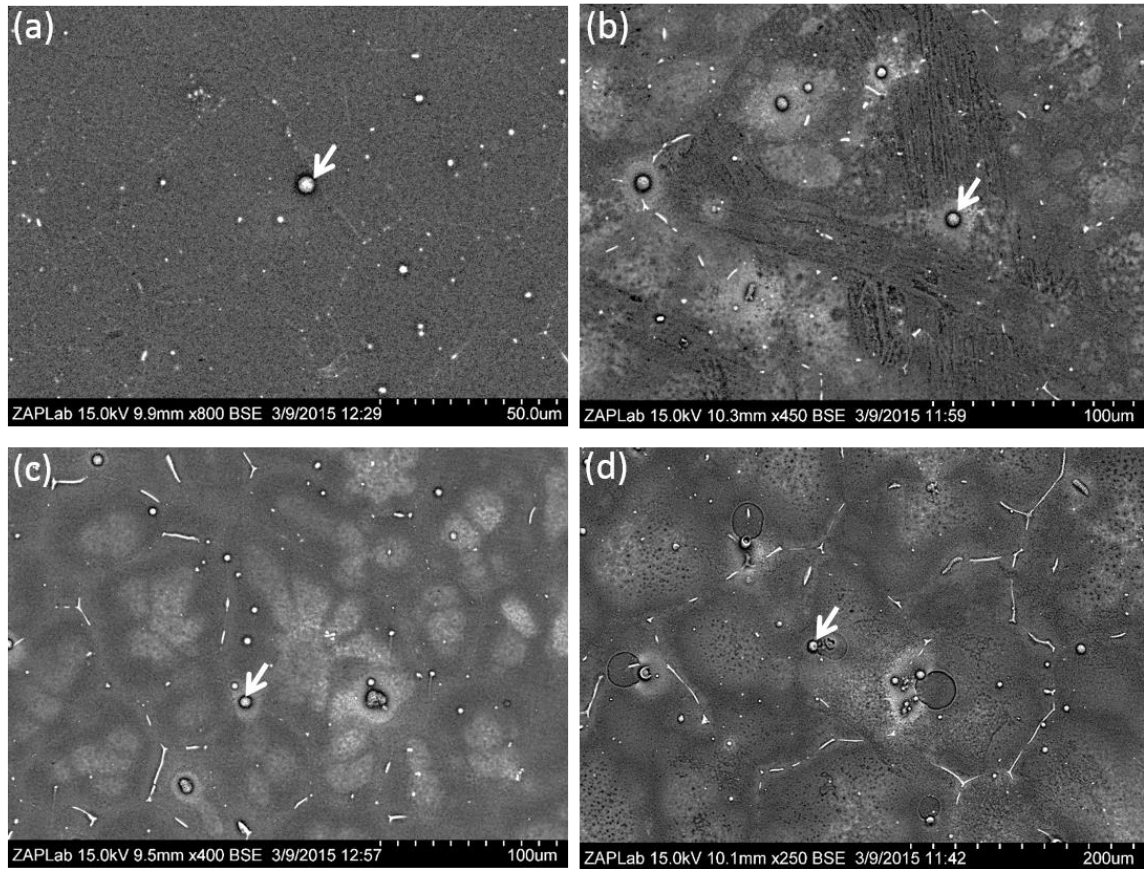


Figure 6.8: SEM micrographs recorded in BSE mode for wedge cast ZEK100 (a) section A, (b) section D, (c) section G and (d) section M following immersion in a 0.03 M NaCl solution for 24 h. Note the differences in the scale bar from image to image. Images show the corrosion morphology of the general alloy surface which is characterized by microgalvanic coupling.

to the more extensive segregation of alloying elements to these locations, Figure 6.2, as the cooling rate during fabrication decreases, with the T-phase IMPs acting as cathodes microgalvanically coupled to the α -Mg matrix. As observed, this promotes the deposition of white $\text{Mg}(\text{OH})_2$ on the T-phase particles due to the locally generated alkalinity and concentrates corrosion damage to the matrix to locations in close proximity in the relatively low ionic strength electrolyte employed in these experiments. Similar behaviour has been

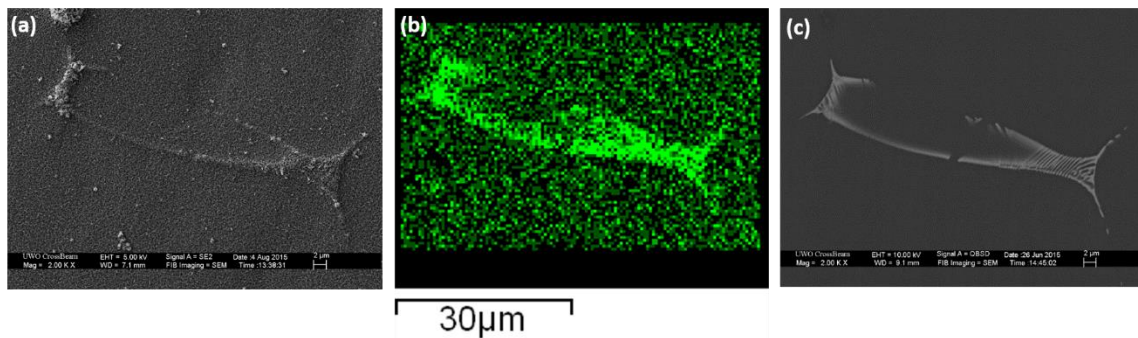


Figure 6.9: (a) SEM micrograph recorded in SE mode of section A of a Mg ZEK100 wedge Alloy following a 24 h immersion in 0.03 M NaCl environment showing the buildup of $\text{Mg}(\text{OH})_2$ corrosion product on $\text{Mg}_7\text{Zn}_3\text{RE}$ T-phase. (b) EDX elemental map for Zn and (c) the corresponding SEM micrograph of the as-polished sample to show that the $\text{Mg}(\text{OH})_2$ buildup in (a) does occur on the T-phase.

observed for other $\text{Zn}^{1,2}$ and Al^{27} containing alloys in which the microgalvanic coupling of similar IMPs.

Figure 6.8 shows SEM micrographs of surface locations subjected to microgalvanic corrosion. Each specimen exhibits the characteristic morphology attributable to microgalvanically-coupled corrosion, demonstrated by the accumulation of white corrosion product deposits on the IMPs. The deposits on isolated particles, indicated by white arrows, and the elongated strips decorating the grain boundaries, the latter more easily seen on G and M, show the location of Zr-containing IMPs, known to be strong cathodes when activated by the codeposition of Fe.¹ A similar deposition of corrosion products on the T-phase is not so readily visible due to the use of a high accelerating voltage (15 kV) and the use of backscattered electrons to record the images. These deposits become visible when using secondary electrons and a smaller accelerating voltage (5kV) to record images. This is demonstrated in Figure 6.9a which clearly shows the $\text{Mg}(\text{OH})_2$ deposit. The Zn content of the phase is demonstrated in Figure 6.9b, and the presence of the T-phase confirmed in the SEM micrograph of the as-polished sample prior to immersion,

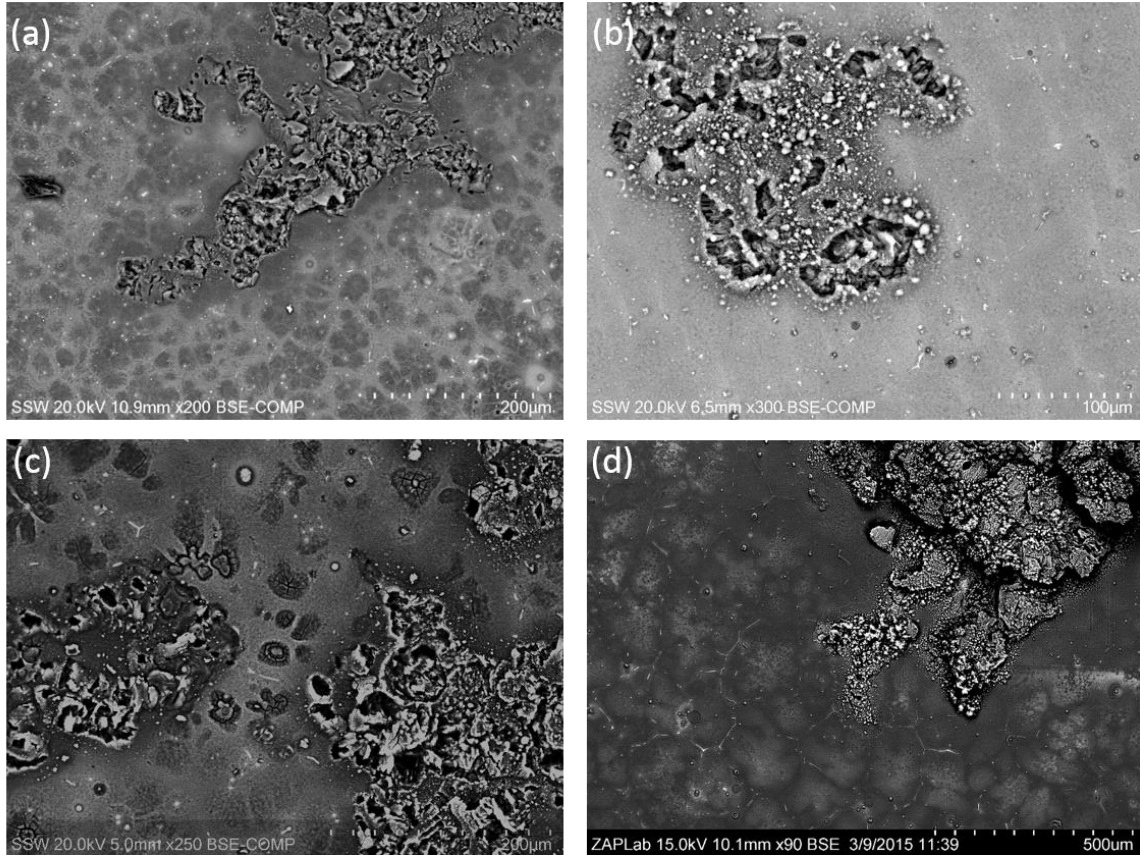


Figure 6.10: SEM micrographs recorded in BSE mode for wedge cast ZEK100 (a) section A, (b) section D, (c) section G and (d) section M following immersion in a 0.03 M NaCl solution for 24 h. Note the differences in the scale bar from image to image. Images show the filiform-like corrosion morphology which exists on each specimen.

Figure 6.9(c). Although not shown many additional such examples are visible on the surfaces of the sections.

A clear distinction between the specimens is the apparent differences on the grain surfaces and on locations close to the grain boundaries. On A the film is coherent, uniformly distributed, and no microstructural features are visible. On the other sections the centres of the grains are lighter in colour suggesting a more copious $\text{Mg}(\text{OH})_2$ deposit and the areas along the grain boundaries dark suggesting a thinner, possibly more coherent, oxide film.

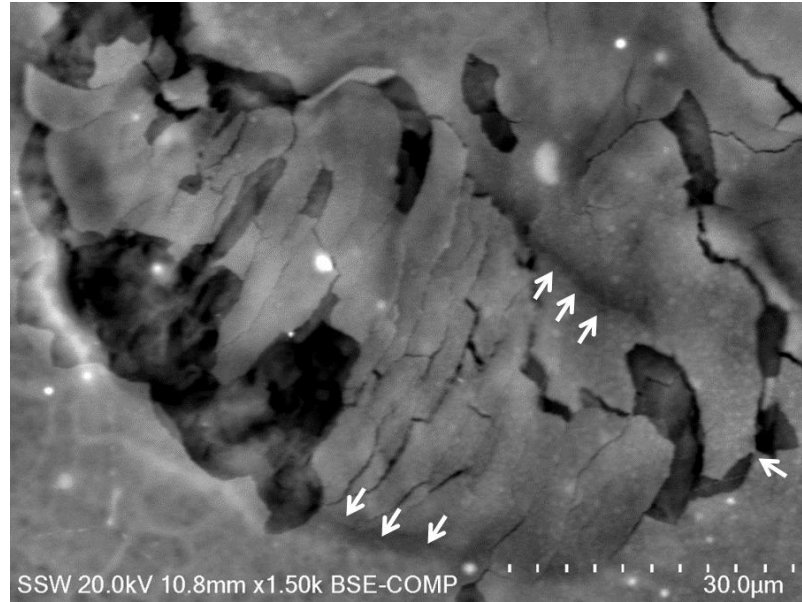


Figure 6.11: SEM micrograph of a corrosion filament formed on section A of a Mg ZEK100 alloy following 24 h immersion in 0.03 M NaCl. Arrows indicate regions where a pre-existing surface layer has been undermined by the propagation of a filament.

Figure 6.10 shows SEM micrographs recorded in BSE mode on areas exhibiting corrosion filaments developed after 24h of immersion. Such filaments are typical of those commonly observed on Mg and its alloys. No significant differences in the filaments on A, D, G and M are observed suggesting their propagation is not clearly dictated by the differences in microstructure, Figure 6.2 and Figure 6.8. When viewed under higher magnification, Figure 6.11, some regions at the margins of the filament remain intact (indicated by white arrows) while the deposit over the main body of the filament is fractured and lifted. This is consistent with the propagation of corrosion underneath the pre-existing corrosion film, as previously claimed by Williams et al.¹⁴

To investigate the nature of the corrosion process occurring in filament tracks the surface corrosion products were removed and the exposed tracks analyzed by SEM and CLSM, Figure 6.12 (a to d). These images clearly demonstrate the extensive corrosion

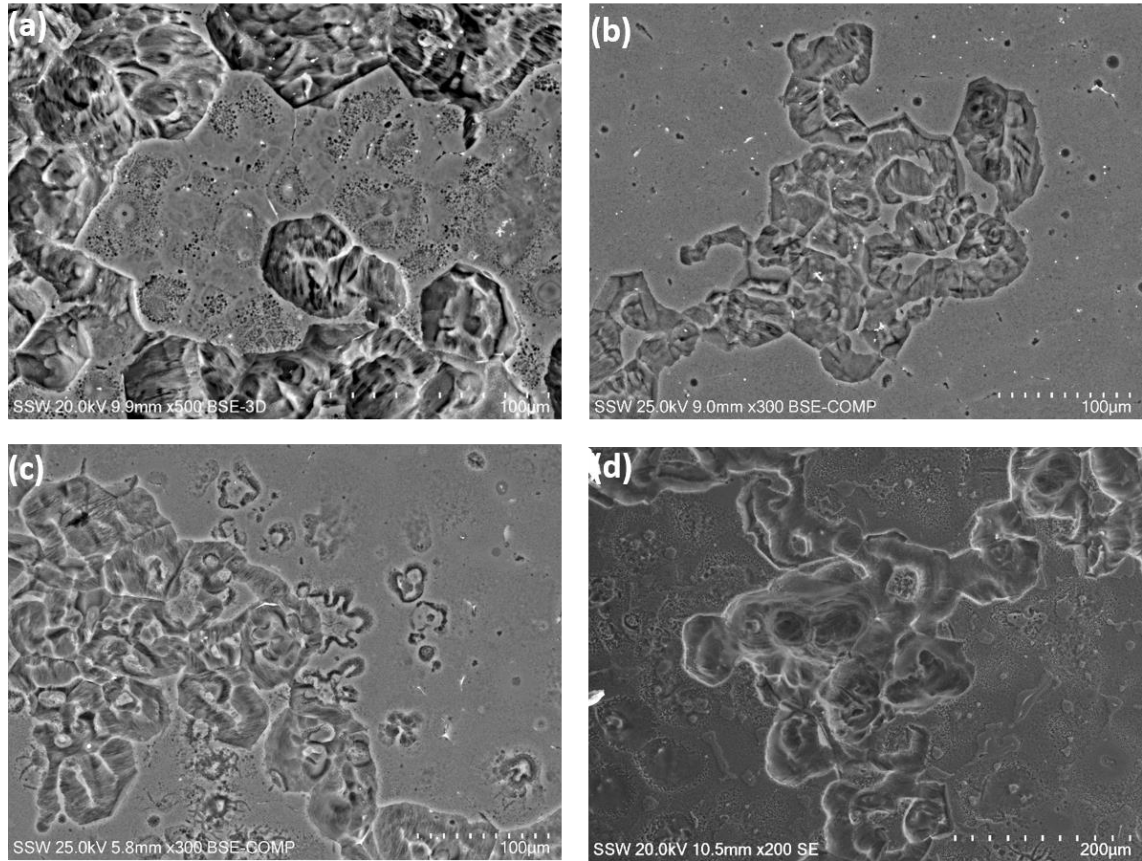


Figure 6.12: SEM micrographs recorded in BSE mode for wedge cast ZEK100 (a) section A, (b) section D, (c) section G and SE mode for (d) section M following removal of the corrosion product film with a chromic acid etch. Prior to the etch samples were immersed in a 0.03 M NaCl solution for 30 h. Note the differences in the scale bar from image to image. Images show both the general surface and the filiform-like corrosion morphology which exists on each specimen.

which occurred in the filament track compared to the relatively minor damage observed on the general surface. There is no evidence that the morphology and directionality of filiform propagation is dictated by the evolution of microstructure (Figure 6.2). One interesting observation is the presence of striations in the Mg matrix at the base of filiform tracks, a feature noted in our previous study for hydride areas within these locations.

To determine whether the cooling rate had any influence on the local corrosion within the filaments, CLSM depth profiles were recorded on three different surface

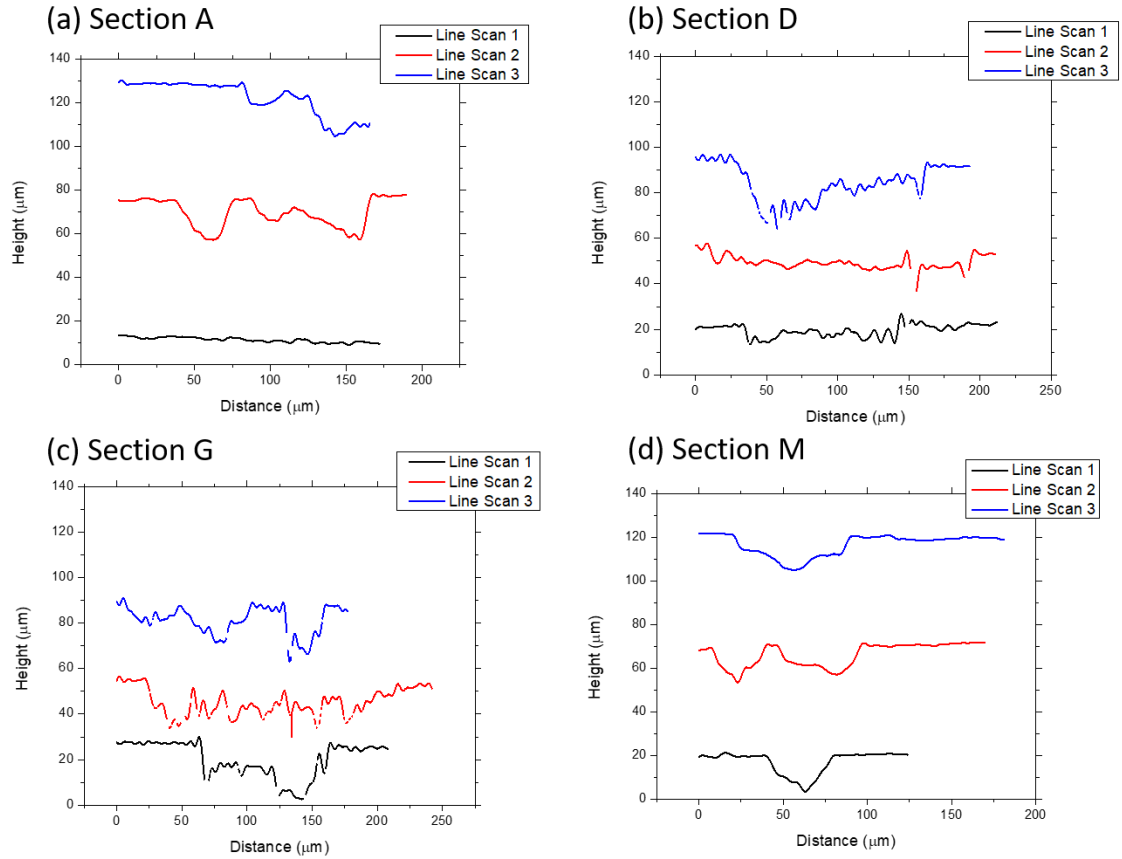


Figure 6.13: Depth profiles recorded on section A, D, G and M of a wedge cast Mg ZEK100 alloy following 30 h immersion in a 0.03 M NaCl solution and removal of the accumulated corrosion product with a chromic acid solution. Three line scans per sample were performed with CLSM in regions that contained corrosion filaments.

locations on each section, Figure 6.13 (a to d). The line scans shown were measured across areas which had experienced filiform corrosion. To provide a reference point, the termini of each scan was located on the general alloy surface. Each alloy exhibited a wide distribution of corrosion depths as well as filament widths. No obvious correlation exists between the depth of corrosion and the cooling rate of the section. On all sections, the maximum depth of penetration was ~ 25 to $30 \mu\text{m}$, confirming that, while lateral propagation was rapid only a limited amount of corrosion occurred at any given location

once the propagating filament front had moved on. These results are consistent with the SVET analyses of Williams et al.¹⁴

6.4 Discussion

Both electrochemical and microscopic analyses demonstrate that corrosion proceeds in two stages, although the first stage is short and only delays the eventual onset of filiform corrosion. Throughout the first stage a protective oxide/hydroxide film was formed with the transition to stage 2 indicating the initiation of the filiform corrosion process. Slow cooling leads to a more extensive segregation of alloying elements into the T-phase and an extension of the duration of stage 1. The film that grows during stage 1 is coherent and leads to a decrease in the overall corrosion rate and there is good evidence that both the T-phase and the Zr IMPs are functioning as microgalvanically-coupled cathodes.

On the rapidly cooled A, E_{CORR} increased rapidly leading to the earlier onset of filiform corrosion. Since little segregation of alloying elements to the vicinity of the grain boundaries occurs in this specimen, the oxide film formed is more coherent (Figure 6.7e and Figure 6.8a), but possibly thinner. This is likely due to the homogeneous distribution of rare earths and Zn in the alloy (Figure 6.2e). Although the effect of adding rare earths on the corrosion of Mg remains uncertain several authors have reported improved corrosion resistance,^{28,29} with the RE atoms being incorporated into surface films leading to their enhanced stability.

With a decrease in cooling rate more extensive segregation of alloying elements to the grain boundary region leads to increased formation of the T-phase and the decoration

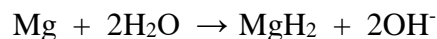
of the grain boundary regions with Zn. Since the formation of the T-phase would strip the α -Mg matrix of the rare earths as well as Zn it is possible this is reflected in the apparently slower rate of film growth (indicated by the slower increase in E_{CORR}) and the observation that the film grown on the surfaces of the grains, Figure 6.8, are whiter suggesting a greater accumulation of $Mg(OH)_2$. A more rapid accumulation of hydroxide over an extended growth period would suggest a more defective (porous) oxide/hydroxide.

Additionally, the patterning in the vicinity of the grain boundaries with Zn and the accumulation of T-phase appears to lead to a more coherent oxide in close proximity to the boundaries (Figure 6.8), but an enhanced corrosion of the grain boundaries themselves (Figure 6.7). This suggests a conflict between opposing effects. The enhanced corrosion in the boundary can be attributed to the influence of the microgalvanically coupled T-phase cathode, an effect which has been previously demonstrated. By contrast, the apparent protection of the areas adjacent to the grain boundaries may be attributable to the concentration of Zn in these regions (Figure 6.2). As noted by Cano et al.¹⁰ for the AZ31B alloy (~ the same Zn content as ZEK100) the films on areas of the surface less susceptible to corrosion, exhibit a thin Zn-enriched layer at the alloy/film interface. The accumulation of alloying elements such as Al in close proximity to the grain boundaries has also been shown to lead to an enrichment of Al at the oxide/Mg interface and a suppression of the corrosion rate. Since the $[Cl^-]$ is the same in all experiments in this study it is the difference in film properties which dictate the time to film breakdown and the transition to stage 2. As noted previously,^{10,11,30} MgO has a smaller molar volume than Mg (i.e., a Pilling-Bedworth ratio <1) and would, therefore, be susceptible to fracture (Figure 6.11). Although we have not examined the chemical nature of the initially grown oxide previous studies

have demonstrated that it will be a thin MgO/Mg(OH)₂.¹¹ On A, the rapid growth of a more coherent layer would be expected to lead to an earlier breakdown.

If it is presumed that fracture of the corrosion product film requires a specific stress level then the redistribution of alloying elements dictated by the different cooling rates of the alloy sections, which leads to differences in the time taken to reach the required stress value (i.e., the duration of stage 1) indicates the change in microstructure does influence the film properties. That a specific stress level is required is supported by the observation that the breakdown of the film initiates at the same E_{CORR} irrespective of the microstructure.

As noted by Williams et al.,¹⁴ and observed in this study, film fracture leads to rapid access of H₂O to the substrate Mg surface and the onset of the filiform process. Once initiated, filiform corrosion propagates at the same E_{CORR} on A, D, G and M at a rate apparently controlled by the area of propagation, indicating that the current density at the head of the filament is not primarily controlled by the differences in microstructure. Based on dynamic SIMS analyses our previous study demonstrated that this rapid corrosion process can be attributed to the enhancement of cathodic kinetics (cathodic activation) due to the rapid chemical formation of MgH₂ on the Mg surface at the breakdown site,



Since hydrides on light metals (Mg, Al, Ti)^{16,18} are catalytic for H⁺/H₂ reduction this leads to rapid corrosion and the evolution of H₂ due to the instability of the hydride which leads to its conversion to soluble Mg²⁺ and the deposition of Mg(OH)₂ in the locally generated alkaline environment



This combination of coupled reactions accounts for the co-location of the anode and cathode at the filament head, a key feature of the overall filiform corrosion process.

As shown previously on this alloy¹ the overall corrosion process is also partially driven by microgalvanic coupling of the filament head to hydride T-phase ($\text{Mg}_7\text{Zn}_3\text{Nd}$) IMPs. However, while the lower level of cathodic activity demonstrated to occur in regions behind the advancing corroding filament head could be attributed to such a microgalvanic coupling process, our results demonstrate this is not the key process driving propagation. By varying the alloy cooling rate the extent of formation of the T-phase is enhanced from section A through to M. Despite this major change the electrochemical behaviour is identical on all sections; i.e., both the variation of E_{CORR} with time and the PDP curves for all specimens remain identical. If the cathodically activated surface area had increased as a consequence of the more extensive formation of T-phase precipitates, then a decrease in E_{CORR} to less negative values and a corresponding shift in the polarization curves would have been observed in keeping with the observations of Williams et al.¹⁴

Two additional observations support a mechanism involving hydrides. Our previous study¹³ showed hydride was formed ahead of the filament tip demonstrating a mechanism for the lateral propagation. For hydride to form at such a location would require access of water to locations underneath the existing oxide film, a key feature of the filiform process. The ensuing rapid catalytic production of H_2 would then account for the fracturing and spallation of the originally-formed oxide we observe at the filiform tip (Figure 6.12). Additionally, the observation that, irrespective of the microstructure of the alloy, the depth of penetration of corrosion within a mature filament remains effectively the same indicates that the corrosion of an aged filament is not enhanced by the availability of

microgalvanically-couplable IMPs. The effective loss of reactivity at locations behind the filament head can be attributed to the conversion of the hydride to hydroxide with the latter offering a degree of protection to the filament track. .

6.5 Conclusions

Four sections of a wedge cast Mg ZEK100 were analyzed for their composition, microstructure and subsequent corrosion performance in aqueous saline solutions. The composition of each section remained nominally identical despite the gradient in cooling rate. The microstructure consisted of a Mg_7Zn_3RE T-phase which segregated to the grain boundaries, evenly dispersed Zr-rich IMPs and α -Mg. Grain size was shown to increase and T-phase particles and Zn distribution were shown to become more localized with a decrease in cooling rate. The change in cooling rate was shown to affect the duration of phase I of corrosion which is dominated by microgalvanic corrosion with the length of phase I increasing as cooling rate decreased. The transition from phase I to phase II was characterized by the onset and propagation of filiform-like corrosion. Initially, corrosion rates, as determined by cathodic Tafel analysis, decreased as phase I progressed but increased as a function of time in phase II. The magnitude of cathodic current densities decreased with cooling rate for both phases. Once phase II initiates, little difference is observed in the behaviour of corrosion filaments with respect to the depth of corrosion damage. This work, coupled with our previous work (see chapter 5) provide strong evidence that (i) MgH_2 is a key intermediate in filiform-like corrosion and (ii) this process (i.e the initiation and propagation) is influenced by the nature of the $MgO/Mg(OH)_2$ film.

6.6 References

- (1) Asmussen, R.M., W.J. Binns, P. Jakupi, and D. Shoesmith, *Corrosion* 71 (2015): pp. 242–254.
- (2) Neil, W.C., M. Forsyth, P.C. Howlett, C.R. Hutchinson, and B.R.W. Hinton, *Corros. Sci.* 51 (2009): pp. 387–394.
- (3) Abbott, T.B., *Corrosion* 71 (2015): pp. 120–127.
- (4) Ma Qian, D.H. StJohn, and M.T. Frost, *Scr. Mater.* 46 (2002): pp. 649–654.
- (5) Paliwal, M., and I.-H. Jung, *J. Cryst. Growth* 394 (2014): pp. 28–38.
- (6) Huehnerschulte, T.A., N. Angrisani, D. Rittershaus, D. Bormann, H. Windhagen, and A. Meyer-Lindenberg, *Materials* 4 (2011): pp. 1144–1167.
- (7) Dziuba, D., A. Meyer-Lindenberg, J.M. Seitz, H. Waizy, N. Angrisani, and J. Reifenrath, *Acta Biomater.* 9 (2013): pp. 8548–8560.
- (8) Nascimento, M.L., C. Fleck, W.-D. Müller, and D. Löhe, *Int. J. Mater. Res.* 97 (2006): pp. 1586–1593.
- (9) Cain, T., L. g. Bland, N. Birbilis, and J. r. Scully, *Corrosion* 70 (2014): pp. 1043–1051.
- (10) Cano, Z.P., M. Danaie, J.R. Kish, J.R. McDermid, G.A. Botton, and G. Williams, *Corrosion* 71 (2015): pp. 146–159.
- (11) Esmaily, M., J.E. Svensson, S. Fajardo, N. Birbilis, G.S. Frankel, S. Virtanen, R. Arrabal, S. Thomas, and L.G. Johansson, *Prog. Mater. Sci.* 89 (2017): pp. 92–193.
- (12) Taheri, M., J.R. Kish, N. Birbilis, M. Danaie, E.A. McNally, and J.R. McDermid, *Electrochimica Acta* 116 (2014): pp. 396–403.
- (13) Binns, W., F. Zargarzadah, V. Dehnavi, Jian Chen, J. Noel, and D. Shoesmith, *Corrosion* (2018), <http://corrosionjournal.org/doi/abs/10.5006/2918> (Sep. 24, 2018).
- (14) Williams, G., H. ap Llwyd Dafydd, and R. Grace, *Electrochimica Acta* 109 (2013): pp. 489–501.
- (15) Birbilis, N., G. Williams, K. Gusieva, A. Samaniego, M.A. Gibson, and H.N. McMurray, *Electrochem. Commun.* 34 (2013): pp. 295–298.
- (16) Adhikari, S., and K.R. Hebert, *J. Electrochem. Soc.* 155 (2008): p. C189.
- (17) He, X., D.W. Shoesmith, and J.J. Noel, *J. ASTM Int.* 5 (n.d.): p. 14.
- (18) Yan, L., S. Ramamurthy, J.J. Noël, and D.W. Shoesmith, *Electrochimica Acta* 52 (2006): pp. 1169–1181.
- (19) Fajardo, S., and G.S. Frankel, *Electrochimica Acta* 165 (2015): pp. 255–267.
- (20) Aung, N.N., and W. Zhou, *Corros. Sci.* 52 (2010): pp. 589–594.
- (21) Khan, M.I., A.O. Mostafa, M. Aljarrah, E. Essadiqi, and M. Medraj, “Influence of Cooling Rate on Microsegregation Behavior of Magnesium Alloys,” *Journal of Materials* (2014), <https://www.hindawi.com/journals/jma/2014/657647/abs/> (Dec. 21, 2018).
- (22) Zhang, J., Z. Fan, Y.Q. Wang, and B.L. Zhou, *J. Mater. Sci. Lett.* 19 (2000): pp. 1825–1828.
- (23) ASTM, “Standard Test Methods for Chemical Analysis of Cuprous Oxide and Copper Pigments” (ASTM International, 2013).
- (24) *Int. Mater. Rev.* 60 (2015): pp. 169–194.
- (25) Gandel, D.S., M.A. Easton, M.A. Gibson, T. Abbott, and N. Birbilis, *Corros. Sci.* 81 (2014): pp. 27–35.

- (26) Danaie, M., R.M. Asmussen, P. Jakupi, D.W. Shoesmith, and G.A. Botton, *Corros. Sci.* 77 (2013): pp. 151–163.
- (27) Asmussen, R.M., P. Jakupi, M. Danaie, G.A. Botton, and D.W. Shoesmith, *Corros. Sci.* 75 (2013): pp. 114–122.
- (28) Birbilis, N., M.A. Easton, A.D. Sudholz, S.M. Zhu, and M.A. Gibson, *Corros. Sci.* 51 (2009): pp. 683–689.
- (29) Coy, A.E., F. Viejo, P. Skeldon, and G.E. Thompson, *Corros. Sci.* 52 (2010): pp. 3896–3906.
- (30) Ismail, K.M., and S. Virtanen, *Electrochem. Solid-State Lett.* 10 (2007): pp. C9–C11.

7 Summary and Future Work

This thesis utilized a combination of electrochemical, both bulk and localized techniques, and surface analysis to investigate the corrosion properties of lightweight alloys for automotive applications. Two general themes were investigated: (i) the fundamental mechanism responsible for the widely observed “filiform-like” corrosion morphology on magnesium and magnesium alloys and (ii) the effect of alloying elements and the resultant microstructure size and distribution on the corrosion of aluminum and magnesium alloys. The following is brief summary of the findings along with suggestions for future work to advance the understanding of each topic.

Chapter 3 examined three Al-Cu-Mn-Mg alloys with different amounts of Mg up to about 2 wt%. It was found that the Mg additions created no noticeable change in the microstructure of the alloys but did activate the matrix towards oxidation. However, over the Mg concentration range studied, this activation effect was minor. Localized electrochemical examination via SECM confirmed the observations found during bulk electrochemical analysis (i.e. slight anodic activation of the matrix). In all cases, it was observed that local cathodic sites were initially static (i.e. remained in one place) but changed position on the surface with time. In accordance with the literature, we postulate that this effect could be due to a dissolution and redeposition of Cu which then can act as a local cathode. Future work in this area should focus on high resolution surface analysis (e.g. TEM, XPS or EELS).

Chapter 4 investigated the effect of the size and distribution of Al-Mn IMPs and $\text{Mg}_{17}\text{Al}_{12}$ β -phase on the corrosion performance of the Mg AM50 alloy. A wide range

of $[\text{Cl}^-]$, immersion times and electrolyte solvents were investigated. We found that the nature of the microgalvanic couple between the Mg matrix and the secondary microstructures was strongly influenced by the $[\text{Cl}^-]$ and the geometry of the microstructure. These factors greatly influence the nature and protectiveness of the $\text{MgO}/\text{Mg}(\text{OH})_2$ film such that fast cooled alloys (i.e. evenly dispersed microstructures) exhibit the greatest corrosion resistance at high $[\text{Cl}^-]$ and slow cooled alloys (i.e. disperse microstructures) are superior at low $[\text{Cl}^-]$. A combination of FIB/SEM/TEM investigations to properly characterize the nature of these films generated in each environment would help to understand the evolving nature of these alloys with respect to immersion environment.

Chapter 5 examined the fundamental corrosion mechanism of the “filiform-like” corrosion morphology often reported for Mg and Mg alloys. Hydrides were grown on the Mg surface by cathodic galvanostatic polarization which are shown to match the filiform morphology seen for samples undergoing free corrosion. SIMS analysis of the corrosion filaments found that while hydrides were sparsely present in the filaments there was a significant enrichment of hydrides at the leading edge of a filament, consistent with a mechanism which relies on the generation and subsequent degradation of a catalytic MgH_2 species. Future work should focus a combined hydrogen collection, electrochemical and SIMS analysis to further understand the mechanism of hydride formation to improve alloy design.

Chapter 6 builds on Chapter 5 by examining the effect of microstructure of the corrosion of Mg ZEK100. Wedge casting is used to create alloys with identical compositions but variable microstructure size and distributions. It was found that

alloys with more coherent films initiated filiform-like corrosion earlier than those with less coherent films. This supports the observations of Chapter 5 which suggest that the semi-protective nature of the MgO/Mg(OH)_2 film is an important factor in the initiation and propagation of filiform-like corrosion. Future work should utilize high resolution surface analysis (e.g. FIB, TEM) to better characterize surface films to better understand this process. Further, producing artificial films with tunable properties on the surface of Mg alloys could offer a unique way to probe the nature of this phenomenon.

Curriculum Vitae

Name: Wilfred Jeffrey Binns

Post-secondary Education and Degrees: The University of Western Ontario
London, Ontario, Canada
2008-2012 B.Sc.

The University of Western Ontario
London, Ontario, Canada
2013-2018 Ph.D.

Honours and Awards: Laurene Paterson Estate Scholarship
2012

Garnet Alexander Woonton Scholarship
2012

Christian Sivertz Scholarship in Physical Chemistry
2013

Province of Ontario Graduate Scholarship
2016, 2017

Related Work Experience Corrosion Scientist
Nuclear Waste Management Organization
2017-present

Teaching Assistant
The University of Western Ontario
2013-2017

Publications:

Senior, N.A., Newman, R.C., Artymowicz, D., Binns, W.J., Keech, P.G., Hall, D.S. A Method to Measure Extremely Low Corrosion Rates of Copper Metal in Anoxic Aqueous Media, *Electrochem. Comm.* submitted **2018**.

Binns, W.J., Zargarzadah, F., Dehnavi, V., Chen, J., Noël, J., Shoesmith, D. Physical and Electrochemical Evidence for the Role of a Mg Hydride Species in Mg Alloy Corrosion, *CORROSION* **2018**, online early: <https://doi.org/10.5006/2918>.

Dehnavi, V., Binns, W.J., J.J. Noël, Shoesmith, D.W., Luan, B.L. Growth behavior of low-energy plasma electrolytic oxidation coatings on a magnesium alloy, *J. Magn. Alloys*, 6 (3) p.229-237.

Asmussen, R.M., Binns, W.J., Partovi-Nia, R., Jakupi, P., Shoesmith, D.W. The stability of aluminum-manganese intermetallic phases under the microgalvanic coupling conditions anticipated in magnesium alloys, *Mater. Corros.*, **2016**, 67 (1) p.39-50.

Asmussen, R.M., Binns, W.J., Jakupi, P., Dauphin-Ducharme, P., Tefashe, U.M., Mauzeroll, J., Shoesmith, D.W. Reducing the corrosion rate of magnesium alloys using ethylene glycol for advanced electrochemical imaging, *Corros. Sci.*, **2015** 93 p.70-79.

Dauphin-Ducharme, P., Binns, W.J., Snowden, M.E., Shoesmith, D.W., Mauzeroll, J. Determination of the local corrosion rate of magnesium alloys using a shear force mounted scanning microcapillary method, *Faraday Discuss.*, **2015** 180 p.331-345.

Asmussen, R.M., Binns, W.J., Jakupi, P., Shoesmith, D.W. The influence of microstructure on the corrosion of magnesium alloy ZEK100, *CORROSION*, **2014** 71 (2) p.242-254.

Dauphin-Ducharme, P., Asmussen, R.M., Tefashe, U.M., Danaie, M., Binns, W.J., Jakupi, P., Botton, G.A., Shoesmith, D.W., Mauzeroll, J. Local hydrogen fluxes correlated to microstructural features of a corroding sand cast AM50 magnesium alloy, *J. Electrochem. Soc.*, **2014** 161 (12) p.C557-C564.

Asmussen, R.M., Binns, W.J., Jakupi, P., Shoesmith, D.W. Microstructural effects on corrosion of AM50 magnesium alloys, *J. Electrochem. Soc.*, **2014** 161 (10) p.C501-C508.

Selected Conference Presentations:

R.M. Asmussen*, **J. Binns**, P. Jakupi, D. Shoesmith “Electrochemical impedance spectroscopy investigation of microstructural effects on the corrosion of magnesium alloys” 15th Topical Meeting of the International Society of Electrochemistry, Niagara Falls, ON, Canada. Apr 30, 2014 (Presentation)

R.M. Asmussen*, **J. Binns**, P. Jakupi, M. Danaie, G. Botton, D. Shoesmith “The microstructural effects on corrosion of AM50 alloys” Materials Science and Technology 2013, Montreal, QC, Oct 27-31 2013 (Presentation)

Asmussen R.M.*, **Binns W.J.**, Jakupi P., Shoesmith D.W. “*Evaluation of the Surfaces of Corroding Magnesium Alloys*” Surface Canada 2013, London, ON, May 8-10, 2013 (Poster)

W.J. Binns*, R.M. Asmussen, P. Jakupi, D.W. Shoesmith “Electrochemical and microscopic investigations of the corrosion performance of AM50 magnesium alloys” Surface Canada 2013, London, ON May 8-10, 2013 (Poster)

R. Matthew Asmussen*, P. Jakupi, **W. Binns**, P. Dauphin Ducharme, U. Telfase, J. Mauzeroll, D.W. Shoesmith “The effect of microstructure on the corrosion of Mg alloys” NACE Corrosion 2013, Orlando, FL, USA, Mar 17-21 2013 (Poster)

W.J. Binns*, R.M. Asmussen, P. Jakupi, D.W. Shoesmith “Electrochemical and microscopic investigations of the corrosion performance of AM50 magnesium alloys” MS&T 2013, Canada 2013, Montreal, QC October 27-31, 2013 (Poster)

W.J. Binns*, R.M. Asmussen, P. Jakupi, D.W. Shoesmith “The Effect of Aluminum Distribution on the Corrosion Behaviour of Magnesium AM50 Cast Alloys in Aqueous and Ethylene Glycol Environments” Gordon Research Conference in Aqueous Corrosion, U.S.A., 2014, New London, NH May 8-10, 2013 (Poster)

W. Jeffrey Binns*, R.M. Asmussen, P. Jakupi, D.W. Shoesmith, “Relating corrosion behaviours of magnesium AM50, AZ31 and ZEK100 alloys to their casting procedures and microstructures” Corrosion 2015, Dallas, TX, Mar 15-19 2014. (Presentation)

W. Jeffrey Binns*, D.W. Shoesmith, “The influence of cooling rate on the corrosion properties of Mg ZEK100 alloy via wedge casting” NACE Student Symposium, Toronto, ON, July 6 2015. (Presentation).

W. Jeffrey Binns*, Jeffrey D. Henderson, D. Zagidulin, D.W. Shoesmith “The Effect of Mg Content on the Cathodic Kinetics of Al₆(Fe,Mn) Particles in Al Brazing Sheets Alloys” Gordon Research Seminar in Aqueous Corrosion, New London, New Hampshire, July 9-10 2016. (Presentation).

W. Jeffrey Binns*, Jeffrey D. Henderson, D. Zagidulin, D.W. Shoesmith “The Effect of Mg Content on the Cathodic Kinetics of Al₆(Fe,Mn) Particles in Al Brazing Sheets Alloys” Gordon Research Conference in Aqueous Corrosion, New London, New Hampshire, July 10-15 2016. (Poster).

W. Jeffrey Binns*, A. Kirkey, V. Dehnavi, D.W. Shoesmith “The influence of cooling rate on the corrosion behaviour of wedge cast Mg alloys” NACE Northern Area Eastern Conference 2016, Toronto, ON, October 31 – November 2 2016.